Doctoral   Science

Photopolymerizable Nanocomposites for Holographic Applications

Elsa Leite
Technological University Dublin

PHOTOPOLYMERIZABLE NANOCOMPOSITES FOR HOLOGRAPHIC APPLICATIONS

Elsa Leite

A thesis submitted for the degree of Doctor of Philosophy to the Dublin Institute of Technology

Supervisors

Dr. Izabela Naydenova, Prof. Vincent Toal and Dr. Svetlana Mintova

Centre for Industrial and Engineering Optics

School of Physics

Dublin Institute of Technology

2010

DECLARATION

I certify that this thesis which I now submit for examination for the award of PhD is entirely my own work and has not been taken from the work of others save and to the extent that such work has been cited and acknowledged within the text of my work.

This thesis was prepared according to the regulations for postgraduate studies by research of the Dublin Institute of technology and has not been submitted in while or in part for an award in any other Institute or University.

The work reported on this thesis conforms to the principles and requirements of the Institute's guidelines for ethics in research.

The Institute has permission to keep, or lend or to copy this thesis in whole or in part, on condition that any such use of the material or the thesis be duly acknowledged.

Signature _____ Date _____

ACKNOWLEDGEMENTS

DEDICATED

to my parents Fernanda and Júlio Leite

and my beloved daughters Beatriz and Anjali

ABSTRACT

Photopolymerizable nanocomposites with good optical properties consisting of an acrylamide based photopolymer and zeolite nanoparticles (Beta, zeolite A, AlPO-18, silicalite-1 and zeolite L) were fabricated and characterized for holographic applications. The colloidal zeolite solutions used in this project were characterized by several techniques including X-Ray Diffraction (XRD), Dynamic Light Scattering (DLS), Scanning Electron Microscopy (SEM) and Raman spectroscopy to ensure their successful synthesis.

The dependence of grating performances in these nanocomposites on recording intensity, spatial frequency and zeolite concentration were studied. It was found that the incorporation of silicalite-1 nanoparticles or a small amount of zeolite A nanoparticles (up to 1% wt.) leads to an improvement of the refractive index modulation of the gratings, while the addition of AlPO-18 and Beta nanoparticles to the photopolymer did not yield higher refractive index modulation. Despite a partial redistribution of nanoparticles during the holographic recording was observed, these results can be explained by the hydrophobic/ hydrophilic nature of the nanoparticles and their interactions/absence of interactions with the host photopolymer (studied by Visible, Raman and ^{13}C NMR Spectroscopy).

Gratings recorded in Beta and AlPO-18 nanocomposites were tested for holographic sensing. The interactions between zeolite L and sensitizing dyes was studied by visible spectroscopy for potential use in variable spectral sensitivity optical materials. A new photopolymerizable material was developed, with less toxic properties than acrylamide monomer and gratings recorded in this type of material were characterized for use in holographic sensor applications.

TABLE OF CONTENTS

LIST OF FIGURES

6

LIST OF TABLES

MOTIVATION & OBJECTIVES

The work described in this thesis is part of a larger project within the Centre for Industrial & Engineering Optics (IEO) group, whose research expertise is in holography and holographic materials development, interferometric systems and devices and optical profilometry.

A decade ago, holographic systems promised to revolutionize data storage and several materials were developed to meet the medium requirements for this application. Previous work showed that the incorporation of silicalite-1 zeolites in acrylamide based photopolymers resulted in an improvement in the dynamic range and the extent of shrinkage during holographic recording.

The focus of this research was to produce a novel generation of photopolymerizable materials that could be successfully used in several holographic applications. These new materials were to incorporate nanoparticles in acrylamide based photopolymers. The project was also expected to produce a model explaining the role of nanoparticles during holographic recording based on the physicochemical mechanism of the interaction between nanoparticles and the host photopolymer.

The ideal material should remain self-processing and water soluble (as the acrylamide based photopolymer already is) but it is expected to have a larger dynamic range (greater than 10^{-2}) while possessing low scattering of light.

The main objectives we intended to achieve with this work were:

- **Study of the influence of nanoparticles on holographic recording properties of nanocomposites**

    ✓ Identification of nanoparticles compatible with acrylamide-based photopolymers

    ✓ Study of optical properties of the newly created nanocomposites

    ✓ Study of the influence of the nanoparticle properties (refractive index, size, structure) on the sensitivity, spatial frequency response and dynamic range of the zeolite nanocomposites

- **Study of the Host/ Dopant Interactions**

    ✓ Study of the interaction of nanoparticles with host photopolymer by relevant analytical techniques

    ✓ Study of the spatial redistribution of the nanoparticles during hoographic recording

- **Propose a model for holographic recording in nanocomposites**

CHAPTER 1: HOLOGRAPHY

1.1 THEORY OF HOLOGRAPHY

In this chapter, the history and principles of holography are briefly discussed. Also, a classification of different types of holograms is given. Since in the present work volume phase holograms were used, this type of hologram is described in more detail. The reason for choosing of this type of hologram was because of their widespread use in holographic data storage and fabrication of sensors, fields that are of much interest to the IEO group.

Holography is a technique by which a wavefront can be recorded and thereafter reconstructed in the absence of the original wavefront. A hologram is formed when a light sensitive material is exposed to the pattern of interference between an object and a reference beam. In all conventional recording techniques such as photography, a flat picture of a three-dimensional scene is recorded on a light-sensitive surface. What is recorded is merely the intensity distribution in the original scene. As a result, all information on the relative phases of the light waves from different points or, in other words, information about the relative optical paths to different parts of the object is lost [1].

The unique characteristic of holography is the recording of the complete wave field, that is to say, both the amplitude and the phase of the light waves scattered by the object. Since all recording media respond only to the intensity, it is necessary to convert the phase information into variations of intensity. This is done by using coherent illumination and adding a reference wave to the wave scattered by the object [1].

The history of holography began with its invention by Gabor in 1948. He described a new method that enabled one to obtain the image of an object from the diffraction pattern

produced by the object. He published the principle of holography and the results of his experiments in *Nature* (1948) [2], *Proceedings of the Royal Society* (1949) [3] and *Proceedings of the Physical Society* (1951) [4].

Gabor's aim when he proposed the idea of holographic imaging was to obtain increased resolution in electron microscopy. Prior to his work, holographic imaging can be traced back to work by Wofke [5] and Bragg [6, 7] in X-ray crystallography, which led to the development of the "Bragg X-ray microscope".

Optical holography was not very successful initially, due mainly to the poor quality of holographic images [1]. The breakthrough which effectively solved the twin image problem and opened the way to the large scale development of optical holography was the off-axis reference beam technique developed by Leith & Upatnieks [8, 9] and the development of the laser in 1960 by T. Maiman. This made available for the first time a powerful source of highly coherent light and made it possible to record holograms of diffusely reflecting objects with appreciable depth [10].

1.2   *THE HOLOGRAPHIC PROCESS*

The holographic process involves two steps: the recording of the hologram and the subsequent reconstruction of the object wave.

The process of recording a hologram can be explained in terms of the theory of superimposition of waves by two beam interference. If two wavefronts overlap interference occurs (as shown in Figure 1.1). This interference pattern can be recorded in a recording

medium and it consists of a set of straight parallel fringes. If one uses two plane waves and the hologram is assumed to lie with its faces parallel to the (x,y) plane and to be of thickness d in the z dimension the fringes are perpendicular to the (x,y)plane.
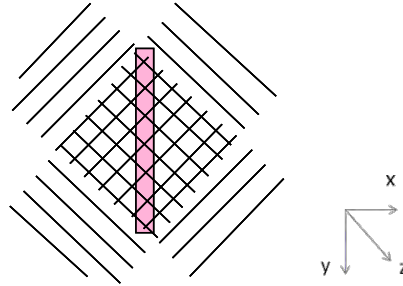
Figure 1.1.   Recording of a plane wave (transmission).

The interference pattern (hologram) diffracts the incident light to reconstruct the original beam (see Figure 1.2).
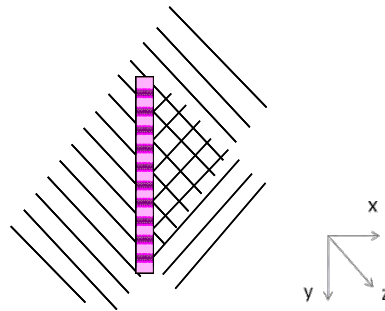
Figure 1.2.   Reconstruction of a plane wave (transmission).

If these two plane wavefronts have complex amplitudes U_1 (object wave) and U_2 (reference wave) at a point r, expressed by [11]:

$$U_1 = u_1 \exp i \left(2\pi f t - k_1 \cdot r \right) \qquad \text{(Eq. 1.1)}$$

$$U_2 = u_2 \exp i \left(2\pi f t - k_2 \cdot r \right) \qquad \text{(Eq. 1.2)}$$

where u_i is the amplitude, f the frequency, t is time and $k_i = \left(\dfrac{2\pi}{\lambda} \right) n_i$, λ is the wavelength and n_i is the refractive index. Omitting the time dependence we can rewrite equations 1.1 and 1.2:

$$U_1 = u_1 \exp \left(-i k_1 \cdot r \right) \qquad \text{(Eq. 1.3)}$$

$$U_2 = u_2 \exp \left(-i k_2 \cdot r \right) \qquad \text{(Eq. 1.4)}$$

and the intensity at a point r is then given by:

$$I = I_1 + I_2 + 2 \sqrt{I_1 I_2} \cos \left(k_1 - k_2 \right) r \quad \text{(Eq. 1.5)}$$

where I_i are the intensities of the waves.

For simplicity the axes are chosen so that n_i lies in the xz-plane and makes equal but opposite angles θ with the z-axis [11]. Hence:

$$n_1 = \sin \theta\, i + \cos \theta\, k \qquad \text{(Eq. 1.6)}$$

$$n_2 = -\sin \theta\, i + \cos \theta\, k \qquad \text{(Eq. 1.7)}$$

and

$$\left(k_1 - k_2 \right) = \left(\frac{4 \pi n}{\lambda} \right) \sin \theta\, i \qquad \text{(Eq. 1.8)}$$

Consider the time-averaged light intensity along a line parallel to the x-axis. Such a line is described by the vector $r = x\, i + z_0 k$, where z_0 is the position of the line in the z-axis. Eq. 1.5 then becomes [11]:

$$I = I_1 + I_2 + 2 \sqrt{I_1 I_2} \cos \left(\frac{4 \pi}{\lambda} \sin \theta \right) \qquad \text{(Eq. 1.9)}$$

This means that the intensity varies sinusoidally along any line parallel to the z-axis and it is known as interference fringe pattern.

The distance Λ (in transmission mode) between the nearest two points with the same intensity in the intensity variation is given by [11]:

$$\Lambda = \frac{\lambda}{2\sin\theta} \qquad \text{(Eq. 1.10)}$$

Λ can be defined as the spatial period of the unslanted grating (fringes are perpendicular to the surface of the material), i.e., the space between two adjacent fringes and $1/\Lambda$ is the spatial frequency of the grating.

1.3   CLASSIFICATION OF HOLOGRAMS

There are four basic hologram types, i.e., the thick and thin versions of amplitude and phase holograms.

1.3.1   AMPLITUDE AND PHASE HOLOGRAMS

The physical change in the recording material must be capable of affecting the reconstructing wave. This means that the hologram must alter either the amplitude or the phase of this wave, which defines the distinction between amplitude and phase holograms. If a hologram affects both amplitude and phase simultaneously it is termed a complex hologram. Other than the thin surface deformation phase type, most holograms are in principle complex since they depend upon variations of refractive index and absorption coefficient, quantities which are inextricably linked by the Kramers-Kronig relations [12].

Amplitude holograms have lower maximum achievable diffraction efficiency and thus have been used more rarely. Some examples of their application are in communications [13], in the fabrication of transmission holographic optical elements (HOE) [14] and in holographic data storage [15] to a lesser extent. On the other hand, phase holograms also find applications in communications [16], fabrication of HOEs [17] and have been widely used in data storage [18]. They also find applications in fields such as holographic scanners [19], spectroscopy [20], medical applications [21] and holographic interferometry [22].

1.3.2 THIN AND THICK HOLOGRAMS

A hologram can be considered thin if its information carrying structure is substantially two-dimensional, that is, if its thickness is small compared with the wavelength of light [12].

Thin holograms and volume holograms correspond to the Raman-Nath and Bragg diffraction regimes, respectively [1]. The distinction between these two regimes is commonly made on the basis of a parameter Q [23] which is defined by the relation:

$$Q = \frac{2\pi\lambda_0 d}{n_0 \Lambda^2}$$

(Eq. 1.11)

where λ_0 is the wavelength of light, d is the thickness of the layer, n_0 is the refractive index and Λ is the spatial period of the grating as defined by Eq. 1.10.

Small values of Q (Q< 1) correspond to thin gratings, while large values of Q (Q>10) correspond to volume gratings. The region $1 \geq Q \geq 10$ represents intermediate regime holograms [24].

Thin holograms, both computer-generated and optically recorded, have shown much utility in the fields of imaging (embossed holograms, such as the images on bank cards), beam shaping [25] and microscopy [26]. On the other hand, volume holograms provide potential for higher efficiency and greater capability for multiplexing information due to their angular and frequency selectivity properties. They will be discussed in more detail in the following sections of this work.

1.4 VOLUME HOLOGRAMS

In this work, volume holograms (also called thick holograms) were recorded since they are very useful in many areas of interest for the IEO research group, such as holographic data storage (HDS) [27, 28], which allows large storage capacities (in the order of TB) and high transfer rates (in the order of GB/s), and sensing [29, 30]. They also find applications in volume HOEs [31], interconnections [32], optical filters [33] and 3-D displays [34].

This type of hologram is a three-dimensional system of layers corresponding to a periodic variation of absorption or refractive index and the diffracted beam amplitude is a maximum only when the Bragg condition is satisfied [1] (for Bragg condition see Eq. 1.17).

.

1.4.1 THE COUPLED WAVE THEORY

When analysing the diffraction of light by thick gratings, it is necessary to take into account the fact that the amplitude of the diffracted waves increases progressively, while that of the incident wave decreases, as they propagate through the grating. One way of doing this is by means of a coupled wave approach, developed by Kogelnik [35].

The grating vector K is perpendicular to the fringe planes. It is of length $|K|=2\pi/\Lambda$, where Λ is the grating period. The refractive index n and the absorption constant α are assumed to vary sinusoidally, their values at any point r being given by the relations [1]:

$$n = n_0 + n_1 \cos(K \cdot r) \qquad \text{(Eq. 1.12)}$$

$$\alpha = \alpha_0 + \alpha_1 \cos(K \cdot r + \varphi) \qquad \text{(Eq. 1.13)}$$

where n_0 is the average refractive index, n_1 is the refractive index modulation, α_0 is the average absorption constant and α_1 is the absorption constant modulation and φ is the phase difference allowed between the refractive index and the absorption constant.

22

The coupled wave theory assumes monochromatic light incident on the hologram grating at or near the Bragg angle and polarized perpendicular to the plane of incidence. If the thickness of the medium is large enough, only two significant light waves are assumed to be present in the grating: the incoming "reference" wave R and the outgoing "signal" wave S [35]. The other diffraction orders violate the Bragg condition strongly and are severely attenuated and so can be neglected [1].

Diffraction efficiency of the grating, η, in the present work is defined as the ratio of diffracted light intensity I_1, to incident light intensity, I_0.

$$\eta = \frac{I_1}{I_0} \qquad \text{(Eq. 1.14)}$$

Thick holographic layers can be used to record transmission and reflection holograms.

1.4.2   VOLUME PHASE TRANSMISSION HOLOGRAMS

Gratings having a refractive index variation given by Eq. 1.12, with $k = \dfrac{2\pi}{d}$ (d being the thickness of the grating) and having negligible absorption can be regarded as volume phase transmission holograms (Fig. 1.3). The reconstructed images have amplitudes whose magnitude is:

$$|A| = \sin\left(\frac{\pi\, n_1\, d}{\cos\theta \cdot \lambda}\right) \qquad \text{(Eq. 1.15)}$$

where n_1 is the refractive index modulation, d is thickness of the layer, λ is the free space wavelength and θ the angle of incidence [12]. This is valid for s-polarized readout.
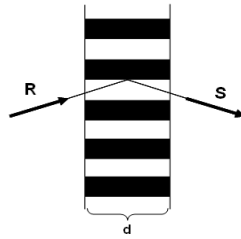
Figure 1.3.   **Transmission Volume Hologram; R is the incoming "reference" wave R and S the outgoing "signal" wave.**

Such holograms can, therefore, achieve a theoretical maximum diffraction efficiency of 100% when $n_1 d = \frac{1}{2} (\lambda \cos\theta)$.

1.4.3   *VOLUME PHASE REFLECTION HOLOGRAMS*

Thick reflection phase holograms (see Fig. 1.4) reconstruct images with amplitude whose magnitude is [12]:

$$|A| = \tanh\left(\frac{\pi\, n_1\, d}{\cos\theta \cdot \lambda} \right) \qquad \text{(Eq. 1.16)}$$
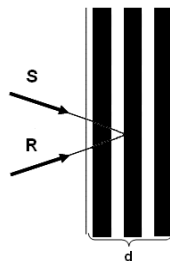
Figure 1.4.   **Reflection Volume Hologram; R is the incoming "reference" wave R and S the outgoing "signal" wave.**

This type of hologram also approaches a limiting diffraction efficiency of 100%, but it does so asymptotically with increasing *$n_1 d$*.

The diffraction efficiency of thick phase holograms is shown in Fig. 1.5.
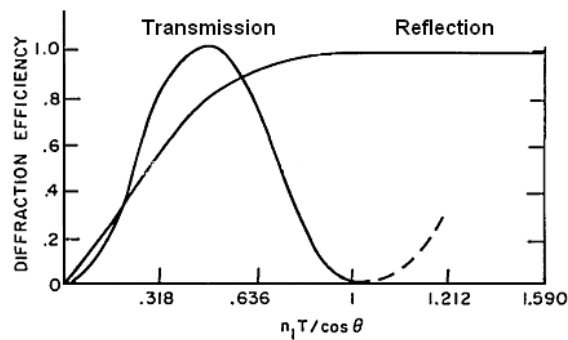
Figure 1.5.   Theoretical diffraction efficiency for thick transmission and reflection phase holograms (after Kogelnik [35]).

1.5   HOLOGRAPHIC EXPERIMENTAL SETUP

The final quality of a holographic image will depend on a number of factors that should be taken into account when building the holographic setup [36]:

- Vibration isolation - any change in the phase difference between the two beams during the exposure will result in a movement of the fringes and reduced modulation of the hologram;

- Coherence of the laser light - in order to obtain maximum fringe visibility, i.e., as high a contrast as possible it is also essential to use a coherent light source. This is because one needs a stable interference pattern;

- Beam expansion - due to high coherence of laser light, the expanded beam invariably exhibits diffraction patterns (spatial noise) due to scattering from dust particles on the optical surfaces in the beam path, which can be eliminated by spatially filtering the beams.

1.5.1   REAL TIME OBSERVATION OF GRATING FORMATION

The grating growth can be monitored in real time by probing it with a laser beam with a wavelength to which the photopolymer is insensitive, incident at the Bragg angle.

This Bragg angle should satisfy the following condition:

$$\frac{\lambda_1}{\sin\theta_1} = \frac{\lambda_2}{\sin\theta_2}$$
(Eq. 1.17)

where λ_1 is the wavelength of the recording beam, λ_2 is the wavelength of the probe beam, θ_1 is half of the angle between the two recording beams and θ_2 is the angle between the probe beam and normal.

Eq. 1.17 arises from Bragg's law [37]:

$$m\lambda = 2d \cdot \sin\theta$$
(Eq. 1.18)

where m is an integer, λ is the wavelength and d is the spacing between the planes in the atomic lattice, and θ is the angle between the incident ray and the scattering planes.

1.6   CONCLUSIONS

Holography is a relatively new field in optics. It was introduced by Denis Gabor who called it "wavefront reconstruction". Although there are dynamic holograms in which the reconstruction and the recording are practically simultaneous, for simplicity the holographic process can be divided in two-steps; first a hologram is recorded using a reference wave coherent with the light scattered or diffracted by an object, so that information about the amplitude and phase of these waves is retained; then from this recorded interference pattern an image of the original object can be reconstructed using just the reference wave. There are many types of holograms, depending on whether amplitude or phase information (amplitude or phase holograms) is recorded, and on the thickness of the recording medium relative to the spatial frequencies that are recorded (thin or thick holograms) and on the recording geometry (transmission or reflection holograms). These

different types of holograms find applications in many fields of optics and some examples were mentioned.

Particularly important for this present work are volume phase holograms and the coupled wave theory by Kogelnik, which explains their holographic behaviour, was briefly discussed.

1.7 REFERENCES

[1]   P. Hariharan, *Optical Holography: Principles, Techniques and Applications,* 1st ed, Cambridge University Press (1984)

[2]   D. Gabor, *A New Microscopic Principle*, Nature 161, 4098, 777-778 (1948)

[3]   D. Gabor, *Microscopy by Reconstructed Wavefronts*, Proceedings of the Royal Society (London) A 197, 454-487 (1949)

[4]   D. Gabor, Microscopy *by Reconstructed Wavefronts: II*, Proceedings of the Physical Society, Section B 64 (Pt. 6) No. 378 B, 449-469 (1951)

[5]   M. Wolfke, *Uber die Moglichkeit der Optischen Abbildung von Molekulargittern*, Physikalische Zeitschrift, 21, No. 18, 495-497 (1920)

[6]   W. Bragg, *A New Type of „X-Ray Microscope'*, Nature 143, No. 3625, 678 (1939)

[7]   W. Bragg, *The X-Ray Microscope*, Nature 149, No. 3782, 470 (1942)

[8]   E. Leith and J. Upatnieks, *Reconstructed Wavefronts and Communication Theory*, Journal of the Optical Society of America 52, No. 10, 1123-1128 (1962)

[9]   E. Leith and J. Upatnieks, *Wavefront Reconstruction with Continuous-Tone Objects*, Journal of the Optical Society of America 53, No 12, .1377-1381 (1963)

[10]   E. Leith, J. Upatnieks, *Wavefront Reconstruction with Diffused Illumination and Three-Dimensional Objects*, Journal of the Optical Society of America 54, No 11, 1295- 1301 (1964)

[11]   R. Jones and C. Wykes, *Holographic and Speckle Interferometry*, Cambridge studies in modern optics, 2nd ed. (1989)

[12] J. Urbach and R. Meier, *Properties and Limitations of Hologram Recording Materials*, Applied Optics 8, No. 11, 2269-2281 (1969)

[13]   J. Salo, J. Meltaus, E. Noponen, M. Salomaa, A. Lönnqvist, T. Koskinen, V. Viikari, J. Säily, J. Häkli, J. Ala-Laurinaho, J. Mallat, and A. Räisänen, *Holograms for Shaping Radio-Wave Fields*, Journal of Optics A: Pure and Applied Optics 4, No. 5, S161-S167 (2002)

[14]   J. Kim, B. Choi, S. Kim, J. Kim, H. Bjelkhagen and N. Phillips, *Holographic Optical Elements Recorded in Silver Halide Sensitized Gelatin Emulsions. Part 1. Transmission Holographic Optical Elements*, Applied Optics 40, No. 5, 622–632 (2001)

[15]   P. Judeinstein, P. Oliveira, H. Krug and H. Schmidt, *Photochromic Organic-Inorganic Nanocomposites as Holographic Storage Media*, Advanced Materials for Optics and Electronics 7, No. 3, 123-133 (1997)

[16]   A. Lönnqvist, J. Mallat, E. Noponen, J. Ala-Laurinaho, J. Säily, T. Koskinen, J. Häkli and A. Räisänen, *A Phase Hologram Compact RCS Range for Scale Model Measurements*, Proceedings of 3rd ESA Workshop on Millimetre Wave Technology and Applications, Espoo, Finland, 511-516 2003)

[17]   M. Collados, J. Atencia, J. Tornos and M. Quintanilla, *Construction and Characterization of Compound Holographic Lenses for Multichannel One-Dimensional Fourier Transformation and Optical Parallel Processing*, Optics Communications 249, No 1-3, 85–94 (2005)

[18] M. Liphardt, A. Goonesekera, B. Jones, S. Ducharme, J. Takacs and L. Zhang, *High-Performance Photorefractive Polymers*, Science 263, No. 5145, 367-369 (1994)

[19] D. Rowe, *Holographic Scanner like Bar Codes in Developments in Holographic-based Scanner Designs*, SPIE Conference on Optical Scanning Systems (1997)

[20]   H. Owen, *The Impact of Volume Phase Holographic Filters and Gratings on the Development of Raman Instrumentation*, Journal of Chemical Education 84, No. 1, 61-66 (2007)

[21] A. Thelen, S. Frey, S. Hirsch, N. Ladriere and P. Hering, *Ultrafast Holographic Topometry of the Face for Medical Applications*, Medical Laser Application 21, No 1, 9-14 (2006)

[22] S. Martin, C. Feely, J. Sheridan and V. Toal, *Applications of a Self Developing Photopolymer Material: Holographic Interferometry and High Efficiency Diffractive Optical Element*, Optical Memory and Neural Networks 7, No. 2, 79-87 (1998)

[23] W. Klein and B. Cook, *Unified Approach to Ultrasonic Light Diffraction* , in IEEE Transactions on Sonics and Ultrasonics SU-14, No. 3, 123-134 (1967)

[24] M. Moharam, T. Gaylord and R. Magnusson, *Criteria for Raman-Nath Regime Diffraction by Phase Gratings,* Optics Communications 32, No. 1, 19-23 (1980)

[25] J. Meltaus, J. Salo, E. Noponen, M. Salomaa, V. Viikari, A. Lönnqvist, T. Koskinen, J. Säily, J. Häkli, J. Ala-Laurinaho, J. Mallat and A. Räisänen, *Millimeter-Wave Beam Shaping Using Holograms*, IEEE Transactions On Microwave Theory And Techniques 51, No. 4 (2003)

[26]   M. Cox and K. Vahala, *Image Plane Holograms for Holographic Microscopy*, Applied Optics 17, No. 9, 1455-1457 (1978)

[27]   C. Denz, G. Pauliat, G. Roosen and T. Tschudi, *Volume Hologram Multiplexing using a Deterministic Phase Encoding Method*, Optics Communications 85, No. 2-3, 171-176 (1991)

[28]   K. Kawamura, N. Sarukura, M. Hirano and N. Nosono, *Holographic Encoding of Permanent Gratings Embedded in Diamond by Two Beam Interference of a Single Femtosecond Near-Infrared Laser Pulse*, Japanese Journal Of Applied Physics Part 2-Letters 39, No. 8A, L767-L769 (2000)

[29]   A. Marshall, D. Young, S. Kabilan, A. Hussain, F. Blyth and C. Lowe, *Holographic Sensors for the Determination of Ionic Strength*, Analytica Chimica Acta 527, No. 1, 13-20 (2004)

[30]   C. Ley and I. Calderara and D. Lougnot, *Holographic Gratings Recorded in Polymer Hydrogels - an Original Application as a Sensor in Aqueous Environment*, Measurement Science & Technology 8, No. 9, 997-1000 (1997)

[31] C-C. Sun and P. Banerjee, *Volume Holographic Optical Elements*, Optical Engineering 43, No. 9, 1957-1958 (2004)

[32] R. Chen, H. Lu, D. Robinson, M. Wang, G. Savant and T. Jannson, *Guided-Wave Planar Optical Interconnects Using Highly Multiplexed Polymer Waveguide Holograms*, Journal Of Lightwave Technology 10, No. 7, 888-897 (1992)

[33] L. Sica, T. Aye, I. Tengara and B. Wexler, *Compensation of Spacer-Thickness Variations in a Holographic Fabry-Perot Filter*, Applied Optics 33, No. 22, 5021-5028 (1994)

[34] Y. Osugi and T. Minemoto, *Increase the Size of $Bi_{12}SiO_{20}$ Real-Time Hologram for Three-Dimensional Display*, Optical Review 3, No. 6B, 552-555 (1996)

[35] H. Kogelnik, *Coupled Wave Theory for Thick Hologram Gratings,* The Bell System Technical Journal 48, No.9, 2909-2947 (1969)

[36] D. Neumann, *Holography of Moving Scenes*, Journal of the Optical Society of America 58, No. 4, 447-454 (1968)

[37]   W. Bragg, *The Diffraction of Short Electromagnetic Waves by a Crystal*, Proceedings of the Cambridge Philosophical Society 17, 43–57 (1913)

CHAPTER 2:   RECORDING MATERIALS

2.1   INTRODUCTION

In this chapter, several recording materials used in diverse holographic applications are reviewed. The recording materials described are silver halide materials, dichromated gelatin, photorefractive crystals, photochromics, photothermoplastics and photorefractive materials. The main advantages are mentioned as well some of the major drawbacks of each material.

Special emphasis is given to photopolymeric materials and photopolymerizable nanocomposites. A brief introduction to the properties of these materials and the theories behind the recording mechanisms in them is given. The concept of introducing nanodopants in photopolymers and the development of photosensitive nanocomposites is also explained.

In order to be able to record a hologram a material must respond to exposure to light (after additional processing where necessary) with a change in its optical properties. The ideal recording material for holography should have a spectral sensitivity well matched to available laser wavelengths, a linear transfer characteristic, high resolution and low noise. In addition, it should be either indefinitely recyclable or relatively inexpensive [1].

2.2   TYPES OF HOLOGRAPHIC RECORDING MATERIALS

Back in 1969 [2] the use of recording materials other than silver halides showed great promise for certain applications but little quantitative information was published. In the last decades many other types of holographic recording materials came of age, and the most widely used will be described in the next sections.

2.2.1   SILVER HALIDE PHOTOGRAPHIC MATERIALS

Silver halide materials have a long tradition and they were the first materials used to record a hologram. A silver-halide recording photographic material is based on one type, or a combination, of silver halide crystals embedded in a gelatin layer, commonly known as the photographic emulsion. This photosensitive emulsion is not really an "emulsion" but rather a thin film of silver-halide microcrystals dispersed in a colloid (gelatin) that is coated on a flexible or stable substrate material. There are three types of silver halides: silver chloride (AgCl), silver bromide (AgBr), and silver iodide (AgI) [3].

Holograms recorded on these emulsions are processed using techniques similar to those used for normal photographic materials. Processing should be carried out immediately after exposure, since such fine grain emulsions exhibit significant fading of the latent image [1]. These type of materials are versatile, commercially available in several sizes, can be coated on both film and glass and cover large formats. These materials can record phase, amplitude, colour and Lippmann holograms (reflection holograms that have been recorded with very short temporal coherence, white light). They can also be handled and processed with a minimum of equipment and have high resolution power. Their sensitivity, unequalled by other materials, is achieved however by means of the time-consuming wet developing process, which makes it also unlikely that silver halide emulsions ever might provide the possibility of local erasure and rewriting, as desired for optical memories [4, 5]. Development is actually an amplification process with a gain of the order of 10^{6}, which yields high sensitivity as well as a stable hologram [1]. Others drawbacks are the fact that they are absorptive, their inherent noise (because of their granular structure), they are irreversible and possess a limited linear response [4, 6].

Photographic emulsions are still widely used in the recording of phase holograms. Because of the relatively low diffraction efficiency of amplitude holograms several techniques have been optimized in order to produce phase holograms on photographic emulsions showing high diffraction efficiencies and low levels of noise. Among these techniques, bleaching processes are one of the most interesting as they involve a relatively small number of steps and produce holograms of high quality [1, 6].

Some of the most used silver halide holographic recording materials include plates from Agfa-Gavaert [7] and Kodak [8]. Due to the discontinuity of some of the most widely used plates, new materials have been introduced such as the plates provided by Slavich [9] and the BB series from HRT materials [10]. Other alternatives are the materials from Konica [11] and the Orwo film from Filmotec.

2.2.2 DICHROMATED GELATIN

Dichromated gelatin (DCG) and other dichromated colloids are among the oldest photographic materials. They record information either as a variation of the index of refraction or as a thickness variation, or as a combination of the two.

Hologram recording makes use of the fact that a gelatin layer containing a small amount of a dichromate such as $(NH4)_2Cr_2O$ becomes progressively harder on exposure to light. This hardening is due to the photo chemically produced Cr^{3+} ion forming localized cross links between the carboxylate groups of neighbouring gelatin chains [1]. Dichromated gelatin is an important holographic material, because it possesses almost ideal properties for the recording of volume phase holograms. When properly used, it forms a clear film that exhibits very little absorption and optical scattering. Furthermore, it has high resolution and

a large index change can be produced in the interior of the gelatin, making possible thick phase holograms of close to 100% efficiency. Both transmission and reflection holograms can be recorded [1, 5].

Despite their high promise, the main reasons why dichromated gelatin holograms have not been widely used are the difficulty of obtaining reproducible results and complex wet processing. The problems can be overcome, but considerable care is required. Also sensitivity to moisture is another issue, as the holograms need to be rigorously protected from humidity, which can result in poor shelf-life [5].

Dichromated gelatin was first used as hologram recording material by Shankoff [12] who found that very large index modulation can be obtained in relatively thin films. Shankoff used hardened gelatin layers as the starting material so that there would be no, or only small, variation in thickness. Recently, better polymeric materials such as dichromated polyvinyl alcohol (DCPVA) and dichromated polyacrylic acid (DCPAA) have been used in several holographic applications and in real time holographic recording [13].

Some applications of this type of materials are in holographic grating couplers [14] and in reflection holography [15].

2.2.3 PHOTOREFRACTIVE CRYSTALS

In some electro-optic crystals, exposure to light frees trapped electrons which then migrate through the crystal lattice and are again trapped at defects in adjacent unexposed regions. The migration usually occurs through diffusion or an internal photovoltaic effect. The spatially varying electric field produced by the resulting space-charge pattern modulates the

refractive index through the electro-optic effect, resulting in the formation of a phase hologram. When desired, this hologram can be erased by uniformly illuminating the crystal, which can be recycled almost indefinitely [1].

It is generally accepted that the mechanism for writing and erasure of holographic gratings in photorefractive materials involves an active impurity (or centre), such as iron, with two valence states (e.g., Fe^{2+} and Fe^{3+}). Negative carriers are photo ionized from donor states (Fe^{2+}) move through the lattice and are finally trapped at the acceptor sites (Fe^{3+}) [16].

The application of these materials for hologram recording was first considered by Chen et al. [17] with his work in undoped $LiNbO_3$. The holograms formed had high diffraction efficiencies and were thermally erasable.

The advantages of photorefractive crystals are their excellent resolution, readout efficiency, reversibility, storage capacity, and sensitivity. In addition, they are useful in both read/write and read-only systems. The read/write operation is particularly simple because the as-recorded holograms can be immediately read out without processing and then erased with the same wavelength used for storage. The prime limitation of these materials at present is that most of the holographic storage properties are strongly interrelated; in enhancing one property (e.g., sensitivity) by proper choice of material or material treatment one finds a tradeoff in others (e.g., storage capacity). Future research, both in materials and in methods of use, is needed before these crystals can fulfil their potential [5].

Among others, crystals such as lithium niobate $LiNbO_3$ [18], lithium tantalate $LiTaO_3$ [19], barium titanate $BaTiO_3$ [20] and barium sodium niobate $Ba_2NaNb_5O_{15}$ [21] have been used.

2.2.4 PHOTOCHROMICS

Photochromic materials have the property of changing absorption (thus colour) reversibly under light illumination. Typically, they are transparent or lightly coloured in the normal or thermally stable state, and become more darkly coloured after irradiation with UV or blue light. The induced photochromic optical absorption decays thermally at room temperature in a time ranging from seconds to days depending on the material. The materials can also be returned to their original state by irradiation with visible light [22].

This characteristic of photochromic compounds (a reversible change is achieved by the action of light with different wavelengths) makes them applicable in the field of rewritable holographic storage [23]. Both organic [24] and inorganic [25] materials have been studied for photochromism. These materials have been the subject of considerable interest as holographic recording media because of their high resolution, lack of grain (no inherent resolution limit) and self-development. They also have fast response time, are re-writable and have nondestructive readout capability [26, 27]. Despite their advantages, photochromics use is limited by their low diffraction efficiency (<2%), poor sensitivity and low storage time. i.e, the stored hologram is degraded during readout, so that for applications requiring many read cycles it is necessary to use a low-intensity read beam [1, 5, 29]. The reconstruction beam usually degrades the stored information. In alkali halide crystals the playback can be non-destructive if the temperature of the material is lowered after recording [30]. The first hologram recorded in photochromic material was reported by Kirk [28]. The photochromic glass functioned as a high resolution three dimensional

recording material that was developed as it was exposed and was erasable. This permitted the making of a hologram, the observation of the hologram without moving the glass and, if not adequately exposed, continuation of the exposure.

2.2.5 PHOTOTHERMOPLASTICS

Thermoplastic materials as holographic recording mediums are a combination of materials and two basic film structures are mostly found: (1) single layer, where a photoconductor is dissolved, or finely dispersed, in a layer of thermoplastic; and (2) separate layers, where a layer of thermoplastic is coated over a layer of photoconductor [31].

The thermoplastic is charged to a high voltage before exposition. Next pulse of electric current, passing through the photoconductor provides the heating of the thermoplastic that becomes soft enough to be deformed by the field. Such heating involves the development of the latent electrostatic image showing itself as geometric relief of the thermoplastic surface. The thermoplastic is cooled to fix the pattern of deformation. Erasing of the hologram requires heating of the thermoplastic to a higher temperature [32]. The use of themoplastics as holographic recording materials was first reported by Urbach et al. [33] in 1966. They used an organic photoconductor overcoated with an insulating thermoplastic and operated in the charge-expose recharge mode using a He-Ne laser.

Such materials have a reasonably high sensitivity over the whole visible spectrum and yield a thin phase hologram with fairly high diffraction efficiency. In addition they have the advantage that they do not require wet processing. If a glass substrate is used the hologram can be erased and the material re-used a number of times [1].

2.2.6 PHOTORESISTS

Photoresists are light-sensitive organic films which form a relief image after exposure and development. Resist holograms are made by exposing the resist, coated on a suitable substrate, to the interference fringe pattern and immersing it in developer. The solubility of the resist in developer is dependent on exposure. Thus a fringe pattern consisting of variations in intensity is recorded as variations in resist thickness. These variations modulate the phase of an incident wave resulting in the formation of a reconstructed image [1, 34]. Several photoresists have been used to record holograms and there are two types of photoresists: negative and positive photoresists. In negative photoresists the areas exposed to light becomes insoluble to the developing solution and are dissolved away during that step. Relatively long exposures are necessary, usually through the back side of the plate, to ensure that the exposed photoresists adheres to the substrate during development. Because of this, positive photoresists in which the exposed areas become soluble and are washed away during development are preferable [1].

The first use of photoresists was reported by Sheridan in 1968 [35] in his work regarding blazed holographic diffraction gratings. In the past these materials were relatively slow, typically requiring an exposure of 10 mJcm^{-2} to blue light (λ=442 μm) and since a thin phase hologram is formed, nonlinear effects are noticeable at diffraction efficiencies greater than 5%. However they had the advantage that replication was easy [1]. Recently, holographic transmission gratings that possess high diffraction efficiency (near unity), high wavefront quality, and high damage threshold have been designed, fabricated and characterized for use in high-power, solid-state laser systems [36].

2.2.7 PHOTOPOLYMERS

A number of organic materials are known to be activated through a photosensitizer to exhibit thickness and refractive index changes due to photopolymerization or cross-linking. Thick layers can be made to yield volume phase holograms with high diffraction efficiency and high angular selectivity, which can be viewed immediately after exposure. After the exposure a continuing dark reaction due to diffusion of the monomer into the zones of polymerization increases the refractive index modulation [1]. Photopolymer systems for recording holograms typically comprise one or more monomers, a photoinitiaton system and an inactive component often referred as a binder. The resulting composition is typically a viscous fluid or a solid with a low glass transition temperature, which is prepared for exposure either by coating onto a solid or flexible substrate, or by containing it between two transparent solid substrates [37].

Photopolymers for holographic recording were first reported by Close [38]. He recorded volume holograms in a photopolymer formulation containing acrylamide and metal acrylates as monomers. The material was fixed by exposure to ultraviolet radiation. The light source was a ruby laser tuned at 694 nm. Photopolymers exhibit high resolution and they possess rapidity and ease of optical processing when compared to wet processing and some are self-developing. They have high sensitivity, real-time image development, large dynamic range, good optical properties, format flexibility, good image stability and relatively low cost. High diffraction efficiency is obtainable. Some of the disadvantages observed are the relatively low signal-to noise ratio due to the presence of light scattering polymer particles, short shelf life time of the prepared materials and that the material cannot be recycled [37, 39].

2.3 HOLOGRAPHIC RECORDING IN PHOTOPOLYMERS

The mechanisms accepted for explaining of the holographic recording in photopolymers involves three processes: the concentration gradient driven diffusion and photopolymerization processes that result in a third process called refractive index modulation of the material.

Vinyl monomers, such as acrylates [40] and methacrylate esters [41] are used in most photopolymer systems. These monomers polymerize through a free radical mechanism. Monomers capable of polymerizing through a cationic ring opening (CROP) have also been reported [42].

Holographic photopolymer systems typically use at least two different molecules to form a photoinitiating system that is sensitive to the visible wavelengths commonly used in optical holography. A photosensitiser molecule absorbs the imaging light and in its excited state interacts with a free radical generator molecule, either through energy transfer or through a redox reaction to produce the initiating species [1]. Two-photon systems have also been developed. Molecular excitation via the simultaneous absorption of two photons can lead to improved three-dimensional control of photochemical or photophysical processes due to the quadratic dependence of the absorption probability on the incident radiation intensity [43]. The binder is sometimes a polymer that is included to modify the viscosity of the formulation, to aid sample preparation and to enhance holographic exposure. Binders can also be small molecules or oligomers that are required for the development of the holographic image [1].

2.3.1 MECHANISM OF FREE RADICAL CHAIN POLYMERIZATION

Initiation of a free radical chain takes place by addition of a free radical ($R^{\bullet}$) to a vinyl monomer (*M*) [44]:

$$R^{\bullet} + M \rightarrow RM^{\bullet} \qquad \text{(Eq. 2. 1)}$$

The propagation is a bimolecular reaction, which takes place by the addition of a new free radical ($RM^{\bullet}$) to another molecule of the monomer (*M*) and by many repetitions of this step [44]:

$$RM^{\bullet} + M \rightarrow RM\,M^{\bullet} \qquad \text{(Eq. 2. 2)}$$

The termination of the growing free radical chains usually occurs by coupling of two macromolecules [44]:

$$RM^{\bullet} \underset{n}{\big)} M^{\bullet} \; + \; RM^{\bullet} \underset{m}{\searrow} M^{\bullet} \rightarrow RM \underset{n+m}{\searrow} M \qquad \text{(Eq. 2. 3)}$$
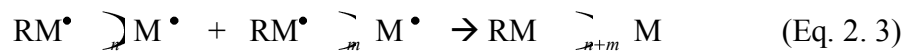
2.3.2 DIFFUSION PROCESSES IN PHOTOPOLYMERS

It is also known that during hologram formation monomer diffusion occurs from the dark to bright fringe areas. Colburn and Haines [45] have shown that gradients in monomer concentration due to differential polymerization by the initial exposure (during exposure the monomer in areas of higher intensity illumination is polymerized to a greater extent than in lower intensity areas) give rise to diffusion of monomer molecules from regions of higher residual concentration to regions of lower concentration. This monomer diffusion effect in the end has a positive influence on the modulation of refractive index in the grating - since polymer has a different refractive index than the monomer and its concentration is greater in the areas of previously higher exposure, a difference of refractive index between the components in the dark and bright fringes occurs, The diffusion of monomer that leads to grating formation can be observed in Fig. 2.1.
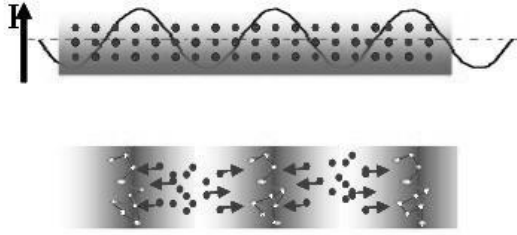
Figure 2.1.   **Light induced redistribution of photopolymer components (where • are monomer molecules and ○- are polymer molecules).**

A widely used theoretical model describing these processes is a one-dimensional standard diffusion equation written for the monomer concentration, which assumes that monomers are free to diffuse in the material:

$$\frac{\partial u(x,t)}{\partial t} = \frac{\partial}{\partial x}\left[D(x,t)\frac{\partial u(x,t)}{\partial x}\right] - F(x,t)u(x,t)$$

(Eq. 2.4)

where $u\,(x,\,t)$ is the monomer concentration, $F\,(x,\,t)$ is the polymerization rate, x and t are the spatial and time coordinates, respectively, and $D\,(x,\,t)$ is the so-called diffusion constant, which is not a constant and might change due to the change in polymer concentration and associated change in the mobility of monomers [46].

2.3.3   REFRACTIVE INDEX CHANGES IN PHOTOPOLYMERS

Tomlinson and Chandross [47] have discussed the possible photochemical mechanism for refractive index changes in organic systems. The most relevant for hologram recording in photopolymers include alteration in molecular electronic structure, density changes and spatial segregation of system components, which will be further discussed below.

Examination of the Lorentz-Lorenz relationship (Eq. 2.5) for an isotropic ideal mixture can provide estimates of these effects [48]:

$$\frac{n^2-1}{n^2+2} = \sum \frac{\rho_i R_i}{M_i} \qquad \text{(Eq. 2. 5)}$$

where n is the average refractive index, ρ_i is the density, M_i is the molecular weight and R_i is the molar refraction of the ith component of the mixture.

Differentiation of Eq. 2.5 for a single component reveals the effects that small changes in ρ and R have on the refractive index [49].

$$\Delta n = \left\{ \frac{\left(n^2+2\right)\left(n^2-1\right)}{6n} \right\} \left\{ \frac{\Delta R}{R} + \frac{\Delta \rho}{\rho} \right\} \qquad \text{(Eq. 2. 6)}$$

Change of electronic structure upon polymerization is responsible for changes in molar refraction when a monomer is incorporated into the polymer chain. During vinyl polymerization, the double bond of the monomer is converted to a single bond in the backbone structure of the polymer. This change in bond order can be responsible for a significant change in molar refraction, as indicated by Tomlinson [47]. In those studies, contributions to refractive index change from changes in molar refraction upon polymerization were estimated to be around 0.05 for the some types of vinyl monomers.

Before polymerization, monomers cannot approach closer to one another than the sum of their van der Waals radii. After polymerization, monomers are linked by covalent bonds and thus the distance between connected monomers is shortened. Polymerization therefore almost always produces a decrease in volume and an increase in density [49]. A density increase must occur by mass transport. During exposure contiguous volume elements, undergoing relatively slow and relatively fast polymerization are established in the recording material by the spatial variation of light intensity in the holographic interference pattern. Density increases in the rapidly polymerizing volume elements require material influx from the surrounding volumes. Spatial variations in polymerization rates produce

monomer concentration gradients that also drive monomer diffusion. These two effects combine to promote spatial segregation of the various components of the photopolymer system. If the components have different refractive indices their spatial segregation will make a significant contribution to the refractive index modulation [1].

2.4 ACRYLAMIDE BASED PHOTOPOLYMER

Acrylamide-based photopolymer systems were first suggested in 1975 by Sugawara et al. [50]. Their composition consisted of acrylamide, methylene-bis-acrylamide with a photoreductant such as acetylacetone or triethanolamine (TEA) and a diffraction efficiency of 65% using a exposure energy of 50 mJcm^{-2} was obtained. By introducing poly-vinyl alcohol binder in the system, Sadlej et al [51] made dry photopolymer layers. Jeudy et al. [52] presented a new composition by adding photochrome (indoline-spiropyran) as sensitiser and polyvinylalcohol (PVA) as binder. Sensitizing action was only activated when irradiated with UV light. The sensitizer shifted its absorption band when excited with UV light and allowed recording at 633 nm. The diffraction efficiency was 80% with exposure energy of 100 mJcm^{-2}. Calixto [53] reported a material which consisted of acrylamide as monomer, triethanolamine as electron donor, poly-vinylalcohol (PVA) as binder and contained methylene blue as a dye. The diffraction efficiency of 10% was achieved with an exposure of 94 mJcm^{-2}. Fimia et al. [54] introduced a method to increase the sensitivity of acrylamide photopolymers by reducing the inhibition period mainly caused by oxygen. The solution consisted of two dyes, methylene blue and rose bengal. The layer was pre-exposed at 546 nm wavelength to generate free radicals which react with oxygen, thus reducing the amount of oxygen in the composition. The monomer was then polymerized at 633 nm and a diffraction efficiency of 40% was achieved with an exposure of 3 mJcm^{-2} at a spatial frequency of 1000 lmm^{-1}. Martin et al. [55] characterized Calixto's

photopolymer at 514 nm region with five xanthenes dyes. By adding a cross-linking monomer, the life time of the recorded gratings was improved and the matrix became more rigid, less permeable and as a result the diffusion process was slowed down. Jallapuram et al. [56] optimized further this photopolymer composition and were able to record reflection holograms with a diffraction efficiency of 35% at 3500 lmm^{-1}.

Several other research groups [57-61] use acrylamide-based photopolymers in their studies. The polymeric matrix is based on polyvinyl alcohol (PVA), the initiator is triethanolamine (TEA), acrylamide and bisacrylamide are used as monomers and erythrosine B is the sensitizing dye (for recording in the green). Acrylamide monomer and bisacrylamide co-monomer, the latter being used as a cross-linker, polymerize and polyacrylamide is formed.

Acrylamide based photopolymer has been used for various applications such as holographic data storage [62], fabrication of polymer dispersed liquid crystal gratings [63], humidity sensors [64] and photo patterning [65].

2.4.1 MECHANISM OF HOLOGRAPHIC RECORDING IN ACRYLAMIDE BASED PHOTOPOLYMERS

In the first process, polymerization, a dye molecule (*XD*) absorbs a photon of light and gets promoted to an excited singlet state. It may then transfer to an excited triplet state, through intersystem crossing, and react with the electron donor (*ED*), triethanolamine, to produce a dye radical anion and a triethanolamine radical cation [55, 66]:

XD + hν $\rightarrow$ XD*   (absorption of light)   (Eq. 2.7)

XD * $\rightarrow$ 3XD*   (intersystem crossing)   (Eq. 2.8)

XD* + ED $\rightarrow$ XD • + ED •   (dye reduction –electron transfer)   (Eq. 2.9)
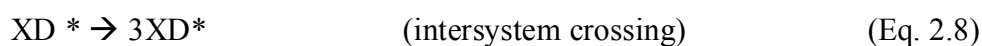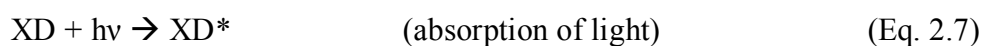
The dye radical is not usually reactive enough to initiate polymerization but the triethanolamine radical will react with an acrylamide molecule (*ACR*) and polymerization may then occur:

$$ED \bullet + ACR \rightarrow ED - ACR \bullet \qquad \text{(initiation)} \qquad \text{(Eq. 2.10)}$$

$$ED - ACR \bullet + ACR \rightarrow ED - (ACR)2 \bullet \qquad \text{(propagation)} \qquad \text{(Eq. 2.11)}$$

$$ED - (ACR)n \bullet + ACR \rightarrow ED - (ACR)(n+1) \bullet \qquad \text{(propagation)} \qquad \text{(Eq. 2.12)}$$

$$ED - (ACR)n \bullet + ED - (ACR)m \bullet \rightarrow ED - (ACR)n + m - ED$$

$$\text{(termination)} \qquad \text{(Eq. 2.13)}$$
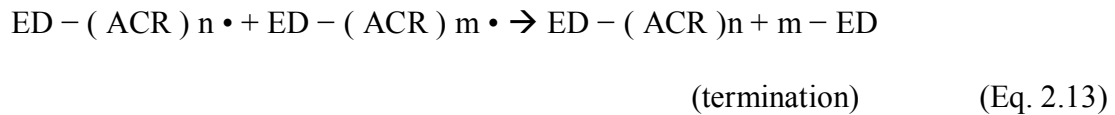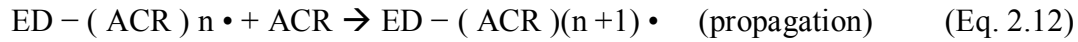
It has been shown [67] that in acrylamide-based photopolymers two different diffusion processes contribute with opposite sign to the refractive index modulation responsible for the diffraction grating build up. While monomer diffusion from dark to bright fringe areas increases the refractive index modulation as discussed previously, a second diffusion process takes place during the recording. This second process decreases the refractive index modulation and we ascribe it to diffusion of short chain polymer molecules and/or radicals from bright to dark fringe areas. The presence of the second process could be responsible for poor high spatial frequency response of the acrylamide based photopolymers.

2.5 *HOLOGRAPHIC RECORDING IN PHOTOPOLYMERIZABLE NANOCOMPOSITES*

It is rather difficult to achieve a large refractive index modulation for pure polymer materials [68]. Different classes of volume holographic recording materials such as organically modified silica glass [69] and sol-gel materials containing zirconium isopropoxide [70] have been developed in the past decade and show improved holographic properties such as higher dynamic range and lower level of shrinkage during holographic

recording and hence have been studied mainly for applications such as holographic memories. A different approach was introduced by Bunning et al. [71] who pioneered the idea of introducing inorganic nanoparticles, having substantially higher (or lower) refractive index (n), in photopolymer mixtures as a movable non-reactive component. Nanoparticles are non-reactive components known for having low scattering, stability in water suspensions and there is a broad range of refractive index available [72]. The idea was further developed by other groups, particularly by Prof. Tomita in Japan [73]. Successful was the use of TiO_2 nanoparticles by Tomita et al. [74] and Smirnova et al. (n=2.55, bulk) [75], but other nanoparticles have been also used, such as ZrO_2 (n=2.1, bulk)/TiO_2 [68, 78] and SiO_2 (n=1.46, bulk) [76, 77, 82].

A summary with the review of the literature on some of the existing photopolymerizable systems is given in table 2.1.

Table 2.1. Grating Performances of photopolymerizable nanocomposites.

Nanoparticle Type	Size (nm)	Photopolymer type (monomers)	Maximum Dynamic Range, n_1	Scattering Losses	Literature Reference
TiO_2	15	Methacrylate	5.1×10^{-3}	20% for 40 µm	74
TiO_2	4	Acrylate	15.51×10^{-3}	12% for 15 µm	40
ZrO_2	3	Acrylate	5.3×10^{-3}	<1% for 40 µm	78
ZrO_2/TiO_2	<10	Acrylic	16.1×10^{-3}	8-10% for 20 µm	68
SiO_2	13	Methacrylate	8×10^{-3}	2-3% for 40-50 µm	82
$Zr(O'Pr)$	4	Acrylate	10×10^{-3}	1.8% for 15 µm	70
Zeolite Si-MFI	60	Acrylamide	3.8×10^{-3}	-	72
$LaPO_4$ (doped with Ce^{3+} and Tb^{3+})	7	Acrylate	1.3×10^{-2}	3% for 20 µm	79
Au functionalized	1.5-3	Acrylate	3.8×10^{-3}	-	80
Silver	5	Acrylic	3.8×10^{-3}	-	81

In addition to obtaining much larger n_1 compared with conventional all-organic photopolymers, the inclusion of nanoparticles results in substantial suppression of polymerization shrinkage, giving high dimensional stability as well [82].

However, these materials are usually sandwiched between two glass slides, which limit their area of exposure to the surrounding environment, which can be a disadvantage if the intended use is for sensing chemical compounds present in the atmosphere.

2.5.1 MECHANISM OF HOLOGRAPHIC RECORDING IN PHOTOPOLYMERIZABLE NANOCOMPOSITES

The dark diffusion mechanisms in photopolymerizable materials have been studied both experimentally [83] and theoretically by several authors [84, 85]. In the particular case of photopolymerizable nanocomposites, it has been proposed that the nanoparticles can be spatially redistributed during the holographic recording, and when nanoparticles with appropriate refractive index are used, this leads to significant improvement in the ultimate refractive index modulation. It has been observed that the nanoparticles are expelled from the bright to the dark fringes areas, in the opposite direction to monomer diffusion [73, 77, 86, 87, 89].

Tomita et al. have proposed that the photo-insensitive nanoparticles, which are not consumed, undergo counter-diffusion from the bright to the dark regions, and their chemical potential increases in the bright regions due to consumption of the monomer. This polymerization-driven mutual diffusion process (i.e., phase separation) essentially continues until photopolymerization is complete [86].

In this way, periodic assembly of nanoparticles under holographic exposure is accomplished - see Figure 2.2 - and as a result a refractive index grating is created owing to the compositional and density difference between the bright and the dark regions [87].
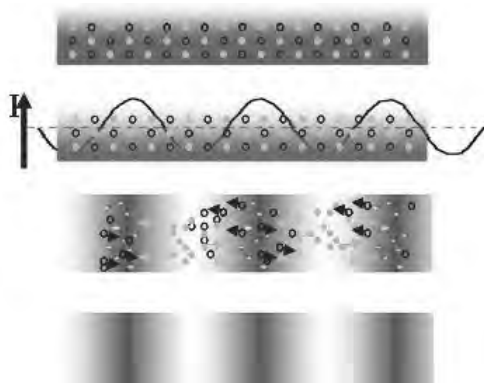
Figure 2.2. **The distribution of constituents of photopolymerizable nancomposites (monomer molecules and nanoparticles) during holographic exposure (where ● are monomer molecules, ◉ nanoparticles and ○- are polymer molecules).**

The effect of Si-MFI zeolite nanoparticles on the final refractive index modulation in acrylamide-based photopolymers [72] and in a recent zeolite doped photopolymer review [88] suggests that they are expelled from the bright to the dark fringes areas, in the opposite direction to monomer diffusion.

The two-dimensional periodic distribution of the polymer and solid nanoparticles in nanocomposite films was experimentally observed indirectly by a novel real-time optical method [87] and directly by a transmission electron microscopy (TEM) [86] Electron-Probe MicroAnalysis (EPMA) [77] and more recently by Raman spectroscopy [89].

Most of the models proposed so far explain the improvement in holographic grating diffraction efficiency by the fact that the inorganic nanoparticles are inert and take part only in mass transport mechanism during holographic exposure, as described above. But

recently, Goldenberg et al. [80] has proposed a new mechanism of the refractive index contrast amplification in new functionalized acrylate monomers and gold nanoparticles in which the non inert inorganic nanoparticles were found to promote the monomer spatial segregation in addition to mass transport effects.

2.6   CONCLUSIONS

Despite the existence of several classes of holographic recording materials, the ideal one has not been yet developed. The advantages and drawbacks of several holographic recording materials have been discussed.

Particularly, photopolymers are a class of holographic recoding materials that have attracted much interest of the research community due to their promising characteristics. The improvement of their holographic characteristics has been one of the major concerns leading to the development of photopolymerizable nanocomposites. The inclusion of nanoparticles promotes better performance of the grating parameters such as refractive index modulation and level of shrinkage.

The achievement of higher refractive index modulation is beneficial for applications like holographic data storage as it provides higher storage capacities. It is also an advantage in the fabrication of spectroscopic devices and holographic optical elements (HOE) as it allows the use of thinner photosensitive layers and hence with less scattering. The reduced level of shrinkage is also beneficial to avoid distortion of the data recorded in the holographic memories.

The holographic recording mechanisms in nanocomposites have been reviewed and the general consensus is that the nanoparticles diffuse from the bright to the dark fringe areas during holographic recording, in the opposite direction to that of the monomer diffusion. This results in higher refractive modulations when compared to the undoped photopolymer systems.

2.7   REFERENCES

[1] P. Hariharan, *Optical Holography: Principles, Techniques and Applications*, 1st ed, Cambridge University Press (1984)

[2] J. Urbach and R. Meier, *Properties and Limitations of Hologram Recording Materials*, Applied Optics 8, No. 11, 2269-2281 (1969)

[3] H. Bjelkhagen, *New Recording Materials for Holography*, Conference of Holography, Art and Design (Holography and Three-Dimensional Displays), London (1998)

[4] H. Bjelkhagen, *Silver-halide Recording Materials: For Holography and Their Processing*, Springer (1995)

[5] H. Smith, *Holographic Recording Materials*, Vol. 20, Springer (1977)

[6] C. Neipp, I. Pascual and A. Beléndez, *Silver Halide Volume Holograms on BB-640 Plates: The Influence of the Developer in Rehalogenating Bleach Techniques*, Optik - International Journal for Light and Electron Optics 22, No. 8, 349-357 (2001)

[7] S. Frecska, *Characteristics of the Agfa-Gevaert Type 10E70 Holographic Film*, Applied Optics 7, No. 11, 2312-2314 (1968)

[8] A. Graube, Advances *in Bleaching Methods for Photographically Recorded Holograms*, Applieds Optics 13, No. 12, 2942-2946 (1974)

[9] Y. Sazonov and P. Kumonko, *Holographic Materials Produced by the "Micron" Plant at Slavich*, in 6th International Symposium on Display Holography, Proceedings of SPIE 3358, 31-40 (1998)

[10] R. Birenheide, *The BB Emulsion Series: Current Standings and Future Developments, in 6th International Symposium on Display Holography*, Proceedings of SPIE 3358, 28-30 (1998)

[11] M. Iwasaki, T. Kubota, M. Watanabe, T. Yamauchi, T. Kumasawa and K. Ueda, *The Recent Holographic Material, Konica P7000*, Proceedings of SPIE, Practical holography XX (2006)

[12] T. Shankoff, *Phase Holograms in Dichromated Gelatin*, Applied Optics 7, No. 10, 2101-2105 (1968)

[13] M. Bolte, R. Lessard, Y. Israeli and A. Rivaton, *Interactivity Holography/ Photochemistry: How the Combined Approach Helps Understand and Optimise the Holographic Recording*, Proceedings of SPIE: Holography, Optical Recording, and Processing of Information, No. 6252, 625203.1-625203.9 (2005)

[14] V. Weiss, E. Millul, E. Joennson, R. Shechter, Y. Amitai and A. Friesem, *Materials for the Recording of Thin Holographic Grating Couplers*, Materials Science in Semiconductor Processing 3, No. 3, 413-418 (2000)

[15] J, Zhu, G. Dong, X. Guo, L.Chen and J.Li, *Methylene-Blue Sensitized Dichromated Gelatin: Wide-Range Colour Adjustment of Reflection Hologram*, Journal of Optics A: Pure and Applied Optics 6, No. 1, 132–136 (2004)

[16] M. Carrascosa and F. Agullo-Lopez, *Erasure of Holographic Gratings in Photorefractive Materials With Two Active Species*, Applied Optics 27, No. 14, 2851-2857 (1988)

[17] F. Chen, J. LaMacchia, and D. Fraser, *Holographic Storage in Lithium Niobate*, Applied Physics Letters 13, No. 7, 223-225 (1968)

[18] A. Yariv, S. Orlov and G. Rakuljic, *Holographic Storage Dynamics in Lithium Niobate: Theory and Experiment*, Journal of the optical society of America B-optical physics 13, No. 11, 2513-2523 (1996)

[19] L. Youwen, K. Kitamura, S. Takekawa, M. Nakamura, Y. Furukawa and H. Hatano, *Nonvolatile Two-Color Holographic Recording in Nondoped Near-Stoichiometric Lithium Tantalate Crystals With Continuous-Wave Lasers*, Applied Physics Letters 82, No. 24, 4218-4220 (2003)

[20] Y. Tomita, *On the Nonphotoactive Ionic Species for Thermal Fixing of Volume Holograms in Undoped Barium Titanate*, Japanese Journal of Applied Physics Part 2 - Letters 38, No. 4B, L440-L442 (1999)

[21] J. Amodei, D. Staebler and A. Stephens, *Holographic Storage in Doped Barium Sodium Niobate ($Ba_2NaNb_5O_{15}$)*, Applied Physics Letters 18, No. 11, 507-509 (1971)

[22] R. Duncan, B. Faughnan and W. Phillips, *Inorganic Photochromic and Cathodochromic Recording Materials*, Applied Optics 9, No. 10, 2236-2243 (1970)

[23] S. Luo, K. Chen, L. Cao, G. Liu, Q. He, G. Jin, D. Zeng, and Y. Chen, *Photochromic Diarylethene for Rewritable Holographic Data Storage*, Optics Express 13, No. 8, 3123-3128 (2005)

[24] D. Belfield, Y. Liu, R. Negres, F. Meigong, P. Guilan, D. Hagan and F. Hernandez, *Two-Photon Photochromism of an Organic Material for Holographic Recording*, Chemistry of Materials, 14, No. 9, 3663-3667 (2002)

[25] L. Glebov, *Volume Hologram Recording in Inorganic Glasses*, Glass Science and Technology 75C1, 73-90, Elsevier (2002)

[26] R. Collier, C. Burckhardt and L. Lin, *Optical Holography*, Academic, New York, 305-309 (1971)

[27] C. Yi, W. Congming, F. Meigong, Y. Baoli and M. Neimule, *Photochromic Fulgide for Holographic Recording*, Optical Materials 26, No. 1, 75-77 (2004)

[28] J. Kirk, *Hologram on Photochromic Glass*, Applied Optics 5, No. 10, 1684-85 (1966)

[29] W. Tomlinson, *Phase Holograms in Photochromic Materials*, Applied Optics 11, No. 4, 823-831 (1972)

[30] P. Judeinstein, P. Oliveira, H. Krug, H. Schmidt, *Photochromic Organic-Inorganic Nanocomposites as Holographic Storage Media*, Advanced Materials for Optics and Electronics 7, No. 3, 123-133 (1998)

[31] L. Lin and H. Beauchamp, *Write-Read-Erase in Situ Optical Memory Using Thermoplastic Holograms*, Applied optics 9, No. 9, 2088-2092 (1970)

[32] J. Urbach, *Thermoplastic Hologram Recording, in Holographic Recording Materials*, Topics in applied physics, Vol. 20, ed. H. M. Smith, Springer (1977)

[33] J. Urbach and R. Meier, *Thermoplastic Xerographic Holography*, Applied Optics 5, N. 4, 666–667 (1966)

[34] M. Beesley and J. Castledine, *The Use of Photoresist as a Holographic Recording Medium*, Applied Optics 9, No. 12, 2720-2724 (1970)

[35] N. Sheridan, *Production of Blazed Holograms*, Applied Physics Letters 12, No. 9, 316-318 (1968)

[36] Holographic Transmission Gratings for Spectral Dispersion, LLE Review, Vol.82 (2000)

[37] H. Coufal, D. Psaltis and G. Sincerbox, *Holographic Data Storage*, In photopolymer systems by R. T. Ingwall and D. Waldman, Springer (2000)

[38] D. Close, A. Jacobson, J. Margerum, R. Brault and F. McClung, *Hologram Recording on Photopolymer Materials*, Applied Physics Letters 14, No. 5, 159-160 (1969)

[39] J. Jenney, *Holographic Recording with Photopolymers*, Journal of the Optical Society of America 60, No. 9, 1155-1161 (1970)

[40] C. Sanchez, M. Escuti, C. van Heesch, C. Bastiaansen, D. Broer, J. Loos and R. Nussbaumer, *TiO_2 Nanoparticle-Photopolymer Holographic Recording*, Advanced Functional Materials 15, No. 10, 1623-1629 (2005)

[41] H-J. Lee, B. Sarwade, J. Park and E. Kim, *Synthesis of New Photopolymeric Methacrylate Thioester With s-Triazine Ring for Holographic Recording*, Optical Materials 30, No. 4, 637-644 (2007)

[42] D. Waldman, H-Y. Li and M. Horner, *Volume Shrinkage in Slant Fringe Gratings of a Cationic Ring-Opening Holographic Recording Material*, *Holography III*, Journal of Imaging Science and Technology 41, No. 5, 497-514 (1997)

[43] S. Kirkpatrick, J. Baur, C. Clark, L. Denny, D. Tomlin, B. Reinhardt, R. Kannan and M. Stone, *Holographic Recording Using Two-Photon-Induced Photopolymerization*, Applied Physics A 69, No. 4, 461-464 (1999)

[44] C. Carraher, *Introduction to Polymer Chemistry*, CRC Press; 1st ed. (2006)

[45] W. Colburn and K. Haines, *Volume Hologram Formation in Photopolymer Materials,* Applied Optics 10, No. 7, 1636-1641 (1971)

[46] G. Zhao and P. Mourolis, *Diffusion Model of Hologram Formation in Dry Photopolymer Materials*, Journal of Modern Optics 41, No. 10, 1929-1939 (1994)

[47] W. Tomlinson and E. Chandross, *Organic Photochemical Refractive-Index Image Recording Systems*, in Advances in photochemistry Vol. 12, 201-276 (1980)

[48] D. van Krevelen, *Properties of Polymers*, Elsevier (1990)

[49] R. Sadhir, *Expanding Monomers: Synthesis, Characterization, and Applications*, CRC Press (1992)

[50] S. Sugawara, K. Murase and T. Kitayama, *Holographic Recording by Dye-Sensitized Photopolymerization of Acrylamide*, Applied Optics 14, No. 2, 378-382 (1975)

[51] N. Sadlej and B. Smolinska, *Stable Photo-Sensitive Polymer Layers for Holography,* Optics &Laser Technology 7, No. 4,175–179 (1975)

[52] M. Jeudy and J. Robillard, *Spectral Sensitization of a Variable Index Material for Recording Phase Holograms with High Efficiency.* Optics Communications 13, No. 1, 25-28 (1975)

[53] S. Calixto, *Dry Polymer for Holographic Recording*, Applied optics 26, No. 18, 3904-3910 (1987)

[54] A. Fimia, N. Lopez, and F. Mateos, *Acrylamide Photopolymers for Use in Real Time Holography: Improving Energetic Sensitivity.* Proceedings of SPIE, Vol. 1732, 105-109 (1993)

[55] S. Martin, P. Leclere, Y. Renotte, V. Toal and Y. Lion, *Characterisation of an Acrylamide-Based Dry Photopolymer Holographic Recording Material*, Optical Engineering 33, No. 12, 3942–3946 (1994)

[56] R. Jallapuram, *Optimization of an acrylamide-based photopolymer for reflection holographic recording*, PhD thesis, Dublin Institute of Technology (2005)

[57] S. Gallego, C. Neipp, M. Ortuño, E. Fernández, A. Beléndez and I. Pascual, *Analysis of Monomer Diffusion in Depth in Photopolymer Materials*, Optics Communications 274, No.1, 43-49 (2007)

[58] M. Gleeson, J. Kelly, C. Close, D. Sabol, S. Liu and J. Sheridan, *Modelling the Photochemical Effects Present During Holographic Grating Formation in Photopolymer Materials*, Journal of Applied Physics 102, No. 2, 023108-023108-9 (2007)

[59] M. Květoň, A. Havránekb, P. Fialaa and I. Richter, *Polymer Holography I – Method and Experiment Polymerization and Networking as a Method of Permanent Holographic Record Formation*, Polymer Bulletin 58, No. 7, 253–259 (2007)

[60] F. Ling, B. Tong, S. Jiang, B. Wang and Y. Zhang, *Optimization of Holographic Storage With Modulated Recording Beams in a Thick Polyvinyl Alcohol/ Acrylamide Photopolymer*, Journal of the Optical Society of America A 24, No7, 1945-1949 (2007)

[61] L. Carretero, A. Murciano, S. Blaya, M. Ulibarrena, and A. Fimia, *Acrylamide-N,N ′-Methylenebisacrylamide Silica Glass Holographic Recording Material*, Optics Express 12, No.8, 1780-1787 (2004)

[62] R. Fuentes, E. Fernández, C, García, A. Beléndez and I. Pascual, *Study of Reflection Gratings Recorded in Polyvinyl alcohol/ Acrylamide-Based Photopolymer*, Applied Optics 48, No. 39, 6553-6557 (2009)

[63] K Pavani, I. Naydenova, J Raghavendra, S Martin and V Toal, *Electro-Optical Switching of the Holographic Polymer-Dispersed Liquid Crystal Diffraction Gratings,* Journal of Optics A: Pure and Applied Optics 11, No. 2, 024023 (2009)

[64] I. Naydenova, R. Jallapuram, V. Toal and S.Martin, *Visual Indication of Environmental Humidity Using a Colour Changing Hologram Recorded in a Self-Developing Photopolymer*, Applied Physics Letters 92, No. 3, 031109 (2008)

[65] I. Naydenova, E. Mihaylova, S. Martin, and V. Toal, *Holographic Patterning of Acrylamide Based Photopolymer Surface*, Optics Express 13, No. 13, 4878-4889 (2005)

[66] S. Martin, C. Feely and V. Toal, *Holographic Recording Characteristics of an Acrylamide-Based Photopolymer,* Applied Optics 36, No. 23, 5757-5768 (1997)

[67] I. Naydenova, R. Jallapuram, R. Howard, S. Martin and V. Toal, *Investigation of the diffusion processes in self-processing acrylamide-based photopolymer system,* Applied Optics 43, No. 14, 2900-2905 (2004)

[68] O. Sakhno, L. Goldenberg, J. Stumpe and T. Smirnova, *Surface Modified ZrO_2 and TiO_2 Nanoparticles Embedded in Organic Photopolymers for Highly Effective and UV-Stable Volume Holograms*, Nanotechnology 18, No. 10, 105704-105710 (2007)

[69] P. Cheben and M.Calvo, *A Photopolymerizable Glass With Diffraction Efficiency Near 100% for Holographic Storage*, Applied Physics Letters 78, No 11, 1490-1492 (2001)

[70] F. Del Monte, O. Martinez, J. Rodrigo, M. Calvo and P. Cheben, *A Volume Holographic Sol-Gel Material With Large Enhancement of Dynamic Range by Incorporation of High Refractive Index Species*, Advanced. Materials 18, No. 15, 2014-2017 (2006)

[71] R. Vaia, C. Dennis, L. Natarajian, V. Tondiglia, D. Tomlin and T. Bunning, *One-Step, Micrometer-Scale Organization of Nano- and Mesoparticles using Holographic Photopolymerization: A Generic Technique*, Advanced Materials 13, No. 20, 1570-1574 (2001)

[72] I. Naydenova, H. Sherif, S. Mintova, S. Martin and V. Toal, *Holographic Recording in Nanoparticle-Doped Photopolymer*, Proceedings of SPIE 6252 (2006)

[73] Y. Tomita, *Holographic Assembly of Nanoparticles in Photopolymers for Photonic Applications*, SPIE Newsroom, Micro/ Nano Lithography & Fabrication (2007)

[74] N. Suzuki, Y. Tomita and T. Kojima, *Holographic Recording in TiO_2 Nanoparticle-Dispersed Methacrylate Photopolymer Films*, Applied Physics Letters 81, No. 22, 4121-4123 (2002)

[75] T. Smirnova, O. Sakhno, V. Bezrodnyi and J. Stumpe, *Nonlinear Diffraction in Gratings Based on Polymer-Dispersed TiO_2 Nanoparticles*, Applied Physics B - Lasers And Optics 80, No. 8, 947-951 (2005)

[76] W. Kim, Y.-C. Jeong and J. Park, *Nanoparticle-Induced Refractive Index Modulation of Organic-Inorganic Hybrid Photopolymer*, Optics Express 14, No. 20, 8967-8973 (2006)

[77] Y. Tomita, K. Chikama, Y. Nohara, N. Suzuki, K. Furushima and Y. Endoh, *Two-Dimensional Imaging of Atomic Distribution Morphology Created by Holographically Induced Mass Transfer of Monomer Molecules and Nanoparticles in a Silica-Nanoparticle-Dispersed Photopolymer Film*, Optics Letters 31, No. 10, 1402-1404 (2006)

[78] N. Suzuki, Y. Tomita, K. Ohmori, M. Hidaka, and Katsumi Chikama, *Highly Transparent ZrO2 Nanoparticle-Dispersed Acrylate Photopolymers for Volume Holographic Recording,* Optics Express 14, No. 26, 12712-12719 (2006)

[79] O. Sakhno, T. Smirnova, L. Goldenberg and J. Stumpe, *Holographic Patterning of Luminescent Photopolymer Nanocomposites*, Materials Science and Engineering C 28, No. 1, 28–35 (2008)

[80] L. Goldenberg, O. Sakhno, T. Smirnova, P. Helliwell, V. Chechik and J. Stumpe, *Holographic Composites with Gold Nanoparticles: Nanoparticles Promote Polymer Segregation*, Chemistry of Materials 20, No. 14, 4619–4627 (2008)

[81] L. Balan, C. Turck, O. Soppera, L. Vidal and D. Lougnot, *Holographic Recording with Polymer Nanocomposites Containing Silver Nanoparticles Photogenerated in Situ by the Interference Pattern*, Chemistry of Materials 21, No. 24, 5711–5718 (2009)

[82] N. Suzuki and Y. Tomita, *Silica-Nanoparticle-Dispersed Methacrylate Photopolymers With Net Diffraction Efficiency Near 100%*, Applied Optics 43, No. 10, 2125-2129 (2004)

[83] O. Martínez-Matos, M.Calvo, J. Rodrigo, P. Cheben, and F. Del Monte, *Diffusion Study in Tailored Gratings Recorded in Photopolymer Glass With High Refractive Index Species*, Applied Physics Letters 91, No. 14, 141115-141118 (2007)

[84] S. Piazzolla and B. Jenkins, *First-harmonic Diffusion Model for Holographic Grating Formation in Photopolymers*, Journal of the Optical Society of America B 17, No. 7, 1147-1157 (2000)

[85] T. Babeva, I. Naydenova, D. Mackey, S. Martin and V. Toal, *Two-Way Diffusion Model for Short-Exposure Holographic Grating Formation in Acrylamide-Based Photopolymer,* Journal of the Optical Society of America B 27, No. 2, 197-203 (2010)

[86] Y. Tomita, N. Suzuki and K. Chikama, *Holographic Manipulation of Nanoparticle Distribution Morphology in Nanoparticle-Dispersed Photopolymers*, Optics Letters 30, No. 8, 839-841 (2005)

[87] N. Suzuki and Y. Tomita, *Real-time Phase-Shift Measurement During Formation of a Volume Holographic Grating in Nanoparticle-Dispersed Photopolymers*, Applied Physics Letters 88, No. 1, 011105-011105-3 (2006)

[88] I. Naydenova and V. Toal, *Nanoparticle Doped Photopolymers for Holographic Applications,* in Ordered Porous Solids: Recent Advances and Prospects by V. Valtchev, S. Mintova and M. Michael Tsapatsis (2008)

[89] K. Chikama, K. Mastubara, S.Oyama, and Y.Tomita, *Three-Dimensional Confocal Raman Imaging of Volume Holograms Formed in ZrO2 Nanoparticle-Photopolymer Composite Materials*, Journal of Applied Physics 103, No. 11, 113108- 113108-6 (2008)

CHAPTER 3: MATERIALS AND METHODS

3.1 INTRODUCTION

In this chapter, information regarding the synthesis of zeolite nanoparticles from colloidal solutions and preparation of photopolymerizable nanocomposites is provided. These materials will be characterized and used in several holographic applications as described in the following chapters of this thesis. Two different types of zeolites, i.e. zeolite A and zeolite Beta were synthesised from clear precursor solutions during a research stay at France at the group of Prof. Mintova, University of Caen. The other types of zeolites studied in this work (zeolite L, AlPO-18 and silicalit-e1) were synthesised by her group and were extensively characterised at the Dublin Institute of Technology, Ireland. The fabrication of acrylamide based photopolymer is described as well as the nanocomposites design methodology.

A number of techniques can be used to analyse and characterize zeolite nanoparticles and nanocomposite materials. Different techniques would suit different materials and our aim was to carry out the most complete analysis of the colloidal solutions to confirm their successful synthesis. The optical properties of the nanocomposites can be related with the grating performances recorded in these materials. The most common analytical techniques in zeolite characterization used in this work were summarized. Regarding the interactions of the nanoparticles with the host material and their redistribution during holographic recording access to NMR, DLS, SEM and TEM was sought. Besides well established analytical techniques, purpose- built systems were utilized such as an optical setup capable of monitoring grating performances such as diffraction efficiency growth and angular selectivity curves, an optical setup for measuring the light scattering properties of materials and an optical fibre test system for sensing purposes.

3.2   ZEOLITES

Zeolites are defined as crystalline aluminosilicate materials with framework structures with regular and uniform pores of molecular dimensions [1]. Structurally, aluminosilicalites zeolites are inorganic materials based on an infinitely extending four-connected framework of SiO_4 and AlO_4 tetrahedra that are linked to each other by shared oxygen atoms. Each AlO_4 tetrahedron in the framework bears a net negative charge that is balanced by an extra framework cation [2]. The general empirical formula is [3]:

$$M_{x/m} = Al_x Si_{2-x} O_4 . nH_2O \qquad \text{(Eq. 3.1)}$$
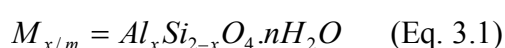
where m is the valence of cations M, n the water content and $0 < x < 1$.

On the other hand, microporous aluminophosphates are a new class of inorganic materials often called zeo-type materials. The basis for the synthesis of these materials is the crystal chemical similarity between Si and P and SiO_2 and $AlPO_4$ in particular [4]. Their framework consists of alternating Al^{3+} and P^{5+} sites and the overall framework is electrically neutral since the positive charge of organic cations is balanced by the simultaneous occlusion of OH^- groups [5]. The general formula is [6]:

$$[(AlO_2)_x(PO_2)_x] \cdot yH_2O \quad \text{(Eq. 3.2)}$$
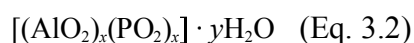
The properties of zeolites are dependent on the topology of its framework, the size, shape and accessibility of its free channels, the charge location and size of the cations within the framework, the presence of faults and occluded material, the order of T-atoms (T is an aluminium or silicon atom in aluminosilicalites or phosphorus in aluminophosphates), and the local environment of T-atoms [7].

Zeolites and zeo-type materials are classified according to their framework type. A framework type is defined on the basis of the connectivity of tetrahedral atoms and is independent of chemical compositions, types of extra-framework species, crystal symmetry, unit cell dimensions, or any other chemical or physical property [5]. An important structural parameter is the size of the pore opening through which molecules diffuse into the channels and cages of zeolites. The pore size is related to ring size defined as the number of tetrahedral atoms forming the pore [5].

Depending on the structural type, the pore sizes range from 0.3 to 1 nm [8]. Among the zeolites, there are materials with small pore openings such as LTA (4.1 Å) with 8 atoms rings, with medium pore openings, i.e. MFI- and MEL (5.5 Å) with 10 atom rings and with large pore openings such as FAU-, LTL-, and BEA- molecular sieves (>7.0 Å) with 12 atom ring [9]. The pore volume of a zeolite is related to the framework density defined as the number of tetrahedral atoms per 1000 Å [5]. The tetrahedra are linked together to form cages connected by pore openings of defined size.

In Fig. 3.1 the framework of the zeolites used in this work are shown. The zeolites are zeolite A(LTA), AlPO-18 (AEI), beta (BEA), zeolite L (LTL) and silicalite-1 (MFI).
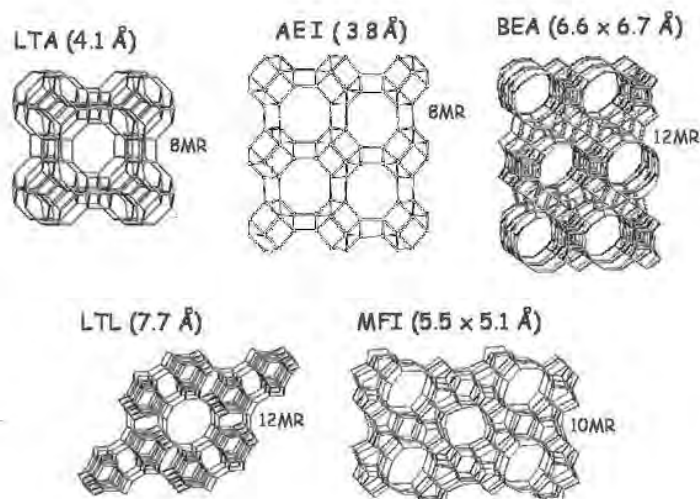
Figure 3.1.   Zeolite framework types used in the present work.

Zeolites are widely used in several applications such as catalysts, especially in the petrochemical industry [10], as molecular sieves in separation technology [11] or as ion exchangers in detergent formulations [12]. New applications of zeolites contribute to environmentally friendly processes and refined zeolites such as catalytic zeolite membranes and zeolites containing exhaust-pipe reactors are being introduced. The possibility to accommodate ions, large molecules or nanostructures in the crystalline matrix has been explored and the electronic, acoustic and photonic modifications of the properties response of the materials has been tested [13].

3.2.1 *ZEOLITE FORMATION IN COLLOIDAL SUSPENSIONS*

Zeolites are usually synthesized from aqueous basic aluminosilicate precursor gels under hydrothermal conditions at elevated temperatures. The complex process of self-assembly of the zeolite involves numerous simultaneous and inter-independent equilibrium and condensation steps [14]. Every zeolite has a specific molar composition range often represented in a ternary compositional phase diagram (Na_2O, Al_2O_3 and SiO_2).

In general, the synthesis of microporous materials is governed by the overall chemical composition of the reactant mixtures and the thermodynamic variables. The zeolite formation process is very sensitive to the initial reactants, conditions of hydrothermal synthesis and post-synthesis treatments [9]. The synthesis of ordered microporous silicas by cooperative self-assembly of organic surfactants and inorganic species was described by Beck et al. [15]. The synthesis of microporous nanocrystals in the form of stable colloidal suspensions was one of the important developments in zeolite science in the past decade [16].

A typical hydrothermal zeolite synthesis could be described by the following steps [17] shown in Fig. 3.2:

- Amorphous precursor gel is obtained by mixing of the silica and alumina sources, mineralizer, template and solvent (water);

- After an aging step, the mixture is heated in a sealed autoclave (for reaction temperatures above 100 °C);

- During the induction period the reactants remain amorphous after raising the synthesis temperature;

- Crystal growth converts essentially all amorphous material into zeolite

- Zeolite crystals are recovered by filtration, washing and drying.
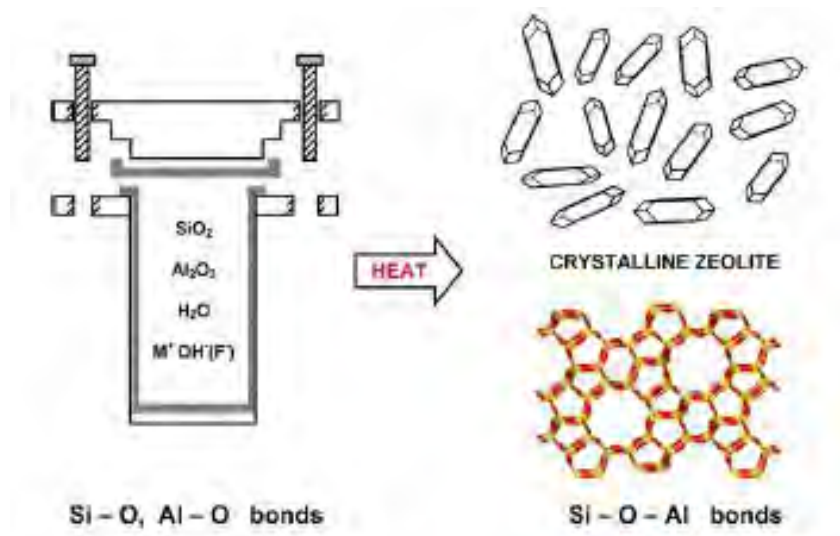
Figure 3.2.   Hydrothermal synthesis of aluminosilicate zeolites [reproduced from Ref. 17].

Regarding the zeolite formation, recent theories propose a solution-mediation model based on crystal growth by localized construction from small, mobile species ordered by the participating cations, stating that the common presence of mobile species renders unnecessary the distinction between „gel rearrangement' and „solid-phase transformation' mechanisms [17].

Hydrothermal conditions make use highly alkaline aluminosilicate gels and temperatures between 100 and 200 °C and yield bulk zeolites of micrometer size. To obtain colloidal zeolite nanoparticles (stable suspensions of discrete zeolite crystals with sizes under 100nm and narrow particle size distribution) one should use clear homogeneous precursor solutions and factors such as low crystallization temperatures (typically 25 and 100 °C) and high levels of supersaturation that potentially can favor nucleation over growth. Another important factor is the steric stabilization of the proto-nuclei, which is often achieved by low alkali content and abundant addition of organic templates. These bulky quaternary ammonium cations can be absorbed on the surfaces of the growing particles and prevent

further agglomeration. The organic cations also act as structure-directing agents, thus directing the growth of certain zeolite framework types by being incorporated into the channels and cages [18, 19].

3.2.2   SYNTHESIS OF ZEOLITE A

Zeolite A was synthesized in the Na^+ form at room temperature, following the procedure described in Ref. 14. Firstly, all reactants (see table 3.1) were mixed except for the organic template, tetramethylammonium (TMA). The template was then added and the solution stirred and kept for 3 days at room temperature. The nearly clear mixture with the molar composition (12 TMAOH: 0.8 Al_2O_3: 5 SiO_2: 0.15 NaOH: 272 H_2O) was transferred to the crystallization vessel and crystallization was performed at 70 °C (see Table 3.1). After crystallization, the mother liquor was separated from the product using a high performance centrifuge (Beckman Coulter, Model Avanti J-30I with 50ml vials) at 20 000rpm for 180 minutes. For further processing, the product was washed twice with an appropriate amount of water using ultrasonication for better dispersion.

Table 3.1.   Experimental conditions for the synthesis of zeolite A.

Molar composition	12 TMAOH: 0.8 Al_2O_3: 5 SiO_2: 0.15 NaOH : 272 H_2O
Precursors	TetramethylAmmonium Hidroxide Pentahydrate (Sigma-Aldrich)
	Aluminium isopropoxide (Acros Organics)
	Silica 30% -Ludox SM (Sigma-Aldrich)
	Sodium hydroxide (Riedel-de-Haen)
	Distilled water
Temperature and time	In the oven: 70 °C @ 65- 72 hours

The following mechanism for zeolite A crystal growth (large crystals) was proposed by Mintova et al. [13] (see Fig. 3.3).
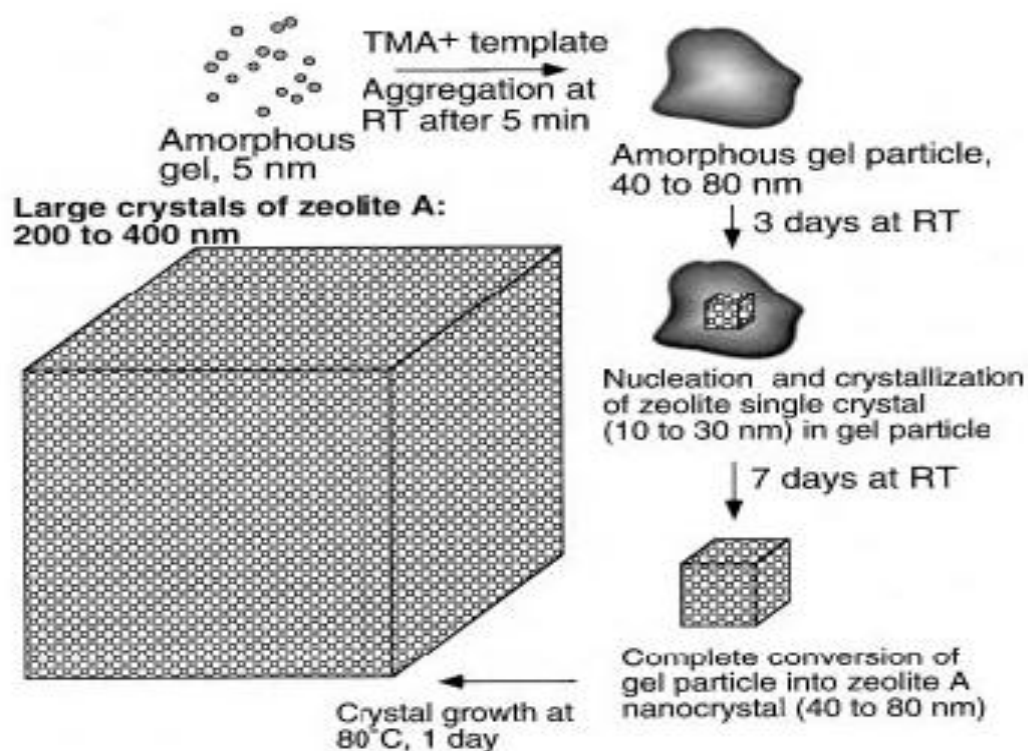
Figure 3.3. **A schematic representation of the proposed zeolite growth mechanism [After Ref. 13].**

In our studies we were interested in small size particles before the crystals grow above 200-400nm as shown in the last step of Figure 3.3.

3.2.3 SYNTHESIS OF ZEOLITE BETA

Zeolite Beta was first synthesized by Wadlinger et al. in the Na_2O-TEAOH-Al_2O_3-SiO_2-H_2O (TEAOH, tetraethylammonium hydroxide) system, wherein the recommended SiO_2/Al_2O_3, Na_2O/TEAOH and TEAOH/SiO_2 molar ratios are in the range 10-200, around 0-0.1 and 0.1-1.0, respectively. Crystallization takes place between around 75 °C and 200 °C and synthesis times vary between 40 days at the lower temperature (although the

crystallization is thought to be incomplete) and 6 days at elevated temperatures (150 °C). The SiO_2/Al_2O_3 molar ratio of zeolite is claimed to be between 10 and 100 although it may be synthesized with a ratio as high as 150 [20].

In our studies, the nanosized zeolite Beta crystals were synthesized from clear precursor suspensions containing the organic template tetraethylammonium hydroxide (TEAOH). The crystalline nanoparticles were extracted from the reaction mixture after the hydrothermal treatment by a three-step centrifugation (20 000 rpm for 180 minutes) and subsequently redispersed in distilled water, thus achieving stabilized zeolite suspensions in water with a concentration of 1%wt. (see Table 3.2).

Table 3.2.   Experimental conditions for the synthesis of zeolite Beta.

Molar composition	9 TEAOH: 0.25 Al_2O_3: 25 SiO_2: 295 H_2O*
Precursors	Tetraethyl Ammonium Hidroxide (Sigma-Aldrich) Aluminum isopropoxide (Acros Organics); Silica 30% -Ludox SM (Sigma-Aldrich) Distilled water
Temperature and time	in the oven: 100 ºC @ 3 to 5 days

* Correction for molar composition was needed because there was no silica 40% available:
9 TEAOH: 0.25 Al_2O_3: 25 SiO_2: 331 H_2O

3.2.4   OTHER SYNTHESIS PROCEDURES FOR ZEOLITES

The following zeolites were also used in the present work and were synthesized in the group of Prof. Mintova according to procedures described below.

AlPO-18

AlPO-18 nanocrystals were prepared according to procedure described in Ref. 21. Briefly, aluminum isopropoxide (Aldrich, 98%) was dissolved in TEAOH (Aldrich, 35%) and distilled water, followed by vigorous stirring until a clear solution was obtained. Phosphoric acid (Acros, 85%) was added drop wise under continuous stirring; the resulting mixture was stirred for 45 minutes in order to ensure a clear solution. The final composition of the precursor solution was 1 Al_2O_3 : 3.16 P_2O_5 : 3.16 $(TEA)_2O$: 186 H_2O. The hydrothermal treatment of the precursor solution (25 ml) was carried out in a microwave oven (800 W) at 180 °C for 5 minutes. The purification of the suspension was carried out using high-speed centrifugation (24 500 rpm for 10 minutes) followed by re-dispersion in water using an ultrasonic bath.

Silicalite-1 (pure silica MFI type zeolite)

Pure silica silicalite-1 particles (Si-MFI) were synthesized by the procedure described in Ref. 22. A pre-hydrolyzed precursor solution having the chemical composition: 7 TPAOH: 25 SiO_2: 150 $4H_2O$: 100 EtOH was used. The silica source used for preparation of this solution was tetraethoxy silane (TEOS, Aldrich, 95%) and the organic template was tetrapropylammonium hydroxide (TPAOH, Aldrich, 1M aqueous solution). After hydrothermal treatment of the precursor solution at 90 °C for 48 hours, the Si-MFI crystals were purified in three steps of high-speed centrifugation (25 000 rpm for 1 hour) and redispersed in distilled water under ultrasonication.

Zeolite L

Nanosized zeolite L crystals [23].were synthesized from a colloidal precursor solution having the chemical composition: 5 K_2O:10 SiO_2: 0.5 Al_2O_3: 200 H_2O. Aluminum

hydroxide and potassium hydroxide were dissolved in water under vigorous stirring. Colloidal silica was then added and aged in a vessel at ambient temperature for 24 hours prior to the further hydrothermal treatment. The nanosized crystals resulting from the hydrothermal treatment of colloidal solutions were purified by separation from the mother liquor by three steps of centrifugation (20 000 rpm for 1 hour).

Some of the colloidal zeolite solutions used in the present work can be seen in Fig. 3.4.
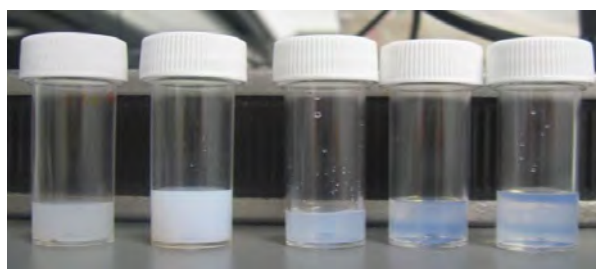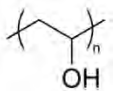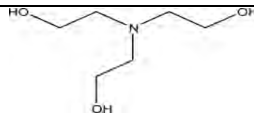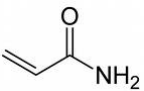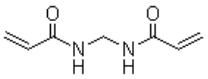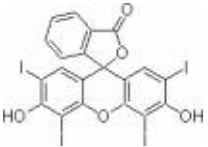
Figure 3.4. **Colloidal zeolite solutions used in the present work. From left to right: Zeolite A (4% wt.), Beta (5% wt.), AlPO-18 (4% wt.), MFI (2% wt.) and zeolite L (2% wt.).**

3.3 PREPARATION OF ACRYLAMIDE BASED PHOTOPOLYMER

Acrylamide based photopolymer consists of two polymerizable monomers (acrylamide and N, N'-methylene bisacrylamide), an electron donor (triethanolamine, TEA) that generates free radicals that initiate the polymerization of the monomers, a photosensitive dye and a binder (polyvinyl alcohol, PVA) acting as a matrix in which the other components are suspended (see table 3.3). The recording wavelength is determined by the photosensitive dye used in the composition, e.g. erythrosine B for recording in the green or methylene blue for recording in red.

Table 3.3.   Standard composition of acrylamide based photopolymer for transmission mode recording in the green.

Component	Molecular Structure	Quantity
PVA Stock solution (10%wt.)		18 ml
TEA		2ml
Acrylamide		0.6g
N, N'-methyleneBisacrylamide		0.2g
Erythrosine B Stock solution (0.11%wt.)		4ml

* 1 - Stock solution of 10%wt. polyvinyl alcohol (PVA) solution is prepared by dissolving 10 g of PVA in 100ml of water under heating and stirring

* 2 - Stock Dye Solution is prepared by dissolving 0.11 g of Erythrosine B in 100 ml of water under stirring

These components were mixed for 30 minutes with a magnetic stirrer at room temperature until a homogeneous solution was obtained. All chemicals were purchased from Sigma. The photopolymer solution can be coated onto glass or plastic substrates and dried for 24 hours in order to obtain dry photopolymer layers (see Fig. 3.5). The tickness is controlled by the amount of solution deposited in each slide.

Figure 3.5. **Acrylamide based photopolymer dry layers sensitized with: (left) methylene blue; (right) erythrosine B.**

3.4   PHOTOPOLYMERISABLE NANOCOMPOSITES

Before use, the aqueous nanoparticle suspensions were sonicated for 20 minutes in order to disintegrate the particles and to ensure homogeneous particle size distribution. These suspensions were filtered and added to the photopolymer solution and the mixture was sonicated for further 10 minutes. Different concentrations of nanoparticles were introduced in the dry layers (detailed compositions will be given in the following chapters). In order to obtain similar mass concentrations of the monomer in the dried layers, deionised water was added to the photopolymer solutions containing different concentrations of nanoparticles to give the same %volume of monomer in solution. The photopolymerizable nanocomposite films were prepared by spreading different quantities of the suspensions (depending on how thick the dry layer is to be) on glass plates with dimensions of 26x38 mm followed by drying for 24 hours.

3.5   GRATING PERFORMANCES

A holographic setup with real time grating growth monitoring capability was developed by N. Pandey [24] and it can be seen in Fig. 3.6.
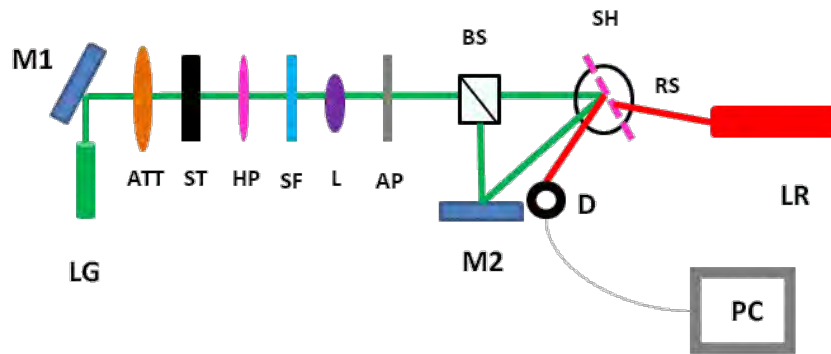
L_G - green laser   *ATT – attenuator*   *ST – shutter*   *HP – half wave plate*

SF – Spatial Filter   *L – lens*   *AP – aperture*   *M – mirror*

BS – beam splitter   *SH – sample holder*   *RS – rotational stage*

L_R *– red laser*   *D - photodetector*
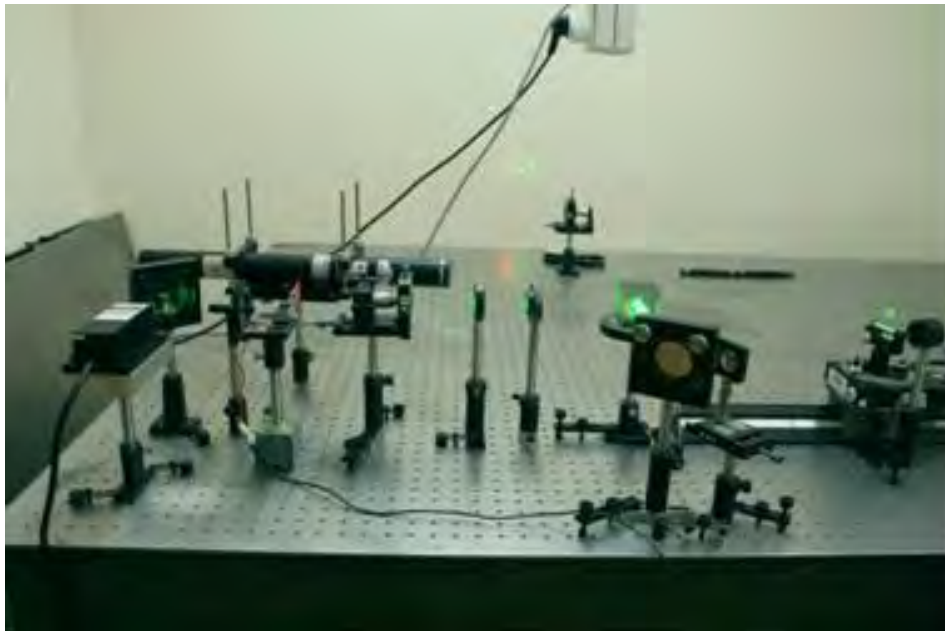
Figure 3.6.   **Experimental set-up for real time grating growth monitoring.**

To record holographic transmission gratings, the recording material is exposed to twomutually interfering s-polarized beams of an NdYVO$_4$ green laser (λ=532 nm). The laser beam goes through a half wave plate to obtain the vertically polarised light beam perpendicular to the *xy* plane of the table, spatially filtered and expanded through a lens. The size of the recorded hologram can be controlled by an aperture placed in front of the

beam splitter. The intensity ratio of the two recording beams is 1:1. The recording beams were incident on the sample in an unslanted configuration and gratings at different spatial frequencies can be recorded, changing the geometry of the setup and the recording intensity can be adjusted (ranging from of 0.1 to 20 mWcm^{-2}). A shutter is also part of the setup and it is controlled by computer. It opens after a delay time of 5 seconds and closes automatically after a preset time. In this way, the recording time can be controlled. To minimize vibrations during recording, the setup lies in a gas floating table (Newport instruments). The sample is held in a rotational stage, which permits adjustment of the incident angle, enabling to record the angular selectivity profile of the grating. The system is computer controlled, which allows recording the diffracted beam intensity measured by a Newport photodetector (model 1830-C) with picowatt sensitivity.

The following grating performances can be determined:

- Dynamics of the grating growth and maximum diffraction efficiency (η)

- Thickness of the samples, obtained by the fitting of the angular selectivity curves, according to Kogelnik theory.

- The refractive index modulation (n_1) of the grating:

$$n_1 = \frac{\lambda \cos\theta}{\pi d} \arcsin\left(\sqrt{\eta}\right) \qquad \text{(Eq. 3.3)}$$

where λ is the reading beam incidence angle, θ is the Bragg angle within the material and d the thickness of the photosensitive layers.

3.6 *LIGHT SCATTERING MEASUREMENT*

To better characterise the compatibility of nanoparticles with the acrylamide based photopolymer a scatterometer based method was used, which is able to measure the light scattering from materials. The theory behind this method [25] is that scattering of electromagnetic waves in any system is attributed to the heterogeneity of that system on the

molecular scale or to the aggregation of many molecules. Since all matter is composed of discrete electric charges, if an obstacle is illuminated by an electromagnetic wave, the electric charges in the obstacle are set into oscillatory motion by the electric field of the incident wave. The accelerated electric charges radiate or scatter electromagnetic energy in all directions.

In figure 3.7 we can see the scatterometer set-up used in this study.
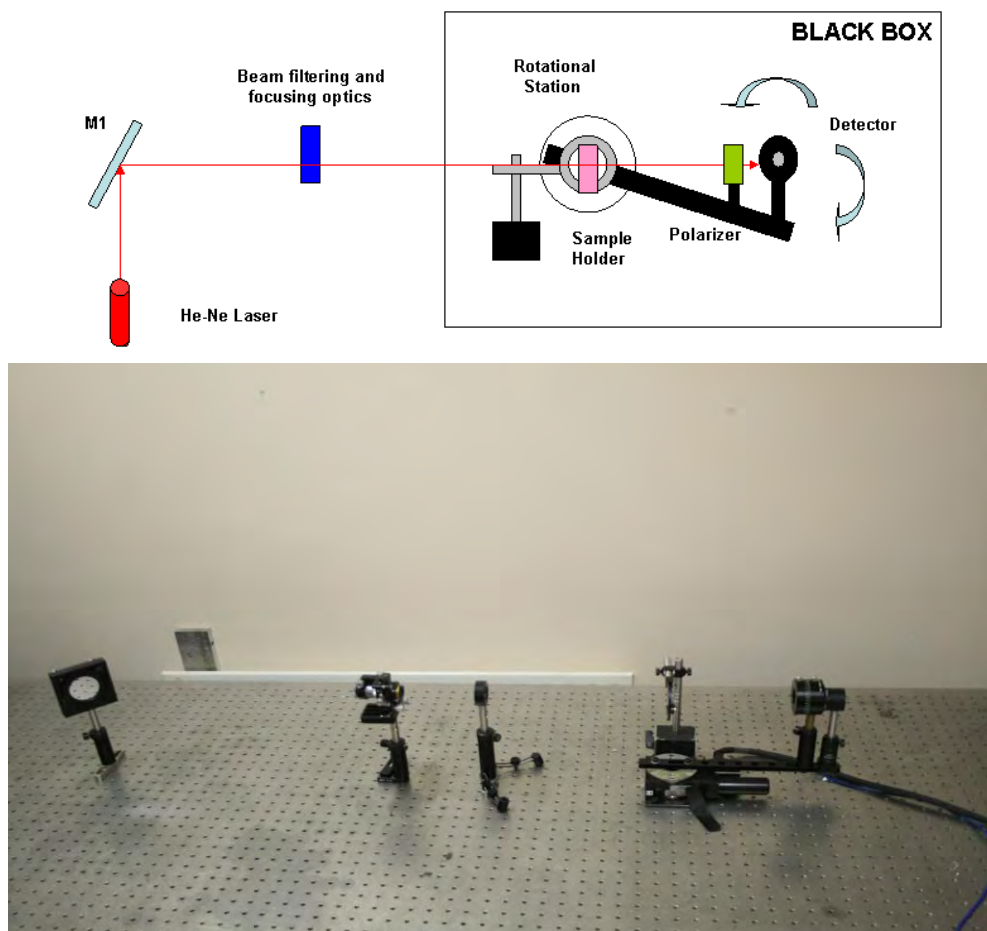
Figure 3.7.   Set-up for light scattering measurements of materials.

The technique for light scattering measurements of surfaces can be based in angle resolved scattering (*ARS*). Angle resolved scattering is defined as the power ΔP_s scattered into the solid angle $\Delta \Omega_s$ normalized to the incident power P_i [26]:

$$ARS(\theta_s) = \frac{\Delta P_s(\theta_s)}{\Delta \Omega_s \times P_i}$$

(Eq. 3.4)

where θ_s is the angle of scattering defined with respect to the surface normal of the sample under investigation. Since the scattering is not isotropic, a polariser was placed in front of the detector. ARS is equivalent to the cosine corrected bidirectional scatter distribution function (BSDF) [25].

3.7 ANALYTICAL METHODS USED IN THE PRESENT WORK

The zeolite nanoparticles and nanocomposites were also characterized by several analytical techniques (Table 3.4).

Table 3.4.   Analytical techniques used in the present work.

TECHNIQUE	NAME	INSTRUMENT USED
DLS	Dynamic light scattering	Malvern Instruments, Zeta sizers – Nanoseries
XRD	X-Ray diffraction (powder)	STOE STADI-P X-ray diffractometer with Ge-monochromated Cu KR1 radiation.
	Nitrogen adsorption	Micromeritics ASAP 2010 surface area analyzer
SEM and SEM-EDX	Scanning electron microscopy (coupled with X-Ray Fluorescence)	Philips XL 30 with Baltec SCD 004 sputter Coater
UV-VIS	Ultra violet and Visible absorption spectroscopy	Perkin Elmer
^{13}C NMR	Carbon Nuclear Magnetic Resonance	Bruker Biospin 400 spectrometer, RF of 106.2 MHz
WLI	White Light Interferometry	MicroXAM S/N 8038
Raman	Raman spectroscopy	Jobin Yvon Raman Spectrometer

3.7.1 DYNAMIC LIGHT SCATTERING

Dynamic light scattering (DLS) [27, 28] is a well established technique for measuring particle size over the size range from a few nanometers to a few microns. The concept is that particles in a suspension move randomly, and the phenomenon is known as Brownian motion and that larger particles move more slowly than the smaller ones if the temperature is the same. According to Einstein developments in his Kinetic Molecular Theory (applied to heat) [29] molecules that are much smaller than the particles can impart a change in the direction of the particle and its velocity.

When a coherent source of light (such as a laser) of known frequency is directed at the moving particles the light is scattered, but at a different frequency. The shift is termed a Doppler shift or broadening. The shift in light frequency is related to the size of the particles causing the shift. Due to their higher average velocity, smaller particles cause a greater shift in the light frequency than larger particles. It is this difference in the frequencies of the light scattered from particles of different sizes that is used to determine the sizes of the particles.

3.7.2 X-RAY DIFFRACTION

X-Ray diffraction (XRD) [30] is applied to identify crystalline phases and to determine certain structural properties such as atom arrangement, grain size, preferred orientation and defect structure.

The conventional method of producing X-Rays is to bombard a metal target with high-energy electrons. Structural information is obtained from the diffraction patterns caused by constructive and destructive interference of X-Rays scattered by the ordered lattice planes.

In certain specific directions, where the scattered X-Rays are "in-phase", the X-Rays scatter cooperatively to form a new wave. This process of constructive interference is called diffraction. The directions of possible diffractions depend only on the size and shape of the unit cell. Certain classes of diffraction are systematically extinguished by lattice centering and by certain space-group symmetry elements. The angular positions (2θ) and intensities of the diffracted peaks of radiation (reflections or peaks) produce a two dimensional pattern. And each reflection represents the X-Ray beam diffracted by a family of lattice planes (hkl). The intensities of the diffracted waves depend on the kind and arrangement of atoms in the crystal structure. It is the study of the geometry of diffraction from a crystal that we use to discern the unit cell dimensions; the missing diffractions give the symmetry of the crystal. The intensities are used to work out the arrangement of atoms. Powder diffraction patterns allow quick identification of crystalline phases by comparison with sample libraries. In this work we used X-Ray to confirm the correct synthesis of the zeolite structures.

3.7.3 NITROGEN ADSORPTION

Analyzing the adsorption of gas molecules, e.g. nitrogen, on solid surfaces is a widespread technique for characterization of porous samples [31]. By recording the adsorption and desorption isotherms, fundamental data including the surface area, pore size distribution and accessible pore volume of a given material can be obtained.

Adsorption isotherms can be described by several different models. The two principal methods currently applied in the study of porous materials are based on the Brunauer-Emmett-Teller (BET) theory and the density functional theory (DFT). The BET theory is based on a number of simplifying assumptions in order to extend the Langmuir model [31]

to multilayer adsorption. The hydrophilicity of any sorbent is quantitatively and qualitatively classified according to IUPAC, based on the type of the water sorption isotherms. The water sorption isotherms are of seven types. The isotherm type I represents a material with high water sorption capacity and very fast saturation at low partial pressure (P/P_0), followed by constant adsorption over a wide range of P/P_0 due to the water saturation in the pores. These sorbents are classified as very hydrophilic due to high affinity for water even at low P/P_0. On the other hand, hydrophilic materials exhibit sorption isotherms of type II or IV, with a very high water sorption capacity at low and moderate P/P_0 [32] (see Fig. 3.8).
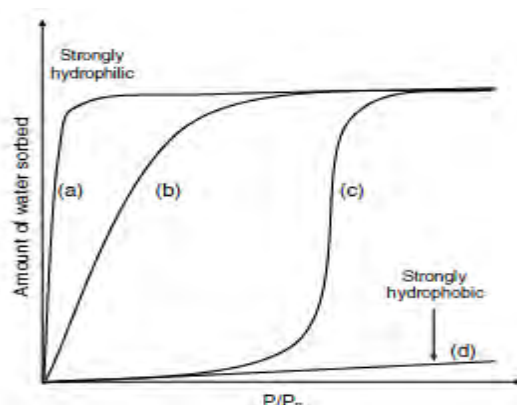
Figure 3.8. **Water sorption isotherms of four nanoporous solids with different degrees of hydrophilicity [reproduced from Ref. 30].**

3.7.4 SCANNING ELECTRON MICROSCOPY

In Scanning Electron Microscopy (SEM) [33] a focused electron beam is generated under vacuum and rastered over the sample surface. As the electron beam penetrates the surface, a number of interactions can occur which result in the emission of secondary electrons or photons. Depending on the desired analysis, the resulting species are detected and evaluated. The amount of secondary and backscattered electrons is dependent on the acceleration voltage of the primary electron beam. However, the number of electrons is

also dependent upon the sample morphology and will increase with increasing angle of incidence as more scattering occurs close to the surface. This change in number of detected electrons and thus signal intensity depending on the change in surface slope of the sample is responsible for the high topological contrast in SEM.

In addition, collisions of primary electrons with core electrons from atoms in the sample result in excited atomic states. After decaying to their ground state, the atoms in the sample emit X-Ray photons with characteristic wavelength distributions for different elements (SEM-EDX) allowing one to determine elemental composition.

3.7.5 *UV-VISIBLE SPECTROSCOPY*

Ultraviolet and visible (UV-Vis) absorption spectroscopy [34] is the measurement of the attenuation of a beam of light after it passes through a sample or after reflection from a sample surface at a single wavelength or over an extended spectral range. This technique gives information about the electronic energy levels of a compound and can be used to identify some functional groups in molecules and secondly, it can be used for determining the concentration of an analyte in solution by measuring the absorbance at some wavelength and applying the Beer-Lambert Law [34].

3.7.6 *WHITE LIGHT INTERFEROMETRY (WLI)*

A white light interferometer [35] allows measurement of roughness and height of a surface on a nanometre scale. In an interferometer, good contrast fringes are obtained only when the two paths of the interferometer are matched in length to within the coherence length of the light source. In a Mirau interferometer, a beam splitter inside the objective divides the incident beam from a white light source into two. The reference beam travels to a reference

mirror whereas the sample beam goes through directly to the sample. Both are reflected back and they interfere with each other when the two paths are matched in length. The measurement of the vertical position of the sample is then carried out for which the fringe contrast is a maximum. Only a single surface height is measured at a time. The typical resolution is 1 nm in the vertical direction and 1-3 μm (depending on the magnification of the objective) in the lateral direction. In this work, WLI was used to measure the surface roughness of the nanocomposites.

3.7.7 *CARBON NUCLEAR MAGNETIC RESONANCE (NMR)*

The ^{13}C NMR [36] technique is used to study the interaction of the nuclei of atoms of carbon isotopes with a static magnetic field. When atoms having nuclear spin are placed in an external magnetic field, the different nuclear spin states are given different magnetic potential energies. The magnetic field produces a small amount of spin polarization and a radio frequency signal of the proper frequency can induce a transition between spin states. This "spin flip" places some of the spins in their higher energy state. If the radio frequency (RF) signal is then switched off, the relaxation of the spins back to the lower state produces a measurable amount of RF signal at the resonant frequency associated with the spin flip. This process is called Nuclear Magnetic Resonance (NMR).

NMR studies of zeolites, and their catalytic reactions, have been thoroughly reviewed in references 37 and 38. One should expect to distinguish organic molecules incorporated or adsorbed in the zeolite framework on the basis of their chemical shifts in the ^{13}C NMR spectra [39].

3.7.8 RAMAN SPECTROSCOPY

Vibrational spectroscopy is applied in two analytical techniques – Infrared (IR) and Raman spectroscopy. Raman and infrared spectroscopy both give molecular information and the methods complement one another [40].

Raman spectroscopy [34] is applied to study the chemical bonding in a material via excitation of vibrational modes. When molecules are irradiated with monochromatic light, a portion of light is scattered. Most of the scattered radiation (about 99%) has the original frequency (Rayleigh scattering or elastic scattering process), but a small portion (less than 1%) is found at other frequencies. This weak inelastic scattering of light from a sample is known as the Raman effect. The difference in frequency between these new frequencies and the original frequencies is characteristic of the molecule irradiated and numerically identical to the vibration and rotational frequencies of the molecule.

Raman Spectroscopy studies of zeolites were reported back in the 70s by Angell [41]. Before that, Dekanter et al. studied the location of cations in zeolites by Infrared and Raman Spectroscopy [42]. In the early 80s, some of the first zeolites studied using Raman spectroscopy were the natural analcime [43] and natrolite [44] zeolites. Studies of zeolites A, X and Y were described later [45]. Since then many other papers have been published in this area. Of particular relevance is the work of Dutta and coworkers [46-50], culminating in three review papers in 1988 [51], 1991 [52] and 2003 [53].

Vibrational spectroscopic methods have proven to be useful tools of structural research. IR and Raman spectroscopy and inelastic neutron scattering (INS) are well established for the characterization of zeolites and molecular sieves [54]. In comparison with the vast amount

of IR work, the field of Raman spectroscopy was rather undeveloped, as stated by Knops in 1997 [55]. Raman did not reach the level of popularity of IR for zeolite studies due to experimental difficulties associated with the technique. One of the main problems associated with Raman is that of fluorescence. There was considerable difficulty in obtaining Raman spectra with acceptable signal-to-noise ratios from highly disperse materials such as zeolites. One cause of fluorescence is that luminescent molecules might be present in the samples. High temperature treatment under oxygen often reduces this problem but n some cases it was found that the heating treatment actually increased the fluorescence background. This may be due to the transformation of simple organic molecules into fluorescent species at high temperature, possibly under the influence of acid sites. Secondly, the presence of Fe impurities in the lattice is known to cause luminescence. The latter problem can be overcome by high purity synthesis, starting e.g. from metallic Al. These problems have been overcome in recent times by using IR lasers and near-IR lasers [56, 57]. In the last years there have been several papers that focus on zeolite structure characterization, for example, characterization of new zeolites or new techniques of zeolites synthesis [58, 59]. Also there is a need to describe the zeolite properties using Raman spectroscopy, usually by studying guest molecules inside the pores of the zeolites [60]. Examples are the applications of zeolites as sorbents [61], ion exchangers [62] and catalysts [63].

The prominent band in the Raman spectra of a zeolitic framework in the 300-600 cm^{-1} region is found to be sensitive to the ring structures present in the framework. This band has been assigned to the motion of an oxygen atom in a plane perpendicular to the T-O-T bonds [51]. In the case of zeolites with even-numbered rings such as 4, 6, 8, 10, and 12 rings, the band is around 500 cm^{-1}. The presence of five-membered rings leads to a

lowering of this frequency to 390-450 cm^{-1} and the precise band pattern depends on the type of rings present. For the ferrierite family of zeolites with 5-, 6-, 8-, and 10-membered rings, this band is at 430 cm^{-1}. The absence of eight-membered rings in this set increases the frequency to 450 cm^{-1}, as in ZSM-23 and NU-10. The presence of 4-, 5-, 6-, 8-, 10-, or 12-membered rings, as in ZSM-5, mordenite, and ZSM-48 leads to bands at 390 and 460 cm^{-1} [51]. Within the above-mentioned groups of zeolites, the symmetric stretching of tetrahedral - ν_S(TOT) - frequency further depends on the value of the average T-O-T angle. A higher T-O-T angle results in a decreased bending force constant, hence in a lower ν_S(TOT) frequency. If within one zeolite structure the individual T-O-T angles are sufficiently different, a splitting of the ν_S(TOT) band can be observed. The influence of the Si/Al ratio on the ν_S(TOT) is less clear. Also, the effects of exchange cations may especially be prominent for zeolites with a high cation exchange capacity, such as zeolite A [51]. The bands of low to moderate intensity that are observable in the high-frequency (850 to 1210 cm^{-1}) are generally ascribed to the asymmetric stretching vibration of the Si-O bond [51].

3.8   CONCLUSIONS

Zeolites are microporous crystalline solids with well-defined structures. Colloidal zeolite nanoparticles can be prepared using clear precursor solutions and bulky quaternary molecules as organic templates. Zeolite A and Beta synthesis procedures were described in detail and were obtained during a research stay at France. The nanocomposites studied in this work were prepared using colloidal zeolite nanoparticles and acrylamide based photopolymer.

The grating performances of volume phase transmission holograms of the nanocomposites were obtained using a computer controlled optical setup which can be used to monitor the grating diffraction efficiency growth curve in real time and the angular selectivity curve. Light scattering and white light interferometry were used to characterize the optical properties of the nanocomposites. Analytical techniques such as DLS, XRD, SEM, nitrogen adsorption and Raman spectroscopy were used to characterize the zeolite colloidal suspensions, confirming their successful synthesis. Analytical techniques such as UV-Vis, SEM-EDX, NMR and Raman spectroscopy were extensively used to study the interactions between the zeolite nanoparticles and the acrylamide based photopolymer. These later techniques are useful for analyzing polymer components adsorbed at the surface of the zeolite or inside the pores of the zeolite or for investigating the redistribution of nanoparticles during the holographic recording process.

3.9   REFERENCES

[1] H. van Bekkum, E. Flanigen, P. Jacobs and J. Jansen, *Introduction to Zeolite Science and Practice*, 2nd ed., Studies in Surface Science and Catalysis, Elsevier Scientific (2001)

[2] A. Dyer, *An Introduction to Zeolite Molecular Sieves*, Wiley, John & Sons (1988)

[3] P. Jacobs, *Carbonogenic Activity of Zeolites*, Elsevier Scientific (1977)

[4] K. Byrappa and M.Yoshimura, *Handbook of Hydrothermal Technology: A Technology for Crystal Growth and Material Processing*, William Andrew Publishing (2001)

[5] P. Yang, *The chemistry of Nanostructured Materials*, World Scientific (2003)

[6] N. Rajić, *Open-Framework Aluminophosphates: Synthesis, Characterization and Transition Metal Modifications*, Journal of the Serbian Chemical Society 70, No. 3, 371–391 (2005)

[7] S. Bhatia, *Zeolite Catalysis: Principles and Applications*, CRC Press (2000)

[8] J. Kecht, B. Mihailova, K. Karaghiosoff, S. Mintova and T. Bein, *Nanosized Gismondine Grown in Colloidal Precursor Solutions*, Langmuir 20, No. 13, 5271-5276 (2004)

[9] S. Kallus, J. Condre, A. Hahn, G. Golemme, C. Algieri, P. Dieudonné, P. Timminsf and J. Ramsay, *Colloidal Zeolites and Zeolite Membranes*, Journal of Materials Chemistry 12, 3343-3350 (2002)

[10] P. Venuto, *Fluid Catalytic Cracking with Zeolite Catalysts*, Marcel Dekker (1979)

[11] C. Coe, *Gas Separation Technology*, Elsevier (1990)

[12] C. Adams, A. Araya, S. Carr, A. Chapple, K. Franklin, P. Graham, A. Minihan, T. Osinga and J. Stuart, *Zeolite Map: The New Detergent Zeolite*, Studies in Surface Science and Catalysis 105 Part B, 1667-1674 (1997)

[13] M. Stacker, H. Kaege, J. Jansen and J. Weitkamp, *Advanced Zeolite Science and Applications* 85, in series Studies in Surface Science and Catalysis, Elsevier (1994)

[14] S. Mintova, N. Olson, V. Valtchev and T. Bein, *Mechanism of Zeolite A Nanocrystal Growth from Colloids at Room Temperature* 283, No. 5404, Science 958-960 (1999)

[15] C. Kresge, M. Leonowicz, W. Roth, J. Vartuli and J. Beck, *Ordered Mesoporous Molecular Sieves Synthesized by a Liquid-Crystal Template Mechanism*, Nature 359, 710-712 (1992)

[16] V. Valtchev, L. Tosheva and K. Bozhilov, *Synthesis of Zeolite Nanocrystals at Room Temperature*, Langmuir 21, No. 23, 10724-10729 (2005)

[17] C. Cundy and P. Cox, *The Hydrothermal Synthesis of Zeolites: Precursors, Iintermediates and Reaction Mechanism,* Microporous and Mesoporous Materials 82, No. 1-2, 1-78 (2005)

[18] N. Feoktistova, S. Zhdanov, W. Lutz and M. Buelow, *On the kinetics of crystallization of silicalite 1*, Zeolites 9, No. 2, 136-139 (1989)

[19] S. Mintova, V. Valchev, *On the Crystallization Mechanism of Zeolite ZSM-5: Part 1. Kinetic Compensation Effect for the Synthesis With Some Diamines,* Zeolites 13, No. 4, 299-306 (1993)

[20] J. Kecht, B. Mihailova, K. Karaghiosoff, S. Mintova and T. Bein, *The Synthesis of Discrete Colloidal Crystals of Zeolite Beta and their Application in the Preparation of Thin Microporous Films*, Journal of Porous Materials 8, No. 1, 13-22 (2001)

[21] H. van Heyden, S. Mintova and T. Bein, *AlPO-18 Nanocrystals Synthesized Under Microwave Irradiation*, Journal of Materials Chemistry 16, 514 – 518 (2006)

[22] S. Mintova, N. Olson, J. Senker and T. Bein, *Mechanism of the Transformation of Silica Precursor Solutions Into Si-MFI Zeolite,* Angewandte Chemistry International Edition 41, No. 14, 2558-2561 (2002)

[23] M. Holzl, S. Mintova and T. Bein, *Colloidal LTL Zeolite Synthesized Under Microwave Irradiation*, Molecular Sieves: From Basic Research to Industrial Applications

Parts A and B 158, Part 1, 11–18 (2005)

[24] N. Pandey, *Studies on Recording Characteristics of Si-MFI Nanoparticle Doped Acrylamide-Based Photopolymer*, DIT MPhil thesis (2009)

[25] A. Duparré, *Scattering From Surfaces and Thin Films*, in Encyclopedia of Modern Optics, eds. R. Guenther, Elsevier (2004)

[26] J. Stover, *Optical Scattering - Measurement and Analysis*, 2nd ed., SPIE-Press (1995)

[27] M. Trainer, P. Freud and E. Leonardo, *High-Concentration Submicron Particle Size Distribution by Dynamic Light Scattering*, American Laboratory 24, 34 (1992)

[28] P. Freud, *Nanoparticle Sizing. Dynamic Light Scattering Analysis in the Frequency Spectrum Mode*, Application Note SL-AN-14 Rev A, Microtrac Inc. (2004)

[29] A. Einstein and R. Albert, *On the Movement of Small Particles Suspended in a Stationary Liquid Demanded by the Molecular-Kinetic Theory of Heat. Investigations on the Theory of the Brownian motion,* Dover publications (1926, reprinted in 1956)

[30] M. Toney, *Encyclopedia of Materials Characterization - Surfaces, Interfaces, Thin Films; XRD - X-Ray Diffraction*, Manning Publications, Greenwich (1992)

[31] F. Rouquerol, J. Rouquerol and K. Sing, *Adsorption by Powders & Porous Solids - Principles, Methodology and Application*, Academic Press, San Diego (1999)

[32] E. Poh and S. Mintova, *Nanoporous Materials With Enhanced Hydrophilicity and High Water Sorption Capacity*, Microporous and Mesoporous Materials 114, No. 1-3, 1–26 (2008)

[33] J. Bindell, *Encyclopedia of Materials Characterization - Surfaces, Interfaces, Thin Films; SEM - Scanning Electron Microscopy*, Manning Publications, Greenwich (1992)

[34] D. Skoog, D. West and F. Holler, *Fundamentals of Analytical Chemistry,* Saunders College Publishing, Fort Worth (1992)

[35] J. Wyant, *White Light Interferometry*, Optical Sciences Center, University of Arizona, Tucson, AZ 85721, AeroSense (2002)

[36] G. Engelhardt, D. Micbel, *High-Resolution Solid-state NMR on silicalites and Zeolites*, Wiley, New York (1987)

[37] A Bell and A. Pines, *NMR Techniques in Catalysis*, Marcel Dekker Inc. (1994)

[38] C. Csicscry, *Shape-Selective Catalysis in Zeolites,* Zeolites 4, No. 3, 202-300 (1984)

[39] B. Mihailova, S. Mintova, K. Karaghiosoff, T. Metzger and T. Bein, *Nondestructive Identification of Colloidal Molecular Sieves Stabilized in Water*, Journal of Physical Chemistry B 109, No. 36, 17060–17065 (2005)

[40] A. Vogel, *Textbook of Practical Organic Chemistry*, 6th Ed., Longman Scientific & Technical, Prentice Hall (2000)

[41] C. Angell, *Raman Spectroscopic Investigation of Zeolites and Adsorbed Molecules*, Journal of Physical Chemistry-US 77, No. 2, 222-227 (1973)

[42] J. Dekanter, L. Maxwell and P. Trotter, *Location of Cations in Zeolites by Infrared and Raman Spectroscopy*, Journal of the Chemical Society - Chemical Communications, 733-734 (1972)

[43] F. Pechar and D. Rykl, *Raman Polarization Spectra of The Natural Zeolite Analcime*, Chemicke Zvesti 35, No. 1, 45-50 (1981)

[44] F. Pechar, I. Gregora and D. Rykl, *Laser Raman Polarization Spectra of Natural Zeolite-Natrolite*, Collection of Czechoslovak Chemical Communications 46, No. 12, 3043-3048 (1981)

[45] F. Roozeboom, H. Robson and S. Chan, *Laser Raman-Study on the Crystallization Of Zeolite-A, Zeolite-X And Zeolite-Y, Zeolites* 3, No. 4, 321-328 (1983)

[46] P. Dutta and B. Delbarco, *Raman-Spectroscopic Studies of Zeolite Framework - Hydrated Zeolite A and the Influence of Cations*, Journal of Physical Chemistry 89, No. 10, 1861-1865 (1985)

[47] P. Dutta and D. Shieh, *Crystallization of Zeolite A: a Spectroscopic Study,* Journal of Physical Chemistry 90, No. 11, 2324-2330 (1986)

[48] P. Dutta, D. Shieh and M. Puri, *Raman-Spectroscopic Study of the Synthesis of Zeolite-Y*, Journal of Physical Chemistry 91, No. 9, 2332-2336 (1987)

[49] P. Dutta and M. Puri, *Synthesis and Structure of Zeolite ZSM-5 - A Raman Spectroscopic Study*, Journal of Physical Chemistry 91, No. 1, 4329-4333 (1987)

[50] P.K. Dutta, B. Delbarco, *Raman-Spectroscopy of Zeolite-A - Influence of Si/Al Ratio*, Journal of Physical Chemistry 92, No. 2, 354-357 (1988)

[51] P. Dutta, D. Shieh and M. Puri, *Correlation of Framework Raman Bands of Zeolites with Structure*, Zeolites 8, No. 4, 306-309 (1988)

[52] P. Dutta, K. Rao and J. Park, *Correlation of Raman-Spectra of Zeolites With Framework Architecture*, Journal of Physical Chemistry 95, No. 17, 6654-6656 (1991)

[53] P. Dutta, *Raman Spectroscopy of Zeolites*, Abstracts of Papers of the American Chemical Society 226, U354-U354 040-Coll Part 1 (2003)

[54] E. Geidel, H. Lechert, J. Dobler, H. Jobic, G. Calzaferri and F. Bauer, *Characterization of Mesoporous Materials by Vibrational Spectroscopic Techniques,* Microporous and Mesoporous Materials 65, No. 1, 31-42 (2003)

[55] P.-P. Knops-Gerrits, D. De Vos, E. Feijen and P. Jacobs, *Raman Spectroscopy on Zeolites,* Microporous Materials 8, No. 1-2, 3-17 (1997)

[56] A. Gujar, A. Moye, P. Coghill, D. Teeters, K. Roberts and G. Price, *Raman Investigation of the SUZ-4 Zeolite*, Microporous and Mesoporous Materials 78, No. 2-3, 131-137 (2005)

[57] Y. Ma, N. Li, N. Guan, S. Xiang, H. Song and H. Wang, *A Novel Zeolite-Like Structure Based On Zinc And Aluminum Phosphate Synthesized From H_3PO_3-Containing Gel*, Microporous and Mesoporous Materials 94, No. 1-3, p. 179-184 (2006)

[58] G. Tompsett, B. Panzarella, W. Conner, K. Yngvesson, F. Lu, S.L. Suib, K. Jones and S. Bennett, *In Situ Small Angle X-Ray Scattering, Wide Angle X-Ray Scattering and Raman Spectroscopy of Microwave Synthesis*, Review of Scientific Instruments 77, No. 12, 124101- 124101-10 (2006)

[59] J. Mesu, T. Visser, A. Beale, F. Soulimani, B. Weckhuysen, *Host-Guest Chemistry of Copper(II)-Histidine Complexes Encaged In Zeolite Y,* Chemistry - A European Journal 12, No. 27, 7167-7177 (2006)

[60] J. Bronic, L. Sekovanic, A. Muzic, T. Biljan, J. Kontrec and B. Subotic, *Host-Guest Interaction Of Iodine With Zeolite A*, Acta Chimica Slovenica 53, No. 2, 166-171 (2006)

[61] H. Wang, E. Turner and Y. Huang, *Investigations of the Adsorption of N-Pentane in Several Representative Zeolites*, Journal of Physical Chemistry B 110, No. 16, 8240-8249 (2006)

[62] A. Basch, M. Hartl and P. Behrens, *The Structural Change of Intercalated Iodine Determined by the Inner Surface Properties of Ion-Exchanged Zeolite A*, Microporous and Mesoporous Materials 99, No. 3, 244-250 (2007)

[63] G. Yan, J. Long, X. Wang, Z. Li, X. Wang, Y. Xu and X. Fu, *Insight Into Photoactive Sites for the Ethylene Oxidation on Commercial HZSM-5 Zeolites With Iron Impurities by UV Raman, X-Ray Absorption Fine Structure and Electron Paramagnetic Resonance Spectroscopies*, Journal of Physical Chemistry- C 111, No. 13, 5195-5202 (2007)

CHAPTER 4: BETA (BEA-TYPE STRUCTURE) DOPED NANOCOMPOSITES

4.1 INTRODUCTION

In this chapter, information regarding the characterization of zeolite Beta colloidal solutions is given. This characterization is required in order to confirm the successful formation of the zeolite, since their syntheses are complex processes. Wherever possible, a combination of well established techniques was used as described in this and following chapters. Using the techniques of confocal Raman Spectroscopy and Scanning Electron Microscopy coupled with Energy Dispersive X-Ray Fluorescence (SEM-EDX), the redistribution of Beta nanoparticles can be investigated. By means of refractive index calculations, the pore volume before and after incorporation of the Beta nanoparticles can show if they are mostly to be empty or filled when the zeolite is added to the photopolymer. For zeolite Beta, they are possibly filled by photopolymer components. The interactions between the photopolymer components and zeolite nanoparticles in the photopolymerizable nanocomposites were characterized by ^{13}C NMR spectroscopy (solid-state NMR is a very sensitive probe of the local environment of a particular atom in the structure) and UV-Visible spectroscopy. It was found that the Beta zeolite nanoparticles (up to 5%wt.) behave as non-inert components during holographic recording, bonding to the triethanolamine (TEA) electron donor molecules, resulting in an effective increase in layer thickness that causes doubling of the diffraction efficiency of the nanocomposite in comparison to that of the undoped photopolymer. Raman spectroscopy also provided evidence of acrylamide molecules bonding to the zeolite.

Transmission gratings of Beta nanocomposites show potential to be used as holographic sensor for chemical detection.

4.2   ZEOLITE BETA NANOPARTICLES CHARACTERIZATION

Nano-sized Beta zeolite crystals (Figure 4.1) in a colloidal suspension were used in the present study.
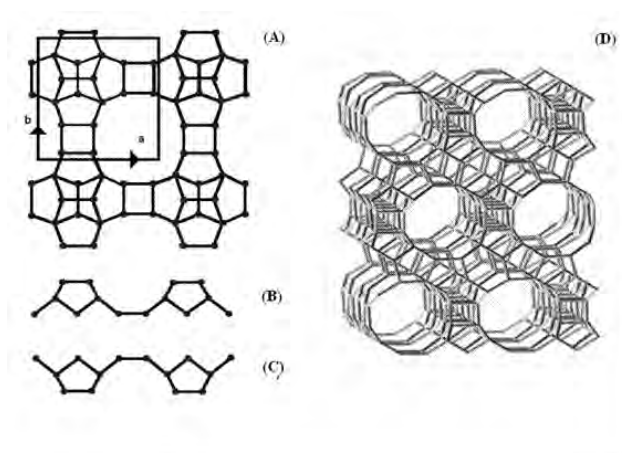
Figure 4.1.   Periodic building unit of the Beta zeolite (BEA-type framework): view along (A) [001], (B) [010] and (C) [100] of the basic layer; (D) pore structure.

Two solutions of zeolite Beta (with different nanoparticle sizes) were used in the present study. The dynamic light scattering results are shown in Fig. 4.2.
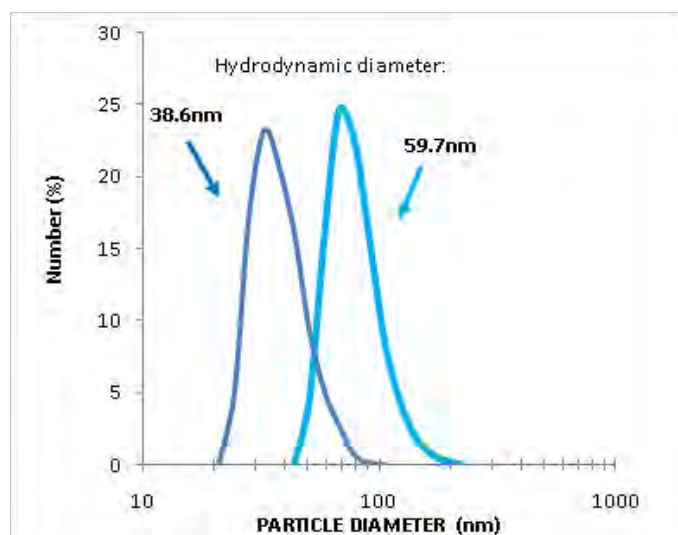
Figure 4.2.   DLS curves of zeolite Beta suspensions.

The results are shown in number of particle counts obtained per unit volume of sample (number weighted). The results show particle sizes of 40 and 60nm, both below 100nm and also both the materials exhibit monomodal particle distribution.

The crystalline nature was determined by examining its XRD pattern (Fig. 4.3).
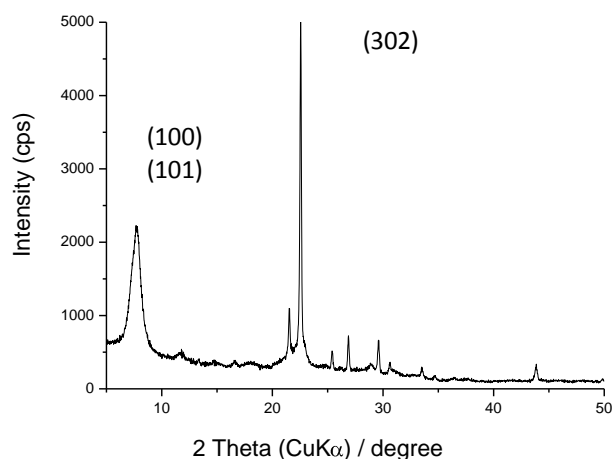
Figure 4.3.   X-ray diffraction pattern of zeolite Beta nanoparticles.

The formation of zeolite Beta was confirmed by comparing its diffractogram with the literature [1]. The most prominent peak, corresponding to (302) reflection appeared at 22.48° and this is characteristic for highly crystalline zeolite Beta. The broad peak at 6° 2θ, is formed by overlaping of two reflections with *hkl* of (100) and (101). The XRD pattern in Fig. 4.3 showed fully crystalline Beta zeolite material and absence of an amorphous phase.

The zeolitic microporosity was demonstrated with the nitrogen sorption isotherm depicted in Fig. 4.4.
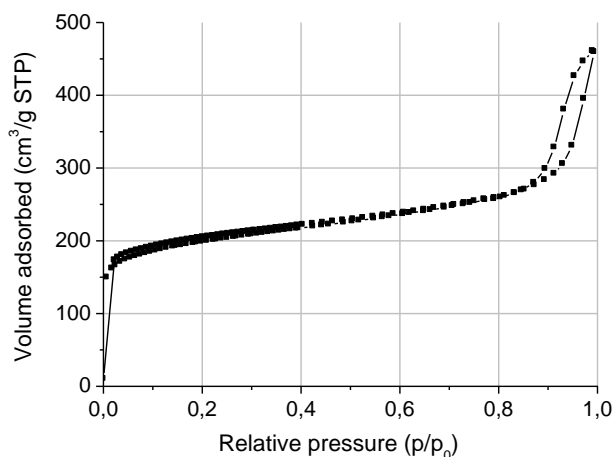
Figure 4.4.   Nitrogen-sorption isotherm of zeolite Beta nanoparticles.

The apparent BET specific surface area was calculated to be 663 m^2g^{-1} and the total pore volume (P/P$_0$=0.97) was 0.71 cm^3g^{-1} (the surface area is calculated according to the BET model from the adsorption branch of the isotherm in the pressure range 0.001–0.15 P/P$_0$ and the total volume is calculated from single point measurements at P/P$_0$ = 0.97).

The nitrogen adsorption-desorption curves possess the typical type IV isotherm in accordance with IUPAC classification [2]. The isotherm exhibits a rapid increase in the amount of nitrogen adsorbed at low relative pressure (P/Po < 0.1), which corresponds to the filling of the micropores with the gas. A nearly flat region follows and then a distinctive hysteresis loop at high relative pressure (P/Po > 0.85) is observed, which is associated with multilayer adsorption in the textural mesopores of the nanosized material. The sample has similar values of total pore volume and BET than the values referred in literature [3]. The total specific pore volume is 0.71 cm^3g^{-1} (of those 0.25 are micropore volume) which is due to the small crystal size of the nanoparticles and the high surface area (> 500 cm^2g^{-1}) is explained by the high degree of crystallinity of the zeolite.

The zeolite morphology was characterized using SEM (Fig. 4.5).
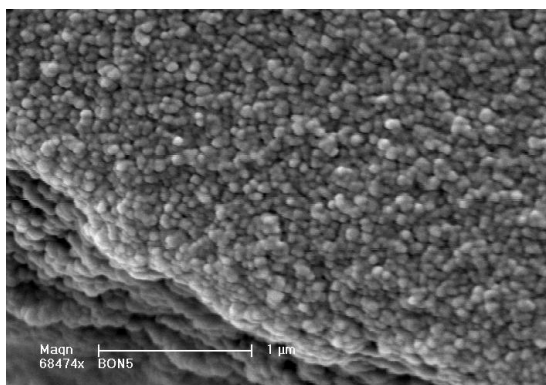
Figure 4.5.   Morphology of Beta zeolite nanoparticles after gold coating.

From Fig. 4.5 we can see that the Beta nanoparticles have a spherical shape, which is the crystal morphology reported before in the open literature [1].

Raman spectroscopy has the ability to detect amorphous substances and to fingerprint different crystalline silicalite and aluminosilicate materials. Raman spectroscopy for examination of the structure of the colloidal zeolite was previously thought to be useful for the following reasons: (i) allows probing of the structure of very small particles; (ii) the intense spectroscopic signals from the organic molecules ensure sufficient sensitivity of the method even in the case of low concentrations of the colloidal suspension; and (iii) stabilized colloidal zeolites with narrow particle size distribution always contain organic molecules [4].

The Raman spectrum of Beta nanoparticles is shown in Fig. 4.6, where the most intense peaks are evidenced.
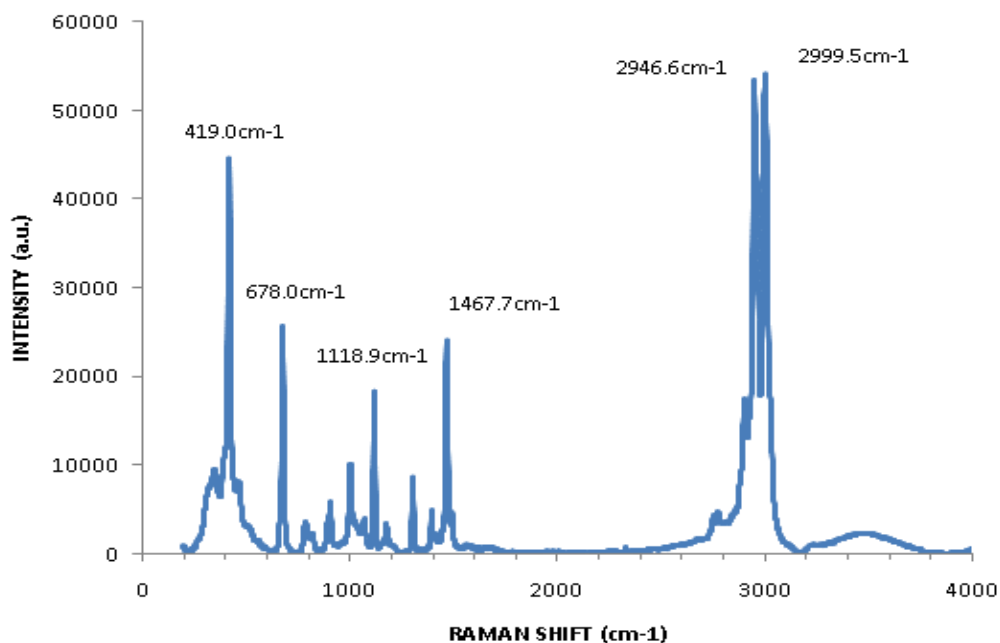
Figure 4.6. **Raman spectrum of zeolite Beta nanoparticles.**

This spectrum was well matched with that in literature [4]. The authors showed that the most appropriate Raman spectroscopic features for detecting zeolite Beta nanocrystallites when compared to the template, tetraethylammonium hydroxide (TEAOH) in water are: (i) a single peak at 674 cm^{-1} instead of two signals at 664 and 674 cm^{-1}, characteristic of free template (ii) red-shift of the peaks at 1004-999 cm^{-1} and of the peak at 1118-1113 cm^{-1}, and (iii) splitting of the band at 2952 cm^{-1} and red-shift of the more intense component to 2945 cm^{-1}.

The prominent band in the Raman spectra of zeolite Beta in the fingerprint region (300-600 cm^{-1}) is found at 419 cm^{-1}. This band is assigned to the motion of an oxygen atom in a plane perpendicular to that of the T-O-T bonds (Fig. 4.7):
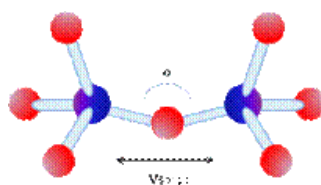
Figure 4.7.   Stretching mode of T-O-T mode in zeolites.

Other prominent bands assigned to zeolites are summarized in Table. 4.1.

Table 4.1.   Raman peak assignments of zeolite Beta.

Raman Peak (cm^{-1})	Functional Group/ Vibration
419.0	T-O-T stretching of zeolite (6 rings)
678.0	C-C-N (template)
1120.3	Stretching of Si-O (zeolite)
1467.7	Deformation of CH (template)
2946.6	Symmetrical Stretching of CH$_3$ (template)
2999.5	Asymmetrical Stretching of CH$_3$ (template)

4.3   BETA NANOCOMPOSITES OPTICAL PROPERTIES

Beta nanocomposites were prepared by adding different quantities of zeolite solution to the photopolymer solution and adding water to obtain the same mass concentration of photopolymer components per volume. An example using PVA 20%wt. stock solution and zeolite Beta 1%wt. is given in table 4.2.

Table 4.2. **Compositions used for preparation of photopolymerizable Beta nanocomposite (NC) layers from zeolite solution 1%wt. (20% PVA stock solution).**

Photopolymerizable Material	Photopolymer Solution (ml)	Nanoparticle Solution (ml)	Water (ml)
Undoped Photopolymer	1	0	2.5
NC Beta 1%wt.	1	0.25	2.25
NC Beta 2.5%wt.	1	0.625	1.875
NC Beta 5%wt.	1	1.25	1.25
NC Beta 10%wt.	1	2.5	0

The compatibility of the zeolite particles suspensions with the photopolymer solutions was characterized by DLS. No aggregation of the zeolite nanoparticles directly after mixing and after 24h aging of the nanocomposite suspensions was observed (Figure 4.8).
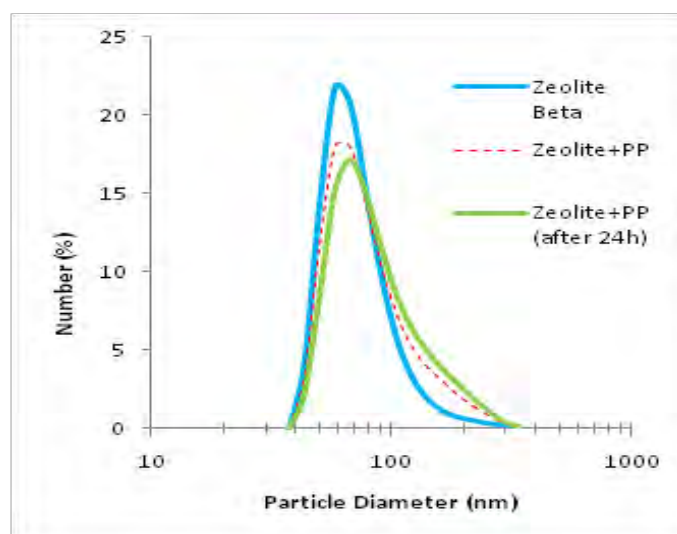
Figure 4.8. **DLS curves (number weighted) of: (blue) zeolite Beta; (red) photopolymer doped with Beta nanoparticles (freshly mixed); (green) photopolymer doped with Beta nanoparticles (24 hours stored at RT).**

The Beta nanocomposite layers after drying were stable for more than 24 hours after preparation as can be seen in Fig. 4.9. In this experiment a large batch of dry layers of Beta

nanocomposite (2.5 and 5%wt.) was prepared and gratings were holographically recorded every day over more than one month and compared with the acrylamide based photopolymer gratings. To prepare the layers, 0.4 ml of each solution was deposited on a glass substrate (13×38 mm^2) to give a thickness of around 40 µm. The gratings were recorded in the green with an exposure of 700 mJcm^{-2} (recording intensity of 5 mWcm^{-2}) at a spatial frequency of 1000 lmm^{-1}.

A)

B)
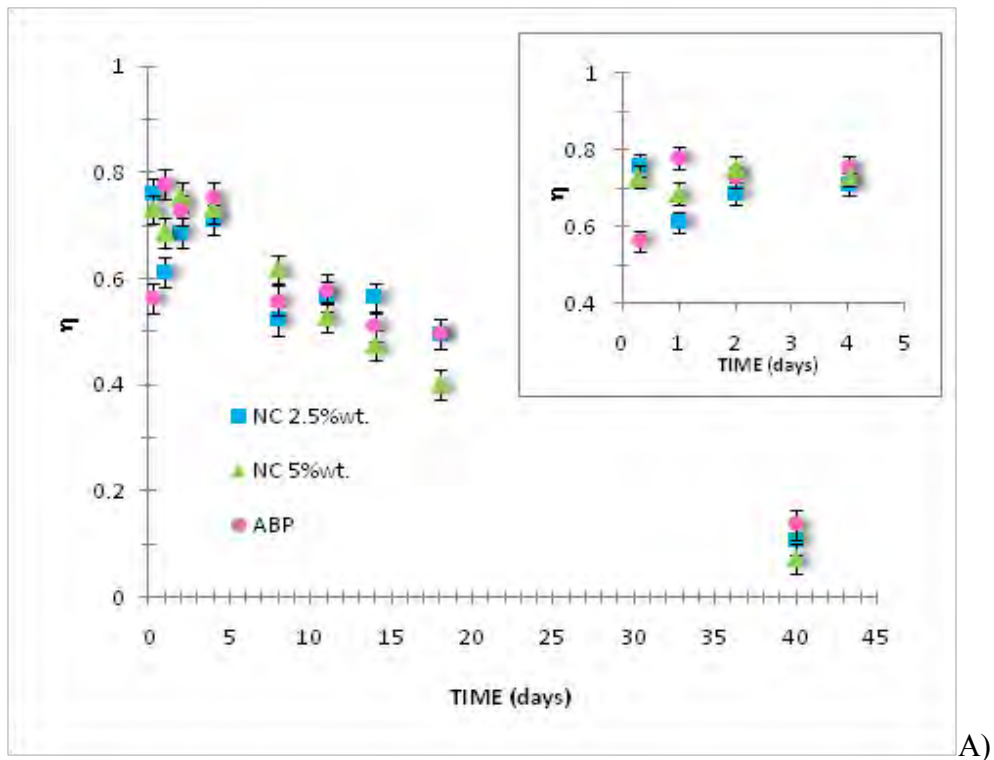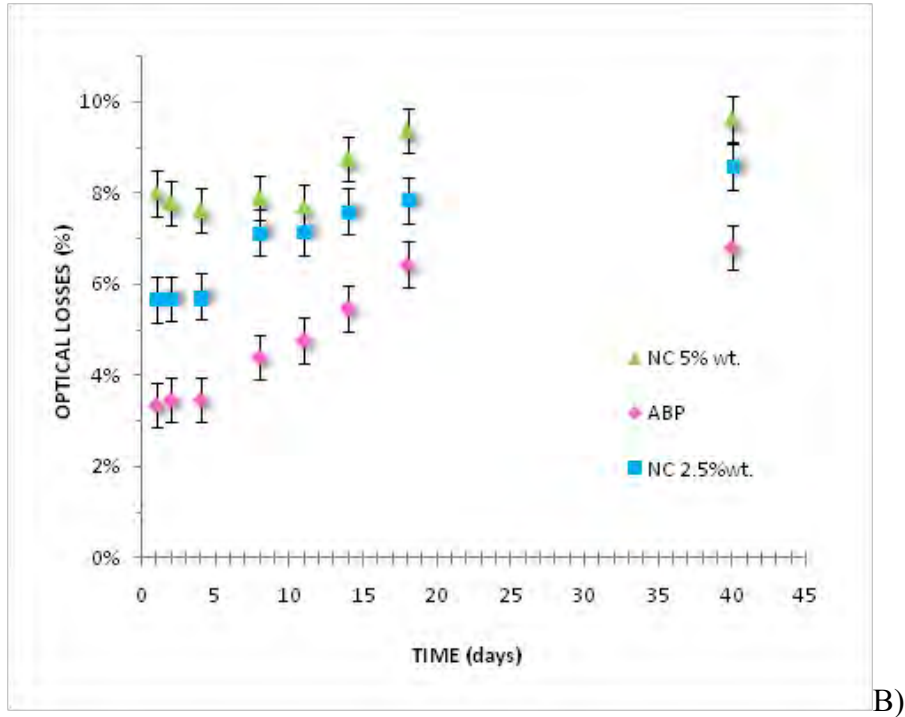
Figure 4.9. **Temporal evolution of (A) diffraction efficiency; (B) optical losses of undoped photopolymer - ABP (pink circle) and containing 2.5%wt. (blue squares) and 5%wt. (green triangles) of Beta nanoparticles; exposure was 700 mJcm^{-2} at a spatial frequency of 1000 lmm^{-1}.**

As can be seen in Fig. 4.9A, the photopolymer materials degrade with time: two weeks after preparation, the diffraction efficiency of gratings recorded decreased by around 30% when compared to initial values. One possible explanation is due to the precipitation of bis-acrylamide, which forms white crystals in the surface of the layer.

Zeolite Beta nanoparticles seem to have no effect on the aging (shelf-life) of the photopolymer. The optical losses (*OL*) of the material were calculated by:

$$OL = 1 - \frac{I_T + I_D + I_R}{I_0} \qquad \text{(Eq. 4.1)}$$

where *I* are the intensities of the transmitted (I_T), diffracted (I_D), reflected (I_R) and incoming (I_0) beams.

The results for the measured optical losses are shown in Fig. 4.9B. The addition of 2.5 and 5%wt. of zeolite Beta nanoparticles to the photopolymer increases the optical losses. With time the optical losses of all materials also increase.

The effect of incorporation of zeolite Beta in the photopolymer was further investigated by analyzing the dependence of optical losses as a function of increasing concentrations of zeolite Beta nanoparticles (see Figure 4.10). Layer thickness was around 20 µm for undoped photopolymer and increased to around 50µm for a nanocomposite containing 10%wt. Beta.
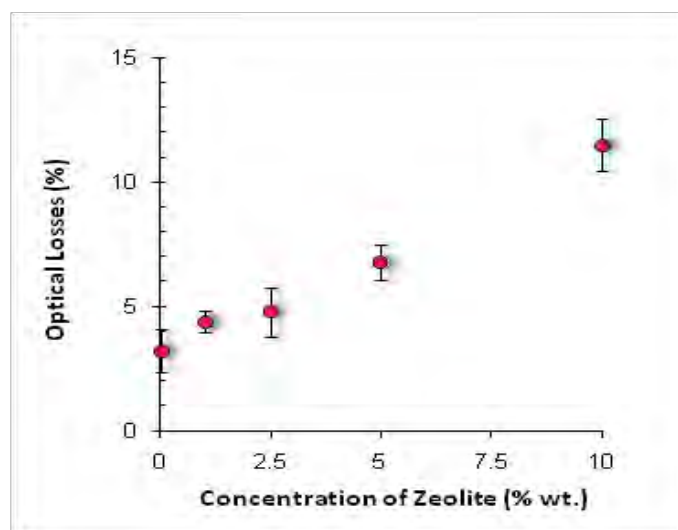
Figure 4.10.   Optical losses of Beta nanocomposites .

As can be seen in Fig.4.10 the optical loss increased from 3% (undoped photopolymer) to 7% when we introduce 5%wt. Beta nanoparticles and to 10% when we add 10%wt. Beta nanoparticles.

In order to investigate in more detail the influence of the concentration of Beta zeolites on the optical properties we measured the bidirectional scattering distribution function (the way in which the light is scattered by a surface) of samples of approximately the same

thickness (around 40 μm) and this is shown in Fig. 4.11. For comparison the scattering of the glass substrate is also shown. The instrument signature wre measured in the absence of the materials or the glass substrate.

A)

B)
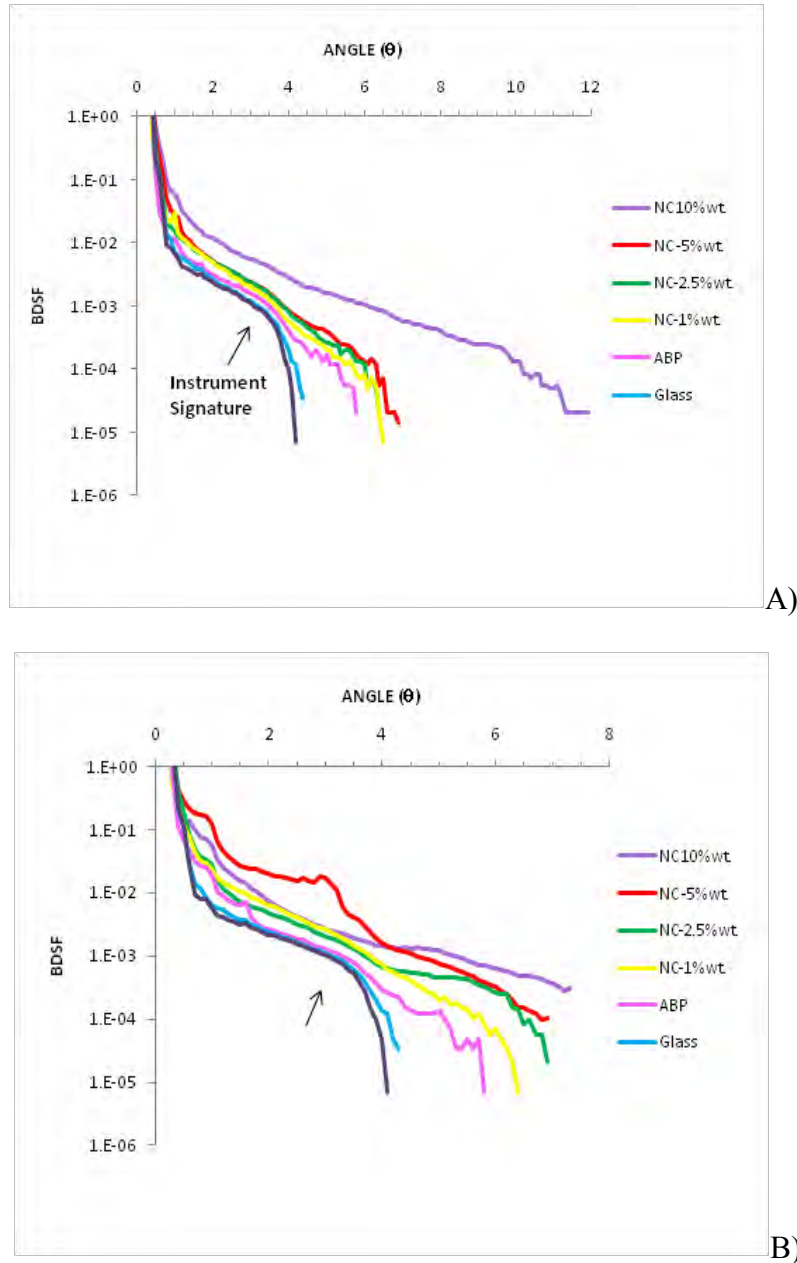
Figure 4.11.   Bidirectional scattering distribution function of glass, acrylamide based photopolymer (ABP) and nanocomposites with several concentrations of Beta indicated in the figure; (A) unpolymerized material; (B) grating of 1000 lmm^{-1} (logarithmic scale).

For the unpolymerized material, the increase in zeolite Beta concentration leads to an increase in the scattering of light. The addition of Beta nanoparticles up to 5%wt. to the photopolymer does not significantly increase the light scattering of the layer compared to undoped photopolymer, but it seems to be a substantial increase for an addition of 10%wt. zeolite Beta (indicated by the BDSF larger amplitude angular spread). After polymerization, the scattering of light by the material seems to be lower. One possible explanation is that the nanoparticles are now evenly redistributed across the photopolymer volume.

For comparison, we have measured the scattering from nanocomposites made with photopolymer and alumina (Fig. 4.12) and titania (Fig. 4.13) nanoparticles.
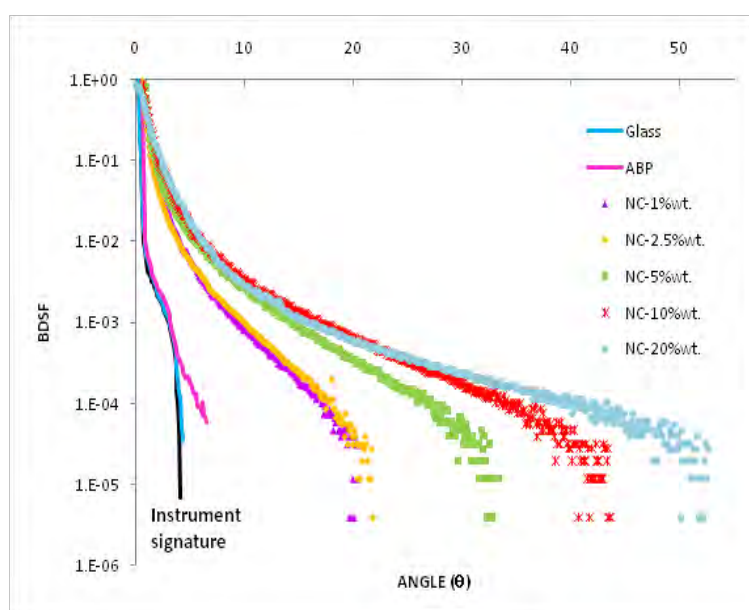
Figure 4.12. **Bidirectional scattering distribution function of glass, acrylamide based photopolymer (ABP) and Al₂O₃ nanocomposites in several concentrations indicated in the figure; grating of 1000 lmm⁻¹ (logarithmic scale).**
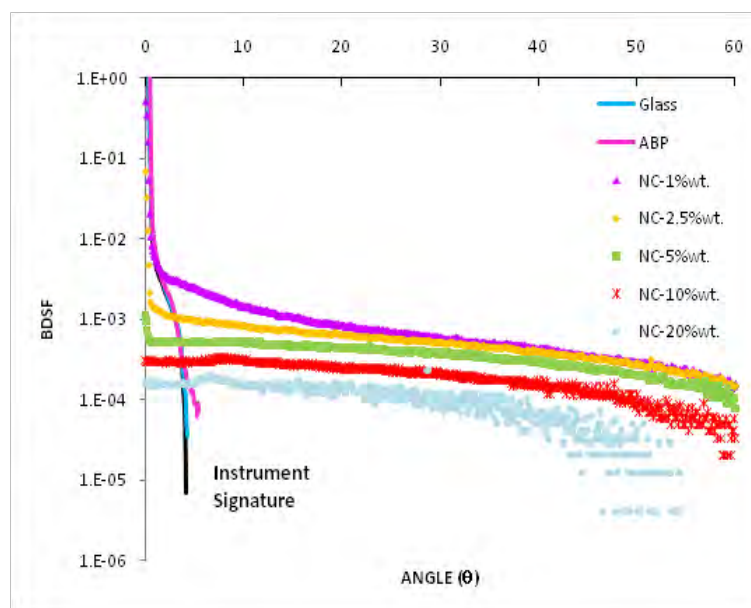
Figure 4.13. **Bidirectional scattering distribution function of glass, acrylamide based photopolymer (ABP) and TiO$_2$ nanocomposites in several concentrations indicated in the figure; grating of 1000 lmm^{-1} (logarithmic scale).**

As can be seen by comparing Figures 4.11 and 4.12, the Beta nanoparticles produce very low scattering (comparable to the undoped layer) as indicated by the lower angular spread, while the alumina nanoparticles aren't compatible with the water soluble photopolymer, resulting in the formation of large aggregates in the material, even visible by a naked eye inspection.

By comparing the data from Figures 4.11 and 4.13, one can see that the addition of titania nanoparticles produces an opaque material (Fig. 4.14B), where the light is not transmitted through the layer, which is not the case for zeolite Beta nanocomposite (Fig.414A).

A)

B)
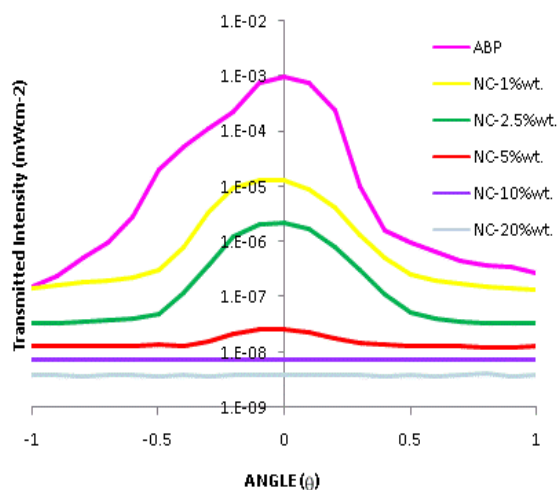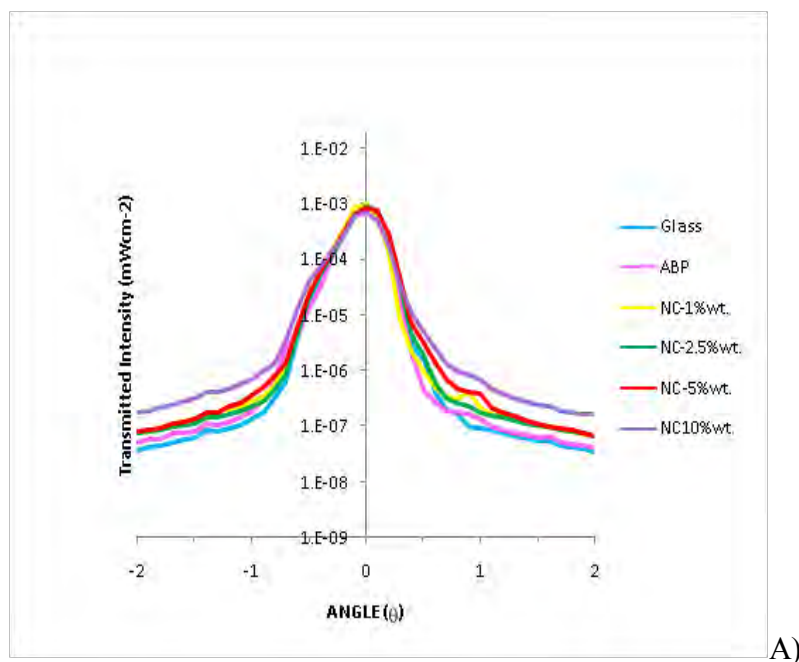
Figure 4.14.   Transmitted light intensity for nanocomposites using (A) zeolite Beta nanoparticles, and (B) titania nanoparticles.

On can see that in the case of titania nanocomposites, most light is scattered. In the case of Beta zeolite, this effect increases as the zeolite concentration increases.

Although the solid nanoparticles, titania (n=2.5) and alumina (n=1.8) have substantially higher refractive index than the acrylamide based photopolymer (n=1.5) they did not

produce optically transparent layers. We chose to focus our work in photopolymerizable materials with zeolites (n~1.3) since we were able to obtain optically transparent layers with low light scattering, as it can be shown by the fact that BDSF functions are spread over similar amplitude of angles as the undoped photopolymer.

After studying the nanoparticle distribution in the photopolymer by light scattering measurements, the surface scattering of the nanocomposites was evaluated. Thus conclusions about the homogeneous distribution of nanoparticles across the photopolymer volume can be made. The surface morphology of several nanocomposites containing from 0 to 10%wt. of Beta zeolite nanocrystals was studied using a white light interferometric (WLI) surface profiler (See Fig. 4.15). For this study. the samples were uniformly polymerized under UV radiation.
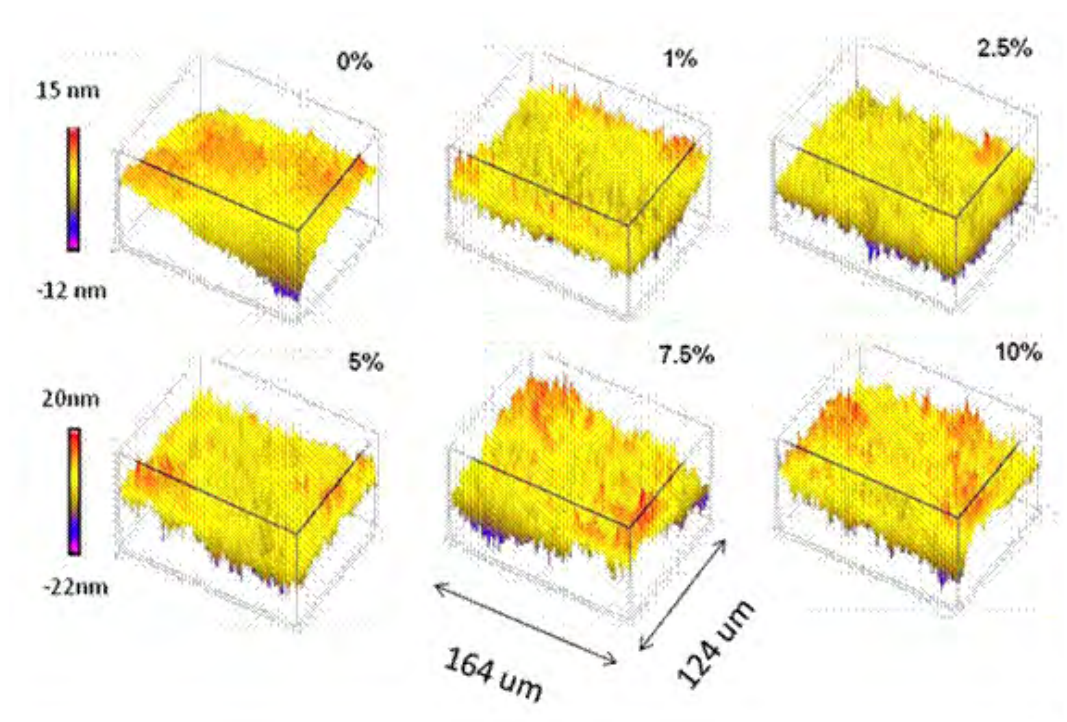
Figure 4.15. **Surface** **profiles** **of** **Beta** **nanocomposites** **using** **white** **light** **interferometric surface profiler; the zeolite concentrations are indicated on the figure.**

When zeolite Beta nanoparticles are added to the acrylamide based photopolymer the surface morphology changes. In the undoped photopolymer the surface is flat and when we add zeolite Beta the surface presents a spatially uniform distribution of sharp peaks a few nanometers in height. From these measurements one can see that the Beta nanoparticles present a good compatibility with the polymeric matrix since the addition of Beta nanoparticles to the acrylamide based photopolymer leads to a not very pronounced roughening of the initially flat undoped surface, which will be next quantified.

The profile height of the layers was measured (Fig. 4.16) in five different locations across the material and from these values, the surface roughness was calculated. This method was used to measure the compatibility of the nanoparticles with the photopolymer; for instance expelling of the nanoparticles to the surface of the photopolymer leads to increase of the surface roughness.
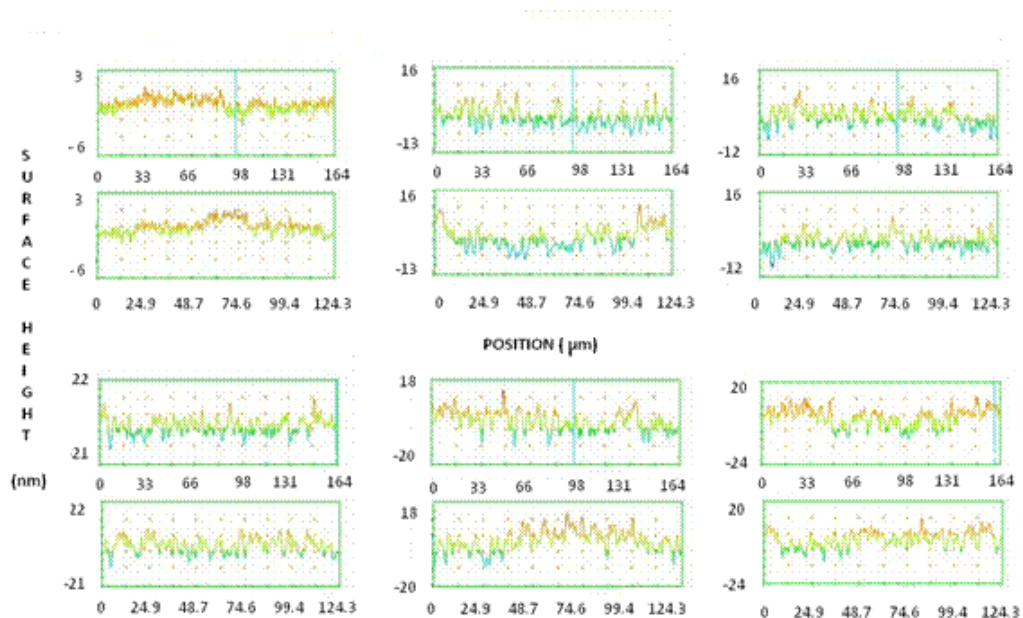
Figure 4.16. Height profile of Beta nanocomposites obtained using White Light Interferometric Surface profiler. The doping level is 0, 1, 2.5, 5, 7.5 and 10%wt. of zeolite Beta (from top left to bottom right).

In Fig. 4.16, one can evaluate the surface height of the materials tested in both x and y directions. As we introduce higher concentrations of zeolite Beta the surface height becomes more pronounced.

The standard deviation of these profile heights is represented by *Rq* or *RMS* (Root-Mean-Square). This is an average of the measured height deviations taken within the evaluation length or area and measured from the mean linear surface and can be used to estimate the surface roughness of the nanocomposite. The results are summarized in Table 4.3 and Fig. 4.17.

Table 4.3.   Surface roughness measurements (RMS) for Beta nanocomposites.

Concentration of Beta (%wt.)	Surface Roughness (nm)	
0	1.1	± 0.3
1	3.0	± 0.1
2.5	3.1	± 0.3
5	5.6	± 0.5
7.5	5.5	± 0.7
10	4.4	± 0.5
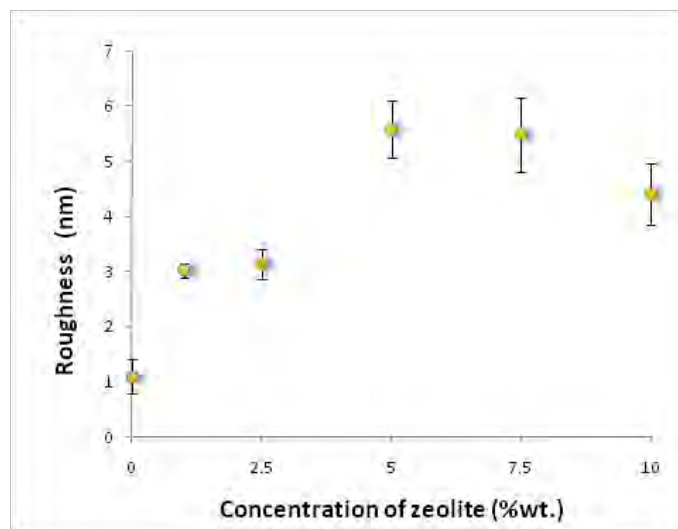
Figure 4.17.   Surface roughness of Beta nanocomposites.

The surface roughness increases initially (1nm for undoped photopolymer) as we incorporate zeolite Beta nanoparticles, reaching a maximum value for 5%wt. zeolite nanoparticles (5.6nm) where it remains constant. Interestingly, there is a slight decrease for the Beta 10%wt. nanocomposite (4.4nm), which is consistent with data in Fig. 4.11B.

As part of optical characterization of the Beta nanocomposites, their refractive indexes were calculated (see table 4.4).

Table 4.4.   Volume refractive index of zeolite Beta nanocomposites at 633 nm.

Zeolite concentration (% wt.)	Refractive Index
0	1.499± **0.005**
2.5	1.493± **0.005**
5	1.483± **0.005**
10	1.471± **0.005**

The method of determining the refractive index was detailed elsewhere [5] and were kindly provided by Dr. T. Babeva. Briefly, the volume refractive indices of the photopolymer nanocomposites) were determined by measuring transmittance, T, and reflectances R_f and R_b from front (air) side and back (substrate) side of the layers, respectively using a UV-VIS-NIR spectrophotometer. The simultaneous determination of refractive index, n, extinction coefficient, k and thickness, d of the layers was performed by minimization of the goal function F consisting of discrepancies between measured ("meas") and calculated ("calc") spectra:

$$F = \left(T_{calc} - T_{meas}\right)^2 + \left(R_{fcalc} - R_{fmeas}\right)^2 + \left(R_{bcalc} - R_{bmeas}\right)^2 \qquad \text{(Eq. 4.2)}$$

F was minimized at each wavelength λ in the spectral range from 400-800nm by a Nelder-Mead simplex method [6] using a dense grid of initial values of n, k and d. Additionally, n and k were determined from combinations (TR_f) and (TR_b) using Newton-Raphson iterative algorithm [7] and thickness values measured with WLI profiler (the measurement is made by making a cut in the sample and calculating the height difference between the glass substrate and the surface of the sample). The refractive index of the photopolymer decreases with the incorporation of Beta nanoparticles (see Table 4.4), which is expected since the refractive index of this zeolite nanoparticles filled with H_2O nanoparticles at 633nm is 1.414 ± 0.005, as calculated from the dispersion curve based on Bruggeman effective media approximation (EMA), the Wemple-Di Domenico dispersion equation and the nonlinear minimization of the appropriate goal function (Eq. 4.2); more details in this method can be found in [5].

107

Since the decrease in refractive index of the beta nanocomposites with the incorporation of this zeolite into the photopolymer is not significant, one hypothesis is that the micropores of zeolite Beta are filled with guest molecules from the photopolymer matrix. This hypothesis was further tested by comparing the pore volumes of zeolite Beta before and after incorporation into the photopolymer.

The pore volume of zeolite Beta before incorporation in the photopolymer was determined experimentally by N_2-sorption data (see fig. 4.4) to be 0.25 cm^3g^{-1}. The refractive index and density of a mixture Al_2O_3: (SiO_2) was calculated by Bruggeman EMA using the refractive index and density of these oxides. Considering both the free volume and the density of a mixture of Al_2O_3 / SiO_2 to be 2.27 gcm^{-3}, the density of BEA zeolites with empty pores was of 1.45 gcm^{-3}. Using the density of zeolite Beta calculated by the method described in reference 6, the density of zeolite Beta when incorporated in the photopolymer is 2.24 gcm^{-3} and thus the pore volume of zeolite Beta after incorporation in the photopolymer was estimated to be 0.006 cm^3g^{-1}. Comparing this value with the 0.25 cm^3g^{-1} one can conclude that zeolite Beta pores do not remain empty after the particles are incorporated in the photopolymer.

In conclusion, the previous results demonstrate that the zeolite nanoparticles are compatible with the photopolymer, thus homogeneous coating suspensions can be obtained and homogeneous dry layers prepared (Figure 4.18), and an optically transparent material is obtained (Fig. 4.19).
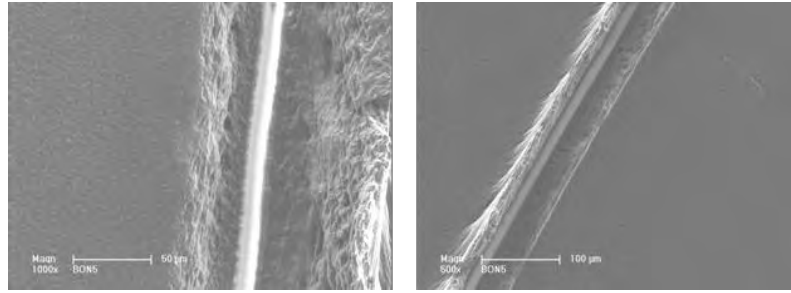
Figure 4.18. Surface analysis of the acrylamide based photopolymer doped with Beta nanoparticles (5%wt.) (50 μm thickness), the white portion is the cut made across the thickness of the layers.

Observing the morphology of the nanocomposite by SEM (Fig.4.18), it can be seen that the nanoparticles are randomly and homogeneously distributed within and at the surface of the film. These results are also shown by surface roughness measurements.

Figure 4.19. Typical layer of Beta nanocomposite film.

4.4   GRATING PERFORMANCES OF BETA NANOCOMPOSITES

4.4.1   AT DIFFERENT RECORDING INTENSITIES

The laser used was a solid state laser at 532 nm. The layer thickness was not measured. The recording intensities used were 5, 10 and 20 mWcm^{-2} and the exposure time was 100 s, when the laser was turned off and further 40s of intensity data were collected. Several samples for each experimental condition were used (in Fig. 4.20 for example, seven different samples were measured) in order to be statistical meaningful and the results are shown in Fig. 4.21.
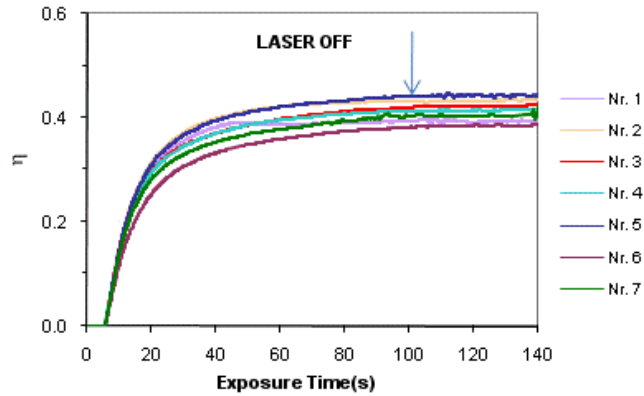
Figure 4.20. **Typical example of diffraction efficiency growth curves for several gratings of nanocomposite containing 5%wt. of zeolite Beta; recording intensity of 20 mWcm^{-2}; arrow indicates time at which the laser was turned off.**
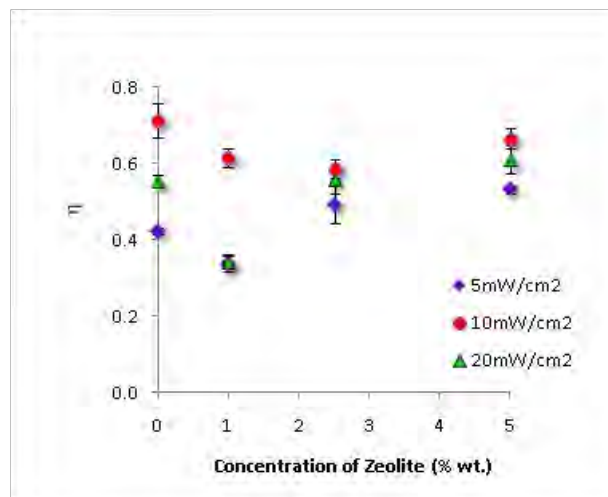
Figure 4.21. Diffraction efficiency for different Beta nanocomposites for different recording intensities; spatial frequency of 1000 lmm^{-1}.

It was observed that the nanoparticles improve the diffraction efficiency (η) at 5 and 20 mWcm^{-2}. For addition of 5%wt. of zeolite Beta, the increase of η, when compared to undoped photopolymer was 26% for a recording intensity of 5 mWcm^{-2}. For the case of recording intensity of 20 mWcm^{-2}, this increase of η was 10%. At a recording intensity of 10 mWcm^{-2} no improvement was observed. A recording intensity of 5mWcm^{-2} was chosen to conduct most of the experiments in this project.

110

At Different Spatial Frequencies

The angular selectivity curves were obtained for four spatial frequencies (500, 1000, 1500 and 2000 lmm^{-1}). The results are shown in Fig. 4.23 for different Beta concentrations and in Fig. 4.22, a typical example of a set of angular selectivity curves is shown.
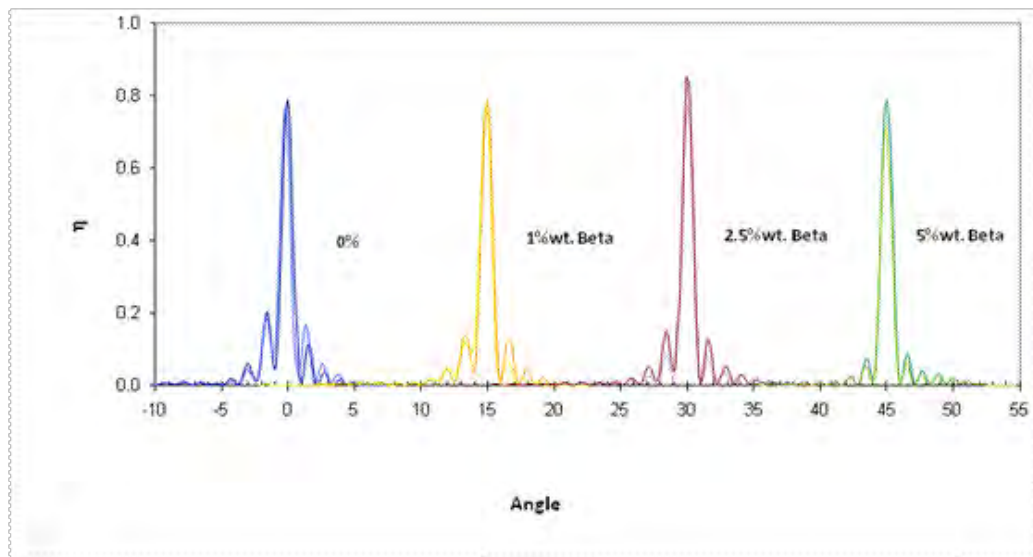
Figure 4.22. Typical angular selectivity curves for different zeolite Beta concentrations indicated in the figure; spatial frequency of 1000 lmm^{-1} and recording intensity of 5 mWcm^{-2}.
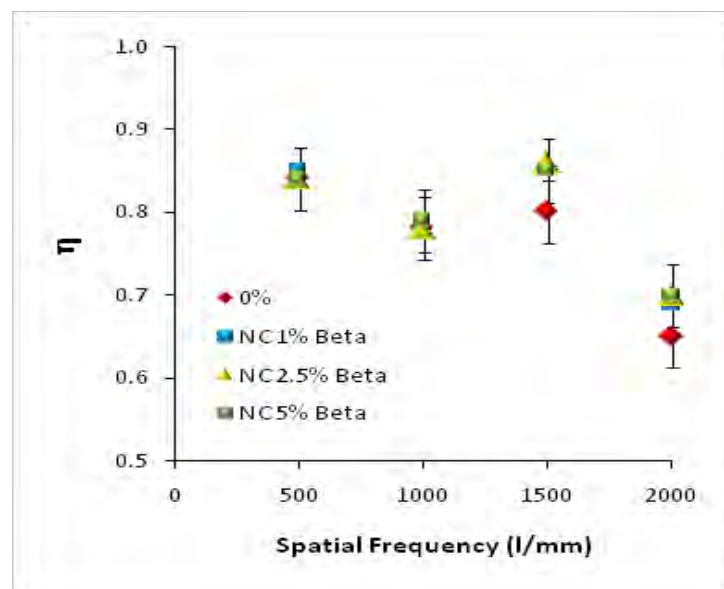
Figure 4.23. Diffraction efficiency dependence on spatial frequency for different zeolite Beta concentrations; recording intensity of 5 mWcm^{-2}.

The reason for not calculating the refractive index modulation for this set of data is that the curves are overmodulated (see example in Fig. 4.24).
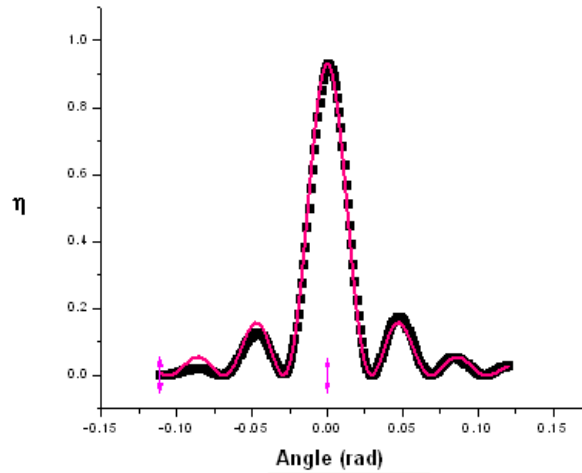
Figure 4.24. Typical overmodulated angular selectivity curve, where points are experimental data and line is the fitting by Kogelnik theory (grating of undoped material recorded with a spatial frequency of 500 lmm^{-1}).

Followed this first experiment (Fig. 4.23) a decision for working with thinner films was made. New layers were prepared and gratings were recorded at four spatial frequencies (200, 500, 1500 and 2000 lmm^{-1}) recorded at a constant intensity of 5 mWcm^{-2} for 100s (Fig. 4.256 and Table 4.5) and two different concentrations (1% and 5%wt. of zeolite Beta) were studied.
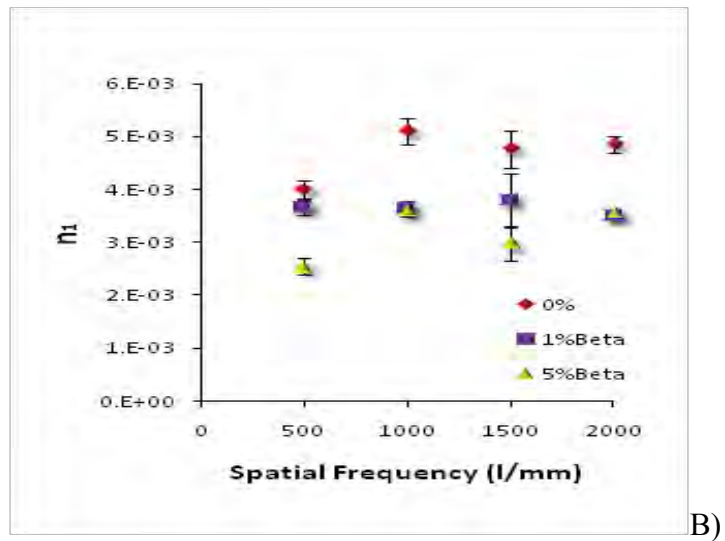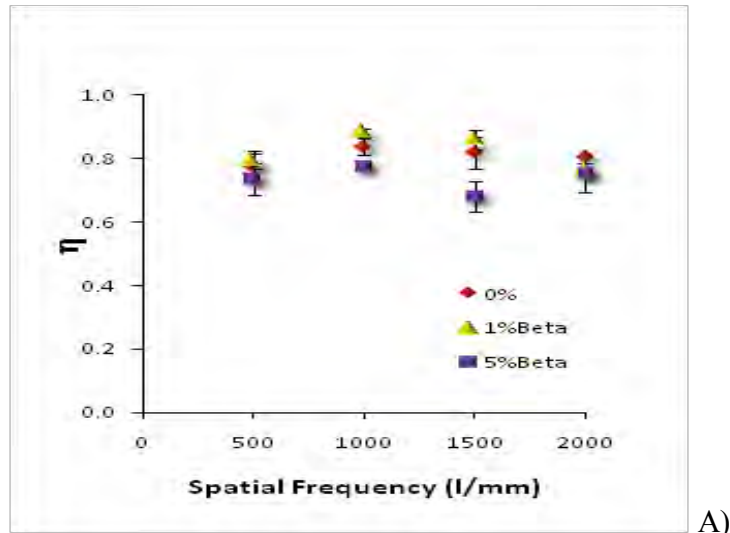
Figure 4.25. **Grating performance dependences on spatial frequency for different Beta concentrations: (A) diffraction efficiency; (B) refractive index modulation; recording intensity of 5 mWcm^{-2}.**

Table 4.5. Thickness of gratings recorded in zeolite Beta films presented in Fig. 4.25 (obtained from the fitting of the angular selectivity curves).

Spatial Frequency (lmm^{-1})	Thickness (µm)					
	Undoped		1%wt. Beta		5%wt. Beta	
500	54	±3	61	±4	95	±2
1000	46	±3	54	±1	73	±6
1500	48	±1	62	±2	88	±2
2000	47	±3	54	±0.2	61	±4

When compared with the undoped photopolymer, the Beta doped photopolymer shows a lower refractive index modulation for all the spatial frequencies tested. The highest refractive index modulation (n_1) observed was of $5×10^{-3}$ for the spatial frequency of 1000 lmm^{-1}. This value is the optimum in the case of undoped photopolymer. In the case of zeolite Beta doped photopolymer it is no conclusive wether there is any dependence of the grating performances on the space fringing. For 500 lmm^{-1} higher orders were observed and diffraction efficiency was calculated using solely the intensity of the first order.

4.4.2 AT DIFFERENT ZEOLITE CONCENTRATIONS

The grating performances were studied as a function of zeolite Beta concentration and the results are presented in Fig. 4.26 and Table 4.6.

A)
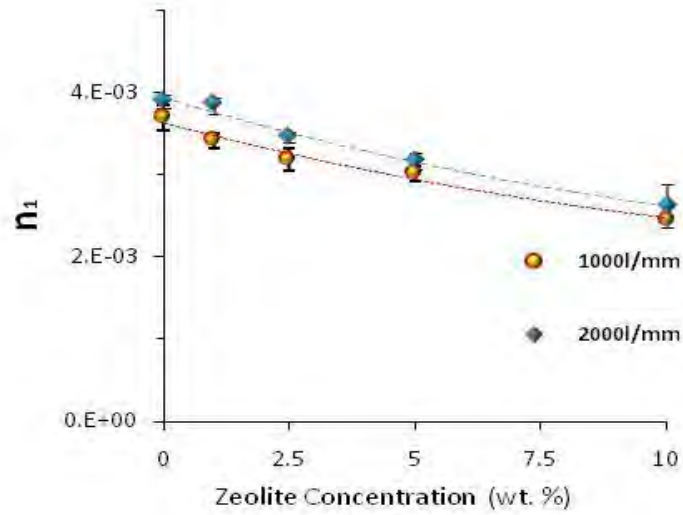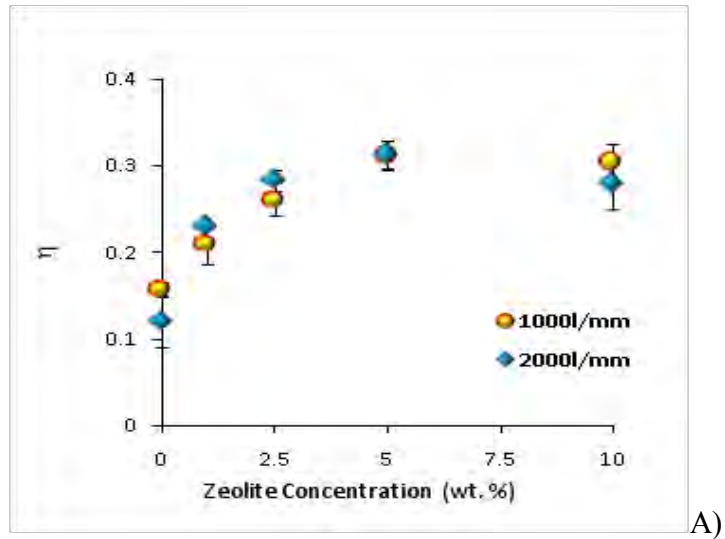
B)

Figure 4.26. Grating performance dependences on concentration of zeolite for 1000 lmm^{-1} and 2000 lmm^{-1}: (A) diffraction efficiency; (B) refractive index modulation; recording intensity of 5 mWcm^{-2} using 20% PVA solution.

Table 4.6. Thickness of gratings recorded in zeolite Beta films shown in Fig. 4.26 (obtained from the fitting of the angular selectivity curves).

Zeolite Beta (%wt.)	Thickness (µm)			
	1000lmm^{-1}		2000lmm^{-1}	
0	22	±2	18	±2
1	28	±2	26	±1
2.5	34	±3	33	±0.3
5	40	±0.4	38	±1
10	48	±2	43	±3

In Figure 4.26, the refractive index modulation of acrylamide based photopolymer is compared with that for the Beta nanocomposite (for spatial frequencies of 1000lmm^{-1} and 2000lmm^{-1}). The incorporation of 10%wt.nanoparticles in the photopolymer results in a decrease in the refractive index modulation of around 25% compared to the undoped acrylamide based photopolymer. This could be due to the fact that the pores of beta zeolite are filled as seen before. It can also be observed that, as the percentage of doping increases, the refractive index modulation decreases. Although the diffraction efficiency of the layers significantly increased from 15% for undoped to 30% for those doped with 10%wt. Beta zeolite, when the thickness of the gratings was taken into account in the calculation of the refractive index modulation, no increase of the latter with the increase of nanoparticle concentration was observed.

4.5   REDISTRIBUTION OF BETA NANOPARTICLES

Scanning Electron Microscopy coupled with Energy Dispersive X-Ray Fluorescence (SEM-EDX) was used to study the redistribution of nanoparticles in the layers as a result of the holographic recording process. SEM pictures of the photopolymer films with the distribution of silicon and oxygen belonging to the zeolite Beta nanoparticles are shown in Figure 4.27. The SEM-EDX analysis shows that the distribution of the nanoparticles changes from a random pattern on the outside of the grating (Fig. 4.27A) to a regular pattern of lines with high and low intensities inside, corresponding to silicon and oxygen clearly originating from the nanoparticles (Fig 4.27B). The spacing is about 2μm, which is in good agreement with the spatial frequency of the holographic grating (500lmm^{-1}). This indicates that there is a redistribution of the Beta nanoparticles in the surface of the photopolymer of the same spatial frequency as that used during holographic recording.
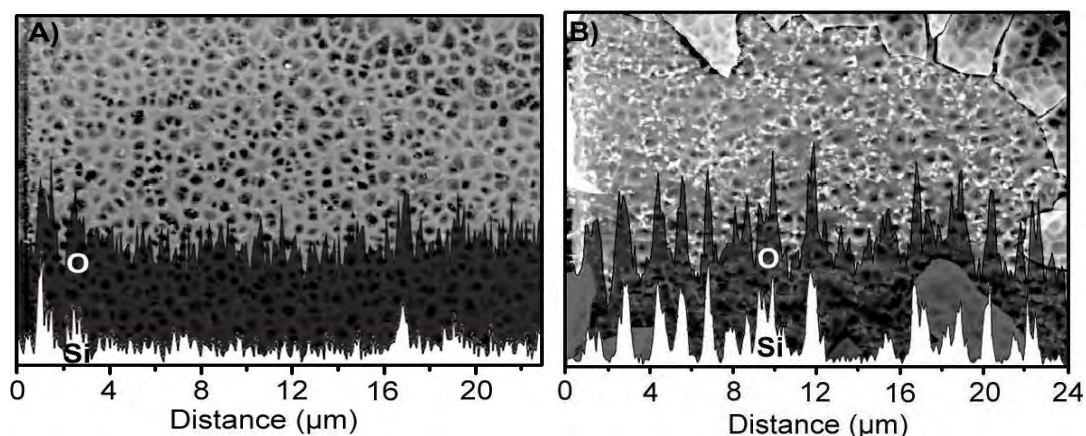
Figure 4.27.   SEM-EDX images of acrylamide based photopolymer film doped with 5%wt. of zeolite Beta; (A) outside the grating and (B) inside the grating (500 lmm^{-1}, 2μm space fringing).

These results were confirmed using Raman spectroscopy. Raman spectra of the acrylamide based photopolymer doped with Beta nanoparticles (Fig. 4.28A) show two well isolated peaks, one at 415 cm^{-1} and other at 673 cm^{-1} originating from C-C-N vibrations of the organic template used for the synthesis of zeolite Beta nanoparticles (Fig. 4.28C), which are absent in the undoped polymer (Fig. 4.28B).
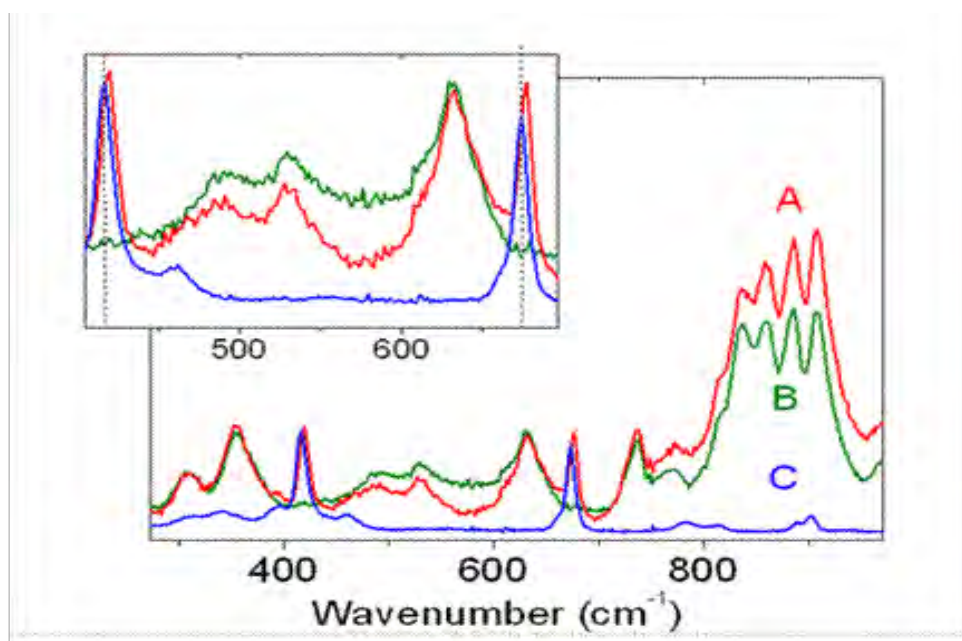
Figure 4.28. Raman spectra of (A) photopolymer doped with 10%wt. Beta nanoparticles; (B) undoped photopolymer and (C) zeolite Beta; (200 lmm^{-1}, 5 µm space fringing); Inset depicts the C-C-N vibrations from the organic template in the zeolite Beta nanoparticles.

A grating was recorded in 5%wt. zeolite Beta nanocomposite. The space fringing of the grating was chosen to be 5 µm (spatial frequency of 200 lmm^{-1}). The reason to choose this space fringing was due to limitations of the spatial resolution of the confocal Raman spectrometer, which is 1 µm.

The variation of the Raman peak intensity at 673 cm^{-1} was monitored in the direction of the grating vector, since this peak was found to be more sensitive to the changes in zeolite concentration. As can be seen in Figure 4.29, the variation of the Raman peak at 673 cm^{-1} intensity in the grating vector direction is cyclic in conformity with the fringe spacing of 5µm in the grating, indicating that there is indeed a redistribution of nanoparticles when a grating is recorded. If one assumes that the intensity of the Raman peak at 673 cm^{-1} is proportional to the concentration of the Beta zeolite nanodopant, one can estimate that around 40% of the nanoparticles are redistributed; this was calculated from the differences between the minimum and maximum Raman intensities at 673 cm^{-1}. As expected, the periodical spatial modulation of the Raman signal was not observed for the nanocomposite outside the grating.
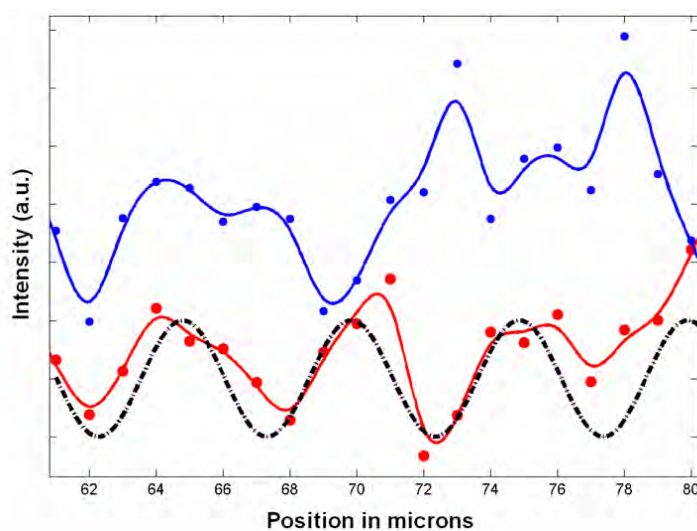
Figure 4.29. Raman spectra scan in grating vector direction (1 µm steps): (blue) outside the grating; (red) inside the grating; (dashed line) Sin function; (dots) experimental data; 200 lmm^{-1}, 5 µm space fringing.

The redistribution of Beta nanoparticles was observed for the first time in the case of acrylamide based photopolymer nanocomposites. Despite this, no improvement of the refractive index modulation with the increase of the concentration of nanoparticles was

observed. A possible reason for this observation is that the difference between the nanoparticles refractive index and the photopolymer matrix is not sufficient to produce an improvement in the refractive index modulation. From the analysis of the refractive index of the nanocomposites with different concentration of zeolite Beta nanoparticles one can estimate the refractive index of the layers doped with 5%wt. nanoparticles to be 1.483 ± 0.005 at 633 nm and the refractive index of the undoped photopolymer matrix at this wavelength is 1.499 ± 0.005 (Table 4.4), a difference of 0.016. If the redistribution of Beta nanoparticles is of around 40%, then one could assume that a maximum increase in refractive index difference of 0.0064 is possible.

4.6   *INTERACTIONS BETWEEN ZEOLITE BETA AND PHOTOPOLYMER COMPONENTS*

To determine how the presence of zeolite nanoparticles affects the grating performances of acrylamide based photopolymer, we have compared the recording characteristics of layers with different concentrations of polymer components. Layers were prepared using stock solutions with 5%, 10% and 20%wt. polyvinyl alcohol (PVA). The compositions of the different suspensions are presented in Table 4.7.

Table 4.7. **Compositions of layers (dry content wt. %) prepared with different concentrations of matrix components: (1) undoped photopolymer; (2) nanocomposite containing 1%wt. of zeolite; (3) nanocomposite containing 5%wt. of zeolite.**

Matrix component	Matrix with 20% PVA			Matrix with 10% PVA			Matrix with 5% PVA		
	1	2	3	1	2	3	1	2	3
PVA	54%	54%	51%	46%	46%	43%	57%	56%	52%
TEA	34%	33%	32%	37%	36%	34%	23%	22%	20.5%
AA	9%	9%	9%	13%	12%	11.5%	15%	15%	14%
BA	3%	3%	3%	4%	4%	4%	5%	5%	4.5%
Zeolite	-	1%	5%	-	2%	7.5%	-	2%	9%

The refractive index modulations for all the above samples are shown in Figure 4.30.
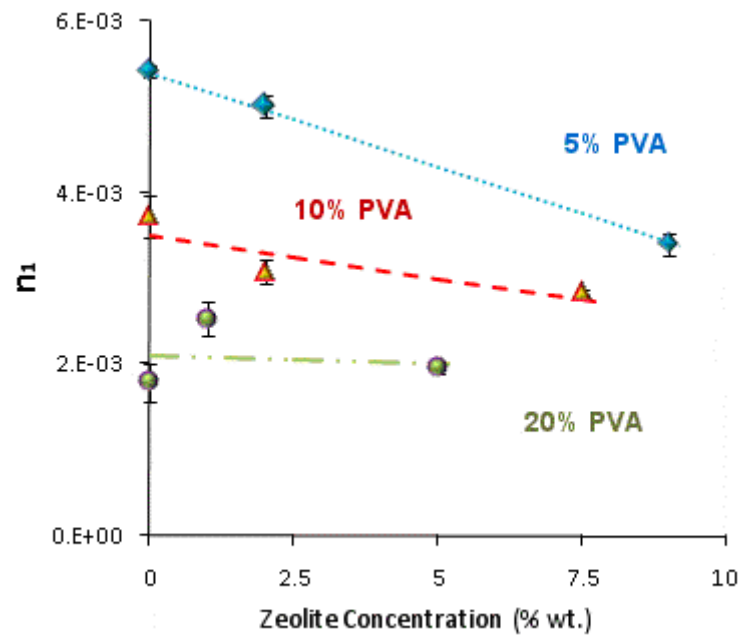
Figure 4.30. Refractive index modulation of Beta nanocomposites, layers were prepared with PVA stock solutions with a concentration of 5% PVA, 10% and 20%wt.; spatial frequency of 1000 lmm^{-1} and recording intensity of 5 mWcm^{-2}.

The layers show a decrease of the refractive index modulation with increasing the PVA concentration, which is expected since the monomer concentration in the dry layer is 20 ± 0.8%wt. in the case of 5% PVA stock solution, 16 ± 0.6%wt. for 10% PVA stock solution and 12 ± 0.3%wt. for 20% PVA stock solution. The standard deviations indicate similar monomer concentrations when using the concentration of the PVA stock solution. Since the observed difference in the decrease in the refractive index modulation for the doped and undoped layers cannot be accounted by differences in the monomer concentration, one can suspect that it could be caused by differences of about 10% in the TEA concentration. This hypothesis was further investigated.

Firstly, the interactions between zeolite nanoparticles and the photopolymer components were studied by means of Visible Spectroscopy. Typical absorption spectra are shown in Figure 4.31 for aqueous solutions of pure erythrosine B (sensing dye) and a mixture of erythrosine B and zeolite.
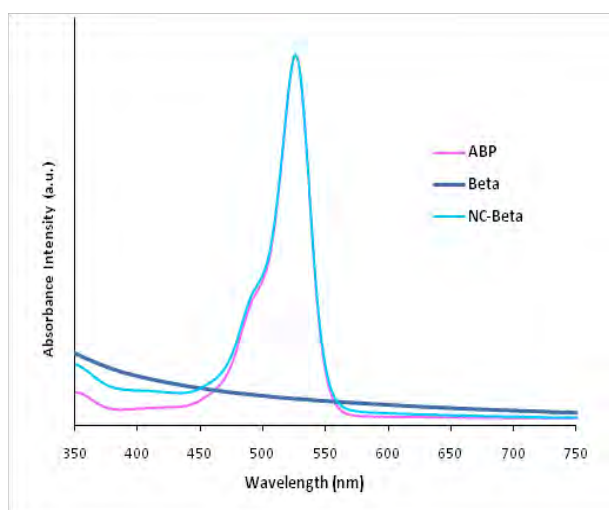
Figure 4.31. Visible absorption spectrum of (pink) aqueous solution of erythrosine B; (dark blue) aqueous solution of zeolite Beta; (blue) aqueous solution of erythrosine B and zeolite Beta.

No shift in the absorption spectrum of the dye was observed after the addition of the zeolite nanoparticles indicating the absence of interaction between the dye and the nanoparticles. Spectra were also taken from photopolymer solutions. The shapes of the spectra remained the same but a red shift of the absorption maximum of 9nm was obtained. This was expected since the absorption maxima of dyes are dependent on solvent polarity. In non-hydrogen-bond donating solvents, solvation of dye molecules probably occurs via dipole-dipole interactions, whereas in hydrogen-bond donating solvents the phenomenon is more hydrogen bonding in nature [8, 9]. Studies in xanthene dyes such as eosin and erythrosin showed that the absorption maximum in aqueous solutions shifts to longer wavelengths in ethanol, and the same type of solvent dependency of the absorption spectra was observed for hidroxyxanthenes, in which the shift in the absorption maximum is due to hydrogen bonding [10].

Different components of the photopolymer (one at a time) were then added to the solution of zeolite and erythrosine B and their visible absorption spectra taken. The shift in the maximum absorption was measured (Figure 4.32).
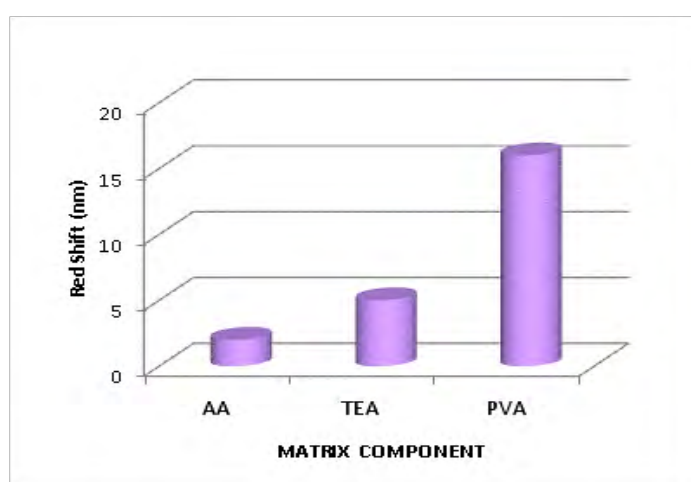
Figure 4.32. Change in the position of the absorption maximum intensity in aqueous solutions containing erythrosine B and zeolite Beta in comparison to aqueous solution in the presence of acrylamide (AA), TEA and PVA.

It was observed that the water dispersions of Beta showed a larger red shift in the absorption peak intensity of erythrosine B in presence of PVA (16 nm). A red shift of 5nm in the absorption peak for zeolite Beta was detected in the presence of TEA, which does not occur in the case of other types of zeolite studied (see chapter 5).

In the second part of this study, the interactions between zeolite Beta and photopolymer components, layers of acrylamide based photopolymer containing 5%wt. of Beta nanoparticles were studied by ^{13}C NMR and compared with undoped layers. The spectra were collected outside and inside the grating area (Figure 4.33).
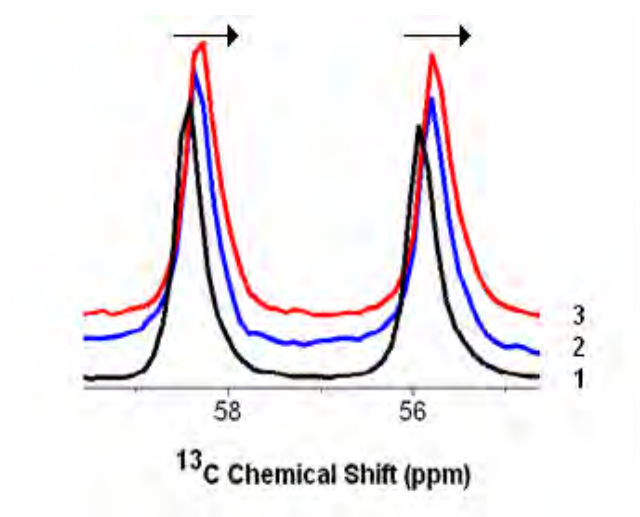
Figure 4.33. [13]**C NMR spectra of photopolymer doped with Beta; (1, black): undoped photopolymer; (2, blue): zeolite doped photopolymer (outside grating); (3, red): zeolite doped photopolymer (inside grating); spatial frequency 1000 lmm^{-1} and recording intensity of 5 mWcm^{-2}.**

In Beta containing nanocomposite the two peaks corresponding to TEA are shifted to lower field as highlighted by the arrows in Figure 4.34 indicating an interaction (possibly hydrogen bonding) between the TEA and the nanoparticles. As can be seen a more

pronounced shift in the C peak is obtained for Beta-nanocomposite inside the grating, thus confirming the strong interactions between the particles and the photopolymer. The addition of acrylamide to the water dispersion of zeolite nanoparticles and erythrosine B dye leads to a 2nm red shift in the erythrosine B absorption peak in solutions containing zeolite Beta (see Fig. 4.33), A study of the interaction of the monomer and Beta nanoparticles was carried out using Raman spectroscopy.

Initially only acrylamide was studied. It was dissolved in water and the solvent was allowed to evaporate. A series of 30 Raman spectra were then taken. It was found that the acrylamide molecules could be in associated (e.g. hydrogen bonding) or free states [11] (Figure 4.34A and 4.34B respectively). The associated state can be distinguished from the free-state by the appearance of a new peak at lower frequency, as denoted by the black arrow in the figure. The second study involved a mixture of acrylamide and Beta nanoparticles. The two components were mixed in water and then the solvent is allowed to evaporate. Analysis of these spectra showed that, in the presence of Beta nanoparticles, the acrylamide molecules were in an associated state (Figure 4.34). The presence of a shoulder (new peak) at lower frequencies indicates the presence of acrylamide molecules in an associated state (e.g. hydrogen bonding) [11]. Black arrows denote bands due to associated species.
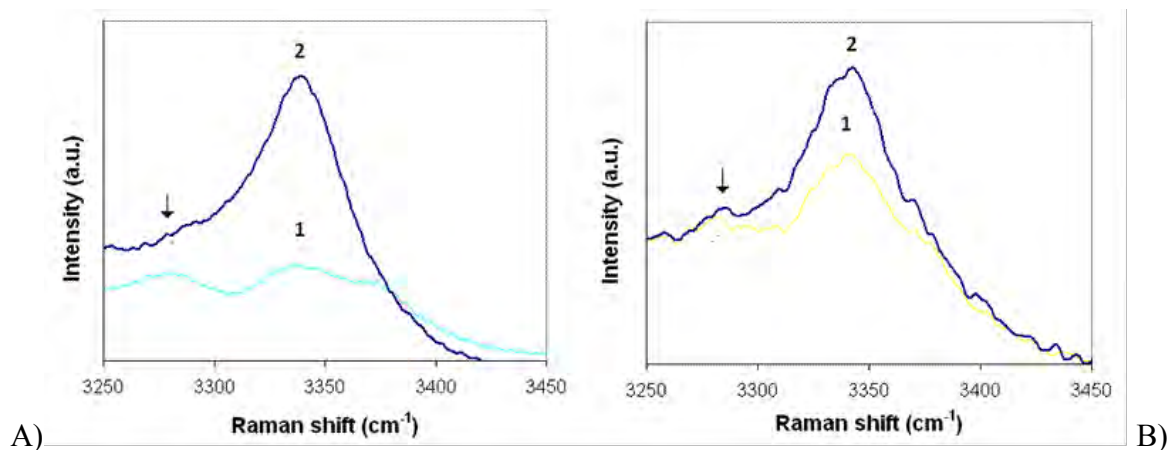
Figure 4.34. **Raman spectra in the region of N-H stretching; (A) associated acrylamide in absence (1) and in presence (2) of Beta nanoparticles; (B) free acrylamide in absence of Beta nanoparticles (1) and some associated acrylamide in presence of Beta nanoparticles (2)**

From these results, one can conclude that, due to an interaction between the monomer and the Beta nanozeolites, the mobility of acrylamide molecules can be significantly reduced if they trapped inside of zeolite pores resulting in decrease in the diffraction efficiencies.

4.7 SENSING OF TOLUENE

Despite the fact that no improvement of the refractive index modulation was observed in this particular nanocomposite, the spatial redistribution of nanodopants observed can be used in fabrication of holographic sensors. Holographic sensors are devices consisting of a hologram that changes its properties (diffraction efficiency or spectral response) when exposed to analyte containing environment. The main advantages of holographic sensors recorded in photopolymers are that they provide visual information, can be easily mass produced and are relatively cheap.

Holographic sensors reported in literature are usually based in reflection holograms [12, 13]. In this type of material the interference fringe structure runs parallel to the layer surface and a physical, chemical or biological mechanism that changes the spacing of the fringes (for instance due to the fact that the polymeric matrices are generally hydrogels that can swell and shrink in the presence of water) or the average refractive index (for instance due to a change of the refractive index of the medium through the absorption of moisture) will generate observable changes in its reconstruction wavelength (color).

In the case of unslanted transmission holograms, the fringe planes are perpendicular to the substrate surface and thus are insensitive to dimensional changes in the polymeric matrix (shrinkage or swelling). In this type of sensor differences in the layer thickness or refraction index of medium due to water/analyte absorption do not lead to fringe spacing change. The diffraction efficiency (η) is given by:

$$\eta = \sin^2\left(\frac{n_1 \pi d}{\lambda \cos \theta}\right) \qquad \text{(Eq. 4.3)},$$

where n_1 is the refractive index modulation, d is the thickness of the layer, λ is the wavelength of light and θ is the angle between the two recording beams.

Diffraction efficiency can be expected to change if a change in the refractive index modulation (Δn_1), thickness (Δd) or light wavelength ($\Delta \lambda$) occurs. The change in efficiency is derived from Eq. 4.3:

$$\Delta \eta = \sin\left(\frac{2 n_1 \pi d}{\lambda}\right) \frac{\pi}{\cos \theta \, \lambda} \left[d \Delta n_1 + n_1 \Delta d - \left(\frac{n_1 d}{\lambda}\right) \Delta \lambda \right] \qquad \text{(Eq. 4.4)}$$

The operating principle of a holographic sensor based on a transmission hologram recorded in a nanocomposite material can be seen in Fig. 4.35.
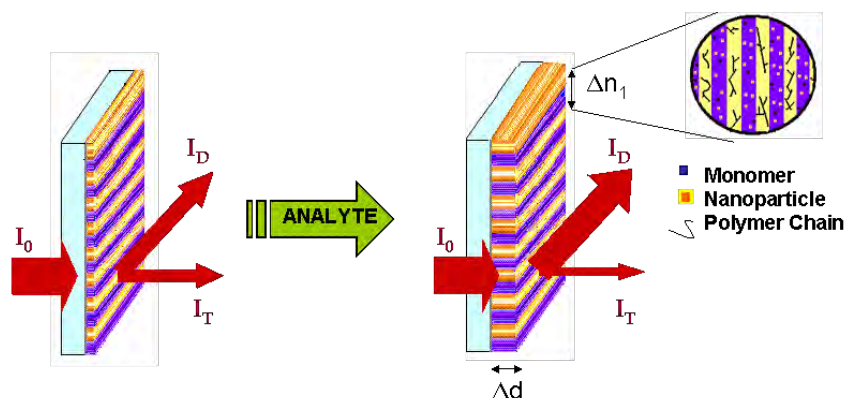
Figure 4.35. Operational principle of a holographic sensor recorded in a nanocomposite material.

Zeolite films have proved to be effective materials for water vapor sensing. The Beta films showed a higher absorption capacity towards water vapor than the zeolite A films [14]. Zeolite Beta is also a promising material for the adsorption of toluene and propene [15, 16]. Chemical vapors such as acetone (n=1.36), chloroform (n=1.45) and toluene (n=1.50) have been reported [17] to change the overall average refractive index of a reflection grating recorded in undoped acrylate polymer. Using toluene as a test probe our aim was to detect volatile organic compounds by the change of the diffraction efficiency of holographic sensors. In order to evaluate the sensing properties of the materials, volume gratings were recorded in undoped photopolymer and Beta nanocomposite. The gratings were then placed in a container into which toluene was added (where the concentration of toluene inside the volume of the container was estimated to be 19 ppm), and the container was sealed for 10 minutes. This experiment was carried out in a fume hood, and contact with ignition sources was prevented.

The angular selectivity of gratings of both undoped acrylamide and Beta photopolymerizable nanocomposite were obtained before and after exposure to toluene (Figure 4.36) and the results are summarized in Figure 4.37.
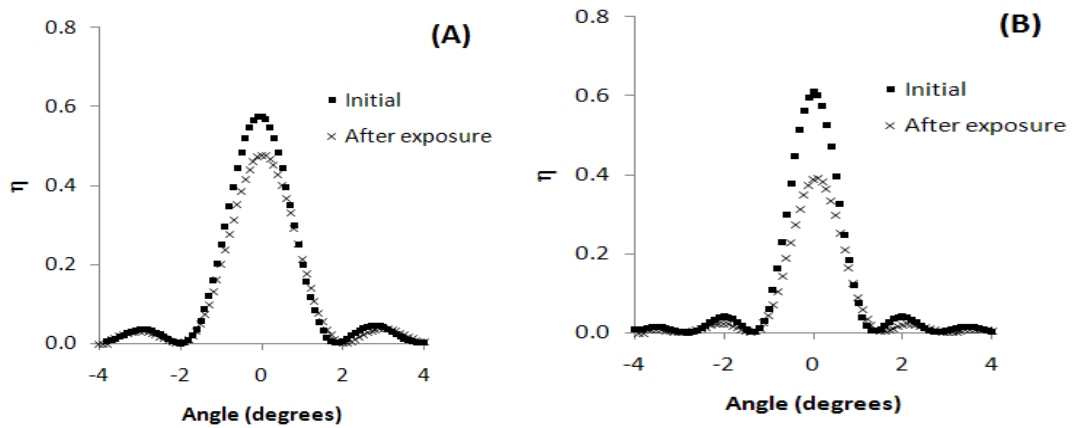
Figure 4.36. Angular selectivity curves measured before and after exposure to toluene (19ppm) for the highest change in the diffraction efficiency observed: (A) undoped photopolymer; (B) photopolymer containing Beta nanoparticles.
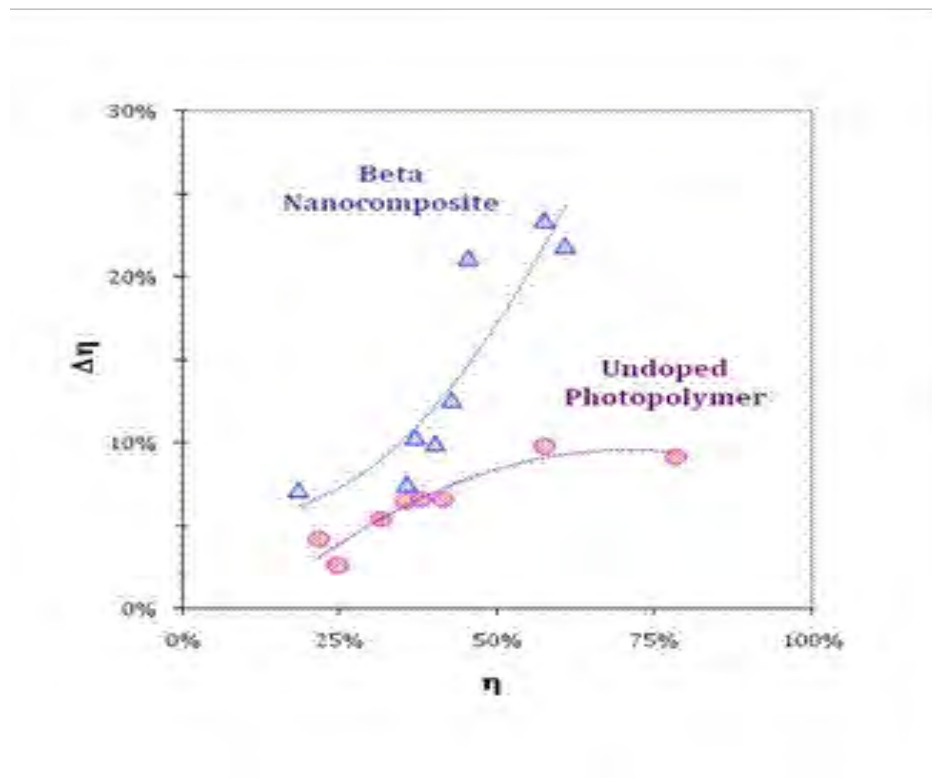
Figure 4.37. Change in diffraction efficiency of a grating exposed to toluene for: (diamonds) Beta photopolymerizable nanocomposite and (circles) undoped acrylamide based photopolymer.

As can be seen, the nanocomposite grating exhibits a greater change in diffraction efficiency than the undoped photopolymer grating. For gratings made in undoped photopolymer with initial diffraction efficiency ranging from 20 to 80% a change in the diffraction efficiency of less than 10% occurred after exposure to toluene (maximum observed was $\Delta\eta$=9.8 % for a grating with initial diffraction efficiency of 58%). As discussed previously, the change in the diffraction efficiency in undoped layers is possibly due to a toluene induced dimensional change of the layer since one would not expect a change in the refractive index modulation. The gratings recorded in the layers containing 5wt% Beta nanoparticles, exhibit a maximum diffraction efficiency change of 22% (double of the value observed for undoped layers) from   values initially ranging from 20 to 60%. An improvement in the sensitivity towards toluene for Beta photopolymer composite (Figure 4.37) is observed. It is also worth noting that the higher the initial diffraction efficiency of the doped layers is, the greater change caused by the exposure to toluene. This can be explained by the fact that in higher diffraction efficiency gratings the redistribution of nanoparticles is more effective, i.e., there is a greater difference between the concentrations of nanoparticles in the bright and dark regions.

It is also expected that the refractive index in the bright regions is higher than the refractive index in the dark regions rich in zeolite nanoparticles. Due to adsorption of toluene in the nanocomposite grating, the refractive index in the dark regions is increased. Thus the resulting refractive index modulation which is defined as the difference between the refractive index in the bright and in the dark regions decreases. This ultimately is observed as a decrease of the measured diffraction efficiency. The observed decrease is expected to be higher when the nanoparticle redistribution is more effective, which is confirmed by the experimental data shown in Figure 4.37.

4.8   CONCLUSIONS

Colloidal solution of zeolite Beta was characterized by DLS, XRD, nitrogen adsorption, SEM and Raman spectroscopy. Beta photopolymerizable nanocomposites were characterized in terms of their optical properties. The results by DLS, light scattering, surface morphology and surface roughness showed that a good optical quality material is produced in the case of the acrylamide-based photopolymer doped with Beta nanoparticles. The stability of films of acrylamide-based photopolymer doped with Beta nanoparticles was compared with that of undoped photopolymer. It was observed that zeolite Beta nanoparticles have no effect on the aging of the acrylamide based photopolymer. We have observed that during holographic recording a 40% redistribution of Beta nanoparticles occurs in the nanocomposite. This was shown both by SEM-EDX and Raman analysis. Although there is a spatial redistribution of Beta nanoparticles during the holographic recording, this effect is attenuated due to the fact that some monomer molecules interact with TEA molecules as shown by ^{13}C NMR and Raman spectroscopy. Also, the interaction between acrylamide with zeolite Beta is shown by Raman spectroscopy. These photopolymer - zeolite interaction ultimately result in no improvement of the refractive index modulation of this nanocomposite. This is confirmed by the refractive index measurements before and after incorporation of Beta nanoparticles in the photopolymer, which showed that the micropores of this zeolite are filled.

This nanocomposite is a good candidate for the fabrication of holographic sensors for chemical detection, as shown here for toluene. Photopolymer doped with Beta zeolite showed increased sensitivity toward toluene when compared to undoped photopolymer.

4.9 REFERENCES

[1] B. Modhera1, M. Chakraborty, P. Parikh and R. Jasra, *Synthesis of Nano-Crystalline Zeolite Beta: Effects of Crystallization Parameters*, Crystal Research and Technology 44, No. 4, 379 – 385 (2009)

[2] J. Rouquerol, D. Avnir, C. Fairbridge, D. Everett, J. Haynes, N. Pernicone, J. Ramsay, K. W. Sing and K. Unger, *Recommendations for the Characterization of Porous Solids (Technical Report)*, Pure and Applied Chemistry 66, No. 8, 1739-1758 (1994)

[3] G. Majano, S. Mintova, O. Ovsitser, B. Mihailova and T. Bein, *Zeolite Beta Nanosized Assemblies*, Microporous and Mesoporous Materials 80, No. 1-3, 227-235 (2005)

[4] B. Mihailova, S. Mintova, K. Karaghiosoff, T. Metzger and T. Bein, *Nondestructive Identification of Colloidal Molecular Sieves Stabilized in Water*, Journal of Physical Chemistry B 109, No. 36, 17060–17065 (2005)

[5] T. Babeva, R. Todorov, S. Mintova, T. Yovcheva, I. Naydenova and V. Toal, *Optical Properties of Silica MFI Doped Acrylamide-Based Photopolymer*, Journal of Optics A: Pure and Applied Optics 11, No.2, 024015 (2009)

[6] F. Abeles and M. Theye, *Méthode de Calcul des Constantes Optiques des Couches Minces Absorbantes à Partir de Mesures de Réflexion et de Transmission*, Surface Science 5, No. 3, 325-331 (1966)

[7] W. Press, S. Teukolsky S and W. Veterling, *Numerical Recipes in C*, Chap. 10, 408-41m0, Cambridge University Press (1992)

[8] C. Reichardt, *Solvents and Solvent Effects in Organic Chemistry*, Wiley-VCH (2003)

[9] M. Rauf, A. Soliman and M. Khattab, *Solvent Effect on the Spectral Properties of Neutral Red*, Chemistry Central Journal 2, 19 (2008)

[10] S. Islam, Y. Yoshikawa, M. Fujitsuka, A. Watanabe and O. Ito, *Studies on Photochemical Processes of Xanthene Dyes by Means of the Transient Absorption Spectra in the Visible/ Near-IR Regions*, Bulletin of the Chemical Society of Japan 71, 1543-1548 (1998)

[11] G. Socrates, *Infrared and Raman Characteristic Group Frequencies – Tables and Charts*, 3rd ed., Wiley (2001)

[12] A. Marshall, S. Kabilan, J. Blyth and C. Lowe, *Analyte-Responsive Holograms for (Bio)Chemical Analysis*, Journal of Physics: Condensed Matter 18, No. 18, S619-S62 (2006)

[13] A. Marshall1, D. Young, S. Kabilan, A. Hussain, J. Blyth and C. Lowe, *Holographic Sensors for the Determination of Ionic Strength*, Analytica Chimica Acta 527, No. 1, 13-20 (2004)

[14] S. Mintova and T. Bein, *Nanosized Zeolite Films for Vapor-Sensing Applications*, Microporous and Mesoporous Materials 50, No. 2-3, 159–166 (2001)

[15] Y. Zhang, Q. Su, Z. Wang, Y. Yang, Y. Xin, D. Han, X. Yang, H. Wang, X. Gao and Z. Zhang, *Synthesis and Toluene Adsorption/Desorption Property of Beta Zeolite Coated on Cordierite Honeycomb by an In Situ Crystallization Method*, Chemical Engineering & Technology 31, No.12, 1856–1862 (2008)

[16] N. Burke, D. Trimma and R. Howe, *The Effect of Silica: Alumina Ratio and Hydrothermal Ageing on the Adsorption Characteristics of BEA Zeolites for Cold Start Emission Contro*", Applied Catalysis. B: Environmental 46, No. 1, 97–104 (2003)

[17] V. Hsiao, W. Kirkey, F. Chen, A. Cartwright, P. Prasad and T. Bunning, *Organic Solvent Vapor Detection Using Holographic Photopolymer Reflection Gratings*, Advanced materials 17, No. 18, 2211–2214 (2005)

CHAPTER 5:   ZEOLITE A (LTA-TYPE STRUCTURE) DOPED NANOCOMPOSITES

5.1   INTRODUCTION

In this chapter we provide information regarding the characterization of zeolite A colloidal solution. In contrast to zeolite Beta, zeolite A is a small pore material with a more hydrophilic nature. The interactions between the photopolymer components and zeolite A nanoparticles were characterized by ^{13}C NMR and UV-Visible spectroscopy and compared with the Beta nanocomposite.

Unlike zeolite Beta nanocomposites, zeolite A nanocomposites showed a maximum improvement of the light induced refractive index modulation of the grating of 16% for a small addition of 1%wt. zeolite A in comparison to the undoped photopolymer. Host photopolymer/ zeolite interactions can explain these results because in the case of zeolite A nanocomposites, the nanoparticles showed no evidence of interaction with the polymer components.

5.2   ZEOLITE A NANOPARTICLES CHARACTERIZATION

Nano-sized zeolite A crystals (Fig. 5.1) in a colloidal suspension were used in the present study.
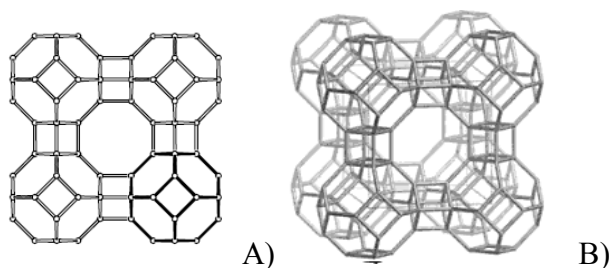
Figure 5.1.   Periodic building unit of the zeolite A family (LTA-type framework): (A) view along [001]; (B) the pore structure of zeolite A.

Two solutions of zeolite A were used in the present study. The light scattering results showed that the particle sizes were around 180nm and 90nm (Fig. 5.2).
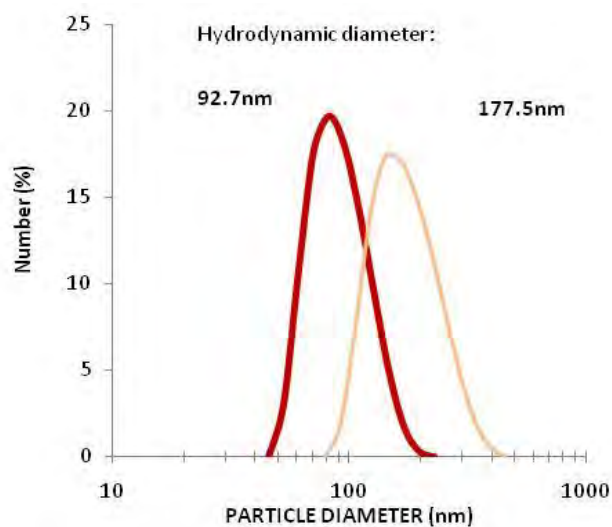
Figure 5.2.   DLS curves of zeolite A suspensions.

Both materials exhibit monomodal particle size distribution, but only the solution of 90nm particles is considered nanosized material. The results were shown in number of particle counts obtained per unit volume of sample (number weighted).

The zeolite morphology was characterized using SEM technique (Fig. 5.3).
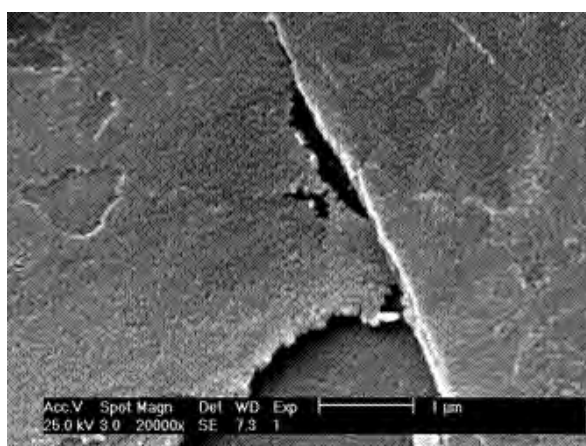
Figure 5.3.   Morphology of zeolite A nanoparticles.

Zeolite A nanoparticles show an almost cubic shape at high magnification, which is typical of larger crystals of zeolite A [1].

Zeolite A was analyzed using Raman spectroscopy which is applied for structure study as well. The Raman scattering in the range 730-770 and 930-980 cm^{-1} is generated from the symmetrical and antisymmetrical NC_4 stretching modes, respectively. The template (tetramethylammonium hydroxide, TMA) species trapped in the precursor amorphous solidified substance during the crystallization of zeolite A exhibits the same Raman spectra as that of TMA in water solution. The Raman signals generated by the N-C stretching are at 753 and 951 cm^{-1}. The appearance of additional, higher-energy shifted Raman scattering at about 770 and 960 cm^{-1} is a strong indication of the formation of crystalline sodalite-type zeolite structure. The Raman signal generated by the sodalite-cage trapped TMA ions appears at $767cm^{-1}$ for zeolite A and there is a blue shift of the band originating from the antisymmetrical C-N bond stretching modes at 958 cm^{-1} [2].

The Raman spectrum of zeolite A nanoparticles is shown in Fig. 5.4.
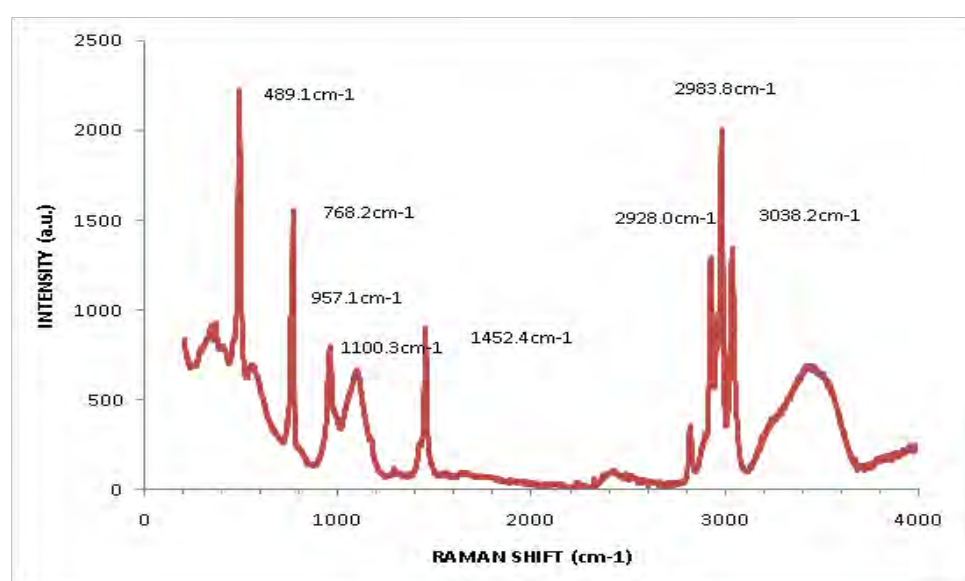
Figure 5.4. **Raman spectrum of zeolite A nanoparticles.**

The prominent band in the Raman spectrum of zeolite A in the fingerprint region (300-600 cm^{-1}) was found at 489 cm^{-1}. This band is assigned to the motion of an oxygen atom in a plane perpendicular to the T-O-T bonds. Other prominent bands observed were also assigned (see Table. 5.1). To observe zeolite redistribution during holographic recording it would be useful to investigate the 489 or 1100 cm^{-1} Raman peaks.

Table 5.1.   **Raman peak assignments of zeolite A.**

Raman Peak (cm^{-1})	Functional Group/ Vibration
489.1	T-O-T stretching of zeolite (6 rings)
768.2	Symmetrical NC$_4$ stretching (template)
957.1	Asymmetrical NC$_4$ stretching (template)
1100.3	Stretching of Si-O (zeolite)
1452.4	Deformation of CH (template)
2983.8	Symmetrical CH3 stretching (template)
3038.2	Asymmetrical CH3 stretching (template)

5.3   *ZEOLITE A NANOCOMPOSITES OPTICAL PROPERTIES*

Zeolite A doped nanocomposites are prepared by adding different quantities of zeolite solution to the photopolymer solution and adding water to have the same concentrations of the remaining components (monomers, TEA, PVA) in unit volume. An example using PVA 10% stock solution and Zeolite A 4.1%wt. stock colloidal suspension is given in Table 5.2.

Table 5.2.   Compositions used for preparation of photopolymerizable zeolite A nanocomposite (NC) layers from zeolite solution 4.1%wt. (10% PVA stock solution).

Photopolymerizable Material	Photopolymer Solution (ml)	Nanoparticle Solution (ml)	Water (ml)
Undoped Photopolymer	1	0	0.5
NC - A 1%wt.	1	0.05	0.45
NC -A 2.5%wt.	1	0.125	0.375
NC - A 5%wt.	1	0.25	0.25
NC - A 10%wt.	1	0.5	0

The compatibility of the zeolite particles suspensions with the photopolymer solutions was measured the DLS. No aggregation of the zeolite nanoparticles directly after mixing and after 24h aging was observed (Figure 5.5).
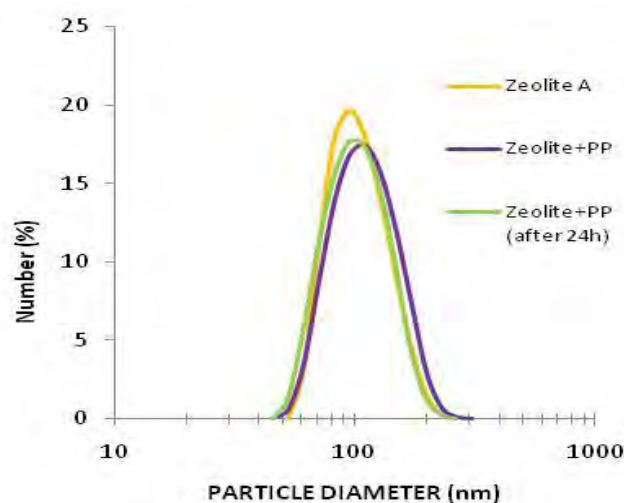
Figure 5.5.   DLS curves of (orange) zeolite A; (purple) photopolymer doped with zeolite A nanoparticles (freshly mixed); (green) photopolymer doped with zeolite A nanoparticles (24 hours stored at RT).

The optical losses of zeolite A nanocomposites (see Eq. 4.1) (layer thicknesses of around 20 μm) were characterized as a function of the concentration of zeolite A nanoparticles (see Figure 5.6).
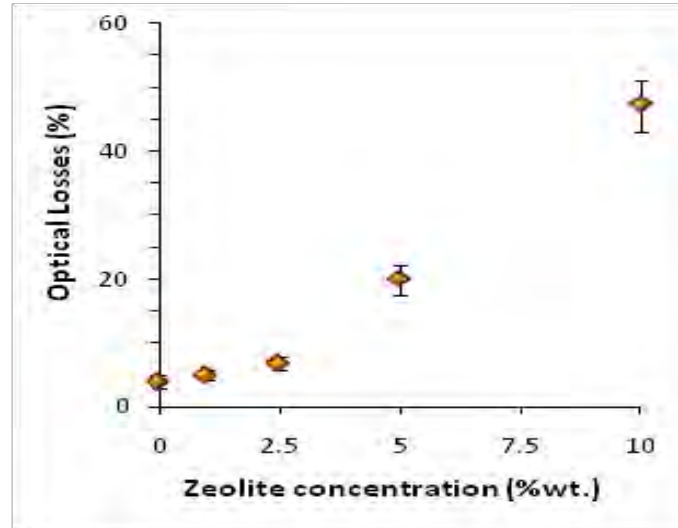
Figure 5.6. **Optical losses of nanocomposites at different concentrations of zeolite A with a mean size of 180 nm.**

As can be seen in Fig.5.6, the optical losses increase from 4% (undoped photopolymer) to 7% when we introduce 2.5%wt. zeolite A nanoparticles. This experiment was conducted with the solution of zeolite A with a mean size of 180 nm. The optical losses of the nanocomposite at 5%wt and 10 % of nanoparticles were 20% and 47%, respectively. One can expect lower optical losses by using zeolite A nanoparticles with a size of 90 nm, which was confirmed by studying its bidirectional scattering distribution function (see Fig. 5.7).
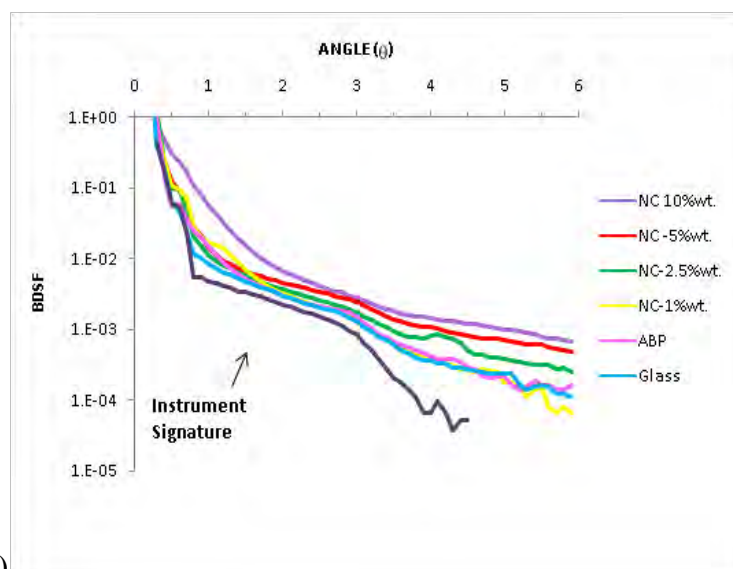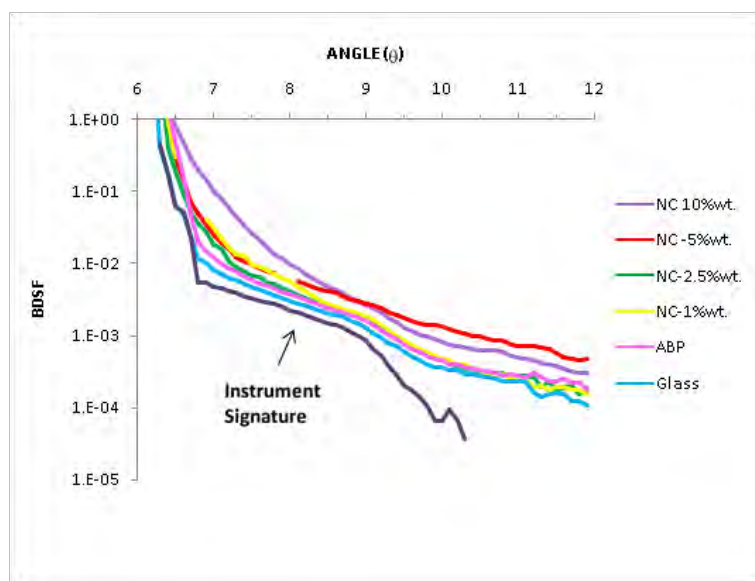
Figure 5.7. **Bidirectional scattering distribution functions of glass, undoped photopolymer and zeolite A nanocomposites (size of A crystals of 90 nm) in several concentrations; (A) unpolymerized material; (B) grating of 1000 lmm^{-1} (logarithmic scale).**

The increase in zeolite A concentration leads to a small increase in the scattering of light, except for the nanocomposite containing 10%wt. of zeolite A, where an increase of light scattering is observe. There was no difference in scattering between the unpolymerized and polymerized material (grating of 1000 lmm^{-1}).

The two solutions of zeolite A are expected to yield different scattering which was firstly investigated by visible spectroscopy, where we have compared the scattering of solutions of zeolite A of these two different sizes: 90 and 180 nm (Fig. 5.8).
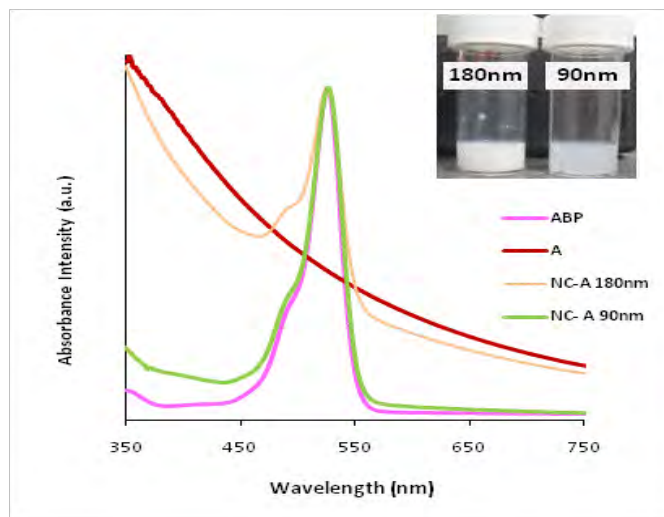
Figure 5.8.   Visible spectra of zeolite A nanocomposites; ABP is the acrylamide based photopolymer, A is zeolite A, and NC are the nanocomposite (180 nm, 1%wt. and 90 nm 4.1%wt.).

The scattering of solution containing 90 nm size zeolite A is much lower than that observed for zeolite A with size of 180 nm as seen by the lower absorbance intensity value of nanocomposite zeolite A (90 nm) at lower wavelengths (<450 nm).

Secondly, the roughness of the nanocomposites made with zeolite A 90 and 180 nm using a white light interferometric (WLI) surface profiler is compared. Figure 5.9 and Table 5.3 show these results.
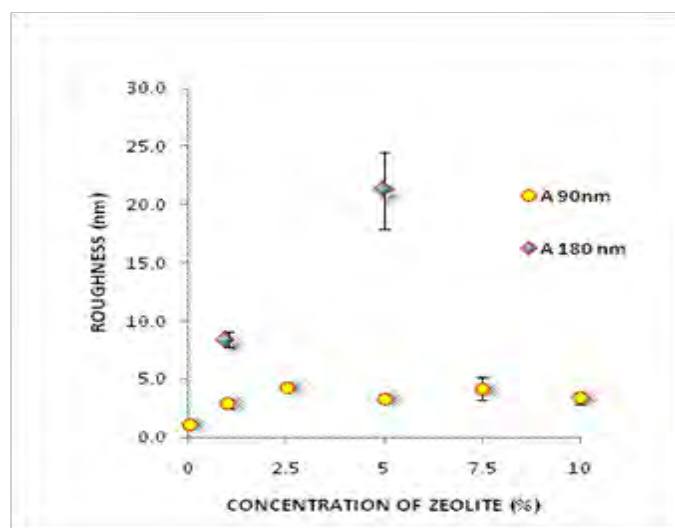
Figure 5.9. **Dependence of surface roughness from the concentration of zeolite A in the two nanocomposites (A nanoparticles of 90 nm and 180 nm).**

Table 5.3. **Surface roughness measurements (RMS) for zeolite A nanocomposites.**

Concentration of zeolite A (%wt.)		Surface roughness (nm)	
	0	1.1	± 0.3
	1	2.9	± 0.3
90 nm	2.5	4.3	± 0.1
	5	3.3	± 0.4
	7.5	4.2	± 1
	10	3.3	± 0.5
180 nm	1	8.4	± 0.7
	5	21.2	± 3.3

The addition of Zeolite A nanoparticles (90 nm) to the photopolymer leads to a not very pronounced roughening of the initially flat undoped surface (1 nm), which is not the case of the 180nm nanoparticles, where a significant roughening of the surface occurs (Fig. 5.9 and Table 5.3). In the case of 90 nm nanoparticles, the roughness increases initially with the addition of zeolite A, reaching a plateau for 2.5%wt. concentration of zeolite A, with a value of 3 nm. The roughness of the nanocomposites made with 180 nm is around six times higher (5%wt.) than the one obtained with the 90 nm zeolite.

It can be concluded that the size of zeolite nanoparticles can influence the optical properties of the nanocomposites. The smaller the size of nanoparticles, the less scattering is expected to occur.

5.4 GRATING PERFORMANCES OF ZEOLITE A NANOCOMPOSITES

5.4.1 AT DIFFERENT SPATIAL FREQUENCIES

Gratings were recorded at four spatial frequencies (200, 500, 1500 and 2000 lmm^{-1}) at a constant intensity of 5mWcm^{-2} for 100s (Fig. 5.10 and Table 5.4) for two different concentrations (1% and 5%wt.) for zeolite A of 180 nm in size.

A)

B)
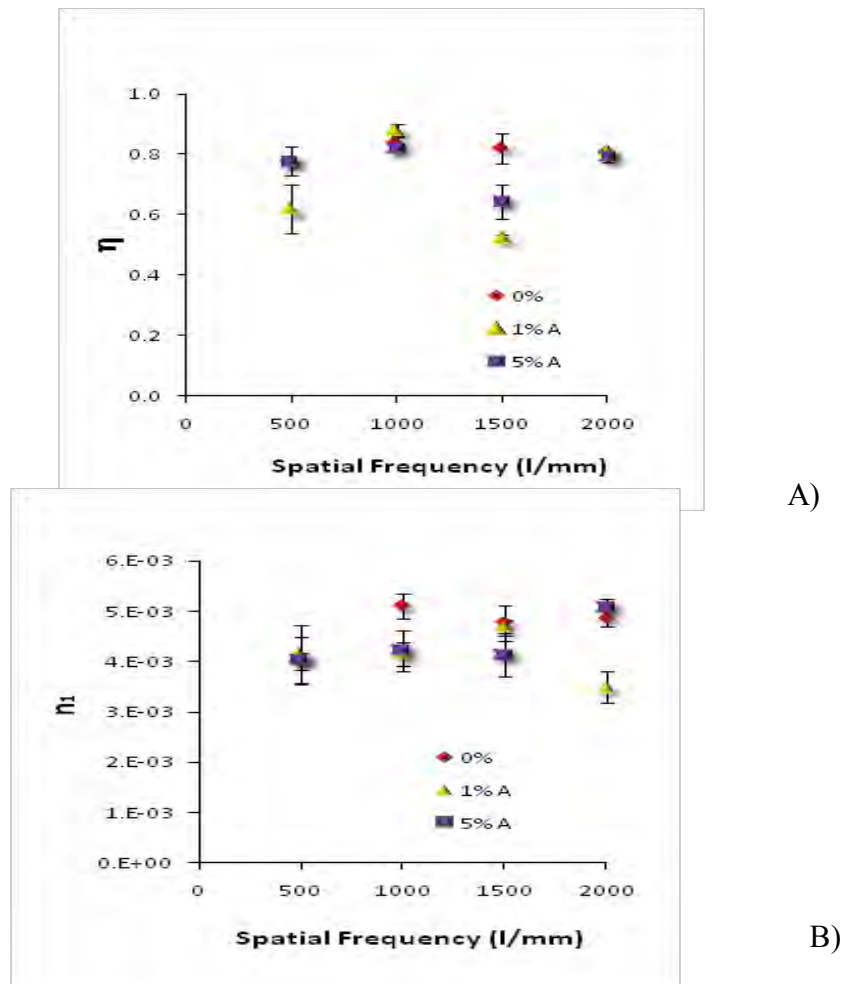
Figure 5.10. Grating performances dependence on spatial frequency for different concentrations of zeolite A (180 nm): (A) diffraction efficiency; (B) refractive index modulation at recording intensity of 5 mWcm^{-2}.

Table 5.4.   Thickness of gratings recorded in zeolite A films presented in Fig. 5.10 (obtained by fitting of angular selectivity curves).

Spatial Frequency (lmm^{-1})	Thickness (µm)					
	Undoped		1% wt. A		5% wt. A	
500	54	±3	44	±5	51	±6
1000	46	±3	54	±2	54	±6
1500	48	±1	35	±2	48	±6
2000	47	±3	53	±2	43	±2

The highest refractive index modulation observed was of 5.1×10^{-3} for both undoped and 5%wt. doped zeolite A nanocomposite. This value is the optimum in the case of undoped photopolymer, observed for a spatial frequency of 1000 lmm^{-1}. For zeolite A 5%wt. nanocomposite, the refractive index modulation increases with the spatial frequency and reaches its maximum value for 2000 lmm^{-1}. For the 1%wt. zeolite A nanocomposite, the refractive index modulation increases with the spatial frequency up to the optimum value of 1500 lmm^{-1}.

5.4.2 DIFFERENT ZEOLITE CONCENTRATIONS

The grating performance dependences on zeolite A concentrations (90 nm) is shown in Fig. 5.11 and Table 5.5.
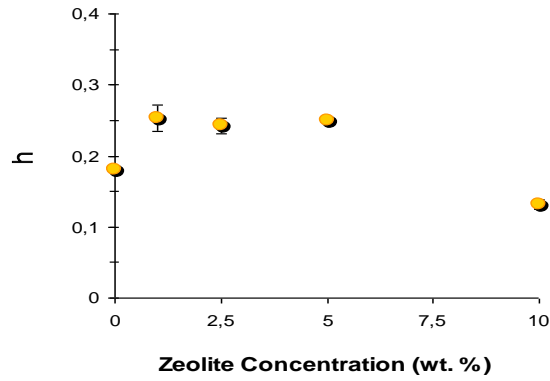
A)
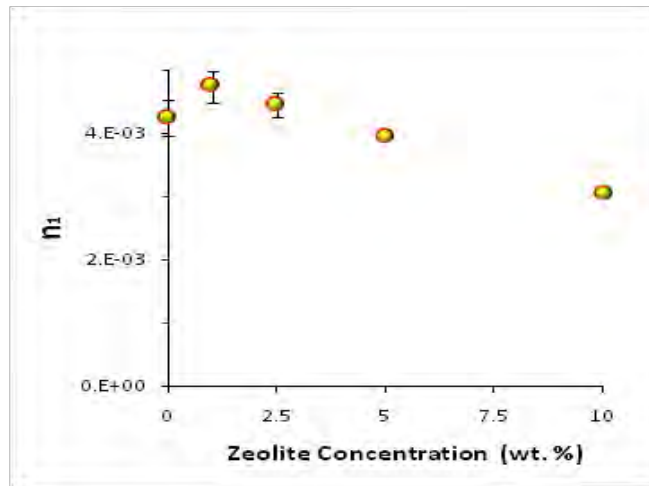
B)

Figure 5.11. **Grating performances dependence on concentration of zeolite A (90 nm) nanocomposites: (A) diffraction efficiency and (B) refractive index modulation; gratings recorded at 1000 lmm^{-1} and recording intensity of 5 mWcm^{-2}.**

Table 5.5. **Thickness of gratings recorded in zeolite A films presented in Fig. 5.11 (measured by the angular selectivity curve).**

Zeolite (%wt.)	Thickness (μm)	
0	19	±1
1	21	±2
2.5	21	±1
5	22	±0.4
10	22	±2

145

The incorporation of small concentrations of zeolite A shows an improvement of the refractive index modulation of 16% and 8 % for a concentration of zeolite of 1%wt. and 2.5%wt., respectively.

5.5 *INTERACTIONS BETWEEN ZEOLITE A AND PHOTOPOLYMER COMPONENTS*

To determine how the zeolite nanoparticles affect the grating performance of the nanocomposites, we have varied the concentrations of zeolite in the polymer components. This was done for both zeolite Beta (see Chapter 4) and zeolite A since these two zeolites have different properties, such as pore size and hydrophilic nature, properties that we suspect would have an influence on holographic properties of the two photopolymerizable nanocomposites.

As previously described, layers containing both zeolites were prepared using stock solutions of 5%, 10% and 20%wt. polyvinyl alcohol (PVA). The compositions of the different suspensions were presented in Table 4.7. The refractive index modulation values determined for zeolite A nanocomposites (90 nm) are shown in Figure 5.12.
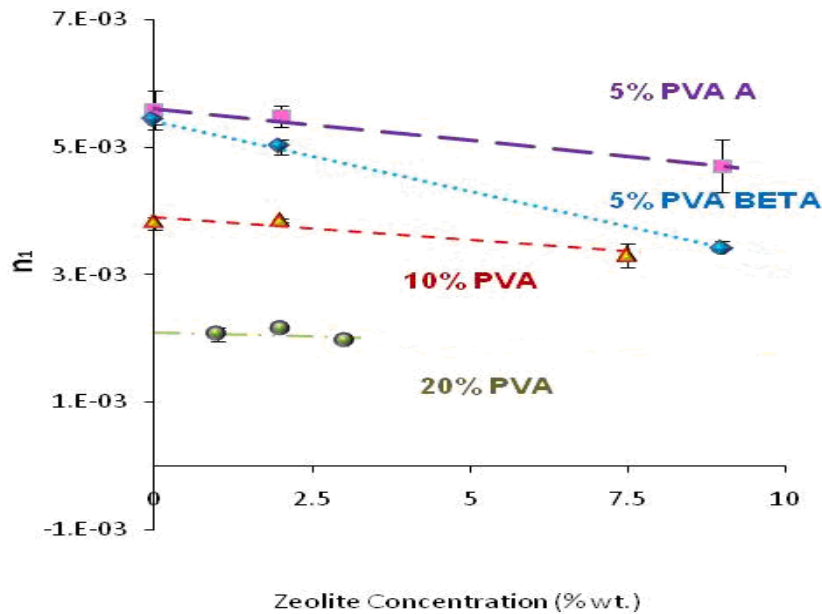
Figure 5.12. Refractive index modulation of photopolymer nanocomposites containing zeolite A nanoparticles; the layers were prepared with PVA stock solutions with a concentration of 5%, 10% and 20% of PVA. For comparison, the data for zeolite beta 5% PVA doped layers is also presented.

The decrease in refractive index modulation in the case of zeolite A nanocomposites (16%) is twice smaller than the one observed for zeolite Beta nanocomposites (37%), as it can be visually seen by observing the slop decrease for both nanocomposites for the case of PVA 5% matrix. This PVA concentration was chosen for comparison since it was the set of data where the decrease in refractive index modulation was more pronounced.

The interactions between zeolite A nanoparticles and the photopolymer components are studied. The same methodology as described before is followed. First, a study by visible spectroscopy was carried out. Different components of the photopolymer (one at a time) were added to the solution of zeolite and erythrosine B (Figure 5.13).
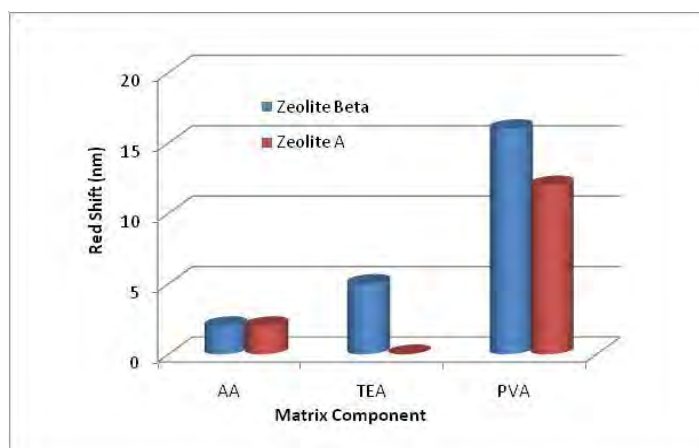
Figure 5.13. **Change in the position of the absorption maximum intensity in aqueous solutions containing erythrosine B and zeolite A and Beta when compared to aqueous solution in the presence of acrylamide (AA), TEA and PVA.**

No shift in the absorption spectrum of the dye (erythrosine B) was observed after addition of the zeolite nanoparticles indicating the absence of interaction between the dye and the nanoparticles. Spectra were also taken from photopolymer solutions. In this case, the shapes of the spectra remained the same but a red shift of the absorption peak of 9nm was measured in the case of solutions with zeolite A.

It was observed that the addition of acrylamide to the water dispersion of zeolite nanoparticles and erythrosine B dye leads to a 2 nm red shift in the erythrosine B absorption peak in solutions containing both zeolite A and Beta. This indicates that a similar change of the solvent polarity after acrylamide addition in the case of zeolite A and Beta. The water dispersions of zeolite showed a larger red shift in the absorption peak of erythrosine B in presence of PVA (16nm) than zeolite A (12 nm). The main difference observed between these two nanoparticles was that a red shift of 5 nm in the absorption peak for zeolite Beta was detected when TEA was present, while no shift occurred in the in the presence of zeolite A.

148

Finally, gratings recorded in a photopolymer doped with 5%wt. of zeolite A nanoparticles (90 nm) were also studied by ^{13}C NMR and compared with undoped layers. The spectra were collected outside and inside the grating area (Figure 5.14).
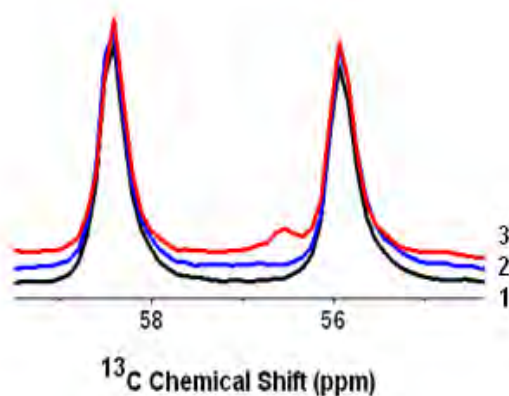
Figure 5.14. ^{13}**C NMR spectra of acrylamide based photopolymer doped with zeolite A: (black, 1) undoped photopolymer; (blue, 2) zeolite doped photopolymer (outside grating); (red, 3) zeolite doped photopolymer (inside grating); spatial frequency 1000 lmm^{-1} and recording energy of 600 mJcm^{-2}.**

In contrast to zeolite Beta doped nanocomposite, where the peaks were shifted to lower field (see Fig. 4.33), in the zeolite A nanomposite the two peaks corresponding to TEA showed no shift, indicating no interaction between zeolite A nanoparticles and the host photopolymer components. The origin of a new peak after polymerization needs further studies.

5.6 CONCLUSIONS

Zeolite A nanocomposites with good optical quality were prepared by incorporating different concentrations of zeolite A into the photopolymer. The nanocomposites were studied by DLS and light scattering surface roughness measurements. The influence of the zeolite A particle size (around 90 and 180 nm) on the optical properties of the nanocomposites was investigated, and it was concluded that the smaller the size of nanoparticles, the less scattering occurs. There was an improvement of 16% in the refractive index modulation upon addition of 1%wt. of zeolite A with a size of 90 nm. One of the possible reasons for this is the luck of interactions between the zeolite A nanoparticles and the photopolymer components, which can be explained by the high hydrophilicity and small pores of this zeolite. Future work on this nanocomposite could investigate the nanoparticles redistribution and the refractive index differences between the nanoparticles and the photopolymer matrix.

5.7 REFERENCES

[1] S. Mintova and T. Bein, *Nanosized Zeolite Films for Vapor-Sensing Applications*, Microporous and Mesoporous Materials 50, No. 2-3, 159–166 (2001)

[2] B. Mihailova, S. Mintova, K. Karaghiosoff, T. Metzger, and T. Bein, *Nondestructive Identification of Colloidal Molecular Sieves Stabilized in Water*, Journal of Physical Chemistry B 109, No. 36, 17060-17065 (2005)

CHAPTER 6: ALPO-18 (AEI-TYPE STRUCTURE) DOPED NANOCOMPOSITES

6.1 INTRODUCTION

AlPO-18 is an aluminophosphate molecular sieve, firstly synthesized by Wilson et al. [1] The framework topology is characterized by a three-dimensional pore system possessing eight-membered intersecting channels with a diameter of 3.8 Å [2].

Optical properties of the AlPO-18 doped nanocomposite were investigated by means of DLS, light scattering measurements, surface roughness and refractive index determination. Grating performances of AlPO-18 nanocomposites (diffraction efficiency and refractive index modulation) on parameters such as recording intensity, special frequency and zeolite concentration were also studied. Raman spectroscopy was used to study the AlPO-18 nanoparticle redistribution during the holographic recording. The optimum redistribution conditions for this type of nanocomposite were obtained. Despite the redistribution effect observed, the pores of zeolite are partially filled (as shown by refractive index calculations) by water molecules and no improvement of the refractive index modulation occurs when we add AlPO-18 to the photopolymer.

The optical properties of the photopolymer layers combined with the ability of the AlPO-18 nanoparticles to be light-induced redistributed during the holographic recording are were explored for fabrication of holographic humidity sensors. It was observed that the addition of AlPO-18 to the photopolymer introduces irreversibility in the humidity response of the layers. This is important for instance in situations where, regardless of current (potentially lower) humidity levels, one would like to know if humidity had previously been higher.

151

6.2   ALPO-18NANOPARTICLES CHARACTERIZATION

The structure of AlPO-18 crystals (AEI type zeolite framework) is shown in Figure 6.1.

A) B)
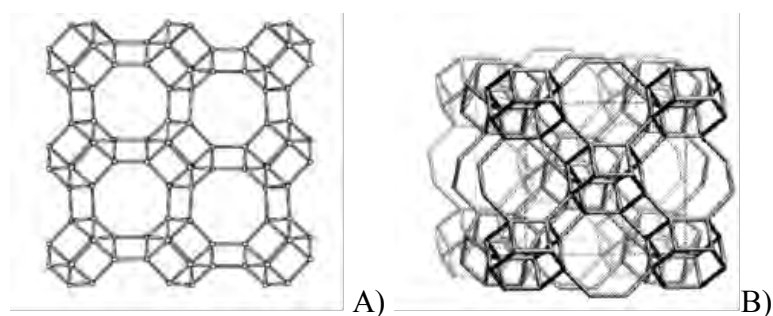
Figure 6.1.   Periodic building unit of .the AEI-type molecular sieve: view along (A) [110]; (B) the pore structure of AlPO-18.

The DLS results showed that the particle size of AlPO-18 was 115 nm (Fig. 6.2) expressed in number of particle counts obtained per unit volume of sample (number weighted).
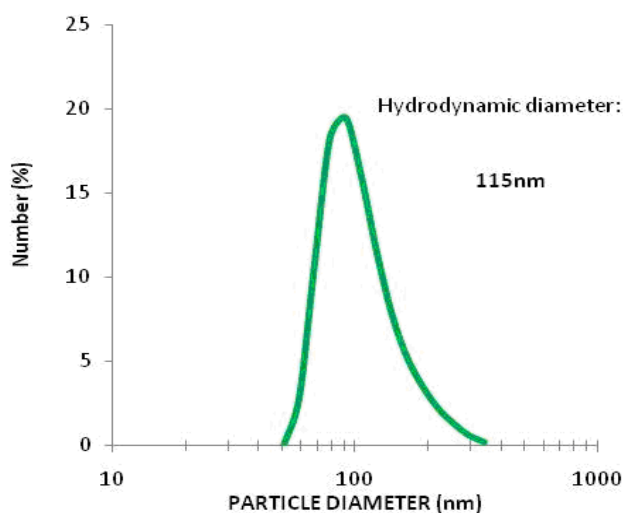
Figure 6.2.   DLS curve of AlPO-18 suspension.

The crystalline nature of the microporous AlPO-18 nanoparticles was proven by the XRD and the patterns are shown in Figure 6.3.
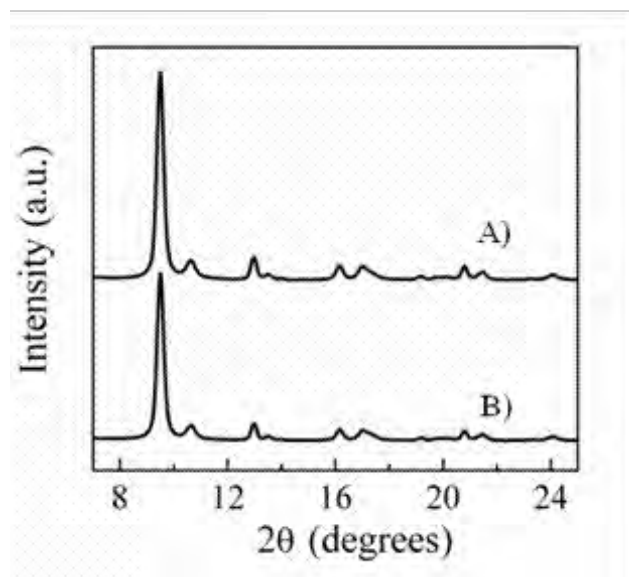
Figure 6.3. **X-ray diffraction patterns of AlPO-18 nanocrystals: (A) as-prepared and (B) calcined (390 °C for 12 h).**

The sharp reflections with high intensities indicate high crystallinity of the sample and the XRD patterns exhibit the typical Bragg reflections for AEI-type crystalline structure [3].

The morphological features of the AlPO-18 nanoparticles were examined by scanning electron microscopy (Fig. 6.4).
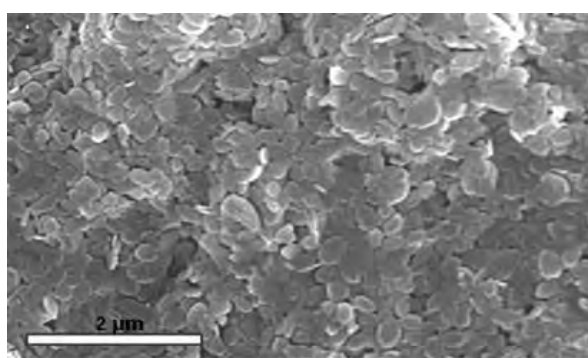
Figure 6.4. **Morphology of AlPO-18 nanoparticles.**

AlPO-18 nanocrystals have elongated elliptical shape with well-shaped single crystals which is typical for this framework [4].

The porosity of the AlPO-18 nanocrystals has been proven by N_2 sorption measurements (Fig. 6.5).
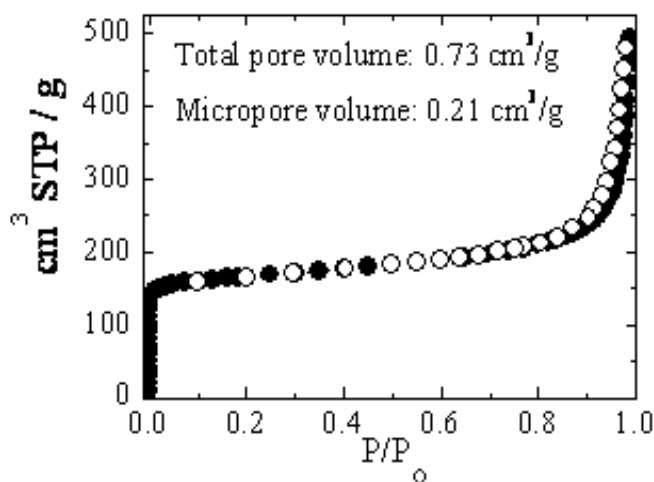
Figure 6.5. **Nitrogen adsorption isotherms of AlPO-18 nanoparticles (open circles denote desorption).**

The nitrogen adsorption-desorption curves possess the typical type IV isotherm in accordance with IUPAC classification [5]. The isotherm exhibits a rapid increase in nitrogen uptake at low relative pressure ($P/P_o < 0.1$), which corresponds to the filling of the micropores (size of 3.8 Å) with nitrogen. A plateau with an abrupt inclination step at high relative pressure ($P/P_o > 0.8$) was observed, which is associated with multilayer adsorption in the textural mesopores of the nanosized material. The micropore volume was calculated to be 0.21 $cm^3 g^{-1}$ and of the total specific pore volume of 0.73 $cm^3 g^{-1}$, which is due to the small crystal size of the nanoparticles. According to literature these are typical values [3].

Raman spectroscopy was also used to characterize the AlPO-18. The spectrum of AlPO-18 nanoparticles is shown in Fig. 6.6.
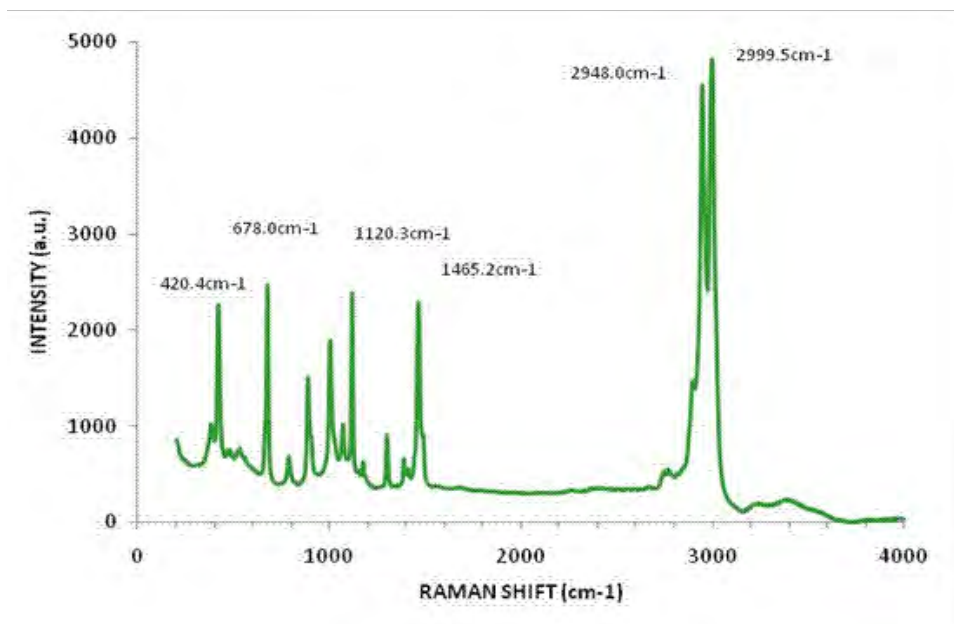
Figure 6.6.   Raman spectrum of AlPO-18 nanoparticles.

The prominent band in the Raman spectrum of AlPO-18 in the fingerprint region (300-600 cm^{-1}) is found at 420.4 cm^{-1}. This band is assigned to the motion of an oxygen atom in a plane perpendicular to the T-O-T bonds. Other prominent bonds observed were also assigned (see Table. 6.1).

Table 6.1.   Raman peak assignments of AlPO-18.

Raman Peak (cm^{-1})	Functional Group/ Vibration
420.4	T-O-T stretching (4 rings)
678.0	C-C-N (template)
1118.9	Stretching of Si-O (zeolite)
1465.2	Deformation of CH (template)
2948.0	Symmetric stretching of CH_3 (template)
2999.5	Assymmetric stretching of CH_3 (template)

For the synthesis of AlPO-18 tetraethylammonium hydroxide (TEAOH) was used, the same template as for zeolite Beta. One can see that the peaks of the template are found at around the same frequencies.

6.3   ALPO-18 NANOCOMPOSITES OPTICAL PROPERTIES

AlPO-18 doped nanocomposites were prepared by adding different quantities to the photopolymer solution and adding water to have the same concentration of the remaining components (monomer, TEA, PVA) in unit volume, as described for the previous nanocomposites. The AlPO-18 concentration in the colloidal suspension was 4%wt.

As before, the compatibility of the AlPO-18 particles with the photopolymer solutions was first characterized by measuring the DLS curves for the photopolymerizable nanocomposites (Figure 6.7).
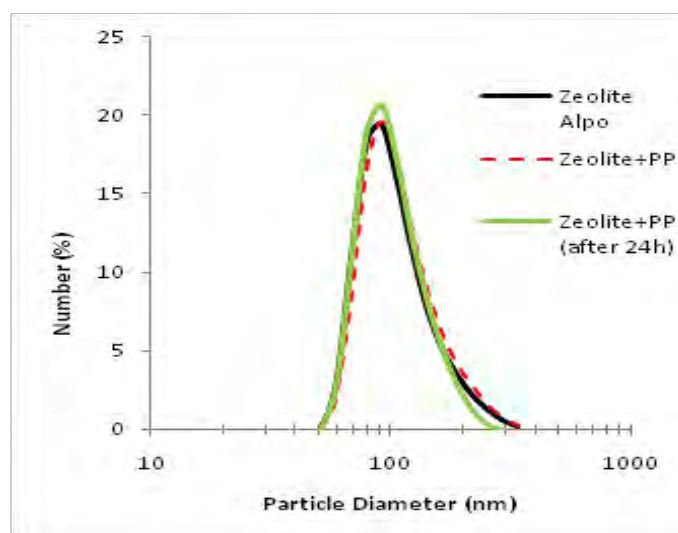
Figure 6.7.   DLS curves (number weighted) of: (black) AlPO-18; (red dashed) photopolymer doped with AlPO-18 nanoparticles (freshly mixed); (green) photopolymer doped with AlPO-18 nanoparticles (24 hours stored at RT).

The size of the AlPO-18 particles does not change after incorporation into the photopolymer, and the DLS curves have the same maximum. One can conclude that no aggregation of the AlPO-18 nanoparticles directly after mixing or after 24h aging was observed.

The scattering of AlPO-18 doped nanocomposites (thickness of around 40 μm) was characterized by light scattering measurements and the results are shown in Fig. 6.8. For comparison the scattering of the glass substrate is also shown.
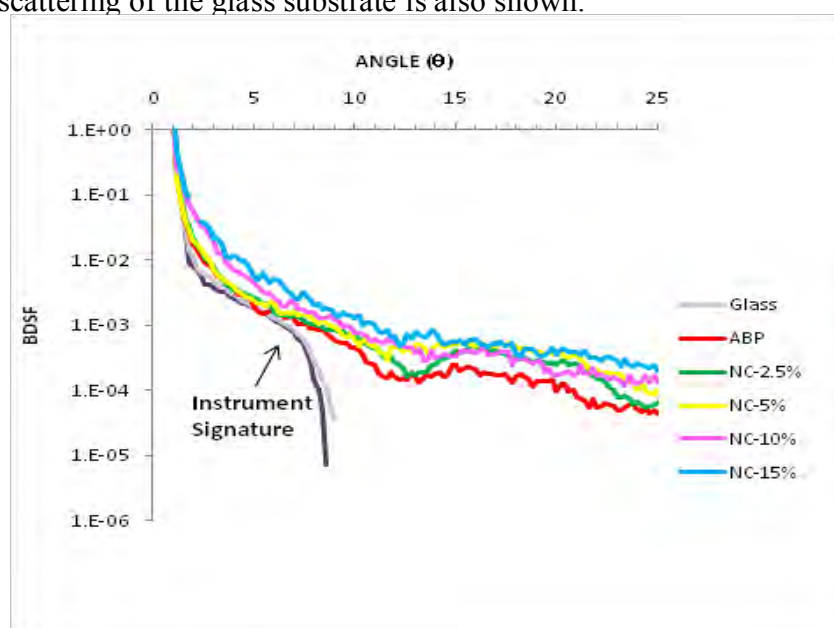
Figure 6.8. **Bidirectional scattering distribution function of glass, acrylamide based photopolymer (ABP) and AlPO-18 nanocomposites in several concentrations as indicated in the figure (logarithmic scale).**

We can see that the BDSF curves for the AlPO-18 nanocomposites up to a concentration of 2.5%wt. show similar dependence with the scattering angle with that for the undoped photopolymer. For 5%wt. and higher concentrations of AlPO-18 nanoparticles there is a significant increase of light scattering when compared to undoped photopolymer. One possible explanation is that the nanoparticles at these concentrations are located at the

157

surface of the layer by a mechanism of segregation of the nanoparticles to the air/polymer interface.

The surface roughness of the AlPO-18 nanocomposites was quantified in five different locations across the material (Fig. 6.9 and Table 6.2). This method was used in the present work as a measure of how compatible the nanoparticles can be with the photopolymer, since if they are, for instance expelled to the surface of the photopolymer, the roughness will increase.

Table 6.2. **Surface roughness measurements (RMS) for AlPO-18 nanocomposites.**

Concentration of AlPO-18 (%wt.)	Surface Roughness (nm)	
0	1.3	± 0.3
1	1.9	± 0.8
2.5	3.0	± 1
5	16.5	± 0.5
7.5	21.3	± 1.2
10	27.0	± 2.6
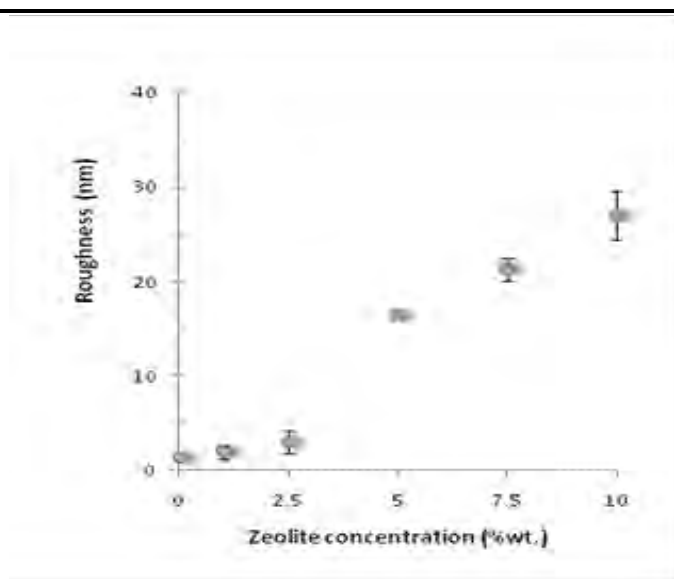
Figure 6.9. **Surface roughness dependence on concentration of AlPO-18.**

158

The undoped photopolymer has almost a flat surface (roughness of 1nm). The addition of AlPO-18 to the photopolymer has a small effect in the increase of the surface roughness up to a concentration of 2.5%wt. The nanocomposite containing 5%wt. has a roughness increase of around 12 times its initial value and for the material doped with AlPO-18 10%wt. the roughness is of 27nm. This data confirms the previous hypothesis that the AlPO-18 nanoparticles are predominantly at the surface of the photopolymer for concentrations above 5%wt. of nanocomposite photopolymer material (see Fig. 6.8).

The refractive index of AlPO-18 nanocomposites was calculated as shown in previous chapters (Eq. 4.2). The value for AlPO-18 doped nanocomposite does not differ much from the undoped photopolymer (see table 6.3). These values will be useful to calculate the pore volume of the zeolite before and after its incorporation into the photopolymer and determine if the pores are empty or filled. This was done by Dr. T. Babeva.

Table 6.3.   Volume refractive index of AlPO-18 nanocomposites (633 nm).

AlPO-18 concentration (%wt.)	Refractive Index
0	1.499 ± 0.005
2.5	1.478 ± 0.005
5	1.505 ± 0.005
10	1.481 ± 0.005

The refractive index of the photopolymer decreases with the incorporation of AlPO-18 nanoparticles (except for the incorporation of 5%wt. alPO-18 nanoparticles), which is expected since the refractive index of this nanoparticles filled with H_2O nanoparticles is 1.414 at 633 nm, calculated from the dispersion curve based on Bruggeman effective media approximation (EMA), the Wemple-Di Domenico dispersion equation and the nonlinear

minimization of appropriate goal function (see Eq. 4.2); more details in this method can be found in [6].

Since the decrease in refractive index before and after incorporation of AlPO-18 in the photopolymer is not significant, one hypothesis is that the micropores of AlPO-18 are filled with guest molecules from the photopolymer matrix.

The pore volume of AlPO-18 before incorporation in the photopolymer determined experimentally by N_2-sorption data (see Fig. 6.5), was of 0.21 gcm^{-3}. The refractive index and density of a mixture Al_2O_3 and P_2O_5 in the ratio 1:1 was calculated by Bruggeman EMA using the refractive index and density of oxides, i.e. 4 gcm^{-3} and 2.4 gcm^{-3} for Al_2O_3 and P_2O_5, respectively. Further if the AlPO-18 nanocrystals consist of two phases – air and (Al_2O_3: P_2O_5) one can calculate the volume fraction of the two phases using the Bruggeman effective media approximation. Using this approach, it was calculated that the AlPO-18 nanoparticles consist of 71% oxides (Al_2O_3: P_2O_5) mixture and 29 % voids. Considering both the free volume and the density of a mixture of Al_2O_3 : P_2O_5 to be 3gcm^{-3}, the density of AlPO-18 particles was determined to be 2.42 gcm^{-3}. Finally, having in mind that the densities of AlPO-18 and (Al_2O_3: P_2O_5) are 2.42 gcm^{-3} and 3.00 gcm^{-3}, respectively 1g of each substance occupies 0.41 cm^3 and 0.33 cm^3 respectively Thus the pore volume of AlPO-18 after incorporation in the photopolymer was estimated to be 0.08 gcm^{-3}. Comparing this value with the value before incorporation, 0.21gcm^{-3}, one can conclude that AlPO-18 pores do not remain empty after the particles are incorporated in the photopolymer. Due to the size of the pores (3.8 Å) only water has dimensions that allow them to enter which is likely to happen due to the hydrophilic nature of this material.

From the DLS and surface roughness data the AlPO-18 nanoparticles show a good compatibility with the polymeric matrix up to concentrations of 5%wt. At higher values there is a significant increase of surface roughness, which can be possibly explained by the expulsion of AlPO-18 nanoparticles to the photopolymer surface. Homogeneous coating suspensions can be obtained (see Fig. 6.10), homogeneous dry layers were prepared and an optically transparent material was obtained.
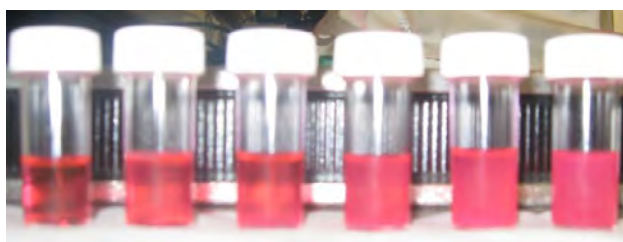
Figure 6.10.   Photopolymerizable AlPO-18 nanocomposites. From left to right: 0%, 1%, 2.5%, 5%, 7.5% and 10%wt.

6.4   *GRATING PERFORMANCES OF ALPO-18 NANOCOMPOSITES*

6.4.1   *AT DIFFERENT RECORDING INTENSITIES*

Gratings recorded in AlPO-18 nanocomposites for different recording intensities were studied. The work was divided in two parts and two independent experiments were carried out: one for higher recording intensities (2.5 to 15 mWcm^{-2}) and another for lower intensities (0.1 to 1 mWcm^{-2}).

Firstly, the recording intensities used were 2.5, 5, 10 and 15 mWcm^{-2}, for a time of exposure of 120s (data was collected up to 140s to observe if there are any dark processes taking place). Undoped photopolymer was compared to a nanocomposite material containing 1.5%wt. of AlPO-18. The reason behind the choice of AlPO-18 concentration is

that preliminary results showed that optimum redistribution conditions in AlPO-18 nanocomposites occurs for a concentration of 1.5%wt. and a recording intensity of 12mWcm^{-2}. Briefly, these studies were made by investigating the surface relief formation in nanocomposites in transmission gratings with spatial frequency of 70 lmm^{-1}. The main reason of relief formation at this spatial frequency is the monomer diffusion from dark to bright area. Since the nanoparticles are expected to diffuse in the opposite direction to the monomer diffusion, it can be expected that the formation of surface relief to be suppressed at some concentrations and intensities where redistribution occurs. As a result a decrease in the surface relief height may be expected and surface relief profile as a function of recording intensity and particles concentration were analyzed.

Several samples for each experimental condition were used and a typical set of experimental data (three different samples, Nr. 1, 2 and 3) is given in Figs. 6.11 and 6.12.
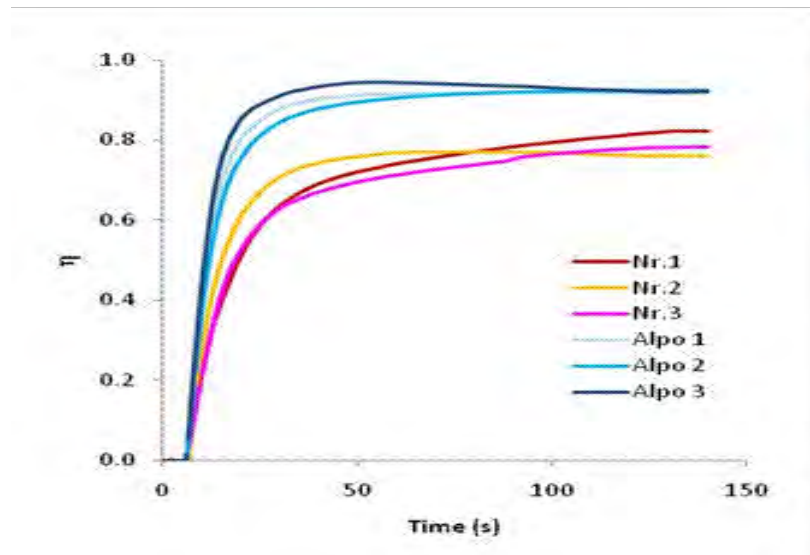
Figure 6.11. Typical diffraction efficiency growth curves; recording intensity is 2.5mWcm^{-2} and Nr. 1, 2 and 3 correspond to different gratings of either undoped photopolymer or AlPO-18 1.5%wt. nanocomposite.

162
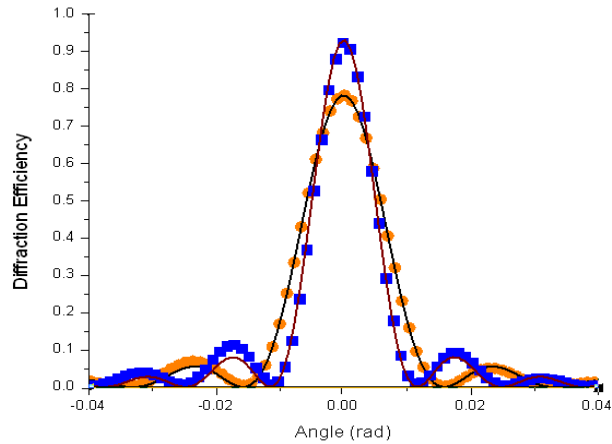
Figure 6.12. Typical angular selectivity curves: (orange circles) undoped photopolymer; (blue squares) nanocomposite 1.5%wt. AlPO-18; Angles were measured inside the recording medium, recording intensity was of 2.5 mWcm^{-2}; points are experimental data and lines are the corresponding fitting functions according to Kogelnik's wave theory.

In Fig. 6.11 one can see that the diffraction efficiency increases initially with time, reaching then a maximum value, which is the value of the maximum intensity peak seen in Fig. 6.12.

In Figure 6.13 and Table 6.4 one can see the grating performances dependence on the recording intensity for several AlPO-18 doped nanocomposites.

A)

B)
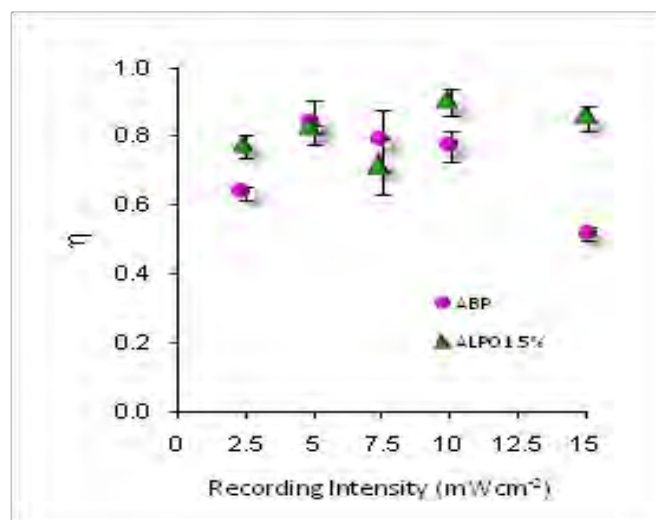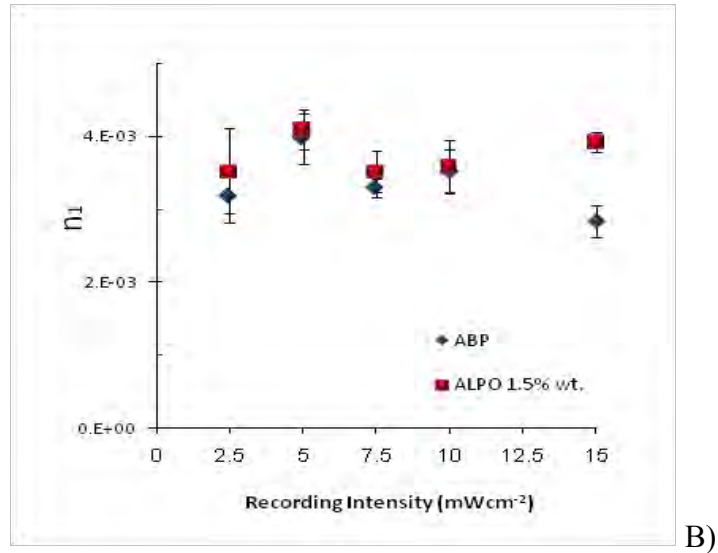
Figure 6.13. **Grating performances as a function of recording intensity (from 2.5 to 15 mWcm^{-2}) for undoped photopolymer (ABP) and 1.5%wt. AlPO-18 nanocomposite: (A) diffraction efficiency; (B) refractive index modulation (1000 lmm^{-1}).**

Table 6.4. **Thickness of gratings recorded in AlPO-18 1.5%wt. films presented in Fig. 6.13.**

Recording Intensity (mWcm^{-2})	Thickness (μm)											
	WLI				Bragg				Average			
	Undoped		AlPO-18		Undoped		AlPO-18		Undoped		AlPO-18	
2.5	53	±4	65	±4	64	±1	57	±6	59	±3	61	±5
5	61	±10	52	±3	56	±2	60	±3	59	±6	56	±3
7.5	64	±5	57	±5	70	±5	58	±2	67	±5	58	±4
10	61	±4	60	±8	62	±4	80	±3	61	±4	70	±6
15	52	±7	55	±7	62	±2	65	±3	57	±5	60	±5

The undoped photopolymer shows an optimum recording intensity of 5 mWcm^{-2} and the material shows lower refractive index modulation for higher recording intensities. The 1.5%wt. AlPO-18 nanocomposite shows no dependence of the refractive index modulation on the recording intensity.

164

Secondly, lower recording intensities were also studied (0.1, 0.5 and 1mWcm^{-2}) and the results are presented in Fig. 6.15 and Table 6.5. The substrate used in this experiment was plastic (since this substrate could be useful in the fabrication of sensors) and a typical example of diffraction efficiency growth curves is shown in Fig. 6.14.
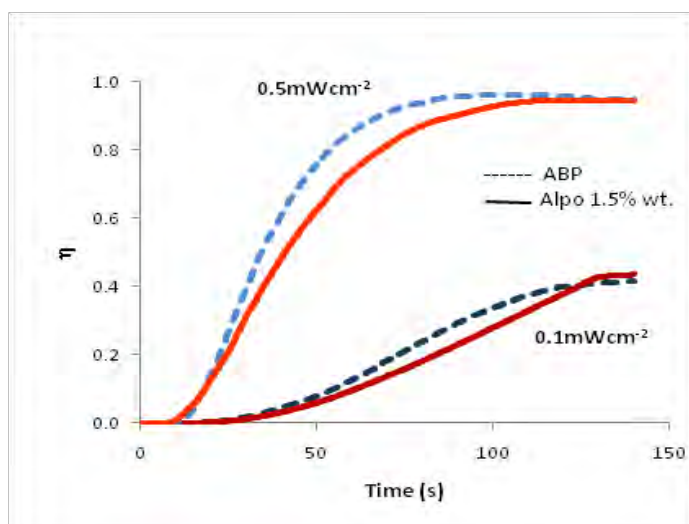
Figure 6.14.   Diffraction efficiency growth curves for recording intensities of 0.1 and 0.5 mWcm^{-2}. The dashed lines correspond to acrylamide based photopolymer (ABP) and the solid lines to AlPO-18 (1.5%wt.) nanocomposite.

At low recording intensity (0.1mWcm^{-2}), the gratings show slow grating-buildup behavior and lower diffraction efficiency due relatively slower polymerization speed of the monomers. Also, the introduction of AlPO-18 seems to slow the diffraction efficiency growth seen in the initial slopes of the curves.

(A)

(B)
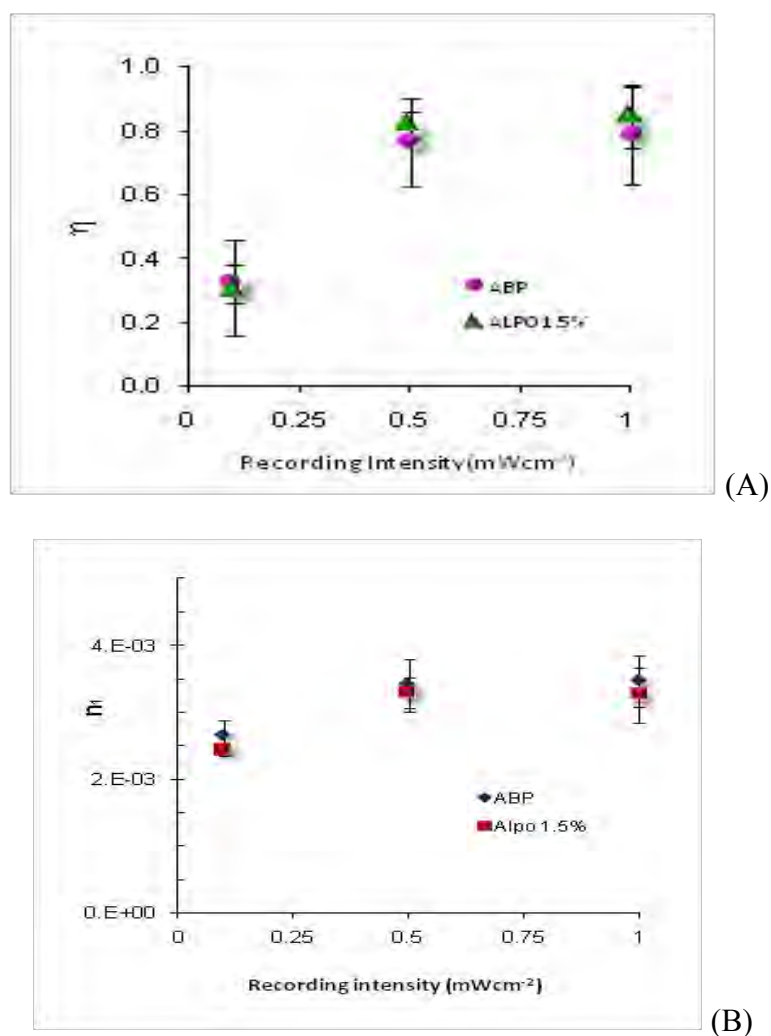
Figure 6.15.   Grating performances as a function of recording intensity (from 0.1 to 5 mWcm^{-2}) for undoped photopolymer (ABP) and 1.5%wt. AlPO-18 nanocomposite: (A) diffraction efficiency; (B) refractive index modulation (1000 lmm^{-1}).

Table 6.5. Thickness of gratings recorded in AlPO-18 films shown in Fig. 6.15 (fitting of the angular selectivity curve).

Recording Intensity (mWcm^{-2})	Thickness (μm)			
	Undoped photopolymer		AlPO-18 1.5%wt.	
0.1	49	± 3	49	± 4
0.5	65	± 13	68	± 4
1	70	± 8	75	± 4

166

Successful recording in photopolymer and AlPO-18 nanocomposite materials coated on plastic substrate can be obtained even using low recording intensities. This can be useful for the design of holographic sensors since one can design versatile sensor platforms. Also at very low recording intensity of 0.1 $mWcm^{-2}$ the polymerization rate is slower than at 0.5 and 1 $mWcm^{-2}$. This may suggest that there is a minimum threshold value for the recording intensity.

The refractive index modulation dependence in all the recording intensities was summarized in Fig. 6.16.
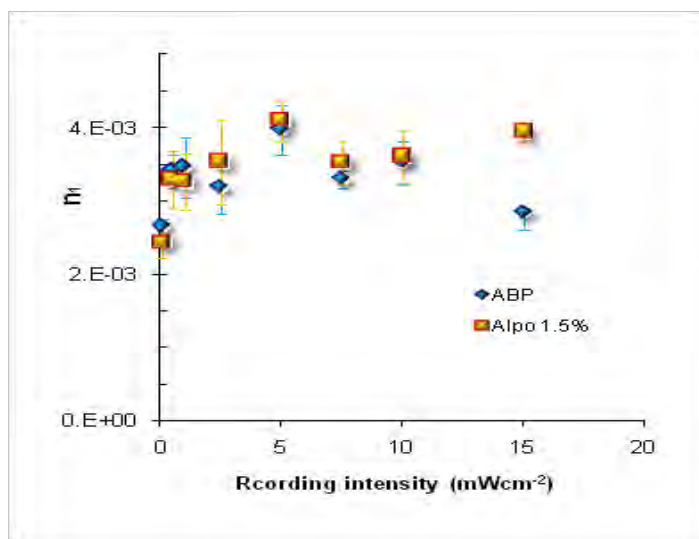
Figure 6.16.   Refractive index modulation as a function of recording intensity for undoped photopolymer (ABP) and 1.5%wt. AlPO-18 nanocomposite.

For both materials, the refractive index modulation monotonically increases up to its maximum value at 5 $mWcm^{-2}$. For higher recording intensities, there is a subsequent decrease in refractive index modulation in the case of acrylamide based photopolymer and a plateau in the case of AlPO-18 doped nanocomposite.

This intensity dependence observed for acrylamide based photopolymer is typical for other photopolymerizable holographic materials [7, 8], where the mechanisms of holographic recording are polymerization and diffusion. The low refractive index modulation at low recording intensities is due to the different rates of polymerization in bright and dark fringes that slow down the polymerization rate. As the intensity increases, the polymerization rate increases until it reaches an equilibrium value between processes of diffusion and polymerization. Then the limiting mass-transport effects are responsible for the lower refractive index at higher intensities. High intensity produces high termination rates and therefore short polymer chains which can more freely escape from bright to dark areas and in this way will decrease refractive index modulation to a greater extent. At high intensities, one can assume that the presence of nanoparticles slows down diffusion and restricts loss of short polymer chains into dark fringe areas thereby maintaining the optimum maximum value of refractive index modulation. Another possible explanation is that a large number of oligomers and/ or short polymer chains would diffuse and sweep the nanoparticles in the desired direction.

6.4.2   *AT DIFFERENT SPATIAL FREQUENCIES AND AlPO-18 CONCENTRATIONS*

The grating performances of undoped photopolymer and AlPO-18 nanocomposites were obtained for two different spatial frequencies (500 and 2000 lmm^{-1}) using a constant recording intensity of $5mWcm^{-2}$ for a time of exposure of 70s (Fig. 6.17). The concentration of nanoparticles studied was from 0%wt. to 15%wt%.

A)

B)
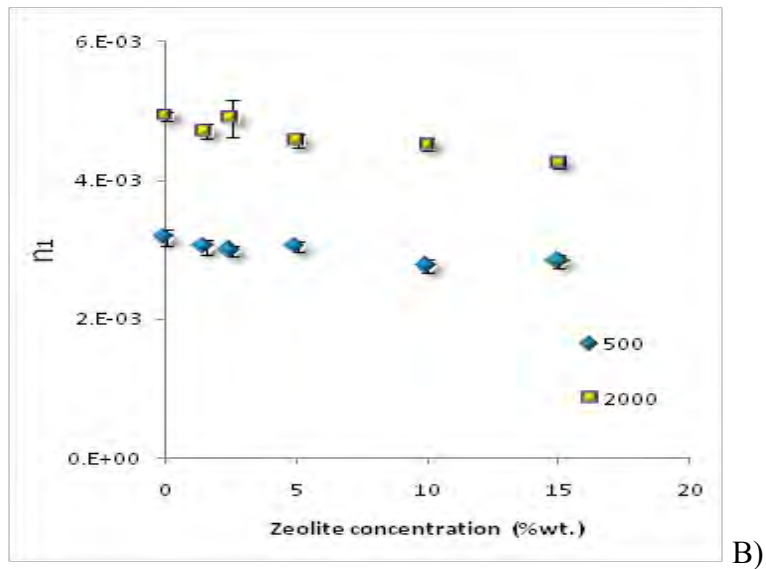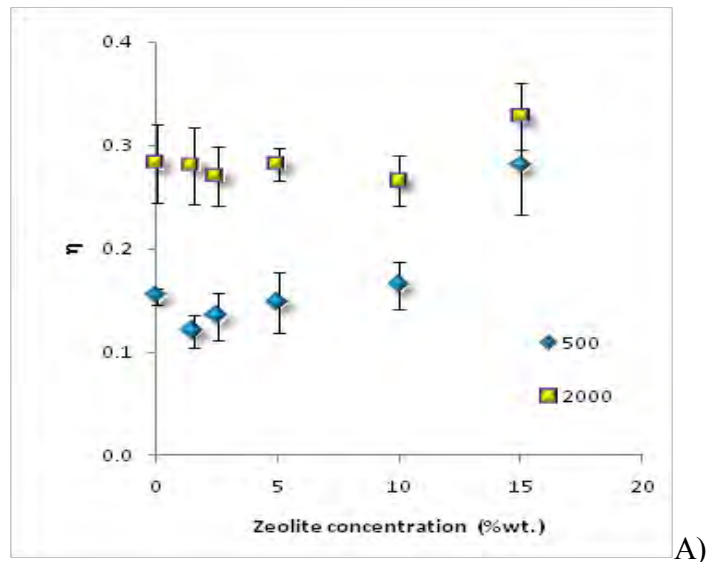
Figure 6.17. Grating performances of photopolymer as a function of AlPO-18 concentration for different spatial frequencies: (A) diffraction efficiency; (B) refractive index modulation; recording intensity of 5 mWcm^{-2}.

At a spatial frequency of 500 lmm^{-1} there were observed higher-order diffractions and the diffraction efficiency was calculated using the first order intensity.

Table 6.6.   Thickness of gratings recorded in AlPO-18 films presented in Fig. 6.17 (fitting of the angular selectivity curve).

AlPO-18 concentration (% wt.)	Thickness (µm)			
	500 lmm^{-1}		1000 lmm^{-1}	
0	26	±1	23	±2
1	23	±2	24	±2
2.5	25	±3	23	±1
5	26	±3	25	±0.7
10	30	±1	24	±2
15	40	±4	29	±2

It was observed that all gratings recorded at spatial frequency of 2000 lmm^{-1} show consistently higher refractive modulation than the layers recorded at 500 lmm^{-1} spatial frequency. Such dependence can be easily explained in the doped layers because with the decrease in the grating period the distance required to be travelled by the photopolymer components decreases, thus more effective refractive index modulation occurs. The second observation is the absence of increased refractive index modulation with the increase of the concentration of nanoparticles. Possible reasons for this are that a very small amount of nanoparticles are redistributed or the difference between the nanoparticles refractive index and the photopolymer matrix is not high enough to improve the refractive index modulation. Since the refractive index of these nanoparticles filled with H_2O is 1.414 at 633nm (section 6.3) and the refractive index of the undoped photopolymer matrix at this wavelength is 1.499 (see Table 6.3) the difference is 0.085. The next step was to see if there is a redistribution of the nanoparticles during holographic recording in this nanocomposite as discussed in the next section.

6.5 REDISTRIBUTION OF ALPO-18 NANOPARTICLES

The redistribution of AlPO-18 during holographic recording was studied by Raman spectroscopy. The Raman spectrum of the acrylamide based photopolymer doped with AlPO-18 nanoparticles (Fig. 6.18) shows one well isolated peak at 420.4 cm^{-1} originating from T-O-T vibrations of the rings of the AlPO-18-nanoparticles which are absent in the undoped polymer.
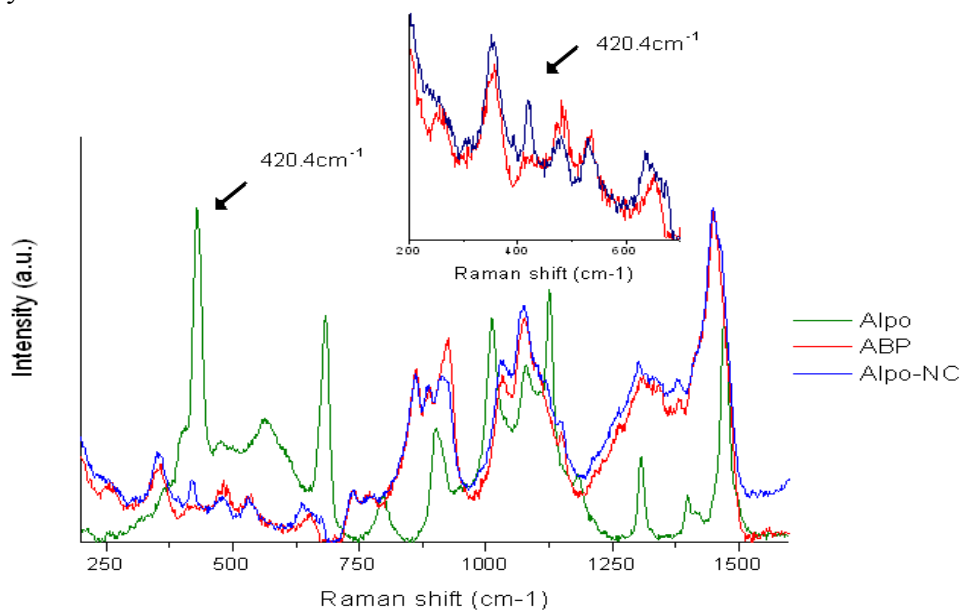
Figure 6.18. Raman spectra of (blue) NC - AlPO-18 photopolymer; (red) ABP - undoped photopolymer; and (green) AlPO-18; (200lmm^{-1}, 5µm grating spacing). Inset depicts the T-O-T vibration present in the AlPO-18 sample.

Gratings were recorded in AlPO-18 nanocomposites. The space fringing of the grating was chosen to be 5 µm (spatial frequency of 200 lmm^{-1}). The reason to choose this space fringing was due to limitations of the spatial resolution of the confocal Raman spectrometer, which is 1µm. We monitored the spatial variation of the Raman peak intensity at 420.4 cm^{-1} in the direction of the grating vector firstly for a concentration of AlPO-18 7.5%wt. in gratings recorded at 1, 5 and 10 mWcm^{-2} (Fig. 6.19).
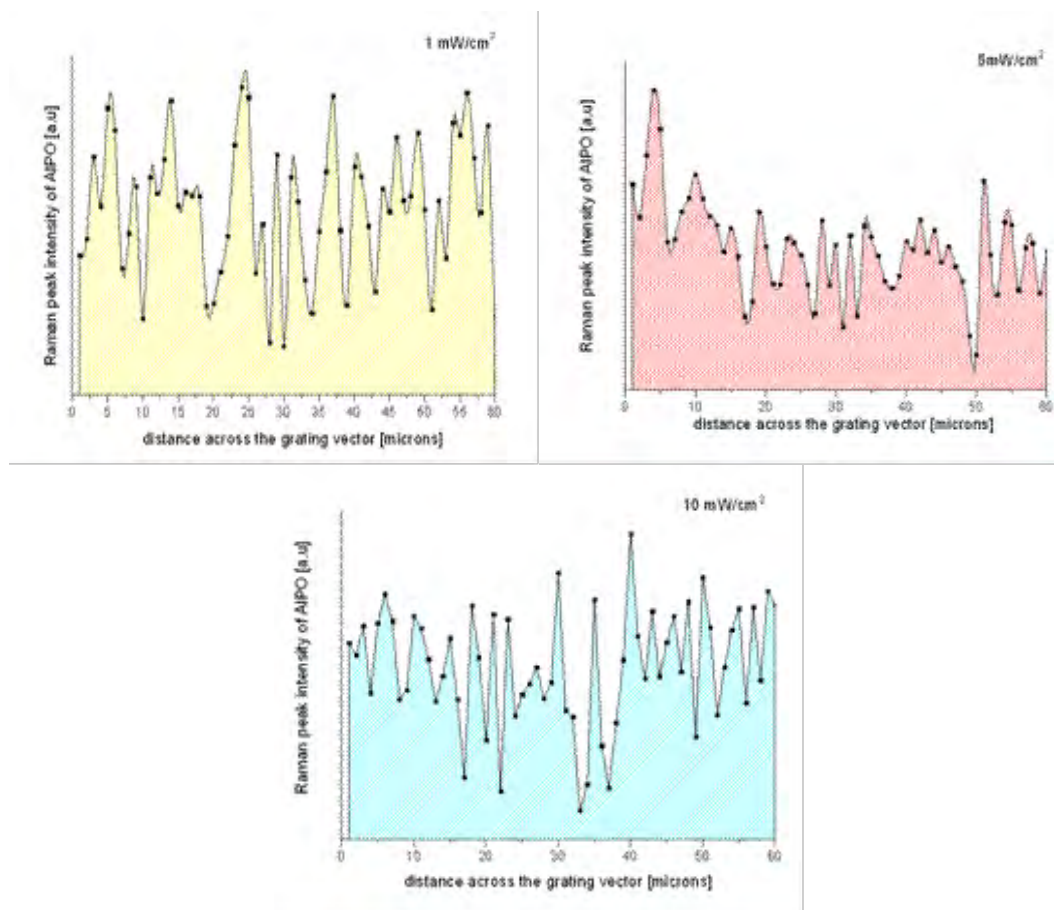
Figure 6.19. Raman spectra scan (grating vector direction, 1 µm steps) of 7.5%wt. AlPO-18 nanocomposite sample with recording intensities of (yellow) 1mWcm^{-2}, (red) 5 mWcm^{-2} and (blue) 10 mWcm^{-2} (200 lmm^{-1}, 5 µm grating spacing).

It was not possible by Raman spectroscopy to visualize the nanoparticle redistribution for the nanocomposite containing 7.5%wt. of AlPO-18 nanoparticles, so two different nanocomposites with lower concentrations of AlPO-18 were then tested, one containing 1% and the other 2.5%wt. of AlPO-18, for three recording intensities: 1, 5 and 10 mWcm^{-2}. For 1%wt., the Raman signal was too weak to be used in this type of experiment so results are only shown for concentration of 2.5%wt. From the results obtained for 2.5%wt AlPO-18 nanocomposites for different recording intensities, the best data were for the recording intensity of 10 mWcm^{-2} (see Fig. 6.20).
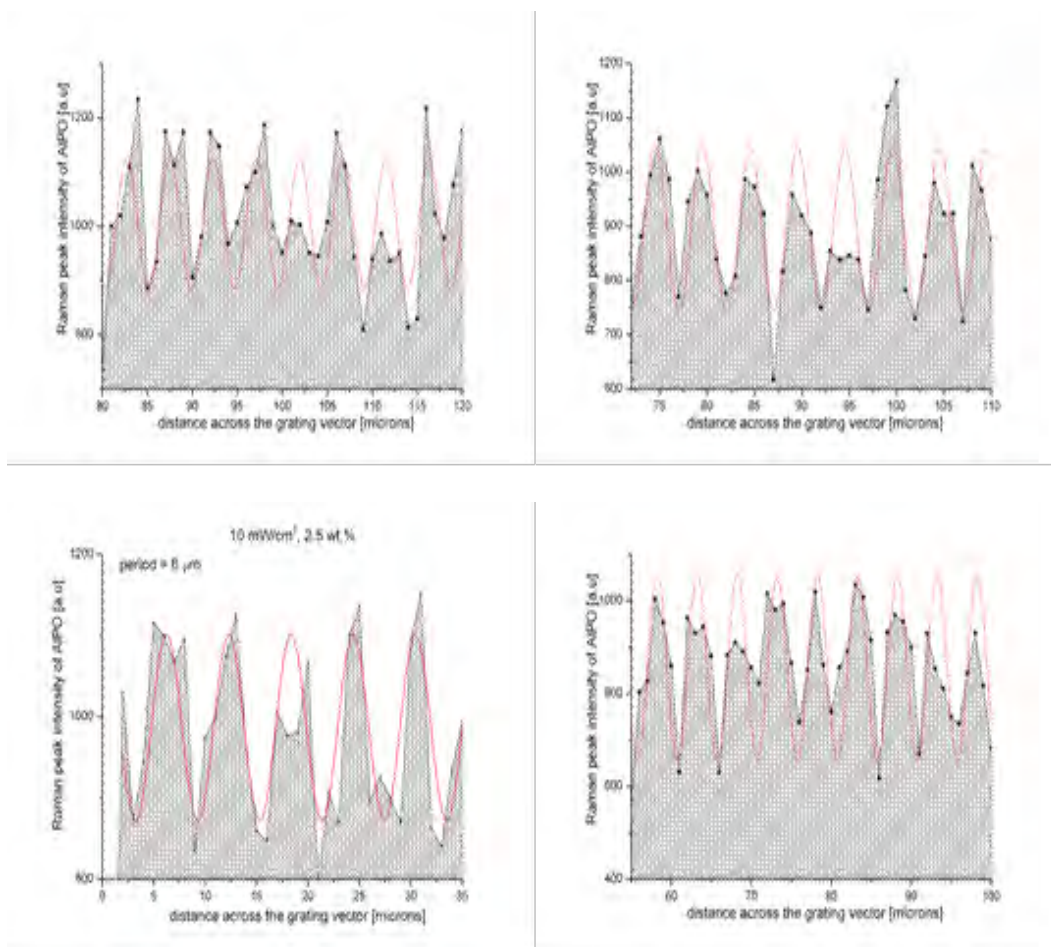
Figure 6.20. **Raman spectra spatial scan (grating vector direction, 1 μm steps) of 2.5%wt. AlPO-18 nanocomposite grating (200 lmm^{-1}, 5μm grating spacing; recording intensity of 10 mWcm^{-2}).**

As can be seen in Figure 6.20, the variation of the Raman peak at 420.4 cm^{-1} intensity in the grating vector direction is cyclic in conformity with the fringe spacing of 5 μm in the grating, indicating that there is indeed a redistribution of AlPO-18 nanoparticles. If one assumes that the Raman peak intensity is linearly proportional to the concentration of the nanoparticles, then the redistributed fraction of the nanoparticles is 31% of the total volume.

173

The contribution of the redistributed nanoparticles to the overall refractive index modulation can be estimated by [9]:

$$\Delta n = \frac{2f_{nanodopants}}{\pi}(n_{nanodopant} - n_{host})\sin(\alpha\pi) \text{ (Eq. 6.1)}$$

where $f_{nanodopants}$ is the volume fraction of nanoparticles in the nanoparticle-rich region, $n_{nanodopant}$ is the refractive index of the nanodopants, n_{host} is the refractive index of the host organic matrix and α is the fraction of the grating rich in nanoparticles. By measuring the diffraction efficiency and determining the refractive index modulation one can estimate the volume fraction of redistributed nanoparticles, $f_{nanodopants}$.

The contribution to the refractive index modulation of the redistributed nanoparticles can be characterised by recording volume transmission phase gratings and estimating the difference in the refractive index modulation in doped and undoped materials.

The density of the water filled nanoparticles is 2.42 gcm^{-3} (as seen in Section 6.3) and knowing the weight of the nanoparticles present in a single nanocomposite layer to be 2.5%wt., one can calculate that the volume fraction of the nanoparticles in the layer is 0.75%. Using Eq. 6.1 (with α=0.5) we calculate the volume fraction of the redistributed nanoparticles to be 2.3x10^{-3}. The difference between the refractive index of the host photopolymer and that of water filled nanoparticles is estimated to be 0.085. Thus the expected refractive index modulation contributed by the redistributed nanoparticles is calculated to be 1.3x10^{-4}. This result explains why there was no improvement of the refractive index modulation through holographic recording in the layers doped with AlPO-18 in comparison to the undoped layers.

6.6 HUMIDITY SENSING

Humidity sensors reported in literature are usually based on reflection holograms [10, 11]. In this work, transmission holograms were tested. The operating principle of a holographic sensor based in a transmission hologram recorded in a nanocomposite material was previously shown in Fig. 4.35 and it is described by Eq. 4.4.

Regarding adsorption properties, almost all of the molecular sieves (especially those with high Al content) show a type I water sorption isotherm, which indicates high affinity for water at low partial pressure. The isotherm type I represents materials with high water sorption capacity and saturation at low partial pressure (P/P_0), followed by constant adsorption over a wide range of P/P_0 due to the water saturation in the pores [3] . The framework density (14.8 T/ 1000 A°) of the AEI topology is among the lowest in the family of aluminophosphate microporous materials. The high hydrophilicity of this molecular sieve accounts for exceptionally high water sorption capacities (27.8%wt. at 22 °C and 24 mbar), which make the material particularly interesting for heat storage, heat exchange and humidity sensing applications [3].

As seen in the previous section the expected refractive index modulation contributed by the redistributed nanoparticles is small (1.38×10^{-4}) due to the fact that most AlPO-18 pores are filled with water molecules. If one can expel the water from the pores of the nanoparticles, the difference in the refractive index between the host polymer matrix (1.499 ± 0.005) and the refractive index of the empty nanoparticles (1.239 ± 0.05) would be approximately three times greater. This effect can be useful for the design of irreversible humidity sensors.

Unslanted volume transmission holograms were recorded in both undoped photopolymer and in photopolymer containing AlPO-18 nanoparticles. To characterize the transmission holograms a controlled environment chamber with humidity control system Electro-Tech systems model 5503-20 was used. It consisted of a glove box, a microprocessor controller, a dehumidification system and an ultrasonic humidification system. The relative humidity in the chamber was varied from 15%–80% (± 1%). The optical test setup was assembled inside the chamber (see Figure 6.21). Light from a He-Ne laser (I_0) was incident on the grating at the Bragg angle and the intensities of the diffracted (I_D) and transmitted (I_T) beams were measured.
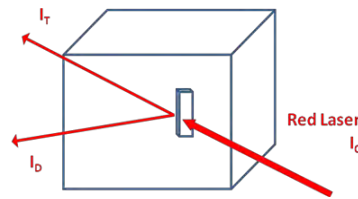
Figure 6.21. Experimental setup for measuring the humidity response of transmission holograms; the humidity in the chamber is controlled by a microprocessor.

The diffraction efficiency was defined in two different ways. Firstly, η_1, was defined as the ratio of the intensity of the diffraction beam to the incident beam intensity and secondly, η_2, defined as the ratio of the first order diffracted intensity to the sum of the transmitted (zero order) and the first-order diffracted intensities (Equation 6.2). The use of Equation 6.2 allows exclusion of reflected and scattered light due to condensation of moisture on the surface of the layer.

$$\eta_2 = \left(\frac{I_D}{I_D + I_T} \right) \qquad \text{(Eq. 6.2)}$$

Volume transmission holograms recorded in undoped photopolymer and containing 2% and 5%wt. of AlPO-18 nanoparticles were placed inside the humidity chamber where the humidity was changed from 15 to 80% and their diffraction efficiency responses were measured (Figure 6.22A). The samples were then baked (i.e. placed in an oven for 15 minutes at 120 $^{\circ}$C), placed in a box containing desiccant and their humidity response was again characterized (Figure 6.22B). The heating at this temperature allows the water to be released from the AlPO-18 pores.

(A)

(B)
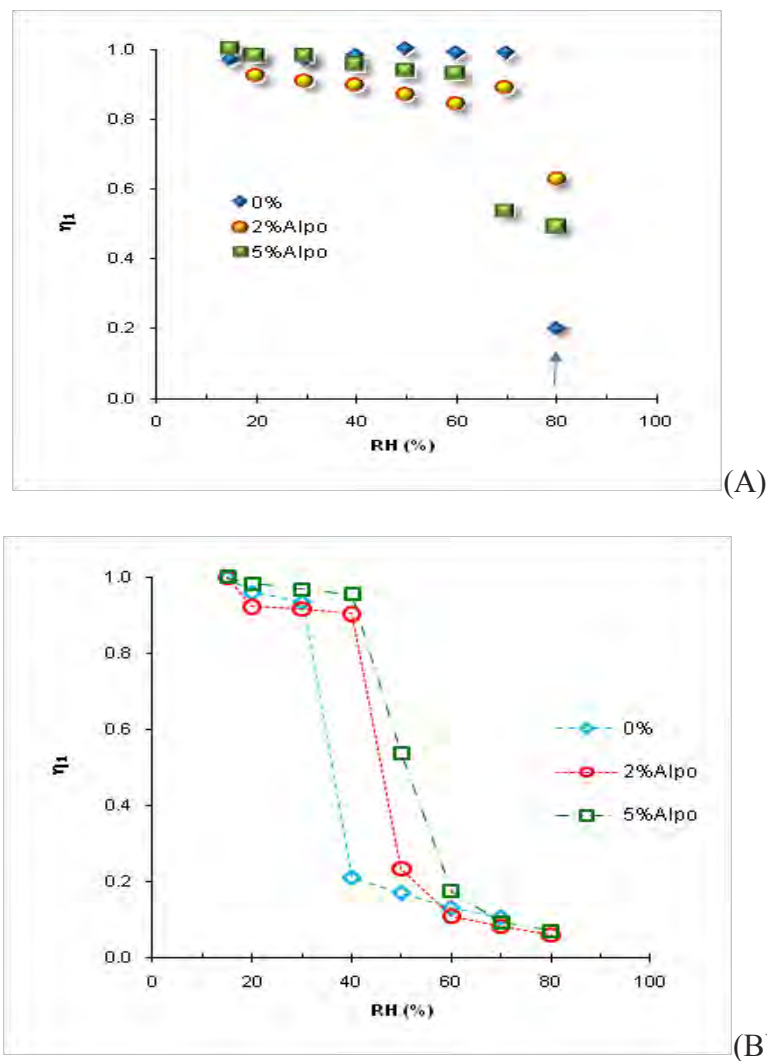
Figure 6.22.   Diffraction efficiency (η_1) response to humidity for undoped (42 µm thickness) and doped with different concentrations of AlPO-18 nanoparticles (58 µm thickness); (A) unbaked; (B) baked at 120°C for 15 minutes.

When exposed to humidity, the water saturated layers (Fig. 6.22A) show no change in diffraction efficiency with the increase of relative humidity (RH) up to 80%RH for the undoped photopolymer and up to 70%RH in the case of AlPO-18 containing photopolymer. After baking (water absorbed in the materials was released), the decrease in diffraction efficiency is noticeable. It starts at 40%RH for undoped material and at 50%RH for AlPO-18, 2%wt. and between 50 and 60%RH for AlPO-18 5%wt. (see Fig. 6.22B). At 5%wt. AlPO-18 more empty volume pore is expected to be available and it takes higher moisture contents to fill this empty pore volume.

By calculating the quantities $\Delta\eta = \eta_{initial} - \eta_{at\ RH\ at\ point\ x}$, we can measure the amount of change in diffraction efficiency when compared to its initial values (see Fig. 6.23). The values of $\Delta\eta$ were normalized to respect to the maximum value observed, in order to give the same initial diffraction efficiency to all gratings.

A)

178
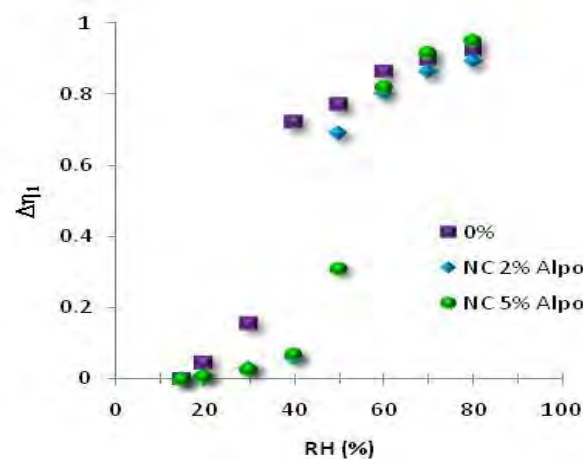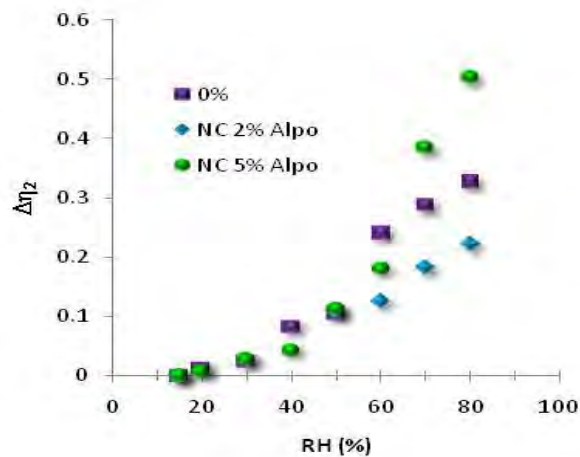
B)

Figure 6.23. Change in diffraction efficiency (Δη) response to humidity for undoped (42μm thickness) and doped with different concentrations of AlPO-18 nanoparticles (58μm thickness): (A) Δη₁ (B) Δη₂.

One could visually observe the formation of a moisture film that decreases the diffraction efficiency in a similar way for both undoped and nanocomposite containing AlPO-18 (Fig. 6.23A). By removing this effect, i.e., excluding the scattered and reflected light, one can see that the gratings recorded in 5%wt. AlPO-18 present a bigger increase in the change of diffraction efficiency for higher RH (RH> 70%) when compared to the gratings recorded in the other materials studied (Fig. 6.23B). It is also seen that a noticeable change of diffraction efficiency appears al lower values of RH for undoped photopolymer (RH of 40%) than for AlPO-18 nanocomposites.

The next step was to investigate the dynamics of the change in diffraction efficiency when the materials were exposed to high humidity. This was done by measuring the time for samples to reach stable diffraction efficiency. The materials were placed in the humidity chamber initially at 15%RH and then exposed to 60%RH (Fig. 6.24). The change in

humidity from 15 to 60%RH occurred within 9 minutes and the change in the diffraction efficiency was noted. The values of $\Delta\eta$ were normalized to respect to the maximum value observed, in order to give the same initial diffraction efficiency to all gratings.
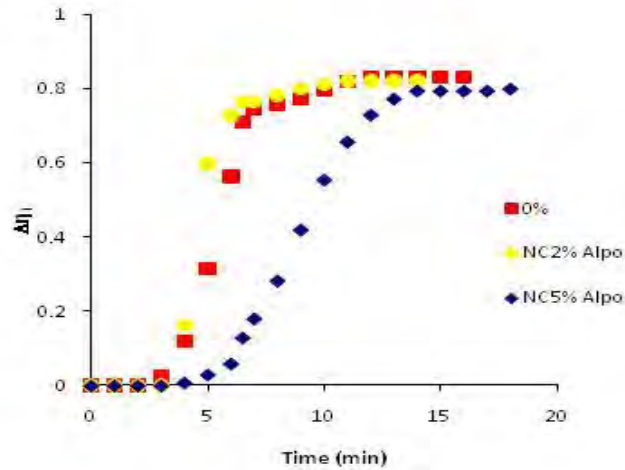
(A)
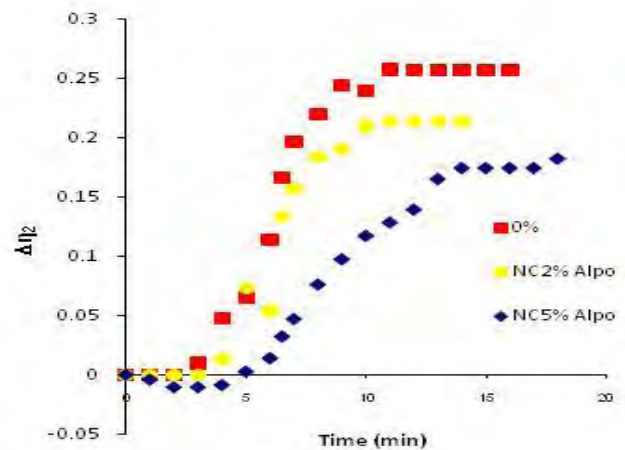
(B)

Figure 6.24.   Dynamics of the change in diffraction efficiency when exposed to high humidity; (A) $\Delta\eta_1$ (B) $\Delta\eta_2$.

It is seen from Fig. 6.24, that the material containing 5%wt. AlPO-18 takes more time to reach stable diffraction efficiency. One possible explanation could be the fact that the materials had different initial diffraction efficiencies. The $\Delta\eta$ values are determined and normalized the diffraction efficiencies to its maximum values, so that we could fairly

compare trends minimizing the influence of parameters such as initial diffraction efficiency, but this factor was also investigated. Therefore, the influence of the initial diffraction efficiencies on the humidity response of photopolymer containing 5%wt. AlPO-18 was compared to that of the undoped photopolymer for two different initial diffraction efficiencies (see Fig. 6.25).
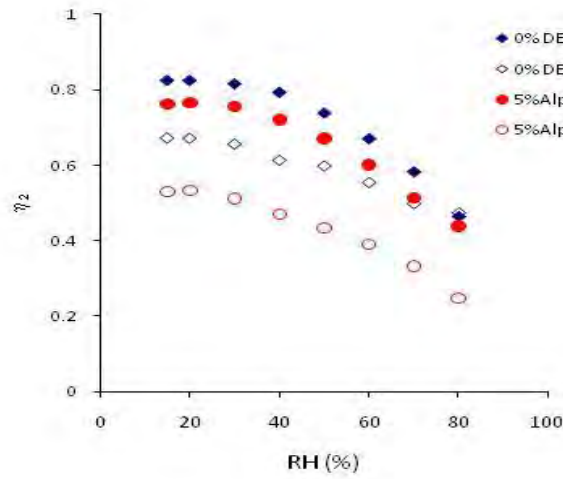
A)
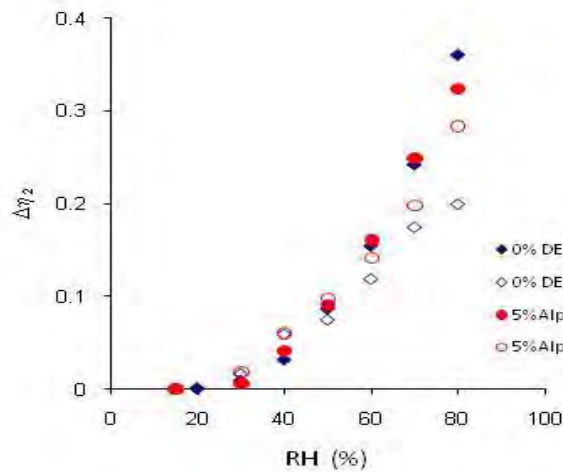
B)

Figure 6.25. Diffraction efficiency response to humidity for undoped gratings and gratings doped with 5%wt. AlPO-18 nanoparticles for two different initial diffraction efficiencies; (A) η_2 (B) $\Delta\eta_2$.

From Fig. 6.25A one can see that the initial diffraction difference between the two undoped gratings is 15% while the two gratings recorded in AlPO-18 5%wt. nanocomposite is 23%. One can conclude that the initial diffraction efficiency has a bigger impact on the change of diffraction efficiency in the case of undoped photopolymer (see Fig. 6.25B). At high RH (80%RH), the difference $\Delta\eta$ between the two gratings was of 16% for gratings recorded in undoped photopolymer and 4% for gratings recorded in the AlPO-18 nanocomposite.

The reversibility was studied for an exposure of an 80%RH (see Fig. 6.26). The gratings were exposed to 80%RH and then brought back to 15%RH and its diffraction efficiency monitored over time.
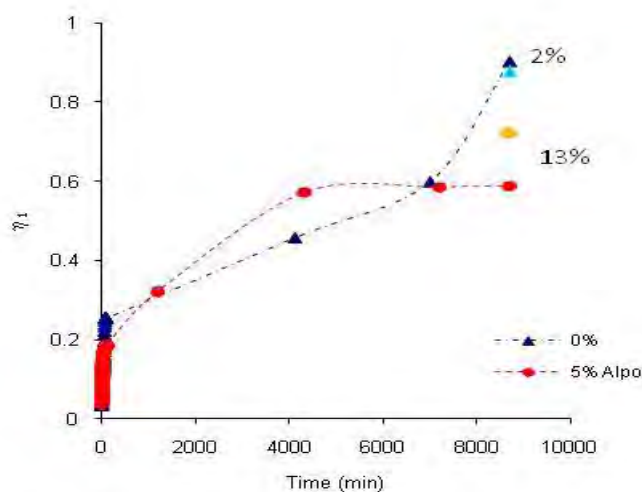
Figure 6.26. Study of the reversibility of the materials when exposed to 80%RH; initial diffraction value: (light blue) undoped photopolymer (orange) AlPO 5%wt. nanocomposite.

The material containing 5 %wt. AlPO-18 shows a degree of irreversibility (13% difference between the final value and initial value of diffraction efficiency) when compared to the undoped photopolymer (2% difference). It is also faster to reach a plateau value of

182

diffraction efficiency. At this very high humidity the materials took several days to reach an equilibrium value of diffraction efficiency, which is not very practical in the design of sensors.

Since not many applications require an exposure to such high humidity, the sensor was checked for changes of diffraction efficiency after exposure to high humidity of 60%RH. The materials were then brought back to low humidity of 15%RH (see Fig. 6.27) and its diffraction efficiency monitored over time.
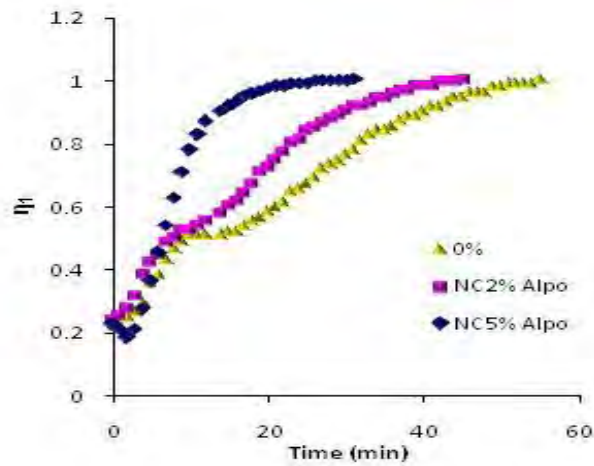
A)
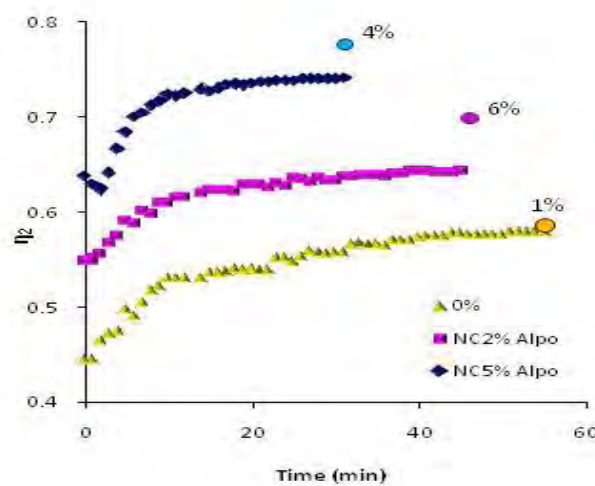
B)

Figure 6.27.   Reversibility of the materials when exposed to 60%RH; (A) η_1 (B) η_2.

The materials containing AlPO-18 nanoparticles recover faster from the high humidity (Fig. 6.27A) and present a degree of irreversibility (Fig. 6.27B), 6% for nanocomposite containing 2%wt. AlPO-18 and 4% for nanocomposite containing 5%wt. AlPO-18. As a reference, the acrylamide based photopolymer showed a difference to the initial value of diffraction efficiency of 1%.

The biggest irreversibility effect was for the nanocomposite containing 2%wt. AlPO-18, which is in good agreement for the maximum redistribution effect observed in the previous section. If one repeats the calculations for the contribution to the refractive index modulation of the redistributed nanoparticles, this time for the empty pores of AlPO-18, one can estimate that the refractive index contribution of the redistributed nanoparticles is 3.9×10^{-4}. Since the initial diffraction efficiency (after baking) of the doped layer was 70%, the corresponding refractive index modulation at the start of the experiment can be estimated. After exposure to high humidity this refractive index modulation will decrease by 2.6×10^{-4} (the difference between the contribution of the redistributed nanoparticles with empty and water filled pores). Thus the final diffraction efficiency of the hologram was estimated to be 63.4%. The measured diffraction efficiency is 64%, which is in very good agreement with the value determined from the theoretical model. Although this is a relatively small irreversible change in the diffraction efficiency of the hologram, it is achieved by adding a modest volume of AlPO-18 nanoparticles (less than 1%).

6.7   CONCLUSIONS

Colloidal solution of AlPO-18 was prepared and stabilized in water suspension. Good compatibility between the photopolymer and the AlPO-18 up to a doping concentration of 5%wt. was shown by DLS, light scattering and surface roughness results.

The grating performances of AlPO-18 nanocomposites were determined as a function of different parameters. The decrease of the refractive index modulation after its maximum value at intensity of 5 mWcm^{-2} occurs only in the undoped photopolymer and the presence of AlPO-18 nanoparticles suppresses this effect. One possible explanation is that the nanoparticles slow down the diffusion and restrict loss of short polymer chains into dark fringe areas thereby maintaining the optimum maximum value of refractive index modulation. Another possible explanation is that a large number of oligomers and/ or short polymer chains would diffuse and sweep the nanoparticles in the desired direction. It was observed that the highest refractive modulation was for gratings recorded at spatial frequency of 2000lmm^{-1}, due to the fact that the distance required to be travelled by the photopolymer components compared to the distances for other spatial frequencies studied.

With the increase of the concentration of nanoparticles there was a decrease of the refractive index modulation of the gratings recorded in AlPO-18 doped photopolymers when compared to the undoped photopolymer. This was observed despite the fact that about 31% redistribution of AlPO-18 nanoparticles effect during the holographic (studied by Raman spectroscopy) recording was achieved.

The decrease of the refractive index modulation could be explained by the fact that many pores of AlPO-18 are filled with water (as shown by the calculation of the pore volume of

AlPO-18 incorporated in photopolymer) and therefore only a small contribution to the overall refractive index modulation has been made by redistributed nanoparticles.

It was also found that the AlPO-18 nanocomposite can be deposited on plastic substrates and low recording intensities can be used to record gratings in this material, which allows versatility in the design of sensors. The fact that the AlPO-18 molecules can be redistributed during holographic recording and that their pores can be filled with water also shows potential for the fabrication of holographic sensors using this type of material.

The humidity response for AlPO-18 nanocomposites was determined for potential development of holographic humidity sensors and a degree of irreversibility was observed with the introduction of AlPO-18 nanoparticles in the acrylamide based photopolymer.

6.8 REFERENCES

[1] S. Wilson, B. Lok and E. Flanigen, US Pat. 4 310 440 (1982)

[2] A. Simmen, L. McCusker, C. Baerlocher and W. Meier, *The Structure Determination and Rietveld Refinement of the Aluminophosphate AlPO$_4$-18*, Zeolites 11, No.7, 654–661 (1991)

[3] L. Tosheva, E.-P. Ng, S. Mintova, M. Holzl, T. Metzger and A. Doyle, *AlPO-18 Seed Layers and Films by Secondary Growth*, Chemistry of Materials 20 , No. 17, 5721-5726 (2008)

[4] H. van Heyden, S. Mintova and T. Bein, *AlPO-18 Nanocrystals Synthesized Under Microwave Irradiation*, Journal of Materials Chemistry 16, No. 5, 514-518 (2006)

[5] J. Rouquerol, D. Avnir, C. Fairbridge, D. Everett, J. Haynes, N. Pernicone, J. Ramsay, K. Sing and K. Unger, *Recommendations for the Characterization of Porous Solids (Technical Report)*, Pure and Applied Chemistry 66, No. 8, 1739-1758 (1994)

[6] T. Babeva, R. Todorov, S. Mintova, T. Yovcheva, I. Naydenova and V. Toal, *Optical Properties of Silica MFI Doped Acrylamide-Based Photopolymer,* Journal of Optics A: Pure and Applied Optics 11, No. 2, 024015 (2009)

[7] L. Goldenberg, O. Sakhno, T. Smirnova, P. Helliwell, V. Chechik and J. Stumpe, *Holographic Composites with Gold Nanoparticles: Nanoparticles Promote Polymer Segregation,* Chemistry of Materials, 20, No. 14, 4619–4627 (2008)

[8] O. Sakhno, T. Smirnova, L. Goldenberg and J. Stumpe, *Holographic Patterning of Luminescent Photopolymer Nanocomposites*, Materials Science and Engineering: C 28, No. 1, 28–35 (2008)

[9] R. Vaia, C. Dennis, L. Natarajan, V. Tondiglia and T. Bunning, *One-Step, Micrometer-Scale Organization of Nano- and Mesoparticles Using Holographic Photopolymerization: A Generic Technique,* Advanced Materials 13, No. 20, 1570-1574 (2001)

[10] I. Naydenova, R. Jallapuram, V. Toal and S. Martin, *A Visual Indication of Environmental Humidity Using a Colour Changing Hologram Recorded in a Self-Developing Photopolymer*, Applied Physics Letters 92, No. 3, 031109 (2008)

[11] I. Naydenova, J. Raghavendra, V.Toal and S. Martin, *Characterisation of the Humidity and Temperature Responses of a Reflection Hologram Recorded in Acrylamide-Based Photopolymer*, Sensors and Actuators B: Chemical, Vol. 139, No. 1, 35-38 (2009)

CHAPTER 7: SILICALITE-1 (MFI-TYPE STRUCTURE) DOPED NANOCOMPOSITES

7.1 INTRODUCTION

In this chapter, information regarding the characterization of silicalite-1 (MFI-type framework) colloidal solutions is provided. Silicalite-1 is a pure siliceous MFI-type material with two sets of perpendicular, intersecting channels, one defined by 10-membered rings and the other by 8-membered rings. Silicalite-1 doped photopolymerizable nanocomposites were prepared and the compatibility between the zeolite and the photopolymer was verified by DLS and measurements of the nanocomposite surface roughness.

The grating performances of gratings recorded in silicalite-1 nanocomposites as a function of recording intensity and zeolite concentration were studied. It was found that an improvement of refractive index modulation occurs with the increasing the amount of silicalite-1 nanoparticles to the photopolymer for recording intensities of $5mWcm^{-2}$ and higher. Refractive index determinations before and after incorporation in the photopolymer showed that the pores of this zeolite remain empty. This could be explained by the fact that being a pure silica material exhibits hydrophobic properties, unlike the previous studied nanocomposites, containing Beta and AlPO-18 particles.

7.2 SILICALITE-1 NANOPARTICLES CHARACTERIZATION

The MFI-type framework structure of silicalite-1 is shown in Figure 7.1.

A)   B)
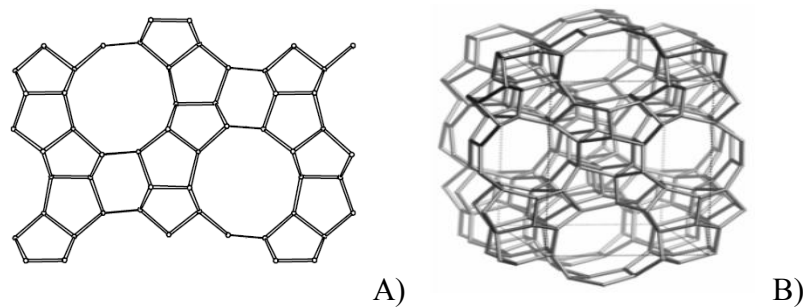
Figure 7.1.   Periodic building unit of the silicalite-1 zeolite: (A) unit cell; (B) the pore structure.

The DLS results showed particle sizes of around 30nm (Fig. 7.2)
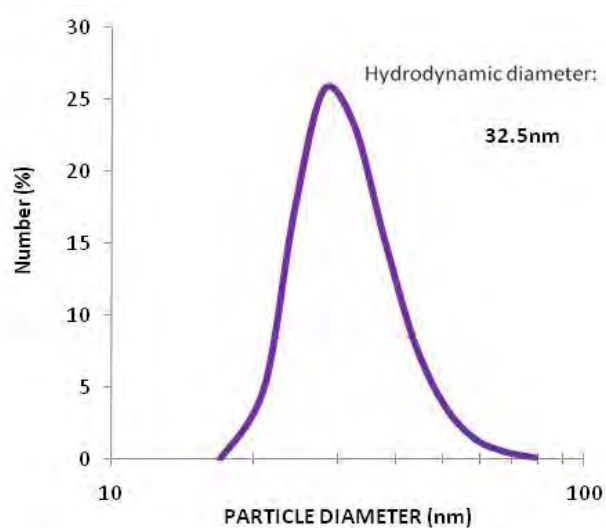
Figure 7.2.   DLS curve of silicalite-1 suspension.

The zeolite colloidal dispersion is characterized by a monomodal particle distribution.

The crystalline nature was determined by XRD (Fig. 7.3).
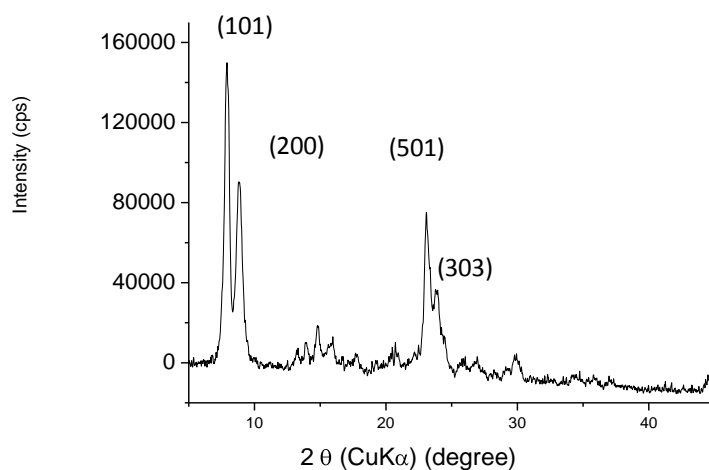
Figure 7.3. **X-ray diffraction pattern of silicalite-1.**

The XRD pattern in Fig. 7.3 showed the peaks characteristic of crystalline silicalite-1 [1].

The zeolitic porosity is demonstrated by the nitrogen sorption isotherm shown in Fig. 7.4.
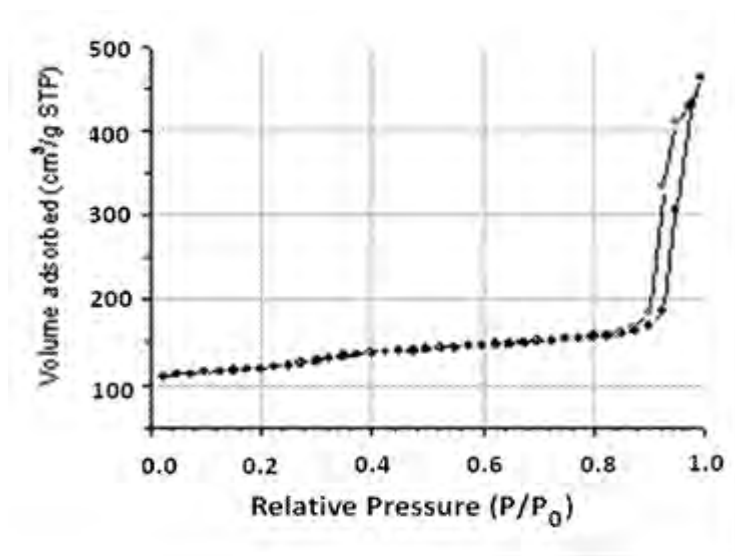
Figure 7.4. **N_2-sorption isotherm of silicalite-1 nanoparticles.**

The nitrogen adsorption-desorption curves show the typical type IV isotherm in accordance with IUPAC classification [2]. The rise of sorption at $P/P_0 <0.05$ corresponds to the filling of the micropores belonging to the zeolitic structures. The small increase of amount adsorbed at relative pressure $P/P_0 = 0.3$-0.4 indicates the presence of mesopores. The hysteresis loop at $P/P_0 > 0.6$ is related to the capillary condensation in the inter-particle voids [3]. The micropore volume was of 0.17 cm^3g^{-1} (P/P_0=0.05 and the apparent BET specific surface area was 390 m^2g^{-1}. According to literature these are typical values [4].

The zeolite morphology was characterized using SEM (Fig. 7.5).
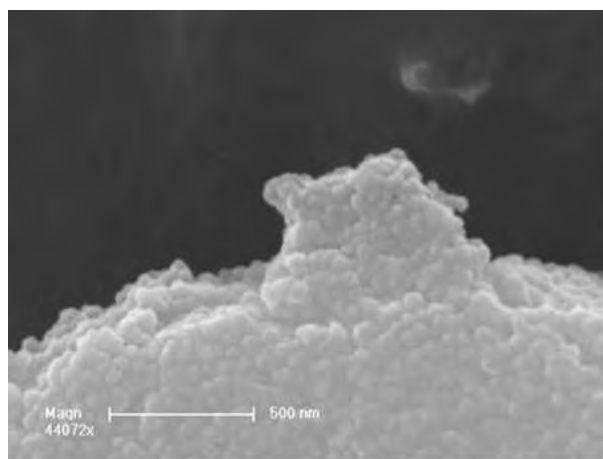
Figure 7.5.   Morphology of silicalite-1 nanoparticles.

From Fig. 7.5 we can see the silicalite-1 nanoparticles have a spherical shape and they tend to agglomerate during drying [3].

The Raman spectrum of silicalite-1 nanoparticles is shown in Fig. 7.6. The Raman bands to be considered (when compared with the template tetrapropylammonium – TPA) are: red-shift of the C-H stretching mode from 2954 to 2937 cm^{-1} and splitting and change in the relative intensities of the CH_2 modes in the range 1130-1370 cm^{-1}[4].
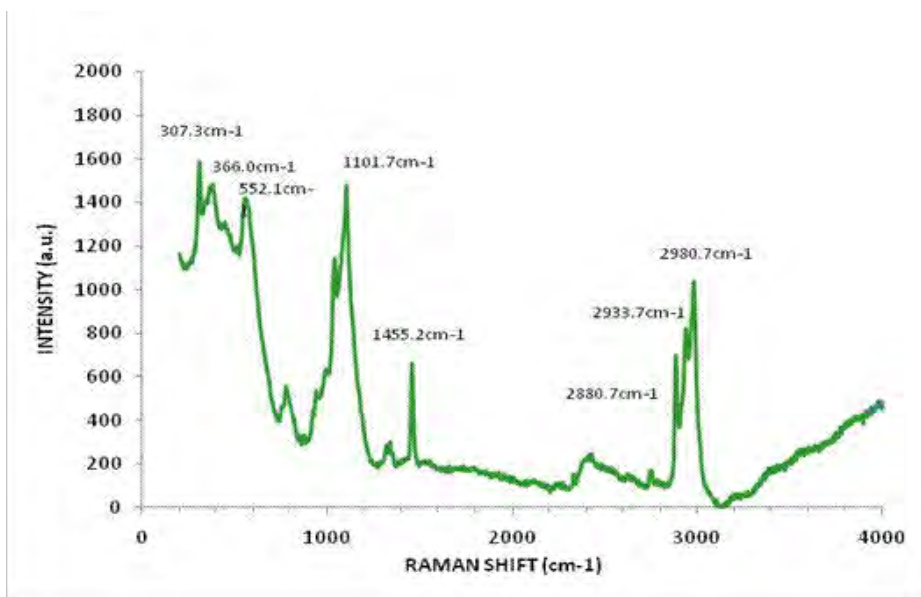
Figure 7.6.   **Raman spectrum of silicalite-1 nanoparticles.**

The prominent band in the Raman spectrum of e silicalite-1 in the fingerprint region (300-600 cm^{-1}) is found at 366 cm^{-1}. This band is assigned to the motion of an oxygen atom in a plane perpendicular to the T-O-T bonds.

Other prominent bonds observed were also assigned (see Table. 7.1). The split bands typical of MFI structure can be seen in the spectrum (between the 1101.7 and the 1455.2 cm^{-1} peaks), but were not assigned due to their low intensity.

Table 7.1.   Raman peak assignments of silicalite-1.

Raman Peak (cm^{-1})	Functional Group/ Vibration
307.3	T-O-T stretching of zeolite
366.0	T-O-T stretching of zeolite
552.1	C-C-C-N (template)
1101.7	Stretching of Si-O (zeolite)
1455.2	Deformation of CH (template)
2880.7	Stretching of CH$_2$ (template)
2933.71	Symmetric Stretching of CH$_3$ (template)
2980.7	Asymmetric Stretching of CH$_3$ (template)

7.3   SILICALITE-1 NANOCOMPOSITES OPTICAL PROPERTIES

The compatibility of the zeolite particles suspensions with the photopolymer solutions was first characterized by DLS (Figure 7.7).
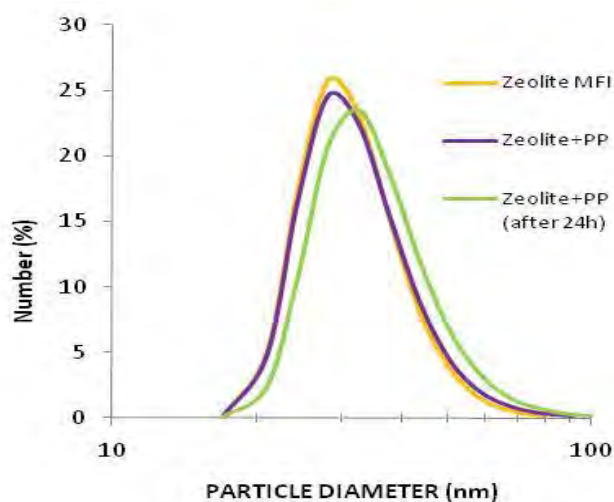
Figure 7.7.   DLS (number weighted) of: (orange) silicalite-1; (purple) photopolymer doped with silicalite-1 nanoparticles (freshly mixed); (green) photopolymer doped with silicalite-1 nanoparticles (24 hours stored at RT).

193

After 24 hours a shift in the peak maximum was observed. One possible explanation could be due to the hydrophobic nature of silicalite-1 zeolite, causing a small shell around the particle and thus increasing the hydrodynamic diameter of the nanoparticles.

The optical losses (calculated as described before by Eq. 4.1) (thickness of layers of around 40 µm)were obtained as a function of concentration of silicalite-1 nanoparticles (see Figure 7.8).
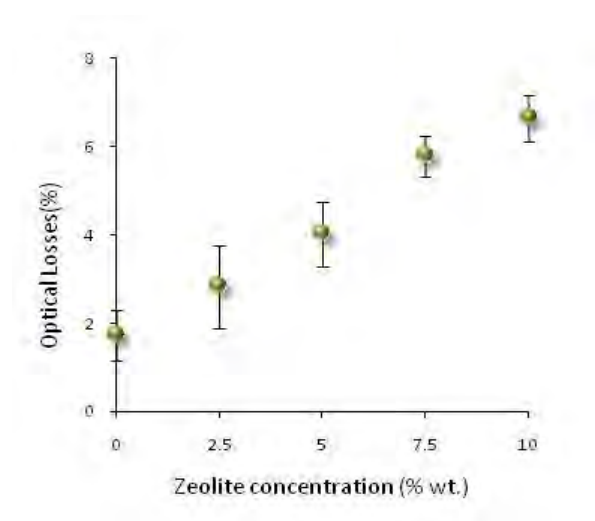
Figure 7.8.   Optical losses of silicalite-1 nanocomposites.

As can be seen in Fig.7.8, the optical losses increase linearly from 2% (undoped photopolymer) to 7% when we introduce silicalite-1 10%wt. nanoparticles. This maximum value of 7% is lower than the values observed for zeolite A (40% optical losses for a doping of 10%wt.) and comparable with zeolite Beta nanocomposites (10% optical losses for the same level of doping).

The surface morphology of several nanocomposites containing from 0 to 10%wt. of silicalite-1 zeolites were studied using a white light interferometric (WLI) surface profiler. In a recent publication [3] it was shown that silicalite-1 nanoparticles are distributed

randomly on the surface and that there is a correlation between the doping level and height and density of particles on the surface. The increase of zeolite concentration in the layers leads to increase of peak heights and a decrease of the distance between them. As described before, the surface roughness was quantified in five different locations across the sample and the results are summarized in Fig. 7.9 and Table 7.2. This method was used in the present work as a measure of how compatible the nanoparticles can be with the photopolymer, since if they are, for instance expelled to the surface of the photopolymer, the roughness will increase.

Table 7.2.   Surface   roughness   measurements   (RMS)   for   silicalite-1 nanocomposites.

Concentration of silicalite-1 (%)	Surface roughness (nm)	
0	1.2	± 0.1
1	1.3	± 0.3
2.5	1.9	± 0.3
5	2.5	± 0.4
7.5	2.8	± 0.3
10	2.1	± 0.3
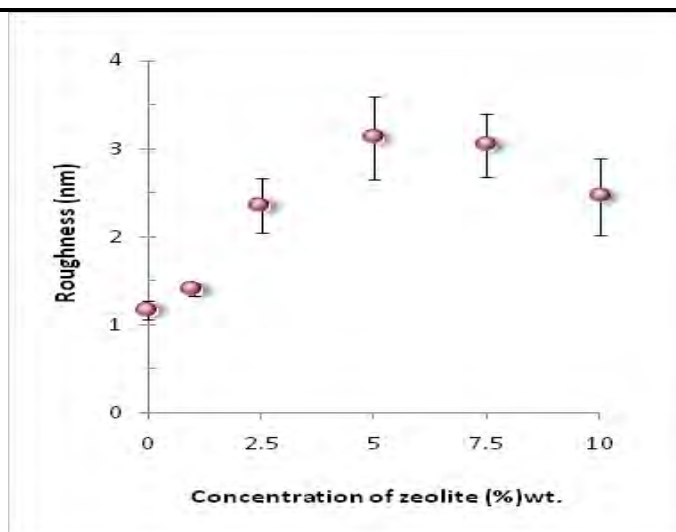
Figure 7.9.   Surface roughness dependence on concentration of silicalite-1.

The undoped photopolymer had a surface roughness of 1nm that increased to 3nm in there case of 5%wt. nanocomposite. There was a decrease at 10%wt. concentration of zeolite silicalite-1 (2 nm). The literature [3] refers to an increase of roughness from 1nm to 7 nm for a concentration of silicalite-1 of 7%wt. The roughness values for silicalite-1 nanocomposites are lower than the ones obtained for the previously studied nanocomposites, whose size was of 60nm.

Finally the refractive index of the nanocomposites was determined as this parameter is useful in the calculations of the next section. This was done by Dr. T. Babeva.

Table 7.3.   Volume refractive index of silicalite-1 nanocomposites (633 nm).

Silicalite-1 concentration (%wt.)	Refractive Index
0	1.499 ± 0.005
1	1.494 ± 0.005
3	1.483 ± 0.005
7	1.447 ± 0.005

If one considers silicalite-1 as an effective medium consisting of two phases – air and amorphous silica one can calculate the volume fraction of the two phases using the Bruggeman effective media approximation described in detail in [3]. The density of zeolite MFI (empty pores) was calculated as 1.74 gcm^3, while the density of zeolite incorporated in the photopolymer (filled pores) was 1.78 gcm^{-3}. On the other hand the pore volume in zeolites is estimated to be 0.11 cm^3g^{-1}. In that same study, the pore volume was found to be 0.12 cm^3g^{-1}, while our determinations suggest a value of 0.17 cm^3g^{-1} (see Fig. 7.4). This difference is probably due to differences in crystallinity in the materials.

The comparison between pore volume of the zeolite before and after addition to the photopolymer suggests that most probably silicalite-1 pores remain empty after the zeolite is added to photopolymer, due probably to their hydrophobic nature.

By DLS and surface roughness measurements one could demonstrate that the silicalite-1 zeolite nanoparticles are compatible with the photopolymer, thus homogeneous coating suspensions can be obtained and homogeneous dry layers of optically transparent material can be prepared.

7.4 GRATING PERFORMANCES OF SILICALITE-1 NANOCOMPOSITES

The grating performances recorded in silicalite-1 nanocomposites dependence on recording intensity and concentration of zeolite were studied. Four different recording intensities were used: 1.75, 5, 10 and 16.7 mWcm^{-2}, for a time of exposure of 100 s.

Three gratings were recorded for each of these recording intensities (Nr. 1, 2 and 3) and for each of the concentration of silicalite-1 added to the photopolymer, from 0% to 10%wt. (see fig. 7.10). The results are shown in Fig. 7.11.
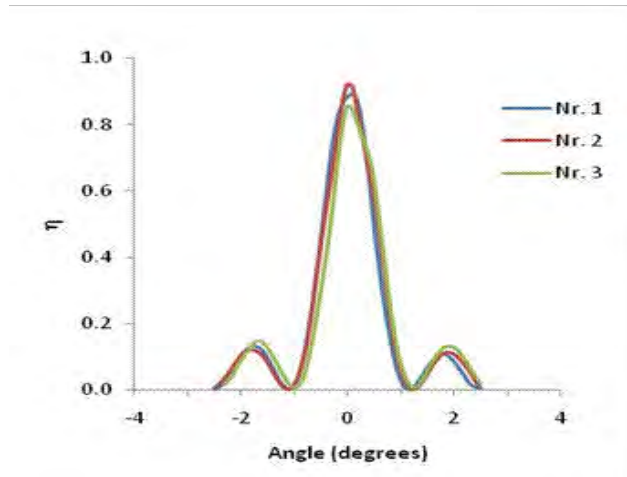
Figure 7.10. Typical angular selectivity curves for three different gratings recorded in 5%wt. silicalite-1 nanocomposite; recording intensity of 5 mWcm^{-2} and spatial frequency of 1000 lmm^{-1}.
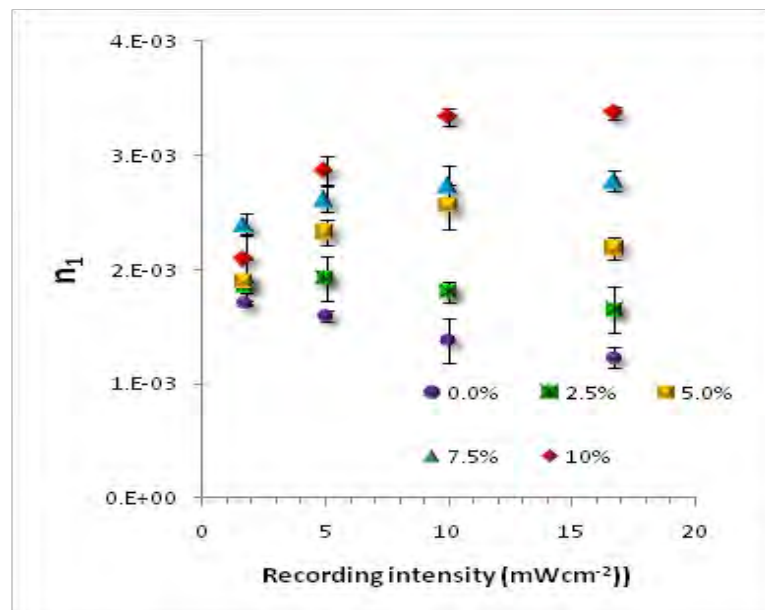
Figure 7.11. Refractive index modulation as a function of recording intensity for gratings recorded in silicalite-1 nanocomposites (with concentrations as indicated in the figure); (1000 lmm^{-1}).

The first conclusion is that silicalite-1nanoparticles improve the refractive index modulation (n_1) for all the recording intensities. The refractive index modulation increases with the concentration of zeolite. This was previously observed in preliminary results obtained in [6]. In this study the addition of 60 nm silicalite-1 nanoparticles to the photopolymer doubled the refractive index modulation from $1.8x10^{-3}$ (undoped photopolymer) to $3.5x10^{-3}$ (nanocomposite containing 6%wt. concentration of nanoparticles). Except for the lowest intensity (1.75 mWcm^{-2}), where an optimum concentration of zeolite was observed (7.5%wt. of zeolite) the refractive index modulation increases linearly with the zeolite concentration for all the other recording intensities. Calculating an average refractive index modulation for each concentration, we found a similar result to that previously reported for 60nm nanoparticles: the refractive index modulation doubled from $1.5x10^{-3}$ (undoped photopolymer) to $3.2x10^{-3}$ (nanocomposite containing 10 %wt. concentration of nanoparticles). For undoped photopolymer, the refractive index modulation decreases as the recording intensity increases. This is expected for material behavior under high intensity exposure. High intensity produces high termination rates and therefore short chains, and lower diffraction efficiency is obtained for the same exposure. This is also the case for a nanocomposite containing 2.5%wt. of silicalite-1. For higher concentrations of zeolite, we observe an improvement of the refractive index modulation with increasing recording intensity up to 10 mWcm^{-2}. One explanation for the observed improvement of the diffraction efficiency of the nanoparticle-containing photopolymers at high intensity of recording could be that at higher intensity the number of shorter polymer chains is expected to be higher and consequently a larger number of oligomers and/or short polymer chains would diffuse and sweep the nanoparticles in the desired direction. Another possible explanation could be that the

presence of porous silica nanoparticles slows down diffusion and restricts loss of short polymer chains into dark fringe areas thereby improving the diffraction efficiency

Unlike Beta and AlPO-18 which have a hydrophilic nature, the silicalite-1 zeolite is made of pure silica and thus has a hydrophobic nature. We have seen in section 7.3 that calculations of pore volume of the zeolite before and after incorporation in the photopolymer showed that the zeolites are empty. Also, it was also observed that silicalite-1 nanoparticles are able to undergo redistribution, being expelled from the bright fringes [7]. The fact that the nanoparticles were redistributed during holographic recording and that in the case of this nanocomposite, the difference in refractive index is higher due to the void pores of the zeolite results in a refractive index modulation increase observed, in contrast to the nanodopants studied previously.

7.5 CONCLUSIONS

A good optical quality material is prepared in the case of the acrylamide-based photopolymer doped with silicalite-1 nanoparticles. The grating performances recorded in silicalite-1 nanocomposites were studied and it was found that there is an improvement of the refractive index modulation with the addition of silicalite-1 nanoparticles for the four recording intensities studied. It was found that on average the refractive index modulation doubled from 1.5×10^{-3} (undoped photopolymer) to 3.2×10^{-3} (nanocomposite containing 10%wt. concentration of nanoparticles). The addition of silicalite-1 in concentrations higher than 5%wt. to the photopolymer also inverted the effect of decreased refractive index modulation at high intensities. The hydrophobic nature of this type of zeolite is probably the reason why zeolite pores are probably empty after its inclusion in the

photopolymer (as shown here by refractive index calculations) and this material could be further improved for use in the fabrication of holographic memories.

7.6 REFERENCES

[1] M Naskar, D. Kundu and M. Chatterjee, *Silicalite-1 zeolite Membranes on Unmodified and Modified Surfaces of Ceramic Supports: A Comparative Study*, Bulletin of Material Science 32, No. 5, 537–541 (2009)

[2] J. Rouquerol, D. Avnir, C. Fairbridge, D. Everett, J. Haynes, N. Pernicone, J. Ramsay, K. W. Sing and K. Unger, *Recommendations for the Characterization of Porous Solids (Technical Report)*, Pure and Applied Chemistry 66, No. 8, 1739-1758 (1994)

[3] T. Babeva, R. Todorov, S. Mintova, T. Yovcheva, I. Naydenova and V. Toal, *Optical Properties of Silica MFI Doped Acrylamide-Based Photopolymer,* Journal of Optics A: Pure and Applied Optics 11, No. 2, 024015 (2009)

[4] P. Prokesova-Fojtıkova, S. Mintova, J. Cejka, N. Zilkova and A. Zukal, *Porosity of Micro /Mesoporous Composite,* Microporous and Mesoporous Materials 92, No. 1-3, 154-160 (2006)

[5] B. Mihailova, S. Mintova, K. Karaghiosoff, T. Metzger and T. Bein, *Nondestructive Identification of Colloidal Molecular Sieves Stabilized in Water*, Journal of Physical Chemistry B 109, No. 36, 17060 (2005)

[6] I. Naydenova, H. Sherif, S. Mintova, S. Martin, and V. Toal, *Holographic Recording in Nanoparticle-Doped Photopolymer*, Proc. SPIE 6252, 625206 (2006)

[7] A. Ostrowski, I. Naydenova and V. Toal, *Light-Induced Redistribution of Si-MFI Zeolite Nanoparticles in Acrylamide-Based Photopolymer Holographic Gratings,* Journal of Optics A: Pure and Applied Optics 11, No. 3, 034004-034007 (2009)

CHAPTER 8: INITIAL STUDIES OF INTERACTIONS BETWEEN SENSITIZING DYES AND ZEOLITE L

8.1 INTRODUCTION

In this chapter, the characterization of zeolite L (LTL-type structure) is presented. The interactions between several dye molecules (rose bengal, erythrosine B, rhodamine B, rodhamine 6G, acroflavin, safranin O and methylene blue) and the different zeolite molecules used in this project (zeolite Beta, zeolite A, AlPO-18, silicalite-1 and zeolite L) were studied. Particularly interesting were the effects of interactions between the cationic dye methylene blue and zeolite L, observed by visible spectroscopy. Because of the spectroscopic changes observed when the dye molecules and their aggregates are adsorbed in the zeolite L surface, one can expect to use them in optical materials for holographic recording, with tunable spectral sensitivity controlled by dye concentrations. The effect of pH on the spectroscopic changes of MB+ - zeolite L dispersion is discussed as well.

8.2 ZEOLITE L NANOPARTICLES CHARACTERIZATION

Nano-sized zeolite L crystals have LTL framework type structure and this is presented in Fig. 8.1.

A)   B)   C)
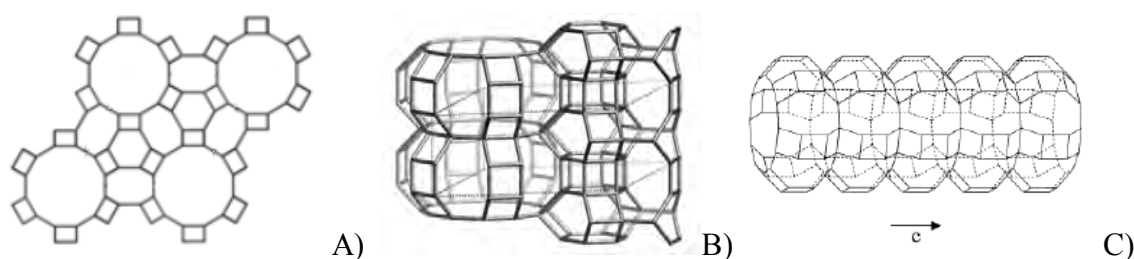
Figure 8.1.   Periodic building unit of zeolite L: (A) top view perpendicular to the c-axis; (B) pore structure of zeolite L (view normal to 001); (C) view along the c-axis.

Zeolite L crystals consist of cancrinite cages linked by double six-membered rings, thereby forming columns in the c-direction. Connection of these columns gives rise to 12-membered rings with a free diameter of 7.1Å. As a consequence, zeolite L possesses one-dimensional channels running parallel to the c-direction through the entire crystal. The free diameter varies from 7.1 Å (narrowest part) to 12.6 Å (widest part). The main channels are linked via non-planar eight-membered rings forming an additional two dimensional channel system with openings of about 1.5 Å [1].

The dynamic light scattering (DLS) results showed that the particle size of Zeolite L was 65nm (Fig. 8.2).
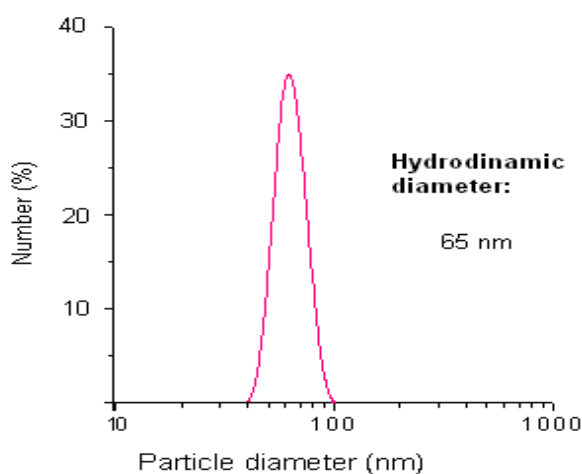
Figure 8.2.   DLS curve of zeolite L suspension.

The zeolite colloidal dispersion shows a monomodal particle size distribution.

The crystalline nature of the nanoporous zeolite L nanoparticles was investigated by the XRD (Figure 8.3).
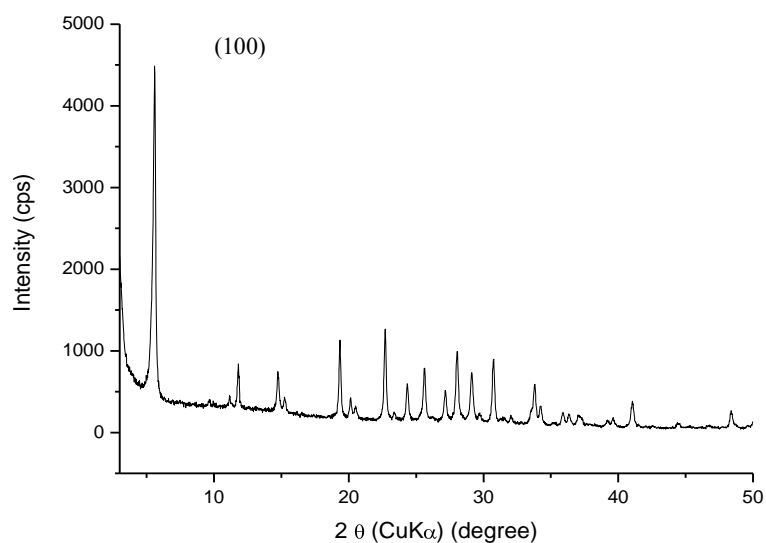
Figure 8.3. **X-ray diffraction pattern of zeolite L nanoparticles.**

The XRD pattern showed fully crystalline zeolite L-type material and the absence of an amorphous phase and the most intense (100) reflection peak appears at 5.54° 2 θ [2].

The nitrogen sorption isotherm of zeolite L is shown in Fig. 8.4.
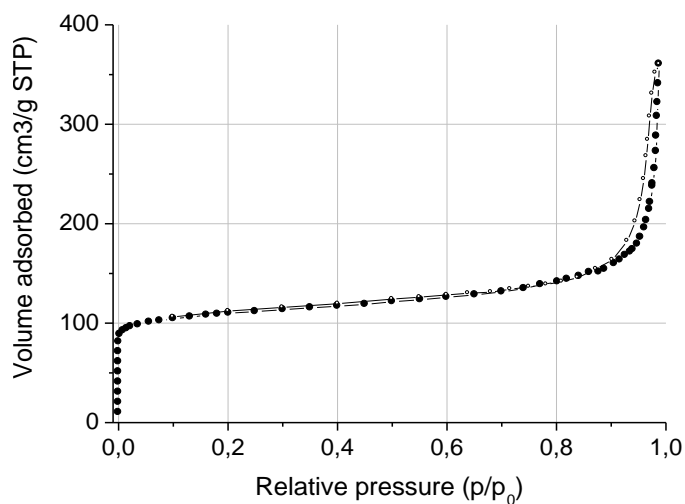
Figure 8.4. **N₂-sorption isotherm of zeolite L nanoparticles.**

The nitrogen adsorption-desorption curves possess the typical type IV isotherm [3]. The material has BET high surface area of 349 m^2g^{-1} which is in good agreement with literature [4] values for specific pore volume of 0.205 cm^3g^{-1} as synthesized and 0.163cm^3g^{-1}, lower values than the ones obtained in the present work, where the total specific pore volume was 0.48 cm^3g^{-1} (P/P$_0$=0.98) and this means that there is more accessible pore volume (free space) available for species to enter the zeolite.

The Raman spectrum of the nanoparticles is shown in Fig. 8.5.
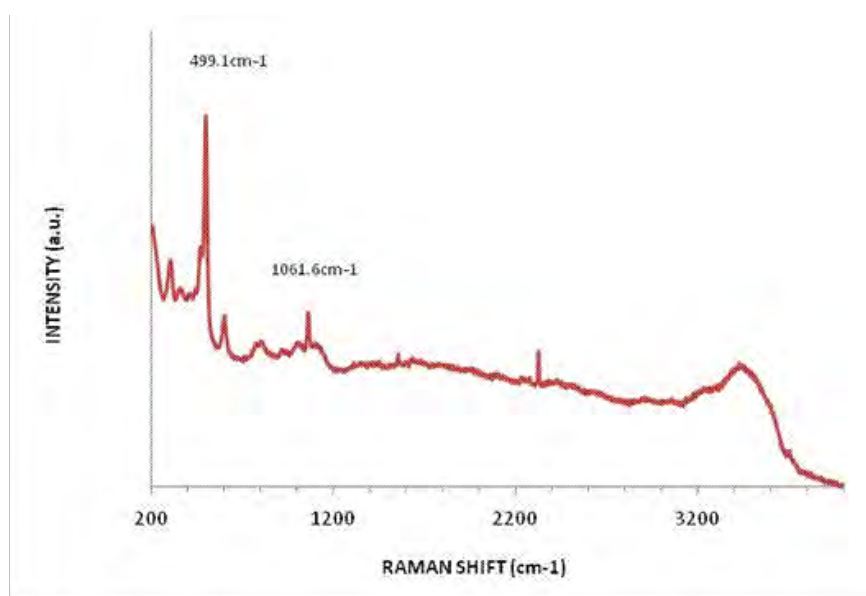
Figure 8.5.   Raman spectrum of zeolite L nanoparticles.

The prominent band in the Raman spectrum of framework type materials are in the fingerprint region (300-600cm^{-1}) and for zeolite L is at 499cm^{-1}. This band is assigned to the motion of an oxygen atom in a plane perpendicular to the T-O-T bonds (framework vibration) and is the only strong feature.

8.3   GUEST- HOST SYSTEMS BASED ON ZEOLITES

The channels and cavities of a zeolite framework provide ideal space for incorporation, stabilization and organization of complex species of organic, luminescent dyes, metal clusters or semiconductor materials [5]. Host-guest systems based on zeolite crystals have been under investigation and used in applications such as artificial antenna systems [6], microlasers [7] and optical sensors [8]. Materials such as AlPO-5 [9], zeolite L [10], zeolites Y, ZSM-5 and mesoporous material MCM-41 [11] have been used as hosts for the incorporation of neutral as well as cationic dyes inside their channels.

Interestingly, it has been reported that AlPO-5 modified with methylene blue favors optical data storage through the effect of hole burning [9].

The types of molecules that fit inside the channels are [10]:

(1) Molecules that are small enough to fit inside a unit cell;

(2) Molecules the size of which makes it hard to guess their position and orientation in the channel;

(3) Molecules that are so large that they can only align along the c-axis.

Dyes can be inserted into the cavities of zeolites from gas phase, by ion exchange (if cations are involved), by crystallization inclusion or by an in situ synthesis inside the zeolite cages [6].
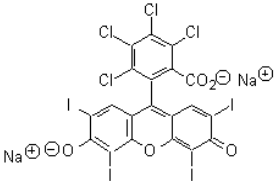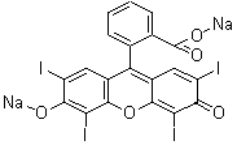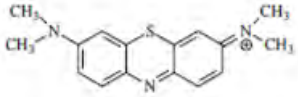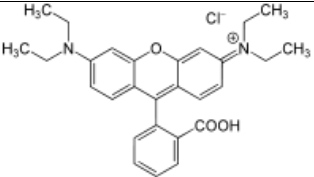
On the other hand all cationic and neutral dyes have the tendency to be adsorbed at the outer surface of the zeolite nanocrystals. Cationic dyes form aggregates at the surface of the zeolite as can be observed by UV-Vis spectroscopy [6].
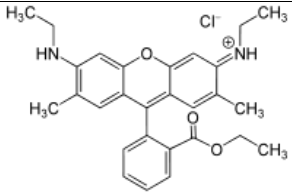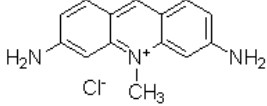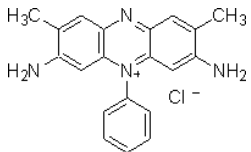
In the case of zeolite L, the efficient transport of electronic excitation energy by the chains of electronically non-interacting chromophores is the most prominent feature of this material [1].

8.4 INTERACTIONS BETWEEN DYES AND ZEOLITES

Several sensitizing dyes commonly used in holographic recording (except for rhodamine dyes that were chosen for their size and cationic nature) are listed in table 8.3.

Table 8.1.   Dyes used in the present study (dye concentrations is 0.11%wt.).

Name	Formula	
Anionic dyes		
Rose Bengal		
Erythrosine B		
Cationic dyes		
Methylene Blue		
Rhodamine B		

Name	Formula	
Rhodamine 6G		
Acriflavine		
Safranin O		

Sensitizing dyes usually used in full color holography (methylene blue for recording in the red, erythrosine B for recording in the green and acroflavine for recording in the blue) were first investigated. Visible absorption spectra of aqueous solutions (3 mgl^{-1}) are presented in Fig. 8.6.
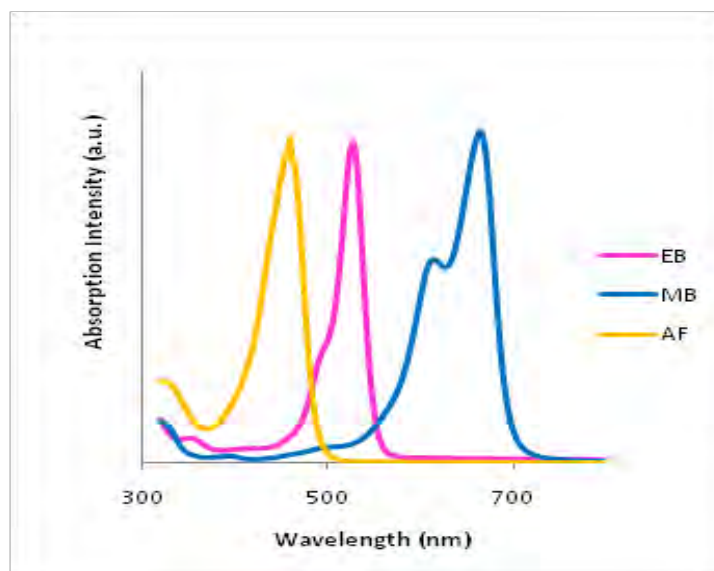
Figure 8.6.   Visible spectra of aqueous dyes: (EB) erythrosine B; (MB) methylene Blue; (AF) acriflavine.

Then 0.5 mg of different zeolites studied in this work - zeolite A, L, Beta, silicalite-1 and AlPO-18 were added to each vial and the visible spectra were measured. Results are shown for two different solvents: water and photopolymer solution (see Fig. 8.7).
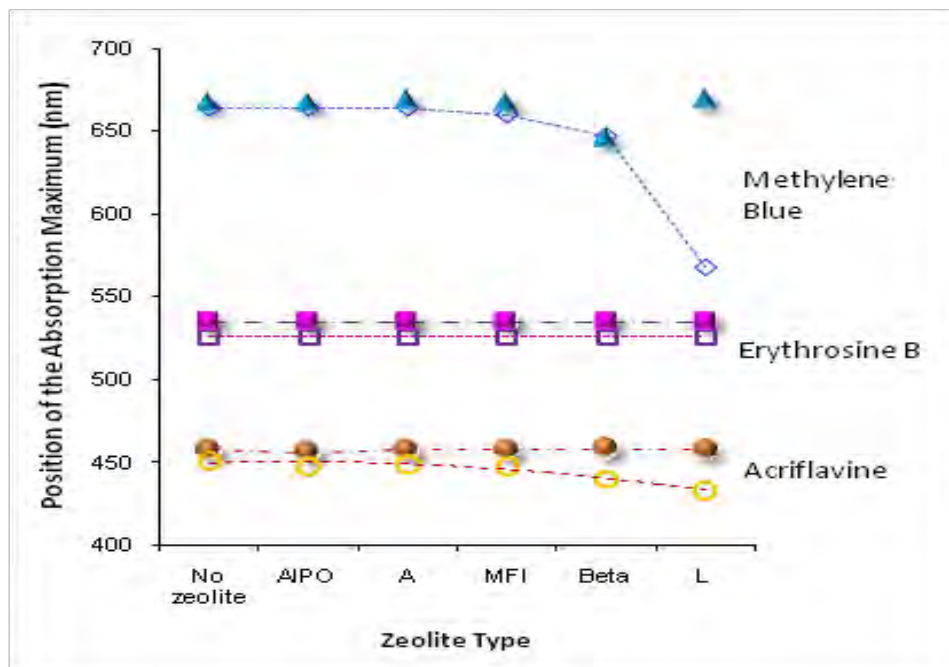
Figure 8.7. **Peak position of the maximum intensity absorption in the presence of several zeolites: water (empty symbols) and photopolymer (filled symbols).**

From Fig. 8.7 one can see that the shift of the maximum absorption peak position normally happens only in aqueous solutions. Only in the case of methylene blue in the presence of zeolite L and photopolymer solution does a noticeable shift in the absorption maximum occur. The large size anionic dye, erythrosine, did not show a spectral change in the presence of any zeolites. Both the other dyes (methylene blue and acriflavine) of smaller size and cationic type showed a change in shape of the spectral peak as well a blue shift of its maximum absorption peak. Interestingly, the bigger the zeolite pore size, the greater this shift, although one can suspect that due to their nature these dyes are adsorbed at the external surface of the zeolites.

The greater change in the maximum absorption peak was found for the pair MB^+ - zeolite L, where one can immediately observe a purple color when we add the zeolite to the aqueous solution of MB (Fig. 8.8), most probably due to the formation of aggregates at the outer surface of the zeolite.
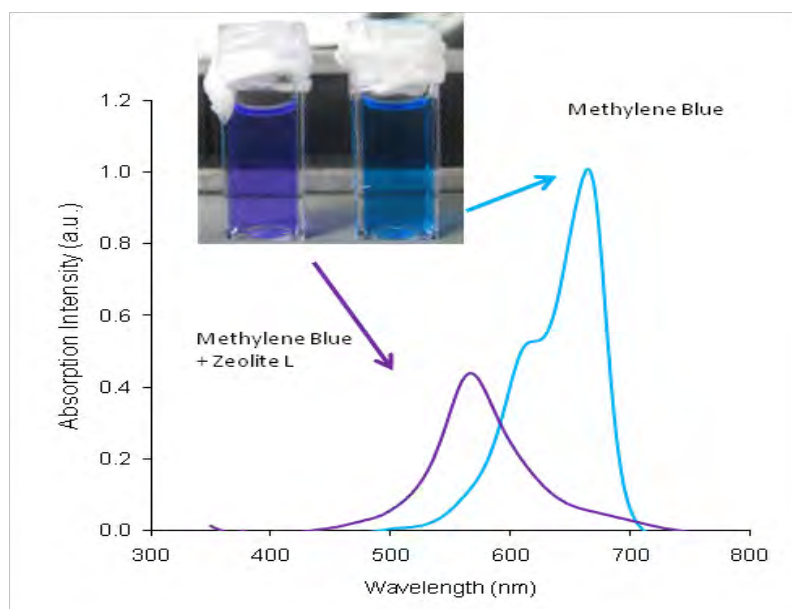
Figure 8.8.   Visible absorption spectra of methylene blue in water and in presence of zeolite L.

Solutions with different concentrations of methylene blue were analyzed. The effect of different zeolite concentrations was also studied (see Fig. 8.9).
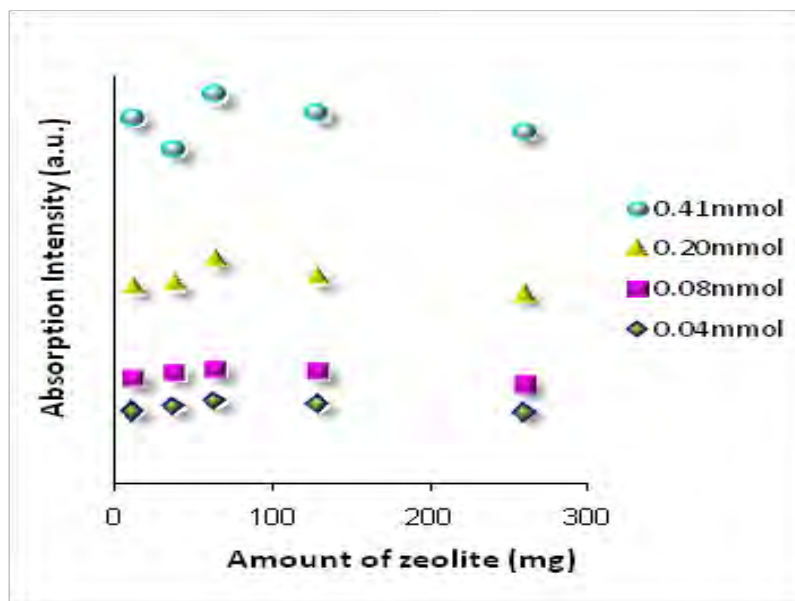
Figure 8.9. Influence of the concentration of zeolite L on the absorption intensity of the maximum absorption peak for several concentrations of methylene blue (0.05, 0.08, 0.20 and 0.41 mmol); maximum absorption intensity peak position was found at 566 ± 1 nm.

From Figure 8.9 one can see that for the concentrations of methylene blue of 0.04, 0.08 and 0.20 mmol there is initially a linear increase of the absorption maximum as the zeolite concentration increases and then the values remain fairly constant. For higher concentration of methylene blue (0.41 mmol) the zeolite concentration seems to have little no effect on the maximum absorption intensity peak position.

Following these results, several other dyes were studied, this time only in the presence of zeolite L and different solvents (Fig. 8.10) of interest, namely water, acrylamide based photopolymer, NIPA based photopolymer (described in more detail in the next section) and PVA (polyvinyl alcohol).
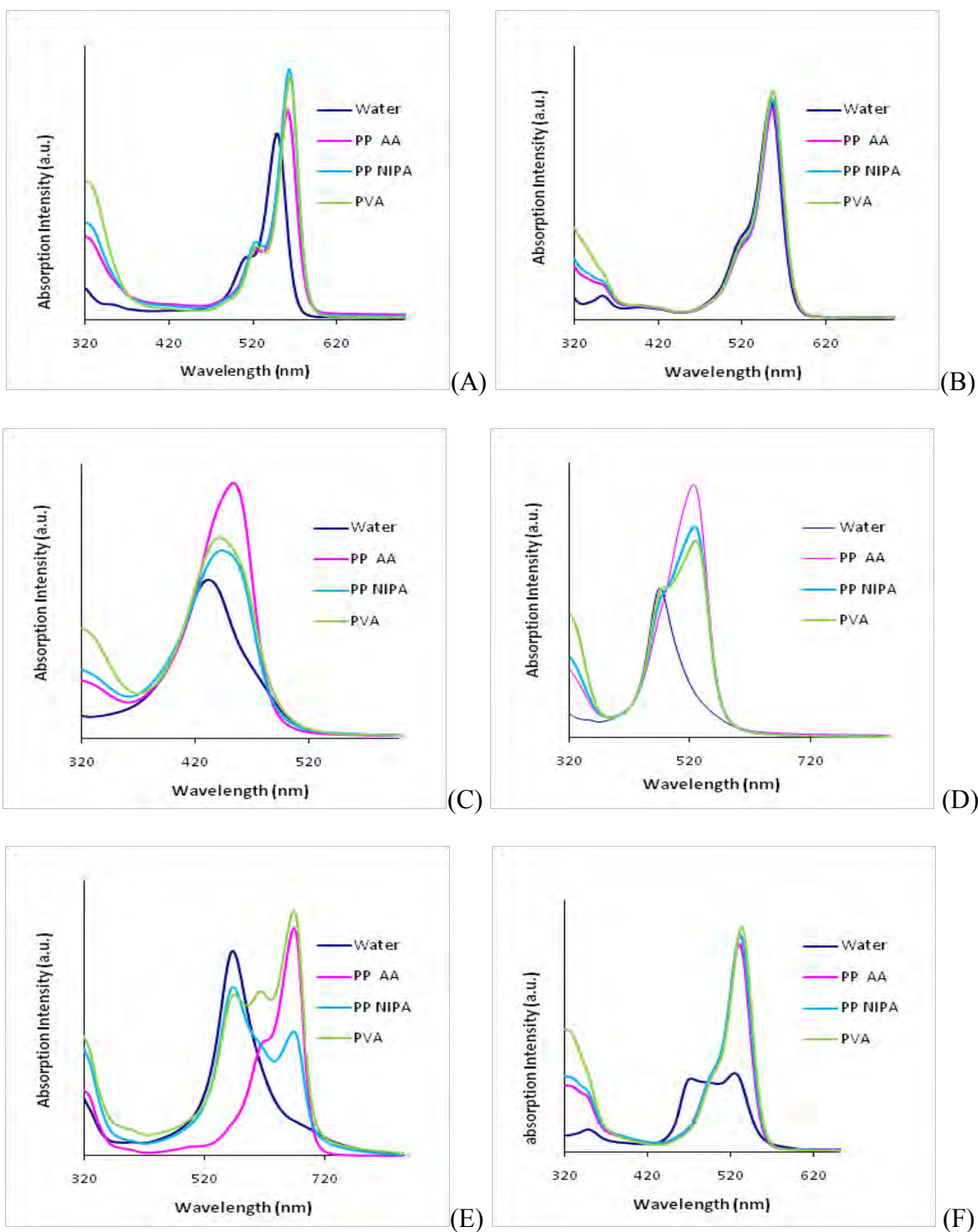
Figure 8.10. Visible absorption spectra of: (A) rose Bengal; (B) rhodamine B; (C) acroflavin; (D) safranin O; (E) methylene blue; (F) rhodamine 6G in different solvents (PP AA is acrylamide based photopolymer, PP NIPA is NIPA based photopolymer and PVA is polyvinyl alcohol.

In case of methylene blue and rodhamine 6G, there are different forms of the dye in the presence of the different solvents, since a different absorption spectra are recorded. For the most part, the position of the maximum absorption peak position changes in the different environments. These shifts are plotted in Fig. 8.11, where the shift observed in the maximum absorption intensity peak position for each dye in the different solvents was compared to its respective value in aqueous solution.
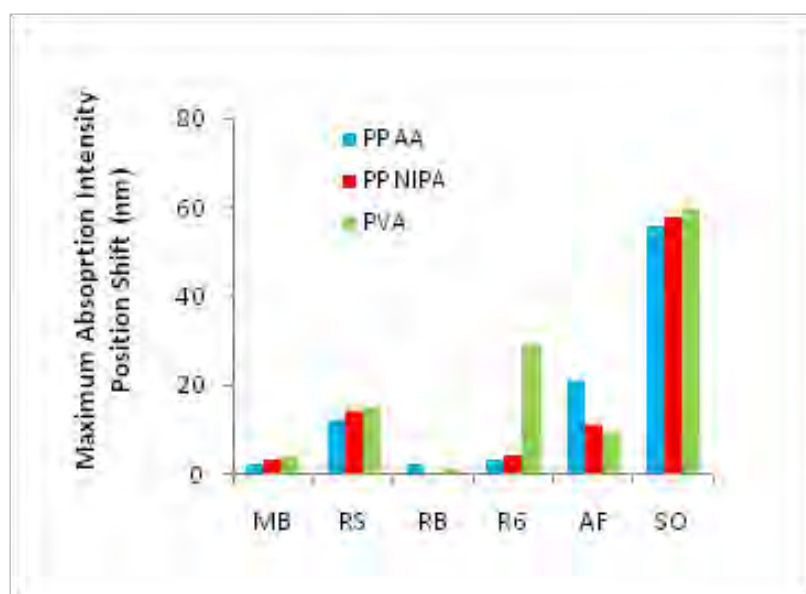
Figure 8.11. Shift of the maximum absorption intensity peak position of each dye relative to respective position in aqueous solution for different solvents: PP AA (acrylamide based photopolymer); PP NIPA (NIPA based photopolymer) and PVA (Polyvinyl alcohol) for different dyes (MB is methylene blue, RS is rose bengal, RB is rodhamin B, R6 is rodhamin 6G, AF is acrofavin and SO is safranin O).

In the particular cases of two dyes, methylene Blue (Fig. 8.12 A) and rhodamine 6G (Fig. 8.12B), a shift in the maximum absorption intensity peak position was also observed when we added zeolite L nanoparticles to the same solvent.
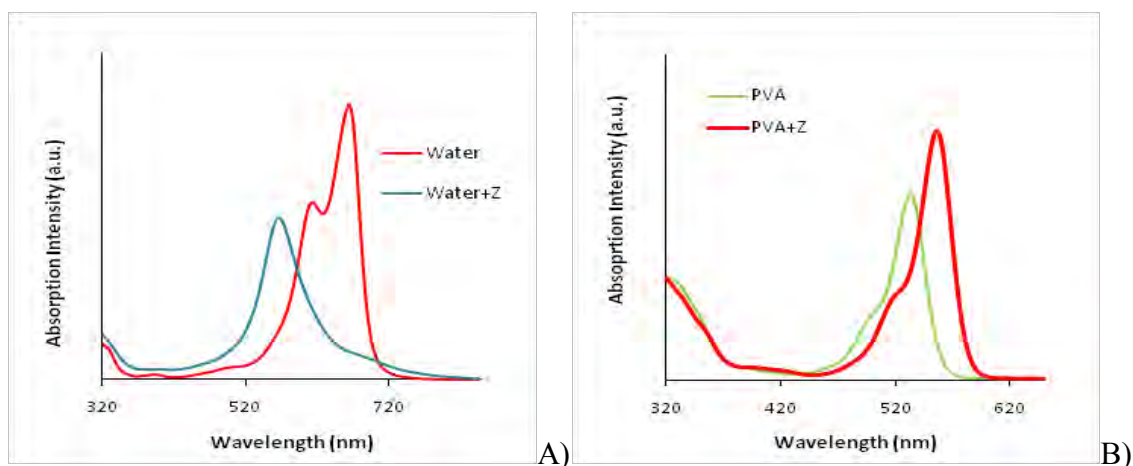
Figure 8.12. **Visible absorption spectra of (A) methylene blue in water without and in the presence of zeolite L (water + Z); (B) rodhamine 6G in PVA without and in the presence of zeolite L (water + Z).**

The change in water is large because the MB^+ ion is only adsorbed at the outer surface where it is surrounded by the water, under which conditions MB^+ forms aggregates. The aggregates are readily formed as we can immediately observe the color change. A similar effect must happen in the case of rodhamine 6G in PVA.

Acrylamide based photopolymer doped with zeolite L (sensitized for recording in red with methylene blue) was prepared for holographic recording. The aim was to fabricate materials with tunable spectral properties able to record in the red without zeolite nanoparticles and in the green in the presence of zeolite L. The samples were prepared as previously described. After evaporation of the solvent (drying process) however the changes in wavelength were reversed (see Fig. 8.13).
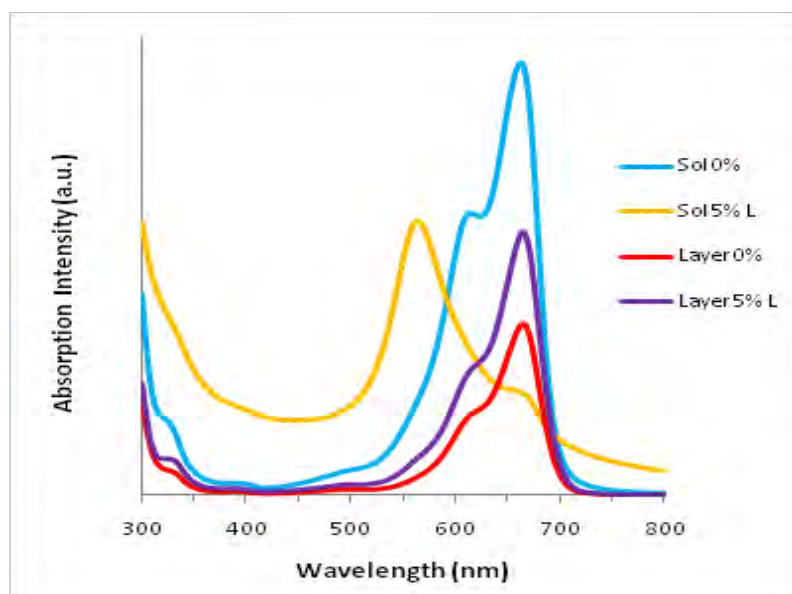
Figure 8.13.   Visible absorption spectra of acrylamide based photopolymer (0%) and in the presence of 5%wt. zeolite L nanocomposite sensitized with methylene blue; in liquid solutions and after drying for 24 hours.

The fact that the spectral change disappears after evaporation of solvent not desirable and we were not able to record gratings using a green laser.

The pH of the photopolymer solution is around 8. In order to investigate if the wavelength change could be caused by pH, visible absorption spectra of aqueous solutions of methylene blue at different pH were taken. First only solutions of methylene blue were tested, after which 0.5mg of zeolite were added to each vial (Fig. 8.15).
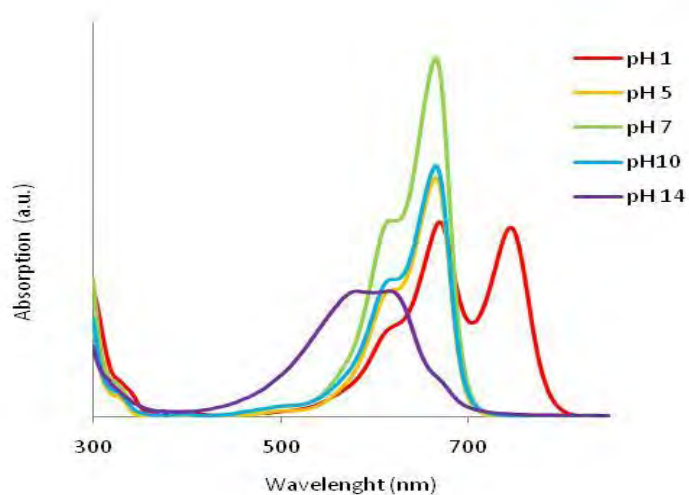
A)
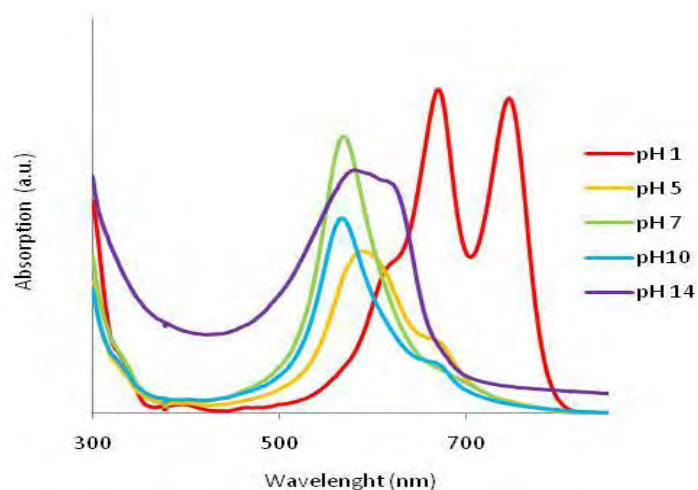
B)

Figure 8.14. Visible absorption spectra of methylene blue solutions at several pH: (A) in water; (B) with the addition of zeolite L.

From Fig. 8.14, several species of methylene blue were identified. At very low pH, the protonated monomer of methylene blue (MBH^{2+}) occurs, where the vibronic components show absorption maximum at 745±1nm, a second maximum at 669nm and a shoulder at ~610nm. In pH range from 5 to 10, aqueous solutions of monomer methylene blue (MB^+) exists with spectra showing the characteristic features of the equilibrium monomer-dimer

(Fig. 8.16) with a maximum absorption at 665nm (monomer) and a shoulder at ~615-625 nm (dimer). For a pH of 14 there is a broad peak at ~570-620 nm possibly due to the formation of aggregates of the dye.
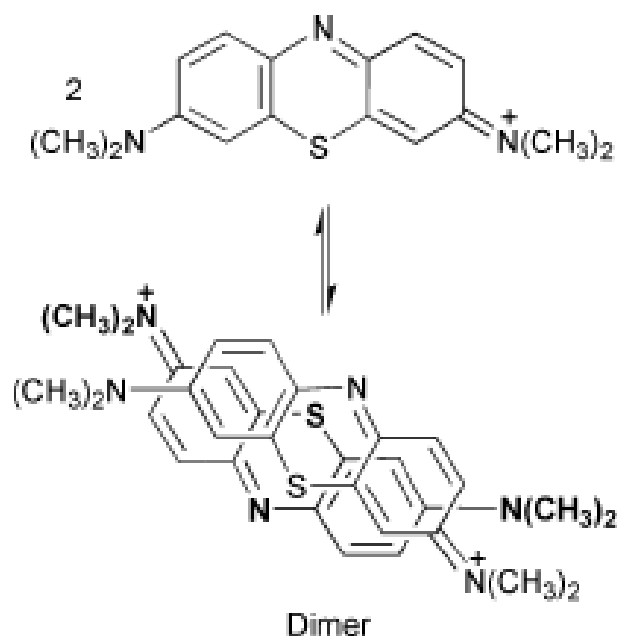
Figure 8.15. Monomer-Dimer equilibrium of methylene blue [reproduced from Ref. 13].

In the presence of zeolite L in the range of pH 7 to 10, there is a formation of aggregates trimers with one band at 566±1 nm. In the pH range of 5-10, the formation of methylene blue aggregates is not dependent on the pH of the solution but occurs due to the presence of zeolite L. When we add zeolites to the solution, methylene blue can be adsorbed on the surface of the nanoparticles. In the extreme values of pH it seems the adsorption is very little.

8.5   CONCLUSIONS

Colloidal LTL suspensions are characterized in detail. The host-guest interactions between several sensitizing dyes (erythrosine B, methylene blue, acroflavine, rhodamine B, rhodamine 6G, rose bengal and safranin O) and several types of zeolite used in this project (zeolites Beta, A, AlPO-18, silicalite-1 and L) were studied.

The concentration and pH dependences on the methylene blue –Zeolite L visible absorption spectra were studied. It was found that the presence of zeolite L promotes the formation of dye aggregates in the range of pH 7 to10 (band at 566±1 nm). In the pH range of 5-10, the formation of methylene blue aggregates is not dependent on the pH of the solution but occurs due to the presence of zeolite L. When we add zeolites to the solution, methylene blue can be adsorbed on the surface of the nanoparticles. In the extreme values of pH it seems there seems to be very little adsorption.

The aim was to fabricate tunable optical materials, but further work is needed to achieve this since the spectral change is reversible when the photopolymer doped with zeolite L dries.

8.6   REFERENCES

[1] D. Brühwiler and G. Calzaferri, *Selective Functionalization of the External Surface of Zeolite L*, Comptes Rendus Chimie 8, No. 3-4, 391–398 (2005)

[2] S. Hassani, F. Salehirad, H. Aghabozorg and Z. Sobat, *Synthesis and Morphology of Nanosized Zeolite L*, Crystal Research and Technology 45, No. 2, 183-187 (2009)

[3] J. Rouquerol, D. Avnir, C. Fairbridge, D. Everett, J. Haynes, N. Pernicone, J. Ramsay, K. W. Sing and K. Unger, *Recommendations for the Characterization of Porous Solids (Technical Report)*, Pure and Applied Chemistry 66, No. 8, 1739-1758 (1994)

[4] B. Hennessy, S. Megelski, C. Marcolli, V. Shklover, C. Ba1rlocher and G. Calzaferri, *Characterization of Methyl Viologen in the Channels of Zeolite L*, The journal of Physical Chemistry B 103, No. 17, 3340-3351 (1999)

[5] P. Simoncic and T. Armbruster, *Cationic Methylene Blue Incorporated into Zeolite Mordenite-Na: a Single Crystal X-ray Study*, Microporous and Mesoporous Materials 81, No. 1-3, 87-95 (2005)

[6] G. Calzaferri, S. Huber, H. Maas and C. Minkowski, *Host-Guest Antenna Materials,* Angewandte Chemie International ed. in English 42, No. 32, 3732-3758 (2003)

[7] U. Vietze, O. Krauß, F. Laeri, G. Ihlein, F. Schüth, B. Limburg and M. Abraham, *Zeolite-Dye Microlasers*, Physical Review Letters 81, No. 21, 4628–4631 (1998)

[8] J. Meinershagen and T.Bein, *Optical Sensing in Nanopores, Encapsulation of the Solvatochromic Dye Nile Red in Zeolites*, Journal of the American Chemical Society 121, No. 2, 448–449 (1999)

[9] M. Ehrl, F. Deeg, C. Braeuchle, O. Franke, A. Sobbi, G. Schulz-Ekloff and D. Woehrle, *High-Temperature Non-Photochemical Hole-Burning of Phthalocyanine-Zinc Derivates Embedded in a Hydrated AlPO$_4$-5 Molecular Sieve*, The Journal of Physical Chemistry 98, No. 1, 47–52 (1994)

[10] D. Brühwiler, N. Gfeller and G. Calzaferri, *Resorufin in the Channels of Zeolite L*, The Journal of Physical Chemistry B 102, No. 16, 2923–2929 (1998)

[11] K. Senthilkumar, P. Paul, C. Selvaraju and P. Natarajan, *Preparation, Characterization, and Photophysical Study of Thiazine Dyes Within the Nanotubes and Nanocavities of Silicate Host: Influence of Titanium Dioxide Nanoparticle on the Protonation and Aggregation of Dyes*, The Journal of Physical Chemistry C 114, No. 15, 7085–7094 (2010)

[12] S. Megelski, A. Lieb, M. Pauchard, A. Drechsler, C. Debus, S. Glaus, A. Meixner and G. Calzaferri, *Orientation of Fluorescent Dyes in the Nano Channels of Zeolite L*, The Journal of Physical Chemistry B 105, No. 1, 25–35 (2001)

[13] K. Patil, R. Pawar and P. Talap, *Self-aggregation of Methylene Blue in Aqueous Medium and Aqueous Solutions of Bu$_4$NBr and Urea*, Physical Chemistry Chemical Physics 2, No. 19, 4313–4317 (2000)

CHAPTER 9: INITIAL STUDIES IN THE DESIGN OF NEW NIPA BASED PHOTOPOLYMER

9.1 INTRODUCTION

In this chapter we present a new photopolymer with holographic features similar to the standard photopolymer - acrylamide based photopolymer – but with reduced toxicity.

The acrylamide monomer was replaced by N-isopropylacrylamide (NIPA), and the composition was optimized in terms of monomer and co-monomer (N,N'-methylene bisacrylamide) concentrations for holographic recording. The refractive index before and after polymerization was obtained and it was found that a bigger differences exists in the case of NIPA photopolymer when compared to acrylamide based photopolymer. Besides a lower toxicity, the choice of NIPA was also justified because this hydrogel is known to be sensitive to external stimuli such as temperature [1], which could be useful in the design of sensors.

Initial studies in using NIPA photopolymer in holographic sensing were made. NIPA photopolymer sensitized with methylene blue were used to record reflection holograms. The temperature response of this material at three different relative humidities (RH) was recorded in a controlled environment and its spectral changes recorded. It was found that the swelling of the photopolymer induces a wavelength shift that depends on the temperature.

9.2 THE NIPA BASED PHOTOPOLYMER

The main drawback of the acrylamide based photopolymer is the toxicity of its main monomer, acrylamide. Acrylamide is a known neurotoxicant, reproductive toxicant, and carcinogenic substance [2]. N,N'-methylene bisacrylamide, a larger molecule that is not as readily absorbed through the skin or vaporized into the air, is a suspected mutagen and

teratogen, but is not nearly as dangerous as acrylamide [3]. After acrylamide and bisacrylamide are polymerized, the polymer is safe to handle and use, as long as there is no residual unreacted monomer [3]. Acrylamide substitutions have been made [4] using sodium acrylate with toxicity of lower than that of acrylamide and comparable grating performances were obtained, i.e maximum diffraction efficiency and energetic sensitivity for these two types of photopolymer.

In our work, we have chosen N-Isopropylacrylamide (NIPA) to replace acrylamide as a monomer. This compound presents less danger for health than acrylamide [5, 6]. Results from these studies have shown that the NIPA monomer may have some toxic effects, thought the resulting polymer is biocompatible.

One of the main reasons for studying this monomer is that fact that it is a thermosensitive material. Thermosensitive hydrogels can be classified as positive or negative temperature-sensitive systems. A positive temperature-sensitive hydrogel has an upper critical solution temperature (UCST). Such hydrogels contract upon cooling below the UCST. Most hydrogels belong to this category. In the other hand, negative temperature-sensitive hydrogels have a lower critical solution temperature (LCST). These hydrogels contract upon heating above the LCST, and are known as thermoreversible hydrogels as the contraction is totally reversible upon cooling [7]. Poly(N-isopropylacrylamide) demonstrates a lower LCST at about 32 °C [8], i.e. it shrinks with increasing temperature. Poly (N-isopropyl acrylamide) forms swollen hydrogels of crosslinked species due to the presence of both hydrophilic amide groups and hydrophobic isopropyl groups in its sidechains. The PNIPA hydrogel in an aqueous solution exhibits a rapid and reversible hydration–dehydration change in response to small temperature changes around its LCST.

Below this temperature the hydrogel is swollen, hydrated and hydrophilic, whereas above the LCST, the hydrogel shrinks and forms a collapsed, dehydrated and hydrophobic state due to the breakdown of the delicate hydrophilic/hydrophobic balance in the network structure [9].

9.3   INITIAL STUDIES IN NIPA PHOTOPOLYMER OPTIMIZATION

9.3.1   COMPOSITION OF THE PHOTOPOLYMER

In initial investigations concerning the suitability of the NIPA monomer for holographic recording we have studied compositions with different monomer quantities.

Firstly, several compositions containing different amounts of the monomer – NIPA while maintaining the other components concentrations constant were prepared (see Table 9.1). The amount of co-monomer (bisacrylamide) in each composition was 0.2 g.

Table 9.1.   Composition of samples prepared with different concentrations of NIPA.

Sample Nr.	Monomer (g)	Monomer (mmol)
1	0.2	1.8
2	0.4	3.5
3	0.6	5.3
4	0.8	7.1
5	1.6	14.2
6	2.4	21.2

The samples were used to record transmission gratings and were compared against gratings recorded in a material with the standard composition (monomer acrylamide is 0.6 g or 8.4 mmol). The results for the grating performances (Nr. 1 to 6 of Table 9.1) are shown in Figure 9.1.

222

A)

B)
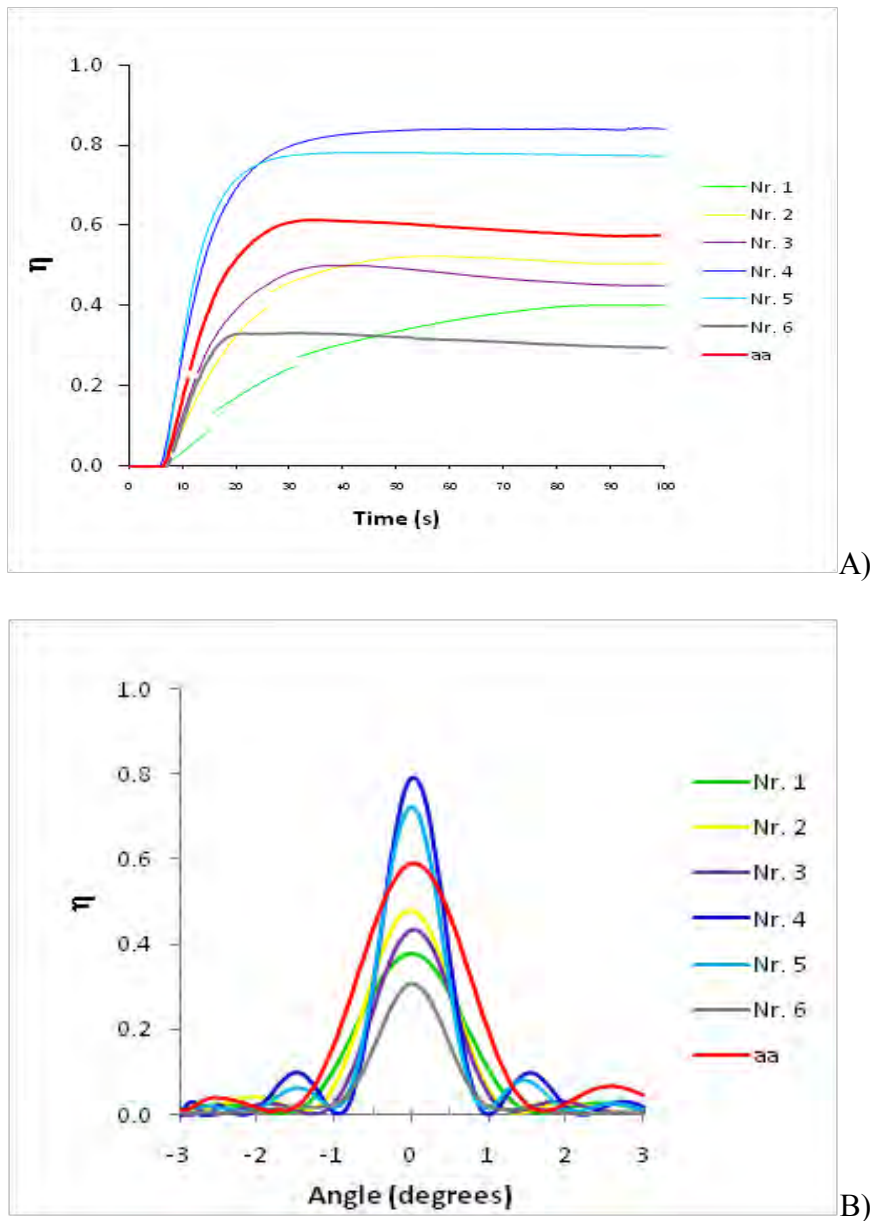
Figure 9.1.   Grating performances obtained for different NIPA monomer quantities - Table 9.1 where "aa" represents the standard composition with acrylamide: (A) growth curves; (B) angular selectivity curves (1000 lmm^{-1} and 5 mWcm^{-2}).

The diffraction efficiency for NIPA photopolymer increases with time until a plateau is reached. This is the same kinetics as acrylamide based photopolymer. The angular selectivity curves for the gratings recorded in this material showed that the gratings are in a typical non overmodulated regime.

Although one deposited the same amount of solution in the substrate (0.6 ml) the thickness of the dry layers varied and a better comparison is to observe their refractive index modulation (See Fig. 9.2), calculated with thicknesses measured by WLI.
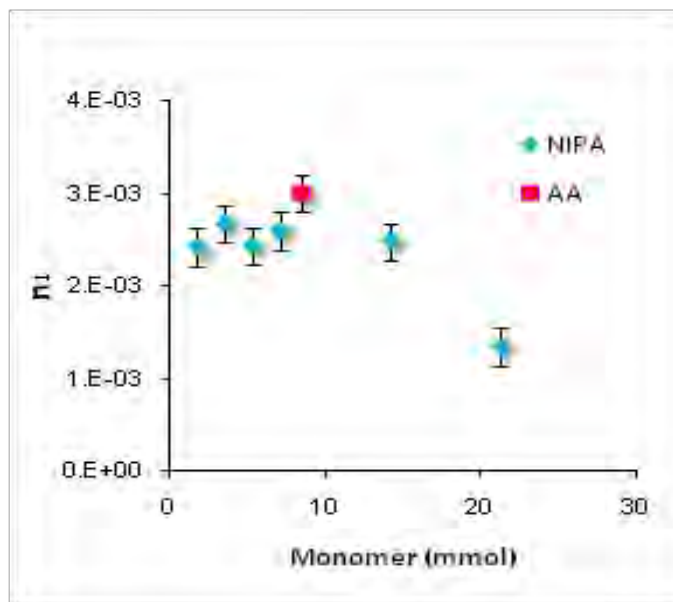
Figure 9.2. **Refractive index modulation for photopolymers where monomer is: (blue diamonds) NIPA or (red square) acrylamide (1000 lmm-1 and 5 mWcm-2).**

It is seen that the highest refractive index modulation value was observed for 3.5 mmol of NIPA (0.4 g) and that this value is 11% lower than the one obtained for the standard composition containing acrylamide.

The next step was to vary the co-monomer concentration. We have prepared several compositions containing different amounts of the co-monomer, N,N'-methylene bis acrylamide, while maintaining the other photopolymer components concentrations constant (see Table 9.2). The amount of monomer NIPA in each composition was 0.4 g.

Table 9.2. **Composition of samples made with different concentrations of N,N'-methylene bisacrylamide (co-monomer) and NIPA (monomer).**

Sample Nr.	Co-Monomer (g)	Ratio to monomer
1	0.05	8
2	0.1	4
3	0.2	2
4	0.25	1.6
5	0.3	1.3
6	0.4	1

The samples were used to record transmission gratings and were compared against gratings recorded in a material with the standard composition, where 0.6g of acryamide and 0.2g of N,N'-methylene bisacrylamide (ratio of monomer/ co-monomer of 3) was used. The results for the grating performances (Nr. 1 to 6 of Table 9.2) are shown in Figure 9.3.

A)

B)
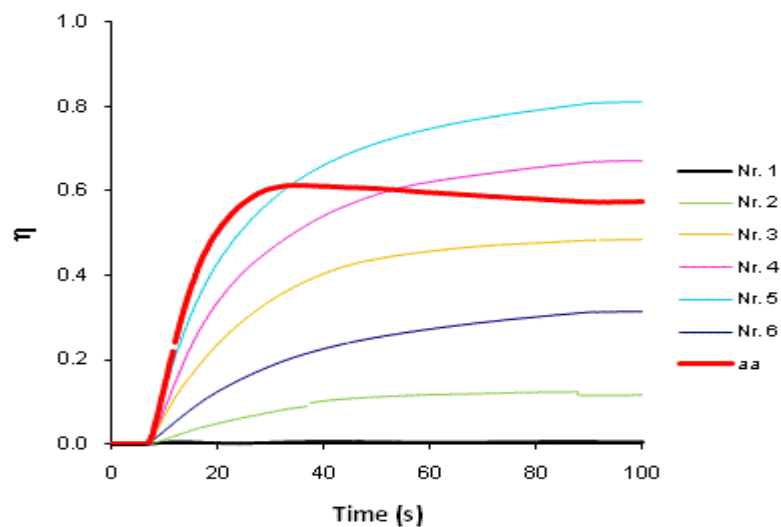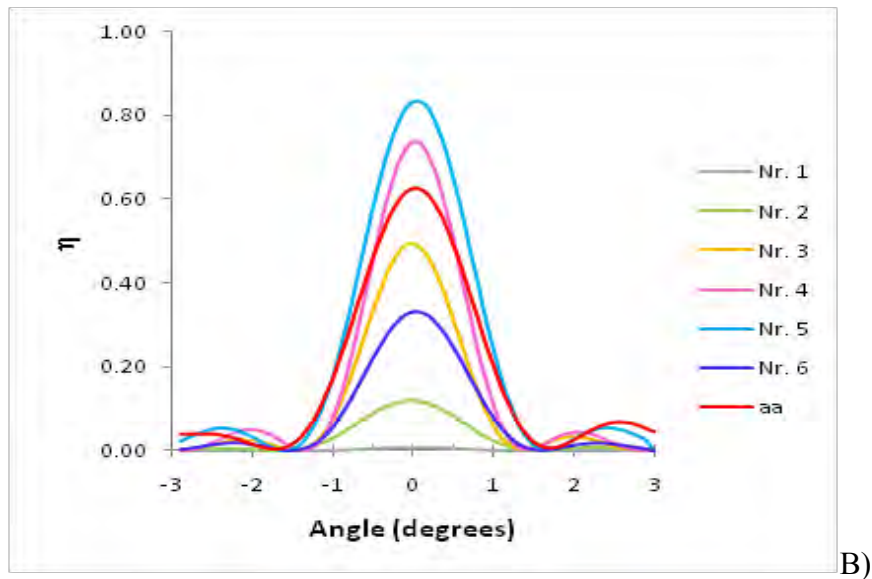
Figure 9.3. **Gratinng performances obtained for different NIPA monomer/N,N'-methylene bisacrylamide co-monomer ratios - Table 9.2, where "aa" represents the standard composition with acrylamide: (A) growth curves; (B) angular selectivity curves (1000 lmm^{-1} and 5 mWcm^{-2}).**

The diffraction efficiency for grating 1 (ratio between monomer/co-monomer of 8) is very low (0.8%) and that for grating 2 (ratio between monomer/ co-monomr of 4), the diffraction efficiency decreases when the laser is off (at 90s). We can also observe that the initial slopes of the growth curves increase as the quantity of comonomer increases. This can be explained by the fact that when the concentration of N,N'-methylene bisacrylamide is increased, the quantity of double bonds in the system increases and thus the polymerization rate is larger. The gratings are in a typical non overmodulated regime

The maximum diffraction efficiencies obtained are shown in figure 9.4. In this case, the thicknesses of the gratings were very similar.
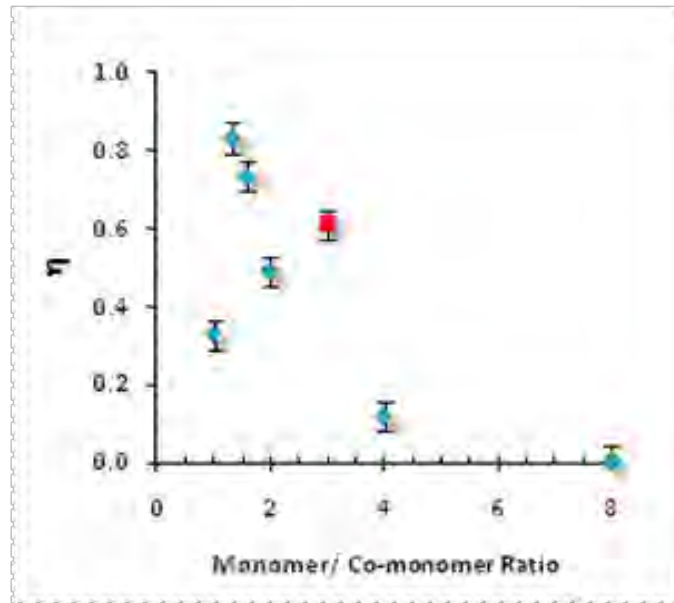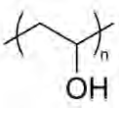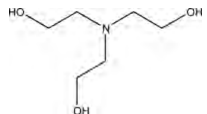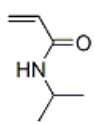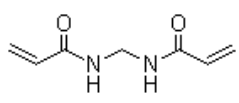
Figure 9.4. **Maximum diffraction efficiency as a function of monomer / bis acrylamide co-monomer ratio where monomer is: (blue diamonds) NIPA or (red square) acrylamid; (1000 lmm^{-1} and 5 mWcm^{-2}).**

It is seen that the monomer// co-monomer ratio has a large influence on the diffraction efficiency, the best performance observed being for the pair NIPA 0.4g/ Bisacrylamide 0.3g, where we can observe a final diffraction efficiency of around 83%. Layers were prepared containing only NIPA and no bisacrylamide but they didn't dry and hence were not recorded.

The final composition used to record volume gratings in NIPA photopolymer is presented in Table 9.3.

Table 9.3.   Composition of NIPA Photoplymer.

Component	Molecular Structure	Quantity
PVA Stock solution (10%wt.)		18 ml
TEA		2 ml
N-Isopropylarylamide		0.4 g
N,N'-methylne Bisacrylamide		0.3 g
Dye Solution Stock Solution (0.11%wt).		4 ml (Transmission) or 3 ml (Reflection)

* 1 - Stock solution of 10%wt. polyvinyl alcohol (PVA) solution is prepared by dissolving 10 g of PVA in 100 ml of water under heating and stirring

* 2 - Stock Dye Solution is prepared by dissolving 0.11 g of Dye in 100 ml of water under stirring; For transmission mode Erythrosine B is use, while for reflection mode Methylene Blue was used

9.3.2   REFRACTIVE INDEX MEASUREMENTS

Refractive index data of polymer films at different wavelengths were measured with the help of Dr. Yovcheva by critical angle determination using diffraction pattern disappearance. The polymer films examined contained acrylamide (0.6 g) and NIPA (0.4 g) photopolymers with 0.2 g of N,N'-methylne bisacrylamide.

The method was described earlier in detail in [10, 11]. Briefly, the determination of the critical angle is carried out with the help of a metal grating allowing observation if total internal reflection at the prism/photopolymer layer interface occurs. The photopolymer layer is located between a prism of high refractive index and the grating. At lower angles of incidence, the laser beam is transmitted through the sample and the grating, and a diffraction pattern is observed. At a critical angle of incidence, total internal reflection occurs, the beam does not pass to the grating and the diffraction pattern disappears.

The refractive indices of the materials were measured before polymerization. Then gratings were recorded using a 532 nm laser (spatial frequency of 1000 lmm^{-1}, 5 mWcm^{-2} for 100 s) and their refractive indices measured again. The results for the difference in refractive index (before and after polymerization) – d(RI) are presented in Fig.9.5.
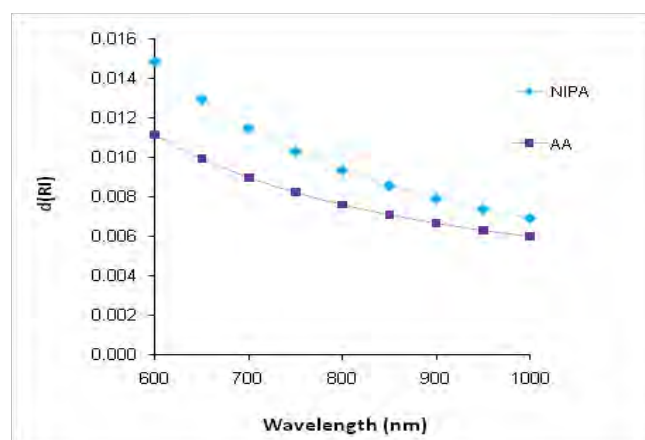
Figure 9.5. **Difference in the refractive index for NIPA and Acrylamide (AA) photopolymers before and after polymerization (1000 lmm^{-1}; 5 mWcm^{-2} at 532 nm).**

One can observe from fig. 9.5 that the difference in the refractive index before and after polymerization is higher in the case of NIPA photopolymer. This is promising for obtaining higher refractive index modulations, but more optimization of this photopolymer needs to be done.

9.4 NIPA PHOTOPOLYMER FOR HOLOGRAPHIC SENSING

Our approach was based in the hydrogel (water-swollen polymer networks) characteristics of PNIPA that undergoes a thermal transition at LCST (32 °C). At temperatures around 35-40ºC this polymer collapses into a denser, more compact structure due to a switch in the balance of solvation and hydrophobic forces. Through the hydrogel volume change in response to external physical or chemical stimuli, reflection gratings can optically sense the variation as observable changes or shifts in its wavelength (color) shift. The hologram acts both as a sensing element and as a transducer.

The general principle of a holographic sensor is that the volume change alters the fringe spacing. This causes a change in the wavelength of the reflected light according to the Bragg equation (Eq. 9.1):

$$\Lambda = \frac{\lambda}{2n\sin\theta} \qquad \text{(Eq. 9.1)}$$

where Λ is spatial period of the grating, n is the average refractive index of the recording medium, λ is the recording wavelength and θ is the half of the angle between the two recording beams.

When the grating is illuminated with white light, the diffracted light in a specific direction will be of wavelength λ given by Eq. 9.1 and a single colour will be observed. The principle of operation of such sensor can be given by differentiation of Eq. 9.1:

$$\Delta\lambda = 2\sin\theta(n\,\Delta\Lambda + \Lambda\,\Delta n) + 2n\Lambda\cos\theta\,\Delta\theta \qquad \text{(Eq. 9.2)}$$

A change of the wavelength of the diffracted light could be caused by change of the average refractive index, change in the grating period or when observing at different angle.

The optical setup for measuring the spectral characteristics of the light diffracted from the hologram was assembled in the humidity chamber (see Fig. 9.6). The probe light from a broad band light source (AvaLight-HAL-S) was fiber guided into the humidity chamber. The diffracted light was then coupled into a second fiber by a lens and guided to a spectral analyser, AvaSpec-2048. In order to obtain the humidity or temperature response of a specific hologram the relationship between the peak wavelength of the light diffracted from the hologram and the RH or the temperature was determined. The light from the white light source (WLS) is guided through optical fibers (OF) and collimated by mean of collimating lenses (CL) to a spectrum analyser (SA).
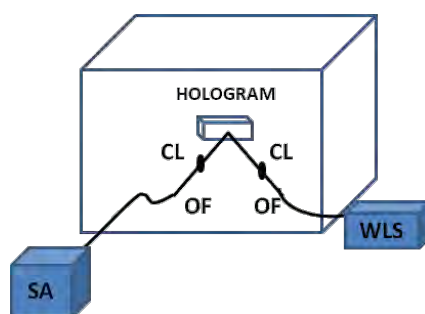
Figure 9.6. **Experimental setup for measuring the humidity and temperature response of reflection holograms. The humidity and temperature in the chamber are controlled by a microprocessor.**

Two reflection holograms were recorded in methylene blue sensitized NIPA recording material, for two different exposure times – 15 and 40s. For both, the change of the spectral response of the hologram as function of temperature was studied at three different levels of humidity– 20, 40 and 60% RH. The results are presented in Fig. 9.7.
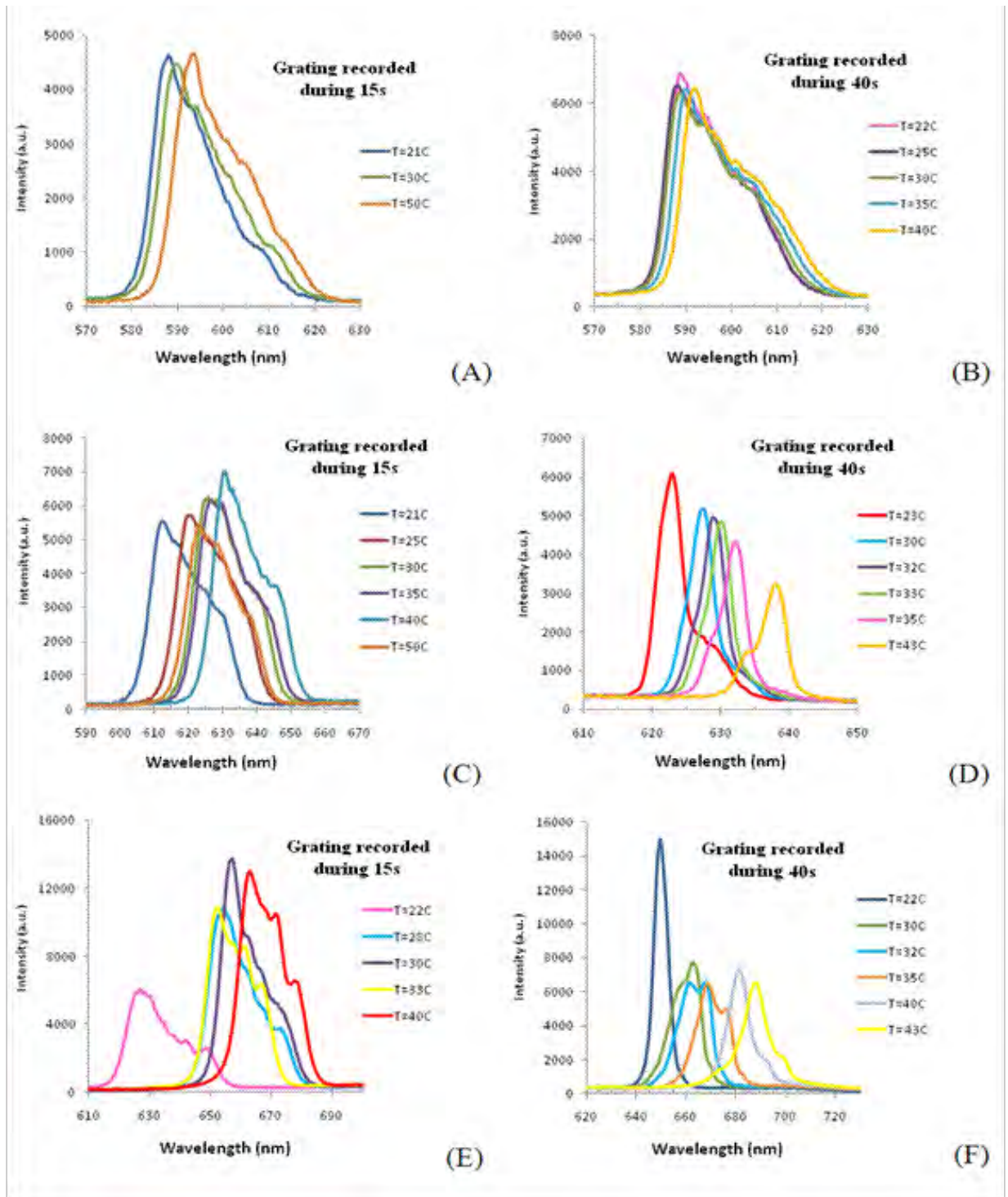
Figure 9.7. **Wavelength selectivity curves for reflection holograms (sensitized with mthylene blue) for different temperatures (T) at: (A)&(B) 20% RH; (C)&(D) 40% RH and (E)&(F) 60% RH.**

For both holograms (recorded during 15 and 40s) it can be seen that there is little temperature dependence of the spectral response of the holograms when the HR is 20%. For higher RH (40% and 60%), there is a dependence of the position of maximum peak with the increasing temperature. These results are plotted in Fig. 9.8.

A)

B)
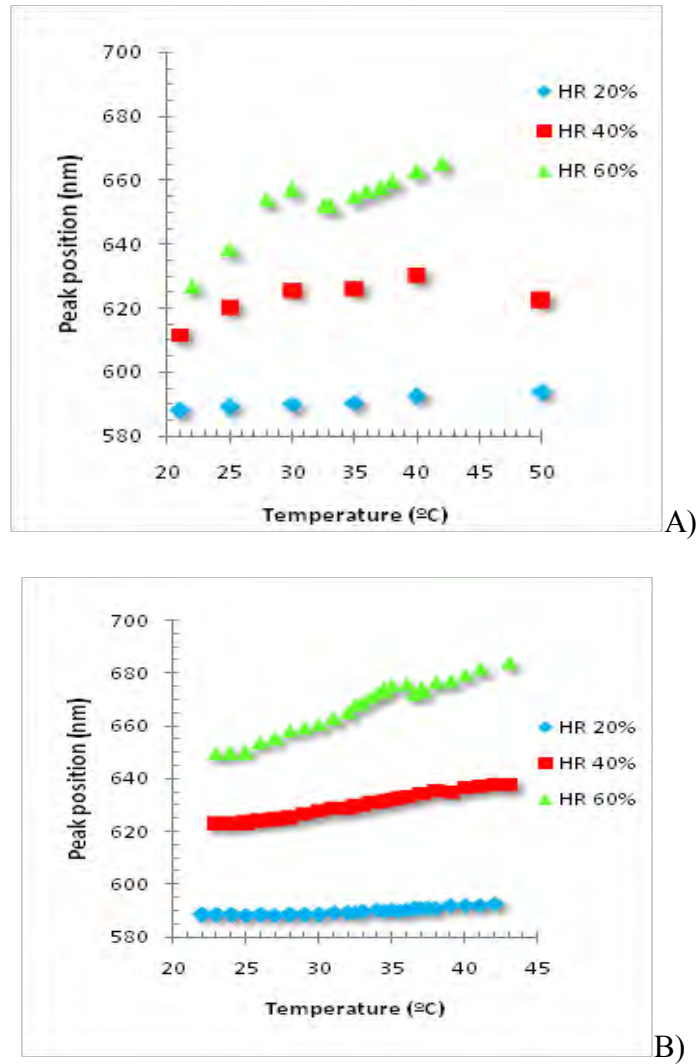
Figure 9.8   Temperature response at constant humidity of reflection holograms recorded in NIPA photopolymer during (A) 15 s; (B) 40 s.

The hologram recorded during 15 s exposure time shows a maximum at ~600 nm and a shoulder around 20 nm higher wavelength values. This spectral feature does not change with temperature increase or RH change. For the hologram recorded during 40s exposure time there is an inversion of the absorption bands intensity (see Fig. 9.7D) after the polymer LCST for RH of 40%.

When the grating is exposed to low RH again (see Fig. 9.7F), this band absorption pattern is still present at T=30 °C and is reversed when the temperature is raised above the LCST. The differences between the two gratings spectral response to temperature could be explained by differences in PNIPA degree of polymerization. For the sample recorded for 40s more polymerization of the NIPA is expected to occur. In the case of the hologram recorded during 15s, the difference between the initial position of the maximum absorption peak (around 20°C) and its final position (around 40°C) is 5, 18 and 24nm for 20, 40 and 60% RH, respectively. For the sample recorded at 40s, this difference is of 4, 15 and 39 nm for 20, 40 and 60% RH, respectively. There seems to be liitle effect of the exposure time in terms of the difference between initial position and final position of the maximum absorption peak position. For an initial temperature of 15 °C and a final temperature of 40 °C the values obtained for acrylamide based photopolymer [13] were of around 5, 5, 15 and 15 nm for 15, 30 and 45% RH. For the same photopolymer at 60%RH the initial temperature was of 15 °C and a final temperature of 25 °C and the shift of the maximum absorption peak position was around 15 nm.

9.5   CONCLUSIONS

A new photopolymer with thermo responsive properties was fabricated using N-isopropylacrylamide (NIPA) cross linked with bisacrylamide (BA). The monomer/ co-monomer best ratio was studied by studying the grating performances and it was found that the composition containing 0.4 g of NIPA and 0.3 g of BA resulted in comparable diffraction efficiencies to the acrylamide based photopolymer.

Two reflection holograms were recorded in this material, one for 15 s and another for 40 s and were tested for holographic sensing applications. The temperature response of the hologram spectral feautures (from around 20 to 40 °C) at three constant relative humidities 20, 40 and 60% RH was characterized. In was seen that at 20% RH the spectral response of the hologram was not temperature dependent. At higher values of RH (40% and 60%) spectral changes did occur and the maximum absorption peak position increasingly shifted to higher wavelengths. For the more polymerized sample (40 s) at higher RH one could observe a conformational change in the peak shape above the polymer characteristic LCST.

9.6   REFERENCES

[1] M. Heskins and J. Guillet, *Solution Properties of Poly(N-isopropylacrylamide)*, Journal of Macromolecular Science Part A 2, No. 8, 1441-1455 (1968)

[2] J. Exon, *A Review of the Toxicology of Acrylamide*, Journal of toxicology and Environmental Health Part B 9, No. 5, 397-412 (2006)

[3] K. McAuley, *The Chemistry and Physics of Polyacrylamide Gel Dosimeters: Why They Do and Don't Work,* Journal of Physics: Conference Series 3, 29–33 (2004)

[4] M. Ortuño, E. Fernández, S. Gallego, A. Beléndez, and I. Pascual, *New Photopolymer Holographic Recording Material with Sustainable Design,* Optics Express 15, No. 9, 12425-12435 (2007)

[5] K. Hashimoto, J. Sakamoto and H. Tanii, *Neurotoxicity of Acrylamide and Related Compounds and Their Effects on Male Gonads inMice*, Archives of Toxicology 47, No. 3, 179-189 (1981)

[6] H. Tanii and K. Hashimoto, *Neurotoxicity of Acrylamide and Related Compounds in Rats (Effects on Rotarod Performance, Morphology of Nerves and Neurotubulin),* Archives of Toxicology 54. No. 3, 203-213 (1983)

[7] J. Pollock and K. Healy, *Mechanical and Swelling Characterization of Poly(N-Isopropyl Acrylamide-co-Methoxy Poly(Ethylene Glycol) Methacrylate) Sol–Gels,* Acta Biomaterialia 6, No.4, 1307–1318 (2010)

[8] N. Peppas, P. Bures, W. Leobandung and H. Ichikawa, *Hydrogels in Pharmaceutical Formulations*, European Journal of Pharmaceutics and Biopharmaceutics 50, No. 1, 27-46 (2000)

[9] Y. Zhang, W. Yang, C. Wang, W. Wu and S. Fu, *Thermosensitive Nanocontainers Prepared From Poly(N-Isopropylacrylamide-co-N-(Hydroxylmethyl)Acrylamide)-g-Poly(Lactide),* Journal of Nanoscience and Nanotechnology 6, No. 9-10, 1–6 (2006)

[10] S. Sainov and N. Dushkina, *Simple Laser Refractometer,* Applied Optics 29, No.10, 1406_1-1408 (1990)

[11] S. Sainov, *Laser Microrefractometer,* Review of Scientific Instruments 62, No.12, 3106-3108 (1991)

[12] I. Naydenova, J. Raghavendra, V.Toal and S. Martin, *Characterisation of the Humidity and Temperature Responses of a Reflection Hologram Recorded in Acrylamide-Based Photopolymer*, Sensors and Actuators B: Chemical, Vol. 139, No. 1, 35-38 (2009)

CHAPTER 10: FINAL CONSIDERATIONS

10.1 CONCLUSIONS

The main challenge of the present work was to find compatible nanoparticles that would disperse in the polymer matrix with causing high optical losses due to the scattering of the light.

Five different microporous nanoparticles (zeolite Beta, A, AlPO-18, MFI and L) were used to fabricate novel photopolymerizable nanocomposites for holographic applications. We have learned that the inclusion of these nanoporous crystals in photopolymers with the right choice of zeolite optical and physico-chemical properties is a flexible tool to design versatile holographic recording materials to be used in applications such as holographic sensing. Each colloidal suspension was characterized by means of several analytical techniques such as DLS, XRD, Nitrogen adsorption, SEM and Raman spectroscopy.

We found that the incorporation of different types of zeolites into acrylamide-based photopolymer produces optical transparent dry layers that can be holographically recorded. The compatibility of the nanoparticles and the acrylamide based photopolymer was investigated by DLS which showed no aggregation of the nanoparticles after incorporation in the photopolymeric matrix. Both the heterogeneity of the whole layer (by light scattering measurements) and the surface roughness of the photopoymers (by interferometric techniques measrurements) were used to characterize the nanocomposites.

To understand the influence of the zeolite properties on the grating performances recorded in the materials developed in the present work, three nanocomposites were compared containing zeolite Beta (BEA), silicalite-1 (MFI) and AlPO-18 (AEI). These nanoparticles

differ in their chemical composition and structure, hydrophobic/hydrophilic nature and dimensions of pores. It was found that although all nanoparticles were partially redistributed during the holographic recording (as verified by means of Raman spectroscopy and also by SEM-EDX in the case of Beta nanocomposites), this effect improves the refractive index modulation only in the case of the silicalite-1 nanoparticles, while no improvement is observed in AlPO-18 and Beta doped layers. The results can be explained by the hydrophobic/hydrophilic nature of the nanoparticles and their interactions/absence of interactions with the host photopolymer. In terms of pore sizes, zeolite Beta is a large pore, zeolite silicalite-1 is a medium pore size while AlPO-18 is a small pore material. This allowed us to distinguish between two situations – when the acrylamide monomer molecules can be trapped inside the nanoparticles (Beta) and when they are larger than the nanoparticles' pore size (silicalite-1, AlPO-18). By Raman spectroscopy, it was indeed proved that the acrylamide molecules bonded with zeolite Beta. Moreover, by means of ^{13}C NMR it was found that interactions also occur with other components of the photopolymer, such as TEA molecules. In this study, zeolite A was used for comparison. Zeolite A has similar chemical composition and structure to zeolite Beta, but smaller pore size.

AlPO-18 material unlike zolite Beta can't accommodate molecules of the photopolymer inside its pores due to small pore size also showed no improvement of the refractive index modulation of gratings recorded in the respective nanocomposites. The explanation for this was given by the hydrophilic nature of the structure.

Gratings recorded in photopolymers doped with AlPO-18, known for its hydrophilic nature and its ability to retain water molecules inside its pores unless heated above a given

temperature were compared with gratings recorded in photopolymer doped with silicalite-1 nanoparticles, a pure silica zeolite whose pores are expected to remain empty due to their hydrophobic nature, i.e, not having affinity to water. By refractive index calculations before and after incorporation of zeolites in the photopolymer (see Table 10.1) it was shown that only hydrophobic silicalite-1 pores remain empty after being added to the photopoymer, as indicated by the small difference between the pore volume before ($0.12 cm^3 g^{-1}$) and after addition to the photopolymer ($0.11 cm^3 g^{-1}$).

Table 10.1. Comparison of pore volume of nanoparticles before and after addition to the acrylamide based photopolymer.

Nanoparticles	Density, empty pores, g/cm³	Density, filled pores, g/cm³	Pore volume, before addition to the nanocomposite, cm³/g	Pore volume after addition to the nanocomposite, cm³/g
MFI	1.74	1.78	0.12	0.11
AEI	1.85	2.42	0.21	0.08
BEA	1.45	2.24	0.25	0.006

Greater diferences in the refractive index of empty pores (air) and photopolymer vs. filled pores and photopolymer are responsible for the improvement of the refractive index modulation (n_1) in the presence of silicalite-1. This is according with the predicted values (see Table 10.2).

Table 10.2. volume fraction of rdistributed nanoparticles and predicted and measured refractive index modulation contributed by the nanoparticles.

Nano particles (NP)	%wt.	Vol. fraction in the solid layer (%)	Vol. fraction Raman %	$f_{redistributed}$ %	$n_{NP} - n_{photopolymer}$	$n_{1\,expected}$	$n_{1\,measured}$
BEA	5	5.6	40	2.3	0.043	6.34×10^{-4}	6.1×10^{-4} $\pm 8 \times 10^{-5}$
AEI	2.5	0.75	31	0.23	0.085	1.3×10^{-4}	1.3×10^{-4} $\pm 1 \times 10^{-5}$
MFI	5	4.6	38	1.75	0.133	2.3×10^{-3}	1×10^{-3} $\pm 1 \times 10^{-4}$

With this work we contributed to a deeper understanding of the role of porous nanoparticles during the holographic recording in photopolymerizable nanocomposites. The modulation of the refractive index n_1 is caused by: 1) polymerization by conversion of the monomer into polymer; 2) density variation due to concentration driven monomer diffusion from dark to bright fringe areas; 3) density variation due to concentration driven short/mobile polymer chains diffusing from bright to dark fringe areas; 4) spatial patterning of the nanosized particles. The latter phenomenon is observed only if the refractive index of the nanoparticles is significantly different from that of the photopolymer matrix and if the volume fraction of the redistributed particles is sufficiently large.

The development of these new materials for use in sensing platforms is demonstrated. An irreversible humidity sensor (i.e. the diffraction efficiency of the sensor changes permanently after exposure to high humidity) based on a transmission holographic grating recorded in AlPO-18 nanocomposite was fabricated. This is important for instance in situations where, regardless of current (potentially lower) humidity levels, one would like to know if higher levels of humidity were ever present. The larger pore Beta zeolite could also be useful in the detection of larger molecules such as volatile orgaic compounds - VOC, demonstrated here for the detection of toluene, where the addition of 5% Beta nanoparticles yielded an increase of 20% in the diffraction efficiency difference on exposure to toluene when compared with the undoped photopolymer.

Finally a photopolymer containing NIPA, a monomer less toxic than acrylamide and with interesting thermo sensitive properties, showed potential as holographic sensor and initial studies characterized spectral features response of reflection gratings recorded in this material to both humidity and temperature.

10.2 SUGGESTIONS FOR FUTURE WORK

Following the preliminary investigations described in this thesis, a number of projects could be taken up in the future:

1. Develop the studies regarding the interactions between sensitizing dyes and nanozeolite L. It would be interesting to investigate how and where molecules such as dyes and water are adsorbed/ absorbed in the zeolite structure. Neutron diffraction could be used, since neutrons are particularly suited for studying organic molecules in the voids and channels of zeolite frameworks due to their sensitivity to hydrogen. These results could be complemented by further NMR experiments.

2. Performing further studies in chemical sensing, particularly by controlling the concentrations of chemicals delivered to the polymer and study the response of the nanocomposites to the exposure to increasing concentrations of chemicals, such as different VOCs of interest

3. Continue the optimization of NIPA photopolymer by finding the composition that gives highest diffraction efficiency and by finding the best experimental conditions (such as recording intensity and exposure time) to record reflection holograms. Explore further this formulation as a sensor, for instance as potential biosensor.

10.3   LIST OF PUBLICATIONS

10.3.1   PUBLICATIONS

1. E. Leite, I. Naydenova, N. Pandey, T. Babeva, G. Majano, S. Mintova and V. Toal, *Investigation of the light induced redistribution of zeolite Beta nanoparticles in an acrylamide-based photopolymer*, Journal of Optics A: Pure and Applied Optics 11, No. 2, 024016-024024 (2009) (Special issue in nanocomposites)

2. E. Leite, I. Naydenova, T. Babeva, L. Lecquerq, S. Mintova and V. Toal, *Photopolymerisable Nanocomposites for Holographic Recording and Sensor Application*, Applied Optics 49, No. 19, 3652-3660 (2010)

3. E. Leite, Tz. Babeva, , E.-P Ng, V. Toal, S. Mintova and I. Naydenova, *Optical properties of photopolymer layers doped with aluminophosphate nanocrystals*, accepted for publication in The Journal of Physical Chemistry

4. I. Naydenova, E. Leite, Tz. Babeva, N. Pandey, T. Baron, T. Yovcheva, S. Sainov, S. Martin, S. Mintova and V. Toal, *Optical properties of photopolymerisable nanocomposites containing nanosized molecular sieves*, submitted

10.3.2 CONFERENCE PRESENTATIONS

1. I. Naydenova, Tz. Babeva, <u>E. Leite</u>, N. Pandey, S. Martin, V. Toal, Holographic sensors in photopolymerisable nanocomposites containing zeolite nanoparticles, 3rd Int. Symposium in Advanced micro- and mesoporous materials, Bulgaria 6-9 Sept 2009

2. <u>E. Leite</u>, I.Naydenova,S. Mintova and V. Toal, Acrylamide-Based Photopolymer Layers Nanocomposites for Holographic Recording, 3rd Int. Symposium in Advanced micro- and mesoporous materials, Bulgaria 6-9 Sept 2009

3. I. Naydenova, T. Babeva, <u>E. Leite</u>, N. Pandey , T. Yovcheva, S. Mintova and V. Toal, Optical Properties of Photopolymerisable Nanocomposites Containing Zeolite Nanoparticles, ODS 2009 Optical Data Storage, Florida, USA, 11-13 May 2009

4. <u>E. Leite</u>, I. Naydenova, S. Mintova and V. Toal, Acrylamide-Based Photopolymer Layers Nanocomposites for Holographic Recording, 1st International school on "Laser-surface interactions for new materials production: tailoring, structure and properties", Venice, 13-20 Jul 2008

5. <u>E. Leite</u>, I. Naydenova, S. Mintova, V. Toal, Nonlinear microscopy and Optical Control, Acrylamide-Based Photopolymer Layers Doped With Nanoparticles For Holographic Recording,, Münster, Germany, February 19-20, 2008

6. <u>E. Leite</u>, I. Naydenova, S. Mintova, V. Toal, Acrylamide-based photopolymer layers doped with nanoparticles for holographic recording, IOP Spring Meeting 2008,. Carrickmacross, Ireland, 7-9 March 2008

7. <u>E. Leite</u>, I. Naydenova, S. Mintova, V. Toal, Acrylamide-based photopolymer layers doped with nanoparticles for holographic recording, Photonics Ireland 2007, 24-26 Sept Galway, 2007